ANNUAL PROGRESS REPORT

Project Title:	Synthesis and Optimization of the Sintering Kinetics of Actinide Nitrides
Covering Period:	July 2005 – December 2008
Date of Report:	03/31/2009
Recipient:	Boise State University
Award Number:	DE-FC07 – 05ID14650
Subcontractors:	University of Florida
Other Partners:	None
Contact(s):	Darryl P. Butt, 208-426-1054, DarrylButt@BoiseState.edu Boise State University 1910 University Drive Boise, ID 83725-2075
Project Team:	John Carmack, INL (not funded); Ken McClellan, LANL (not funded); Ron Baney, UF (funded); James Tulenko, UF (funded); Tim Gerhardt, UF (funded); Le Song, UF (funded); Ravi Kumar Vasudevin, UF (funded); Brian M. Marx, BSU (funded); A. S. Hamdy (not funded); Patrick Callahan, BSU (funded); Brian Jaques, BSU (funded); Dan Osterberg BSU (funded).
Authors:	Darryl P. Butt and Brian Jaques

BOISE STATE
UNIVERSITY

TABLE OF CONTENTS

LIST OF TABLES

LIST OF FIGURES

NOMENCLATURE AND ACRONYMS

$\alpha_{)}$ – Reaction ratio
AAA – Advanced accelerator applications
ABR – Advanced burner reactor
AEI – Advanced energy initiative
AFCI – Advanced fuel cycle initiative
AmN – Americium nitride
BN – Boron nitride
$CaSo_4$ – Calcium Sulfate
CeN – Cerium nitride
CH_4 – Methane
CO – Carbon monoxide
Cu-K_α – Copper K_α electronic transition
$DyCl_3$ – Dysprosium chloride
DyH_2 – Dysprosium hydride
DyN – Dysprosium mononitride
Dy_2O_3 – Dysprosium oxide
E_a – Activation energy
E_b – Bond energy
E_{diss} – Dissociation energy
EDS – Energy dispersive x-ray spectroscopy
E_{phys} – Physisorption energy
FAST – Field assisted sintering technique
Fe_3N – Iron nitride
GdN – Gadolinium nitride
GFR – Gas-cooled fast reactor
GNEP – Global nuclear energy partnership
H_2 – Hydrogen gas
H_2O – Water
HCN – Hydrogen cyanide
He – Helium
HNO_3 – Nitric acid
JAEA – Japan Atomic Energy Agency
JAERI – Japan Atomic Energy Research Institute
JCPDS – Joint committee on powder diffraction standards
k_0 – Reaction rate
LANL – Los Alamos National Laboratory
LFR – Lead-cooled fast reactor
Li_3N – Lithium nitride
LMFBR – Liquid metal fast breeder reactors
NH_3 – Ammonia
NERI – Nuclear energy research initiative

PECS – Pulsed electric current sintering
ppb – Parts per billion
ppm – Parts per million
SEM – Scanning electron microscope
SFR – Sodium cooled fast reactor
TiN – Titanium nitride
TRU – Transuranic
U_2N_3 – Uranium sesquinitride
UC – Uranium monocarbide
UH_3 – Uranium trihydride
UHP – Ultra high purity
UN – Uranium mononitride
UO_2 – Uranium dioxide
UREX – Uranium extraction
XRD – X-ray diffraction/diffractometer
ZrN – Zirconium nitride

CHAPTER I: OBJECTIVE AND EXECUTIVE SUMMARY

1. Objective

Nitride nuclear fuels, based on UN and PuN and containing other actinides and lanthanide nitrides are candidates for the Advanced Fuel Cycle Initiative (AFCI) which currently serves, synergistically, as a fuel development program for the Global Nuclear Energy Partnership (GNEP) program. Such fuels have a combination of higher uranium loadings (thus lower enrichment can be used) and higher thermal conductivity compared to other fuel forms. It is also possible to produce inert matrix fuels from these nitrides owing to their compatibility with candidate matrices such as ZrN and refractory metals. Although several processes have been developed for synthesizing powder and monolithic forms of actinide nitrides, the sintering kinetics and mechanisms are not yet well understood. Having a quantitative understanding of the mechanism and kinetics of densification and grain coarsening is critical to both the outcome economics and product performance of any ceramics fabrication process. Through optimized processing conditions, sintering temperatures, and greatly reduced equipment size can leading to increased production rates and decreased cost. Moreover, the material and energy output properties of the fuel forms can be improved and more precisely controlled. The research conducted during this investigation will facilitate the synthesis of actinide nitride powders and provide knowledge of the kinetics of sintering of these powders. Consequently, this project will aid production of nitride fuels by reducing the infrastructure footprint, resources, and cost associated with fuel processing (and re-processing) in the advanced nuclear fuel cycle.

2. Executive Summary

Research conducted for this NERI project has advanced the understanding and feasibility of nitride nuclear fuel processing. In order to perform this research, necessary laboratory infrastructure was developed; including basic facilities and experimental equipment. Notable accomplishments from this project include: the synthesis of uranium, dysprosium, and cerium nitrides using a novel, low-cost mechanical method at room temperature; the synthesis of phase pure UN, DyN, and CeN using thermal methods; and the sintering of UN and $(U_x, Dy_{1-x})N$ $(0.7 \leq X \leq 1)$ pellets from phase pure powder that was synthesized in the Advanced Materials Laboratory at Boise State University. To date, the work reported in this document has been shared in the form of 2 scientific journal publications, one master's thesis, and 13 conference presentations on subjects including:

- Novel Ball-Milling Synthesis Route:

  This route was demonstrated by nitriding pure uranium, dysprosium, and cerium metal flakes at room temperature for 24 hours and less, yielding phase pure U_2N_3, DyN, and CeN, respectively.
- Direct Nitridation Synthesis Route:

This route was demonstrated by nitriding 99.9% pure dysprosium metal flakes at 1300°C yielding a phase pure DyN powder with an oxygen content of 0.33%.

- Hydriding prior to Nitridation Synthesis Route:

  This route was demonstrated by the synthesis of UN, DyN, and CeN. Pure uranium metal ingot pieces produced UN and UO_2, suggesting that pure UN is feasible. Pure dysprosium and cerium metal flakes produced very high purity DyN and CeN with 0.043% and 1.4% oxygen contents, respectively.
- Carbothermic Reduction prior to Nitridation Synthesis Route

  This route was demonstrated by the synthesis of UN, DyN, and CeN. The carbothermic reduction of UO_2 has proven to provide the largest amount of phase pure UN for other related studies. Also, this route has been utilized to produce low quality DyN and CeN.
- $(U_x, Dy_{1-x})N$ Pellet Sintering

  Pure UN was sintered using a traditional pressing and sintering technique in order to develop feasible procedures for sintering $(U_x, Dy_{1-x})N$ pellets. The sinterability of UN was studied by sintering 6.5 mm diameter pellets and varying multiple processing parameters including: milling time, binders, lubricants, compaction pressures, compositional range (0 – 30 mol% DyN), sintering atmosphere, sintering time, and sintering temperature.
- Oxidation Kinetics of DyN

  Thermal gravitational analysis has been performed from room temperature to 800°C to identify a suitable oxidation range for isothermal studies. Multiple isothermal gravitational analysis runs have been made for 6 hours to describe the weight change of the DyN as it converts to Dy_2O_3. The data was then fit to a total of 26 oxidation kinetic models. Initially, the reaction appears to be autocatalytic with most of weight change occurring within the first three minutes of the reaction and by fitting the autocatalytic model to the data it is shown that it fits fairly well, with an r^2 value of 0.9497.
- Solution Routes Analogous to Sol-Gel Processing:

  These routes were attempted at the UF in the synthesis of DyN and CeN but resulted in limited success due to the extremely reactive nature of the nitride materials. This route shows promise for synthesizing pure nitrides and may also be used in the future as a synthesis route for UN.
- Sintering/Hot Pressing:

  The optimum conditions for sintering pure ZrN were determined and the maximum density achieved was approximately 83 % theoretical density. Therefore, hot-pressing was used to achieve higher densities. The results of the ZrN-DyN hot-pressing clearly show that DyN does not form a complete solid solution with ZrN.
- Economic Analysis:

  The novel reactive milling technique will require less infrastructure, smaller footprint, lower energy demands, less engineers/operators, and less cost. The reactive milling technique will cost an approximate 60% less than the carbothermic reduction synthesis route.

CHAPTER II: PROJECT OVERVIEW

1. Introduction

Electricity consumption and energy needs around the world continue to rise. As demand grows, the burden of power generation is predicted to shift away from fossil fuels since they rely on limited natural resources and generate greenhouse gases. Although conservation and renewable energy sources are essential to our future, they cannot yet support a stable national (or global) energy grid. As discussed in President Bush's Advanced Energy Initiative (AEI) of 2005 [1], nuclear power is a cleaner and more stable alternative to fossil fuels and is capable of providing a significant portion of the future global energy needs. In accordance with pursuing the objectives developed within the AEI, the Global Nuclear Energy Partnership (GNEP) was introduced in 2006.

GNEP serves as a world consortium focused on advancing nuclear power generation technology and enabling nuclear power accessibility to non-nuclear nations. As nuclear power occupies a larger role in global energy production, it is vital to increase reactor efficiency, minimize waste generation and storage needs, and to ensure proliferation resistance. Nuclear power generation technologies must be advanced in order to achieve these goals. In pursuit of advancing nuclear power technologies, Generation IV advanced nuclear reactors are in development and expected to become commercial in the near term (by 2030). To support these next generation reactors and current advanced Generation III+ light water reactors, the Advanced Fuel Cycle Initiative (AFCI) of 2003 is pursuing fuel processing and reprocessing technologies for use in the primary and advanced fuel cycles. The AFCI is a direct effect of the U.S. National Energy Policy of 2001 and has been integrated into GNEP with common objectives [2].

A primary objective of AFCI is to extract nuclear energy from spent fuel products thereby eliminating the need for storing high level nuclear waste. This program concentrates on developing candidate fuel systems which emphasize the following characteristics: The fuels should 1) reduce the volume of high-level waste, 2) reduce the stockpile of long-lived and highly radiotoxic elements, and 3) reclaim the valuable energy content of spent nuclear fuel [3]. Additionally, as envisioned within GNEP, the advanced fuel cycle will enhance proliferation resistance by avoiding separations of weapons grade materials, plutonium in particular, by subsequently "burning" this material for further energy production.

Approximately 96% of spent fuel is low level uranium, which can be removed from the spent fuel by, for example, the Uranium Extraction (UREX), UREX+ chemical processes, or by pyroprocessing techniques. The remaining 4% of the spent fuel contains valuable, energy-rich transuranics (TRUs) including Pu, Np, Am, and Cm. There are several variations of the UREX and UREX+ processes available, as shown in Table 1 [4].

These separation processes remove the low level uranium from other products in spent fuel. Some of the transuranics (TRUs) in the products (Pu, Np, Am) can be used to generate additional nuclear energy when properly mixed and synthesized into useful fuel forms. The remaining products (Cs, Sr, Tc) may be transmuted to isotopes with shorter half-lives, at which point they would not be considered high level nuclear waste. The AFCI will increase the amount of energy recovered by partitioning and transmuting spent fuel. These products will then be processed into a new fuel and "burned" in an advanced reactor, thereby reducing the amount of high level waste requiring long term storage in geological repositories such as the proposed Yucca Mountain.

Table 1: Available UREX+ Processes and the Extracted Products [4].

Process	**Products**						
	1	2	3	4	5	6	7
UREX+1	U	Tc	Cs/Sr	TRU+Ln	FP's	-	-
UREX+1a	U	Tc	Cs/Sr	TRU's	FP's	-	-
UREX+2	U	Tc	Cs/Sr	Pu+Np	Am+Cm+Ln	FP's	-
UREX+3	U	Tc	Cs/Sr	Pu+Np	Am+Cm	FP's	-
UREX+4	U	Tc	Cs/Sr	Pu+Np	Am	Cm	FP's
TRUs - Transuranics (Pu, Np, Am, Cm)							
FPs - Fission products other than Cs, Sr, Tc, I, and Ln.							

As previously stated, the TRUs suitable for an additional fuel cycle must be synthesized into useful fuel forms. Once a fuel composition has been identified and produced, the powder may be pressed and sintered into a conventional fuel pellet form for use in an advanced burner reactor (ABR). These fuels aim to comply with the objectives of the GNEP to avoid the risks of proliferation by avoiding the breeding of plutonium. As seen in Table 2, the fuels have been classified into two primary groups, namely: non-fertile and low-fertile fuels. The fuels which contain no uranium are considered non-fertile fuels because they breed no plutonium (due to the daughter product of U being Pu) and the fuels which contain minimal amounts of uranium are considered low-fertile because they breed little plutonium [5-7].

Table 2: Candidate Non-Fertile and Low-Fertile Fuels for AFCI [5-7].

Non-Fertile Fuels
$Pu_{0.48}$-$Am_{0.12}$-$Zr_{0.40}$
$(Pu_{0.50}, Am_{0.50})N$ + 36-wt% ZrN*
$(Pu_{0.20}, Am_{0.80})O_2$ + 65-vol% MgO
$(Pu_{0.50}, Am_{0.50})O_2$ + 70-vol% MgO
$(Pu_{0.23}, Am_{0.25}, Zr_{0.52})O_2$ + 60-vol% Mo^{92}
$(Pu_{0.50}, Am_{0.50})O_2$ + 60-vol% Mo^{92}

Low-Fertile Fuels
$U_{0.35}$-$Pu_{0.29}$-$Am_{0.04}$-$Np_{0.02}$-$Zr_{0.30}$
$(U_{0.50}, Pu_{0.25}, Am_{0.15}, Np_{0.10})N$*

*Fuel compositions of interest to this study.

In Table 2 it is seen that candidate non-fertile and low-fertile fuel forms for Generation IV reactor applications are primarily nitride and oxide fuels. Nitride fuels are favored over the oxide fuels due to their higher density of actinides, lower enrichment, and higher thermal conductivities (by approximately 5-10 times) [5-15], leading to lower "burning" temperatures and decreased cladding compatibility concerns. Although the nitrides are more efficient fuel forms, there are some disadvantages associated with them. Single phase mononitrides can be difficult to synthesize, difficult to handle (especially in the powder form due to their pyrophoric nature when exposed to oxygen), and difficult to analyze. Also, a great concern is the transmutation of ^{14}N into ^{14}C, a long-lived radiotoxic isotope which affects the neutronics of the fuel [7, 16, 17]. Consequently, the fuels will need to be synthesized using ^{15}N, a costly alternative to ^{14}N.

To increase the feasibility of mass production of the nitride fuels, factors affecting the synthesis of high purity single phase mononitrides must be better understood. The gained insight will guide optimized processing conditions and reduced equipment size, leading to increased production rates and decreased costs. However, optimization of processing conditions is characterized by analysis of the microstructure of the sintered pellets. The character of the microstructure is best understood by identifying a quantitative model that accurately describes the affects of changing certain processing parameters. The defined model provides insight to the mechanisms and kinetics of densification and grain coarsening in the synthesis of these fuels. Insight provided by this quantitative model allows for the material properties of the fuel to be precisely controlled and varied. Consequently, this research will aid the production of nitride fuels by reducing the infrastructure footprint, resources, and cost associated with fuel processing (and re-processing) in the advanced nuclear fuel cycle. The research conducted during this investigation facilitates the synthesis of uranium nitride (UN) and dysprosium nitride (DyN) powders and provides insight to the affects of processing parameters on the mechanisms and kinetics of sintering these powders.

2. Surrogate Fuels

In order to fulfill the objectives of this NERI project, it is possible to conduct research on the synthesis of nitride based nuclear fuel systems without necessarily having to use highly radioactive materials. It is known that numerous engineering and administrative controls are required when working with even minute quantities of radio-isotopes such as Pu, Am, and Np. Working with these hot isotopes introduces complications and it is therefore more efficient to begin with non-radioactive elements with similar properties to their radioactive counterparts, also known as surrogates. Using surrogates greatly reduces the number of safety procedures that are required and dramatically reduces the overall time and cost necessary in setting up and performing work in the laboratory. Although surrogates have value, it should be noted that they will not necessarily provide a perfect comparison for actinide synthesis and sintering. They do, however, reduce worker exposure and associated experiment costs. If the surrogates are selected carefully through in-depth comparisons of thermodynamic, crystallographic, and other physical and chemical properties, accurate processing parameters can be identified for use in the synthesis of the actinide systems of interest.

Surrogates for actinide metals, oxides, and carbides have been suggested and studied by numerous authors for many years, dating back to the 1950's [18-42]. However, surrogates for actinide nitrides have primarily been considered since the late 1980's when renewed interests in nitride fuels were invoked with the SP-100 space nuclear program and the succeeding (advanced accelerator applications) AAA, AFCI, and GNEP programs [2, 5, 6, 8, 30, 43-48]. With this timeframe in mind, the effects of nitride surrogates on sintering are inadequately understood because they have been studied less than the other fuels forms.

To begin studying the synthesis of nitride fuel forms, it is convenient to compile a variety of material properties for comparing the candidate surrogate materials. From reviewing literature and multiple materials databases, a distilled list of crystallographic and thermodynamic properties of nitride candidates have been collected and organized. The compiled data includes; crystal structures, lattice parameters, densities, melting points, thermal conductivities, linear thermal expansion coefficients, and free energies of actinide and candidate surrogate materials (APPENDIX A).

For the past 60 years, cerium has been used as chemical surrogate for plutonium, and CeO_2 has been shown to be a good surrogate for PuO_2, based on diffusivities and thermodynamic properties [31, 49, 50]. However, it has not been demonstrated that CeN is necessarily an appropriate surrogate for PuN. The lattice parameters for CeN and PuN are close, but the density and coefficient of thermal expansion for CeN are about half that of PuN (APPENDIX A). In general, free energy data for these materials shows that depleted UN has thermodynamic properties closer to PuN than those of CeN. Further experimental results should provide some insight into whether depleted UN or CeN is the better candidate.

From the data compiled from the reviewed literature, the best candidates for AmN have been identified as GdN, DyN, and ZrN. Due to the adverse effects that the high vapor pressure of AmN induces into the sintering of the nitride fuels, it is one of the main attributes that the identified surrogate should possess. The high vapor pressure of DyN is the primary reason that it has been chosen for these studies. In accordance with the literature review, authors have shown that the electrochemical properties, vaporization behaviors, and nitriding behaviors of DyN and AmN are similar [6, 8, 30, 45-47]. Unfortunately, not all properties for these two materials can be obtained in the reviewed literature in order to make a more complete comparison. Therefore, the use of DyN as a surrogate for AmN is based on some speculation. Also for these studies, highly enriched UN (^{235}U) will be replaced by depleted UN (^{238}U) which is much less radioactive and reduces handling risks.

The two proposed nitride nuclear fuel forms and their corresponding surrogate fuel forms used for research purposes in this project are displayed below:

Actual Fuel = Surrogate Fuel

(Pu0.50, Am0.50)N + 36-w%ZrN = (Ce0.50, Dy0.50)N + 36-w%ZrN

(U0.50, Pu0.25, Am0.15, Np0.10)N = (U0.50, Ce0.35, Dy0.15)N

Although testing and comparison is required to validate the knowledge gained using surrogates, the time and resources saved is advantageous to processing “hot” materials. Moreover, concurrent NERI projects at the University of Nevada Las Vegas, Los Alamos National Laboratory, Arizona State University, University of Florida, and Virginia Tech use similar surrogate methods to aid radiological materials research. Included in these surrogate studies, the Japan Atomic Energy Research Institute (JAERI) and Japan Atomic Energy Agency (JAEA) are also actively pursuing surrogate analysis.

CHAPTER III: FACILITIES

The Advanced Materials Laboratory at Boise State University is continuing to develop all of the technologies required for powder synthesis, characterization and sintering, as related to nitride fuels. Funding for the construction of this new laboratory came partly through this NERI, but primarily through internal university funds and other equipment grants of the principle investigator (PI). The laboratory was initiated with the arrival of the PI of the project in the summer of 2005 and has expanded to accommodate a wide variety of powder synthesis and characterization tools.

1. Gloveboxes

Due to the reactive nature of the metal, hydride, and nitride powders, all of the materials used in this work were handled and stored in inert atmosphere gloveboxes. Figure 1a shows a Plas-Lab 870-CLC (Lansing, MI, USA) glovebox for storing and preparing samples for synthesis and analysis as well as a containment measure for depleted uranium materials. The glovebox is maintained with less than 1000 ppm of oxygen with a constant flow of argon gas. Located inside this glove box are; a hydraulic press for powder pellet pressing, a Scientech (Boulder, CO, USA) balance with 0.01mg accuracy, and an electrochemical oxygen monitor (Advanced Instruments Inc., Pomona, CA, USA). Figure 1b is a heavy duty stainless steel glove box containing a Barnstead Thermolyne 21100 1200°C tube furnace for low temperature hydrogen processes as a precursor to nitride synthesis.

a) b)

Figure 1: Two argon filled gloveboxes for material handling and storage. Figure a) shows the Plas-Lab closed loop containment isolator glove box for sample preparation and storage. The Plas-Lab glovebox also contains a hydraulic press and balance. Figure b) shows the heavy-duty stainless steel glovebox containing a 1200°C tube furnace for low temperature hydrogen synthesis routes.

2. Process Gas Capabilities

Many of the experiments performed in this work require a variety of processing gases with controlled oxygen contents and, in some cases, copious amounts of these gases to run the experiments to completion. The gas handling in the Advanced Materials Laboratory at BSU has been specifically designed to meet these needs. Shown in Figure 2a is the gas manifold that provides processing gases to all furnaces, gloveboxes, and other equipment within the laboratory through 0.25 inch stainless steel tubing. Nitrogen and argon gases both consist of two cylinders of ultra high purity gas in parallel to allow for interchanging the cylinders without disrupting the flow of gas for processing. Also, the manifold is connected to a vacuum system to remove the residual oxygen in the lines due to replacing empty cylinders. Each of the cylinders is regulated through stainless steel or brass regulators to control the outlet pressure from 0-100 psi. This particular manifold contains nitrogen, argon, 20% oxygen with a nitrogen balance, and 6.28% hydrogen with a nitrogen balance. However, in some specific applications this research requires the use of ultra high purity hydrogen and anhydrous ammonia gas. The necessity to store flammable and toxic gases requires a volatile storage cabinet to ensure safety of the laboratory. This cabinet provides shelter from ignition sources as well as containing and ventilating gas leaks. Figure 2 shows the cabinet with the doors open showing the storage of the gases.

a.) b.)

Figure 2: Process gas storage capabilities in the Advanced Materials Laboratory at BSU. a.) Photograph of the ultra high purity gas cylinder distribution manifold containing argon, nitrogen, 20% oxygen with a nitrogen balance, and 6.28% hydrogen with a nitrogen balance. b.) Photograph of the open volatile gas cabinet containing ultra high purity hydrogen and ammonia for gas storage and distribution.

3. High Temperature Tube Furnaces

The furnace capabilities in the Advanced Materials Laboratory are very specialized for nitride powder processing. These furnaces are used to synthesize oxygen sensitive materials from pyrophoric or oxygen sensitive materials themselves. The three main furnace systems used for this work are shown in Figures 3 and 4. Figure 3a shows a high temperature nitrogen, argon, nitrogen/oxygen mixed gas, or nitrogen/hydrogen mixed gas furnace system with 10^{-3} Torr vacuum capabilities. This system contains high purity gas flowing through; a Drierite $CaSO_4$ moisture-getter, MKS digital mass flow controllers, a 3-zone Lindberg tube furnace containing a copper ribbon filled quartz tube for oxygen-gettering, a ppm range Neutronics OA-1 oxygen analyzer, and a 1700°C Thermolyne high temperature alumina tube (2 inch diameter) furnace with molybdenum disilicide heating elements and an attached Leybold vacuum pump. Figure 3b is a Barnstead Thermolyne 21100 tube furnace for low temperature hydrogen processes as a precursor to nitride synthesis. The Barnstead tube furnace is placed in the inert atmosphere glovebox of Figure 1b to allow sample insertion and removal reducing reactions with oxygen. It can be operated in a 10^{-3} Torr vacuum or in argon, nitrogen, nitrogen/hydrogen mixed gas, nitrogen/oxygen mixed gas, and ultra high purity hydrogen. The furnace has capabilities of 1200°C, but with a 1 inch diameter stainless steel reaction chamber, the maximum temperature is significantly reduced.

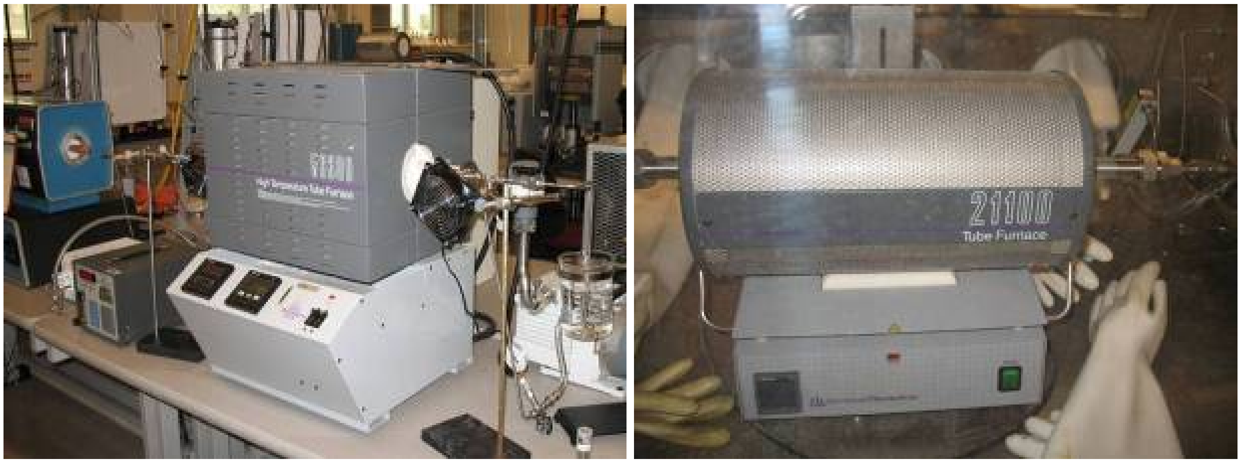

a.) b.)

Figure 3: Furnaces in the Advanced Materials Laboratory for processing nitrides. a) Photograph of a high temperature Thermolyne 59300 tube furnace equipped with oxygen and moisture-gettering capabilities. b.) Photograph of a Barnstead Thermolyne 21100 tube furnace for low temperature hydrogen processes. The Barnstead tube furnace is located in an inert atmosphere glovebox to allow oxygen sensitive sample insertion and removal.

In order to achieve the very demanding atmospheres required for the various synthesis and sintering processes, a high temperature alumina tube furnace (CM Furnaces Inc., Bloomfield, N.J., USA) was redesigned and built. The original 1730-12 High Temperature Furnace and Vacuum Assembly was equipped with a 3.5 inch alumina tube and had capabilities of 10^{-3} Torr pressures via a rotary vane vacuum pump and a maximum working temperature of 1700°C via molybdenum disilicide resistive heating elements (Figure 4a). This furnace was purchased with the intentions of redesigning the system for high temperature and low pressure synthesis routes with, or without, reactive gases. The redesigned furnace components that integrate a turbo-molecular pump into the existing CM system to obtain lower pressures are shown in Figures 4b and 4c. The system was initially designed in a computer aided design software, Solidworks® (Figure 4b) to meet spatial requirements before the respective components were ordered and assembled. The implemented design is shown in Figure 4c. With the new design, the furnace is able to achieve very low pressures (10^{-6} Torr as measured with a Leybold ITR90 hot cathode ionization sensor) and has capabilities of processes containing hydrogen and ammonia as well as the other common gases used for nitride synthesis and sintering experiments. In order to increase and measure the purity of the already high purity processing gases, the non-corrosive gases flow into a Drierite (Xenia, OH, USA) $CaSO_4$ desiccant to remove moisture, a Restek Thermal Gas Purifier (Bellefonte, PA, USA) to remove oxygen, a ppm range Ntron Model OA-1 (Exton, PA, USA) oxygen analyzer, and an Ametek 303B Moisture Monitor (Pittsburgh, PA, USA) prior to being introduced into the 99.8% pure alumina tube (Coorstek, Golden, CO, USA) of the furnace. The corrosive gases flow directly from the compressed gas cylinder into the tube of the furnace. All gases exit the alumina tube through a low pressure (bellows-sealed) valve before entering a water bubbling system and exiting through a glass condenser into the exhaust system.

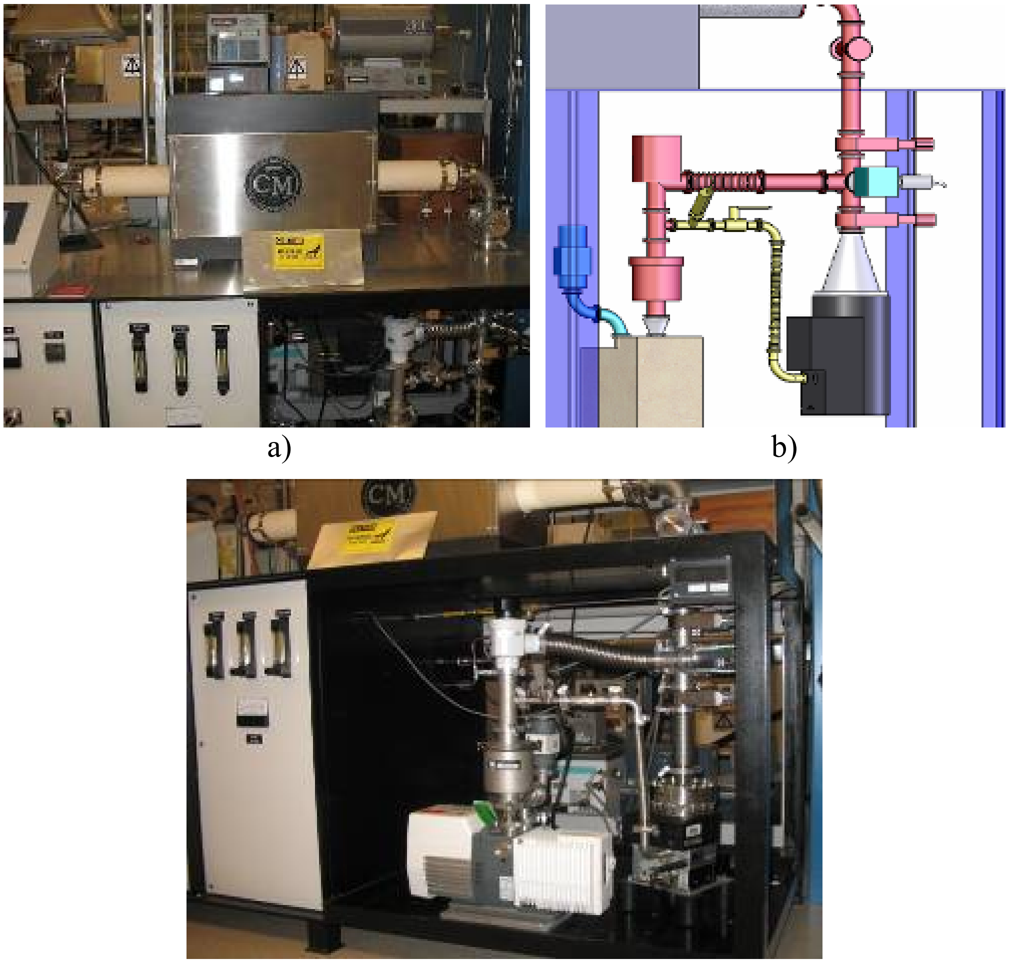

a) b)

c)

Figure 4: a) A high temperature (1700°C), low pressure CM alumina tube furnace for nitride powder synthesis and sintering. This furnace was redesigned in solid modeling software (Solidworks®) to incorporate a turbo-molecular pump to obtain 10^{-6} Torr pressures and handle ultra high purity hydrogen and ammonia gases for nitride synthesis and sintering. Figure c) shows the implemented solid model rendering that is shown in b).

4. Powder Milling System

A Retsch PM 100 planetary ball mill was procured with internal BSU funds to continue to develop the powder processing capabilities in the Advanced Materials Laboratory. The planetary ball mill is a versatile piece of equipment in these applications. The mill is used to implement novel nitride powder synthesis techniques, control particle size distribution, and thoroughly blend, pulverize, or mill powders (both uranium based and non-uranium based). The maximum operating rotational speed of the ball mill is 500 rpm and is used to mill materials to sub-micron particle sizes while accommodating a 500 ml 7 kg container load. The PM 100 is shown in Figure 5a, along with a 250 ml chrome steel milling jar (Figure 5b) containing an aeration cover allowing repeated purges and charges of compressed gas and/or vacuum to replenish/purify the internal environment. It can be charged to a maximum pressure of approximately 485 kPa with gas and can be evacuated to 10^{-3} Torr for novel nitride synthesis applications. This novel route includes the mechanically induced gas-solid reaction of metals with nitrogen to form the desired nitride powders, as further discussed later in this report.

a) b)

Figure 5: a) Photograph of the Retsch Planetary ball mill (PM100) for pulverizing, blending, milling, or synthesis of uranium based and non-uranium based powders. b) Photograph of a 250 ml milling container with aeration cover allowing repeated purges and charges of compressed gas or vacuum for novel powder synthesis capabilities.

5. Particle Size Analyzer

While the mill is able to control the particle size to sub-micron sizes, a particle analyzer is needed to confirm the size. For this reason a Horiba LA-950 Laser Scattering Particle Size Distribution Analyzer (Minami-ku Kyoto, Japan) (Figure 21) has been procured. This analyzer is able to measure particles from 0.01 to 3000 µm in either wet or dry mode with extreme accuracy of ±1% using a folded Reverse Fourier optical arrangement with two solid-state light sources. The particle size is determined by correlating the intensity and angle of scattered light from a particle. As the particle size becomes smaller, the scattered light signal shifts to the side and rear with respect to the light source. In wet mode, it is able to analyze particles in a variety of different dispersants, including but not limited to: water, acetone, toluene, isopropyl alcohol, and various paraffin oils.

Figure 6: Photograph of a Horiba LA-950 Laser Diffraction Particle Size Analyzer for use in characterizing powder particle size, including powders from: Commercial vendors, those synthesized in the planetary ball mill, or those synthesized by conventional furnace techniques for sintering studies.

6. Green Pellet Forming Capabilities

Once the nitride powders have been thoroughly mixed and characterized with the ball mill and particle size analyzer, respectively, the next step is to study their sintering behaviors. Often, it is desirable to press the powders into pellets to simulate a fuel form and provide intimate contact between particles prior to sintering. For green powder pellet pressing, two Carver 12 ton hydraulic presses with heated platens have been set up: one is located in the Plas-Lab inert atmosphere glovebox, as shown in Figure 1a and the other is located on the bench top in atmospheric conditions, as shown in Figure 87a. The Advanced Materials Laboratory has capabilities to press two different diameter pellets with a 13 mm stainless steel pellet die (Figure 87b) and a 6.35 mm carbide pellet die (Figure 87c) with a titanium nitride coated tool steel plunger. A pellet is made by loading the powder into one of the dies, leveling it off, and pressing with the hydraulic ram to a specified pressure/force prior to loading it into a furnace to be sintered.

a) b) c)

Figure 7: Green pellet forming capabilities in the Advanced Materials Laboratory. a) Photograph of a 12 ton Carver hydraulic press with heated platens for pressing nitride powders. There is also one of these presses located inside an inert atmosphere glovebox to control the oxygen exposure to the powders. b) Photograph of a 13 mm pellet die and c) a 6.35 mm pellet die used when making the green pellets for sintering studies of the nitride powders.

7. Balance with the Immersion Density Measurement Kit

After the sintering of a green pellet, one of the most important quantitative measures of characterization is pellet density. Due to the porous nature of ceramic materials, an immersion method based on Archimedes' principal is the most accurate method for density measurements. For this reason, a Mettler Toledo AB54-S/FACT balance (0.1 mg resolution) with a density measurement kit (Figure 8) was purchased.

Figure 8: Photograph of the Mettler Toledo scale with the immersion density measurement kit attached. The kit provides immersion weights that, using Archimedes' principle, can be correlated to the density of nitride fuel pellet.

8. Simultaneous DSC/TGA Equipment

The presented here also includes the study of the oxidation kinetics of the various nitride powders. Therefore, a TA Instruments SDT 2960 Simultaneous DSC/TGA (Figure 9) was setup and calibrated with nitrogen, argon, and nitrogen/oxygen mixed gases. The SDT 2960 communicates with *Thermal Solutions* software for Windows® and is capable of performing both differential scanning calorimetry or differential thermal analysis (DSC/DTA) and thermogravimetric analysis (TGA) measurements at the same time. It is capable of a 100°C/min heating rate to 1000°C and 25°C/min to 1500°C with 1°C accuracy (based on metal melting standards). This instrument was used to conduct initial kinetics experiments on the oxidation of dysprosium nitride, as described later in this document.

Figure 9: Photograph of TA Instruments SDT 2960 Simultaneous DSC/TGA that is used to study the oxidation kinetics of the nitride powders. This instrument is capable of reaching 1000°C in 10 minutes and 1500°C in 30 minutes with 1°C accuracy and can record DSC, DTA, and TGA data.

University of Florida Facilities (For Solution Synthesis Routes)

Another novel synthesis route of the nitrides is a method analogous to the sol/gel method and is being performed at the University of Florida. With this method, the nitrides again have high oxygen affinities. For this reason, the materials must be handled in an inert atmosphere to avoid oxidation and a glove box is a necessity for this novel synthesis route. The glovebox shown in Figure 10a has been setup specifically for handling these materials. The sol/gel route also requires specialized glassware and adequate fume-hood to capture the toxic vapors. The current setup for this at UF is shown in Figure 10b.

a.) b.)

Figure 10: a) Photograph of the UF glove box set-up for handling the cerium compounds use for sol-gel synthesis route. b) Photograph of Schlenk glassware inside a chemical hood at UF used for sol gel synthesis of CeN.

CHAPTER IV: SYNTHESIS OF NITRIDE MATERIALS

Nitride materials have a variety of possible applications due to their refractory nature and high thermal conductivities, making them primary candidates for use in fast-spectrum reactors. As seen in Table 3, three of the six Generation IV reactors proposed by the AFCI of 2003 suggest nitride fuels as a feasible fuel option. Of the reactors listed in the table, the ones able to incorporate nitride fuels include: the Gas-Cooled Fast Reactor (GFR), the Lead-Cooled Fast Reactor (LFR), and the Sodium-Cooled Fast Reactor (SFR) [51, 52]. The nitrides have been identified for these reactor-types primarily due to their desirable properties such as; high melting temperatures combined with greater actinide densities and greater thermal conductivities when compared to other fuel forms [5-15]. However, due to their propensity for oxidation, handling concerns arise when considering different synthesis techniques and the partial pressure of oxygen is a significant factor in the purity of the nitride materials. Due to these concerns stemming from the reactive nature of the nitrides, the work presented in this chapter aims to investigate thermal and novel synthesis techniques to better assess the economic feasibility of producing high purity powders.

Table 3: A table showing characteristics of the six Generation IV reactor candidates. Adapted from [51, 52].

Reactor Type	Acronym	Neutron Spectrum	Temp (°C)	Fuel	Fuel Cycle	Size (MWe)
Gas-Cooled Fast Reactor	**GFR**	Fast	850	UO_2, UN, UC	closed, on site	288
Lead-Cooled Fast Reactor	**LFR**	Fast	550-800	UO_2, UN, UC	closed, regional	50-150
Molten Salt Reactors	**MSR**	Epithermal	700-800	UF_4 in salt	closed	1000
Sodium-Cooled Fast Reactors	**SFR**	Fast	550	UO_2, UN, UC	closed	150-500
Supercritical-Cooled Fast Reactors	**SCWR**	Thermal or Fast	510-550	UO_2	open, thermal	1500
Very High-Temperature Gas Reactors	**VHTR**	Thermal	1000	UO_2	open	250-600

The objective of this chapter is to demonstrate the ability to synthesize high purity select nitrides including uranium mononitride (UN), dysprosium mononitride (DyN), and cerium mononitride (CeN) using starting materials that simulate the products of various separation techniques. These studies focus on thermal and novel (room temperature) synthesis routes to the proposed mononitrides. In addition to demonstrating relatively well known thermal routes, this work also investigated alternative methods such as direct nitriding, hydride to nitride transformations, and a mechanically induced nitridation of the pure metals at room temperature. UN has traditionally been synthesized using a carbothermic reduction of uranium dioxide (UO_2) prior to nitriding, which is a long process at high temperatures but is well documented and studied. However, there exists no documented work prior to this work that demonstrates the synthesis of UN, DyN, or CeN by directly nitriding the metal and only a couple of documents have been found that demonstrate the synthesis of these nitrides using a nitrogen-hydrogen mixed gas. As previously stated, ball-milling a metal at room temperature to produce a nitride is a simple, economic, and novel synthesis route that has never been demonstrated with any actinide or lanthanide.

The better understood and more traditional carbothermic reduction of the oxide prior to nitridation synthesis technique is a thermal route that has been proven to provide large quantities powders, but requires many steps and a relatively costly infrastructure. The costly infrastructure is due, in part, to the high temperatures and long times required to complete the reactions as well as the typical equipment used, including refractory metal furnaces, which require large amounts of space and money. Another major concern with the carbothermic reduction synthesis technique is that it leaves undesirable residual carbon and oxygen impurities in the resultant powder. However, synthesizing a nitride from the pure metal (as opposed to the metal oxide) reduces the number of synthesis steps, thereby minimizing the time and risks associated with handling the nitrides. The fewer steps are a direct correlation to utilizing the pure separated metals as the starting materials. Due to the fact that the end result of the pyroprocessing separation techniques are materials separated in the metal form, it inherently suggests that utilizing the pure metal as a starting material for nitride synthesis will yield the most economic synthesis techniques with the least amount of handling steps, and therefore the least amount of associated risks.

1. Synthesis of Uranium Mononitride (UN)

UN has been considered as an advanced nuclear fuel for space nuclear reactors identified within the SP-100 program as well as developmental fast-spectrum nuclear reactors since the 1970's [11, 13, 14, 53-56]. The potential use of nitride fuel forms as high performance nuclear fuels has been previously established. A historical review paper by Bauer [57] and a detailed book on liquid metal fast breeder reactor (LMFBR) fuels by Matzke [56] provide a comprehensive overview of UN and (U,Pu)N material synthesis, properties and fuel performance. Compared to other material compositions in the nitride-nuclear fuel system, mononitrides are the most stable, experience higher burn-ups, and can handle the highest actinide loading. Conversely, mononitrides are difficult to synthesize and often require reduction from sesquinitrides. If a reduction synthesis route is not pursued, direct nitriding may require intensive refining procedures to reduce the amount of impurities in order to meet the stringent nuclear fuel specifications.

Recently there has been a renewed interest in nitrides for use in new and next generation nuclear reactor fuel cycles in order to efficiently produce power and significantly reduce the amount of high-level radiological waste [13, 58]. Several methods for producing uranium mononitride (UN) powder have been successfully developed and Matzke [56] describes the four primary synthesis routes for UN powder as; directly nitriding uranium metal in NH_3, nitridation by arc melting uranium metal in N_2, hydriding pure uranium metal prior to nitriding, and a carbothermic reduction of UO_2 prior to nitridation. Muromura, *et al.* [59] further classifies these synthesis routes by means of the raw starting materials as follows:

I. Uranium halide
    a. $UCl_4 + NH_3$
    b. $UF_6 + Li + N_2$
    c. $UF_4 + Si + N_2$
    d. $UCl_4 + Al + N_2$
II. Uranium metal or hydrided uranium
    a. $UH_3 + N_2$
    b. $U + N_2$
    c. $UH_3 + NH_3$
    d. $U + NH_3$
III. Uranium oxide
    a. $UO_2 + 2C + NH_3$
    b. $UO_2 + 2C + N_2$
    c. $UO_2 + (2 + x)C + N_2$

A brief background of a number of these established routes as well as more recent efforts in UN synthesis are presented in the following text.

At the time of Bauer's review in 1972, a fairly well established route for bench scale UN production was in existence [57]. The route consisted of hydriding uranium metal to provide a reactive powder at approximately 250°C, followed by nitridation to produce U_2N_3, and finally a vacuum reduction between 800°C and 1500°C. A similar direct nitriding process was also used whereby uranium metal was directly nitrided at 850°C followed by a reduction step at 1150-1400°C. Both of the synthesis routes Bauer *et al.* [57] produced UN with acceptably low (200-500 ppm) oxygen concentration and high purity. However, scaling up production would require a significant infrastructure investment.

Cleveland, *et al.* [60] used a similar approach and also found that the formation of the hydride could be done by reacting the metal with H_2 at 200 – 300°C. Further reaction of the hydride with nitrogen at 750°C formed the nitride and heating the product in vacuum at 1400°C decomposed any U_2N_3 that may have been formed.

The most detailed study of the synthesis of UN via the hydride prior to nitridation method was by Oi, *et al.* [61], who synthesized 50 grams of high purity UN starting with uranium metal that was cleaned with 8 M HNO_3. The metal was first washed with acetone prior to placing in a quartz reaction tube and subjected to high purity H_2 at 160°C for three hours. The gas was then switched to high purity N_2 and the temperature was raised to 320°C for one hour to form U_2N_3. To reduce the powder to uranium mononitride, the atmosphere was changed to high purity argon and the temperature was raised to 1200°C for one hour. However, according to a thermogravimetric study in Oi's work, it is suggested that the hydride step should occur at 320°C and the nitride step at 800°C. Also, at these lower temperatures of hydriding and nitriding it was found that finer particles were obtained, which is typically more ideal for sintering into useful forms.

Using techniques similar to those described by Oi, Cleveland, and Bauer, [57, 60, 61], Paljevic, *et al*. [62] also synthesized UN starting with pure uranium metal. The metal was first cleaned with ethanol and concentrated HNO_3 prior to drying in H_2 and being subjected to 250°C, where the metal was converted to UH_3. The environment was then changed to high purity nitrogen and the temperature was raised to 900°C for 3 hours to form U_2N_3. In order to form the desired mononitride, the U_2N_3 was heated at 1200°C in vacuum for 1 hour resulting in UN (94.38 percent uranium and 5.54 percent nitrogen by weight). Paljevic, *et al*. [62] then used this material to study the oxidation kinetics of UN. Olschewski, *et al*. [17] used a very similar method to achieve similar results.

Rogozkin, *et al*. [63] made a (U,Pu)N solid solution by melting the metallic actinides together in vacuum at 1200°C for 30 minutes. The alloy was placed in an electric furnace in a stainless steel crucible prior to being hydrided with pure H_2 at 220°C and then nitrided in pure N_2 at 220-550°C. These procedures gave 30-40μm dendritic particles with 6.4-6.7 mass percent nitrogen and less than 0.1 mass percent carbon and oxygen.

Similar techniques were used by Delvoye, *et al*. [64], who also described the synthesis of (U,Pu)N. The alloy was synthesized by first hydriding the alloy in an Ar – 10% H_2 mixed gas environment. The environment was then changed to high purity N_2 at an unspecified temperature and a nitride alloy ($O_2 < 100$ ppm) was obtained by reaction with N_2 prior to dissociation under vacuum. However, this particular work focused on limiting the risks of explosion during preparation of these materials and the preparation techniques were rather vague.

In another synthesis route that used the pure metal as the starting material, Cleveland, *et al*. [60] introduced a method where uranium nitride is synthesized by reacting a solution of the iodide with a solution of sodium, potassium, or calcium in anhydrous liquid ammonia. The method was relatively rapid and yielded a product that requireed no ball-milling prior to sintering. The process began by reacting uranium metal with hydrogen at room temperature to produce uranium hydride. The product was then reacted with HgI_2 at 200°C for 2 to 3 hours to form uranium tetra-iodide (UI_4). The product was purified by heating under vacuum at 250°C. Alternatively, one can synthesize UI_4 by reacting UO_2 with a stream of CCl_4 vapor at 800°C to 900°C to form uranium tetrachloride (UCl_4). The UCl_4 was then heated in a mixture with NH_4I to form UI_4 and volatile NH_4Cl. The precipitated UI_4 was purified for 6 hours at 200°C to remove any remaining NH_4Cl. Finally, the UI_4 product was dissolved in ammonia and mixed with a solution of sodium in ammonia whereby UN precipitates form [60]. This chemical synthesis route has several desirable attributes because it is a low-temperature, relatively rapid, and potentially low cost process. The primary drawback is in the purity of the product, which can have an impurity content of approximately 10%. These impurities may escape during sintering, but it is yet to be determined the extent that impurity levels will decrease. It is likely that further purification of the UN would be necessary in order to produce a viable fuel composition with predictable and robust mechanical properties.

A synthesis technique, termed in this document as the carbothermic reduction prior to nitridation synthesis technique, is the only route demonstrated for producing large quantities of high purity UN. Muromura, *et al.* [59] studied this carbothermic reduction prior to nitridation of a UO_2 and carbon powder mixture in NH_3. In this work, the carbothermic reduction was carried out in an evacuated induction furnace ($P = 10^{-8}$ atm) connected to a gas supply system. The pellets were heated in a molybdenum crucible between 1400°C and 1600°C in a 1 atmosphere reactant gas stream. Relatively rapid conversion from the oxide to nitride was achieved (hours to days) in an ammonia gas atmosphere. Muromura, *et al.* [59] observed a strong correlation between the reaction time needed to complete the conversion, the reaction atmosphere, and the C/UO_2 ratio. The reaction time decreased with increasing temperature and the C/UO_2 ratio decreased with increasing hydrogen content in the reaction atmosphere [59]. Although the process has been successfully demonstrated on a small scale at Los Alamos under the SP-100 program, efforts to produce large-scale quantities of high purity nitride fuels have been problematic [65].

Matthews, *et al.* [11] investigated the synthesis of uranium nitride fuel specifically for application of space power reactors and ultimately fabricated a full core of material for the SP-100 program. This work was based upon the methods devised by Muromura, *et al.* [59] and the carbothermic reduction process used to fabricate carbide fuels. The experimental procedure matched the previous method with one minor difference; the reaction involved using a N_2 - 6% H_2 gas mixture instead of NH_3 due to safety reasons. The authors note that the residual oxygen and carbon levels are very sensitive to batch size and reducing-gas flow rate therefore it is likely that this would be a difficult route to scale up to produce larger quantities of nitride powders. Matthews' approach is an adaptation of that of Muromura, *et al.* [65] and hence the positive and negative aspects associated with this process are similar to those previously mentioned.

Of the methods developed for the production of UN, the process investigated by Matthews, *et al.* [11] is the most accepted route. Although the process requires high temperature furnaces, the starting materials (UO_2 and C) are significantly less expensive than those proposed by Cleveland, *et al.* [60] (U metal, HgI_2, CCl_4, and NH_4I). The completely dry carbothermic reduction process also avoids the production of intermediate solutions and unnecessary creation of avoidable waste. More importantly, the process produces a final product that is significantly more pure, resulting in impurities on the order of 500 - 1000 ppm [11]. The disadvantage to this method is the high temperature at which the reactions must take place, which increased processing costs and created challenges for the process engineers that carryout the fabrication steps in gloveboxes.

As presented in the preceding paragraphs, many authors have studied various synthesis routes for producing large quantities of high purity nitride powders [11, 13-15, 17, 57, 59-77]. Much of this previous work has focused on optimizing the carbothermic reduction of UO_2 prior to nitriding to form UN [11, 13-15, 59, 65, 67-70, 72-77]. However, the carbothermic reduction synthesis route requires many steps and a costly infrastructure, as previously described. The many steps could potentially introduce oxygen impurities and the carbothermic reduction can leave residual carbon. Also, in only a few reports, pure uranium metal was used as the starting material for a direct nitridation route via hydriding as well as various aqueous routes [17, 57, 60-64, 66, 71]. This work further explores the synthesis of UN via non-traditional and traditional routes including a carbothermic reduction prior to nitridation synthesis route, a hydride-nitride synthesis route, and a novel ball-milling synthesis route.

1.1. Carbothermic Reduction Prior to Nitridation Synthesis Route to UN

As previously stated, many authors over many years have demonstrated the synthesis of UN via a carbothermic reduction of UO_2 prior to nitriding in a N_2, $N_2 + H_2$, or ammonia gas atmosphere [11, 13-15, 59, 65, 67-70, 72-77]. Much of this work has proven effective and efficient for producing large batches of high purity powders. Due to the fact that this method has been proven and documented, it served as the main source of obtaining sufficient quantities of the high purity powder for the sintering studies. The method that is presented in this document has been adapted from the work of Muromora, *et al.* [59] and Matthews, *et al.* [11] with the primary difference being that the work presented here was done in a low cost tube furnace.

1.1.1. Experimental Procedures of the Carbothermic Reduction Prior to Nitridation Synthesis Route to UN

The starting materials were glassy carbon spherical powder (Alfa Aesar, Ward Hill, MA, USA) and depleted-UO_2 powder (International Bio Analytical Industries Inc., Boca Raton, FL, USA). The carbon and UO_2 powders were weighed and combined at a C/UO_2 molar ratio of 3.11 in the Plas-Lab inert atmosphere glovebox (Figure 1) (Muromura, *et al.* [59, 77] specifies ratios of 3.11 and 3.59 and Matthews, *et al.* [11] suggests less than 2.2 to keep the carbon levels low) prior to being thoroughly mixed by ball-milling in the planetary ball mill for 10 minutes with yttria stabilized zirconia. The combined powders were then placed in a niobium-lined alumina boat and transferred to the CM high temperature alumina tube furnace (Figure 4). The furnace profile took approximately 48 hours to run to completion (Figure 11). It began by evacuating and purging the tube with high purity argon prior to a 5 hour dwell at 1500°C under 10^{-3} Torr vacuum to presumably form uranium monocarbide (UC). This was followed by a 7 hour dwell at 1400°C in a constant flow of ultra high purity (UHP) N_2 at slightly greater than atmospheric pressure where the mononitride (UN) was formed. The atmosphere was then changed to N_2 + 6.28% H_2 where the residual carbon was removed for 14 hours. The sample was cooled to room temperature in high vacuum to prevent the formation of the sesquinitride (U_2N_3). The total reaction of this process is described by Reaction 1 [11].

$$UO_2 + 3C + \frac{1}{2}N_2 + 2H_2 \rightarrow UN + 2CO + CH_4 \qquad \text{(Rxn. 1)}$$

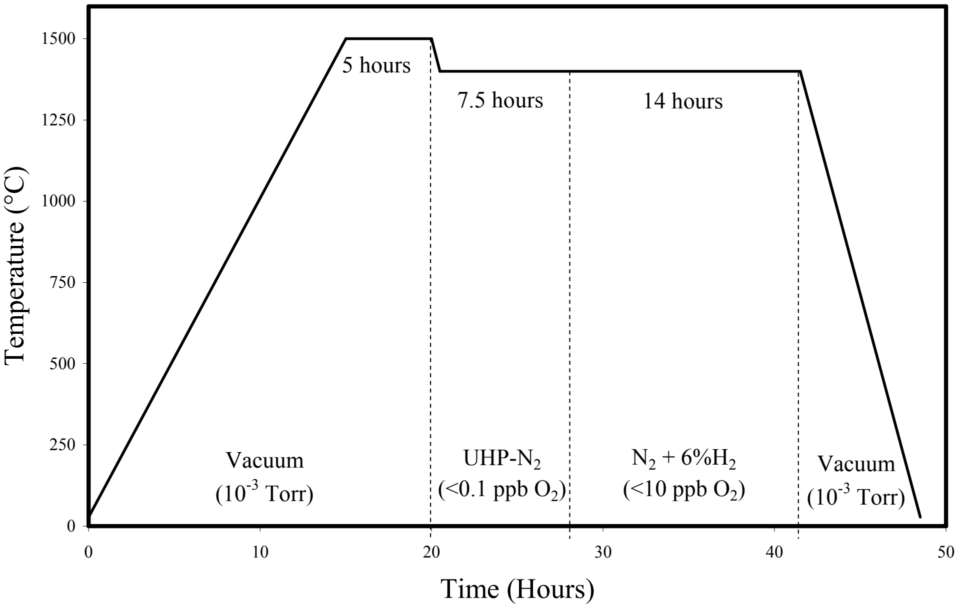

Figure 11: Furnace profile for producing high purity UN from a carbothermic reduction of the oxide prior to nitridation at 1400°C.

1.1.2. Results of Synthesizing UN via a Carbothermic Reduction of UO_2 Prior to Nitridation

The typical colors of carbon and UO_2 are black and dark brown, respectively. Due to the initial mixture being primarily UO_2, the starting powder was dark brown. After the UO_2 and carbon mixture was subjected to the furnace profile in Figure 11, the color of the resultant powder changed to black as seen in Figure 12. The resultant powder was loaded into the stainless steel powder holder of Figure 13, packed, leveled off, and sealed with an x-ray transparent thin film in the inert atmosphere of the Plas-Lab glovebox (Figure 1) for diffraction analysis.

a) b)

Figure 12: a) Depleted-uranium dioxide and carbon powder in a niobium lined alumina boat prior to carbothermically reducing the oxide and nitriding at 1400°C to yield (b) uranium nitride powder.

Figure 13: Stainless steel sample holder used for obtaining XRD patterns. The powder sample is placed and leveled in the center (10 mm diameter) and covered with an x-ray transparent film to temporarily protect it from oxidation during transportation to and during XRD analysis.

The x-ray diffraction (XRD) pattern in Figure 14 shows that the carbothermic reduction of UO_2 prior to nitridation produces high purity UN. Phase pure UN was confirmed by comparison with the accepted data given by the Joint Committee on Powder Diffraction Standards (JCPDS). The diffraction pattern was obtained with a Philips X'pert XRD with a Cu-Kα source (λ=1.5418 Å) and a 4°/min scan rate in Bragg-Brentano geometry. Further analysis of the XRD data using Lorentzian fits of the 3167° ((111) plane) and 36.6° ((200) plane) diffraction peaks was used to find the lattice constant of the face-centered cubic UN. The lattice constant was found as 4.91 ± 0.01Å using Bragg's equation (Equation 1) by assuming a first order diffraction peak (n=1) and the incident Cu-K_α x-rays had a wavelength of 1.5418Å. This calculated d-spacing is in good agreement with the published value of 4.889Å [78]. Further analysis of the (111) and (200) diffraction peaks using the Scherrer relation (Equation 2) determined the average crystallite size as approximately 27 nm, where K is based on crystallite geometry (assumed to be 0.9 in this case) and β is the breadth of the diffraction peak at one half of its maximum value.

$$n\lambda = 2d_{hkl}\sin\theta \qquad \text{(Eqn. 1)}$$

$$L = \frac{K\lambda}{\beta\cos\theta} \qquad \text{(Eqn. 2)}$$

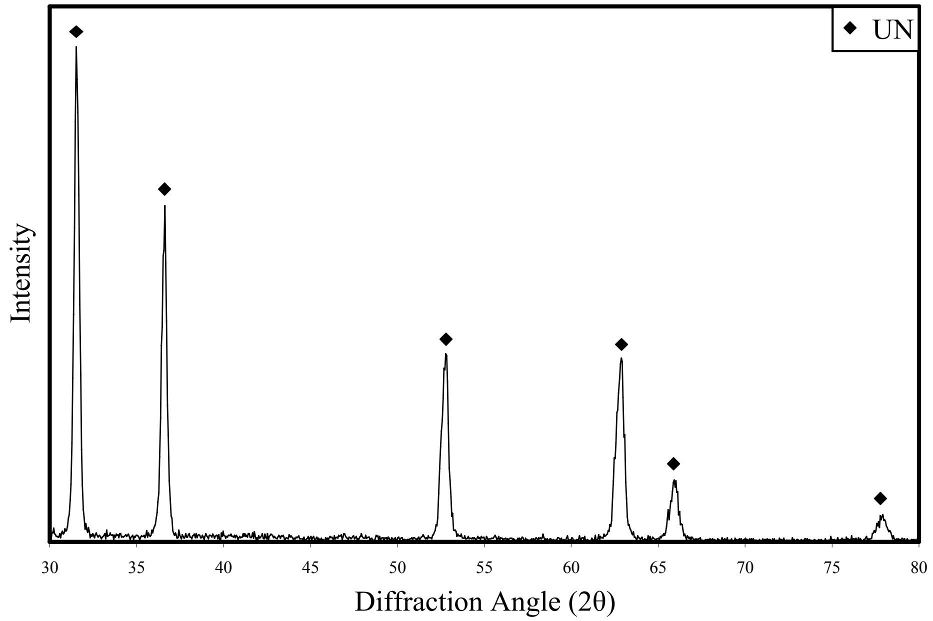

Figure 14: XRD spectrum of UN powder synthesized by carbothermic reduction of UO_2 powder at 1500°C in vacuum prior to 1400°C in nitrogen and hydrogen.

1.2. Hydride prior to Nitridation Synthesis Route to UN

As previously proposed, it seems as though the most economical synthesis route would use a metal as the starting material because metals are what are typically obtained from electrochemical refining technologies. Accordingly, this hydride-nitride method to the synthesis of UN and the previous ball-milling method both use pure uranium metal as the starting material. The work in this section is adapted from a limited number of available published works describing the synthesis of UN from pure uranium metal [17, 57, 60-62, 71].

1.2.1. Experimental Procedures for the Hydride prior to Nitridation Synthesis Route to UN

A high purity, depleted uranium ingot (Figure 15a) was obtained from the Idaho National Laboratories and used as the starting material for this work. Approximately 5.6 grams of uranium metal was cleaved from the ingot in an argon atmosphere glovebox (Figure 1) with a uni-axial hydraulic press and a case-hardened carbon steel wedge. The ingot was cleaved into smaller pieces (less than 1 cm^2 by 0.2 cm thick) for this experiment (shown in Figure 15b).

The pure uranium metal pieces were set on niobium foil in an alumina boat and placed in the modified CM high temperature alumina tube furnace (Figure 4). The reaction was initiated by flowing UHP-H_2 gas over the metal for 5 hours at 160°C converting it to UH_3 [62] as described by Reaction 2. The next step was to flow nitrogen over the hydride for two hours at 320°C to form the sesquinitride (U_2N_3) as described by Reaction 3. The temperature was then gradually increased to 1375°C in an argon environment to reduce the sesquinitride to a mononitride as described by Reaction 4. The furnace profile is seen in Figure 16.

$$U + \frac{3}{2}H_2 \rightarrow UH_3 \qquad \text{(Rxn. 2)}$$

$$2UH_3 + \frac{3}{2}N_2 \rightarrow U_2N_3 + 3H_2 \qquad \text{(Rxn. 3)}$$

$$U_2N_3 \rightarrow 2UN + \frac{1}{2}N_2 \qquad \text{(Rxn. 4)}$$

a) b)

Figure 15: Starting materials (uranium metal ingot obtained from the Idaho National Laboratories that are similar to what is received from electrochemical refining processes) used to synthesize UN via hydriding the metal prior to nitridation. (b) Pieces of uranium metal cleaved from the ingot shown in (a).

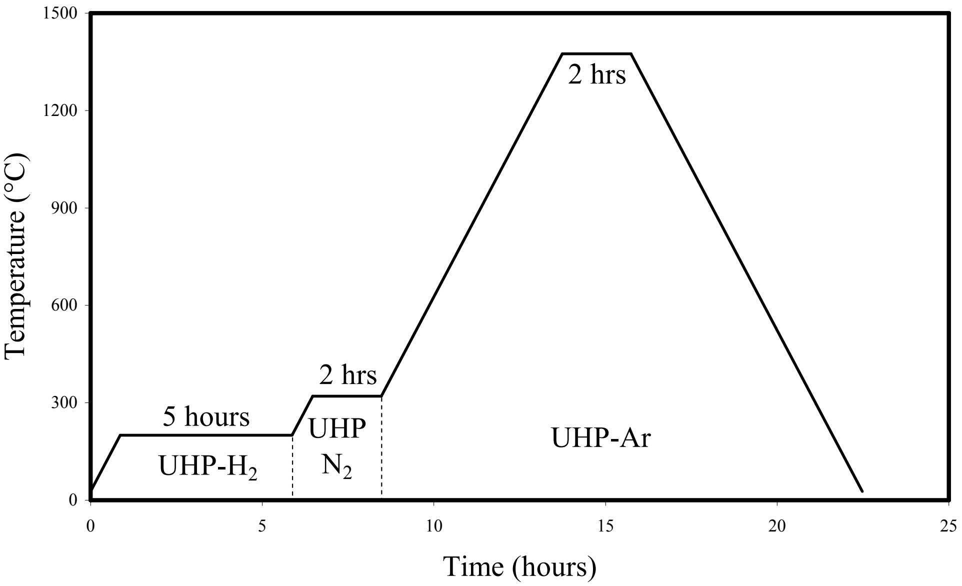

Figure 16: Furnace profile for producing UN from pure uranium metal. The metal was reduced in hydrogen at 160°C prior to nitridation at 320°C forming U_2N_3. The sesquinitride was reduced to a mononitride in argon at 1375°C.

1.2.2. Results of Synthesizing UN via a Hydride prior to Nitridation Synthesis Route

The uranium metal pieces (Figure 15b) cleaved from uranium metal ingot were a silvery metallic color. After hydriding and nitriding, the uranium metal had broken down into powder form and turned to a dark gray color indicating the formation of the nitride, as seen in Figure 17.

Figure 17: Photograph of UN synthesized via a hydride prior to nitridation of pure uranium metal pieces in pure H_2 prior to pure N_2 at 320°C and a pure argon gas at 1375°C.

The resultant powder was loaded into the stainless steel powder holder (Figure 13), packed, leveled off, and sealed with an x-ray transparent thin film and vacuum grease in the inert atmosphere of the Plas-Lab glovebox (Figure 1) for diffraction analysis. Figure 18 shows the XRD spectrum which clearly illustrates the formation of UN by comparison with the data given by the JCPDS. The diffraction pattern was obtained with a Philips X'pert XRD with a Cu-Kα source (λ=1.5418 Å) and a 4°/min scan rate in Bragg-Brentano geometry.

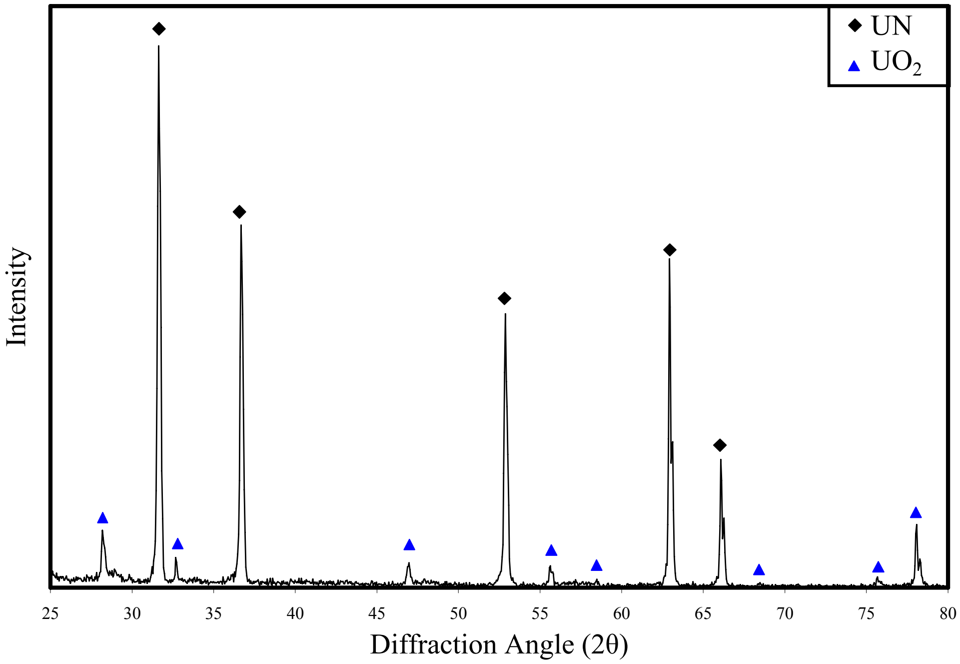

Figure 18: X-ray diffraction spectrum of UN powder produced by hydriding prior to nitriding of high purity uranium metal ingot, similar to what is received from electrochemical refining processes. The oxide likely formed during handling to and from the furnace and the diffratometer.

An estimation received from this diffraction pattern suggests that the powder obtained was approximately 90% pure UN. The oxide likely formed during handling to and from the furnace and the diffractometer. Further analysis of the XRD data using Lorentzian fits of the 31.7° ((111) plane) and 36.7° ((200) plane) diffraction peaks from U_2N_3 was used to find the lattice constant and the average crystallite size of the face-centered cubic UN. The lattice constant was found as 4.89 ± 0.01Å using Bragg's equation (Equation 1) by assuming a first order diffraction peak (n=1) and the incident Cu-K_α x-rays had a wavelength of 1.5418Å. This calculated d-spacing of the nitride is in very good agreement with the published value of 4.889Å [78]. The crystallite size was found to be approximately 43 nm using the Scherrer relation (Equation 2). This hydride prior to nitridation route shows promise as a method for synthesizing high quality UN from pure uranium metal ingot in hydrogen and nitrogen gases.

1.3. Novel Reactive Milling Synthesis Route to UN

When assessing the most economical synthesis route for obtaining these nitride materials, the most logical solution is to use the products directly from one of the aforementioned separation techniques. If these materials are separated as pure metals (via electrochemical refining technologies), then it suggests that the most economical synthesis technique would use the pure metal as the primary starting material. The novel synthesis route presented in this section, the mechanically induced gas-solid reaction (ball-milling) route, uses the pure metal to form a nitride at room temperature. This route reduces the number of handling/processing steps thereby minimizing the time and risks associated with handling the nitrides and is seen as advantageous because it is conducted entirely within a closed system, thus reducing the amount of material lost to evaporation and handling. This technique also requires significantly less infrastructure when compared to the thermal synthesis routes due to the low temperature requirements.

After a detailed literature review, the work of synthesizing any actinide (including UN) at room temperature using a ball-milling synthesis technique has never been reported. However, this technique has previously been demonstrated by a number of authors who reported synthesizing TiN, BN, ZrN, and Fe_3N from the respective metals in a nitrogen or ammonia milling atmosphere [79-90].

The success of this low temperature mechanical route for producing uranium nitride should have profound implications on the advance fuel cycle because it potentially offers the advantages of a simple, inexpensive method for producing nitride fuels for use in fast-spectrum reactors in a closed system where all of the materials are retained. The results of this work were published in the Journal of Nuclear Materials [91, 92].

1.3.1. Experimental Procedures for Uranium Nitride Synthesis via Reactive Milling

The same high purity, depleted uranium ingot (obtained from the Idaho National Laboratories) that was used in the previous hydride prior to nitridation synthesis route was also used as the starting material for this work. Approximately five grams of uranium metal was filed from the ingot (Figure 19b) in an argon atmosphere glovebox with a carbon-steel metal file. The flakes were collected and placed in a 250 mL chrome steel milling vessel along with the milling media (in an argon atmosphere) prior to sealing and removing from the glovebox. The milling vessel contained 70 grams of 5 mm diameter yttria stabilized zirconia (YTZ, TOSOH, Tokyo, Japan) milling media (Figure 20a) providing an optimum metal flake to media mass ratio of 1:14.

a) b)

Figure 19: Shown are the starting materials for the ball-milling synthesis route of uranium nitride at room temperature including (a) a uranium metal ingot obtained from the Idaho National Laboratories and (b) uranium metal flakes obtained from flake the metal ingot with a carbon-steel file.

The milling vessel, shown in Figure 20b, was sealed prior to five purges and charged with ultra-high purity (UHP) N_2 to approximately 4.15 atm (420 kPa). The nitrogen gas was purified by passing it through copper turnings at 550°C, which reduced the oxygen content to less than 0.1

ppb as measured by a Ntron Model OA-1 (Exton, PA, USA) oxygen analyzer. The vessel was fixed in a Retsch high energy planetary ball mill (PM 100, Haan, Germany) (Figure 20c) and the uranium metal was milled for 24 hours at 500 rpm with intermittent nitrogen purges and recharges every 2 hours to replenish the nitrogen atmosphere and keep the nitrogen partial pressure constant. There is approximately 280% (mole basis) excess nitrogen to complete the metal to mononitride conversion and approximately 50% excess nitrogen to complete the metal to sesquinitride (U_2N_3) conversion when the 250 mL vessel is charged to 4.15 atm (420 kPa). However, the multiple purge cycles were to ensure a constant pressure of nitrogen over the uranium metal throughout the milling process.


a) c) b)

Figure 20: (a) Uranium metal flakes and 5 mm diameter yttria stabilized zirconia milling media in a 250 mL chrome steel ball-milling vessel. (b) Milling vessel used to synthesize uranium nitride via a mechanically induced gas-solid reaction (ball-milling) method with a N_2 atmosphere at room temperature. This container allows for multiple charges/purges to 4.15 atm (420 kPa) with extremely pure nitrogen gas during the milling process in the (c) PM100 planetary ball mill.

After milling, the powder was separated from the milling media in an inert atmosphere glovebox and prepared for XRD and particle size analysis. The XRD system used for this analysis did not have inert atmosphere capabilities. Therefore, the powder was temporarily protected from oxidation by loading it into a stainless steel powder holder and sealed with an x-ray transparent thin film (Figure 13). The XRD data were collected in air at room temperature using a Philips X'pert XRD with a Cu-K_α source (λ=1.5418 Å) and a 4°/min scan rate in Bragg-Brentano geometry. The chemical composition was further analyzed in a scanning electron microscope (SEM) by energy dispersive x-ray spectroscopy (EDS).

The resultant uranium nitride powder was dispersed in de-ionized water and analyzed with a Horiba LA-950 Laser Scattering Particle Size Distribution Analyzer (Minami-ku Kyoto, Japan) (Figure 21a) for particle size distribution. The LA-950 uses folded Reverse Fourier optical arrangement with two solid-state light sources to measure particle size by correlating the intensity and angle of scattered light from a particle as shown in the illustration in Figure 21b. As the particle size becomes smaller, the scattered light signal shifts to the side and rear with respect to the light source.

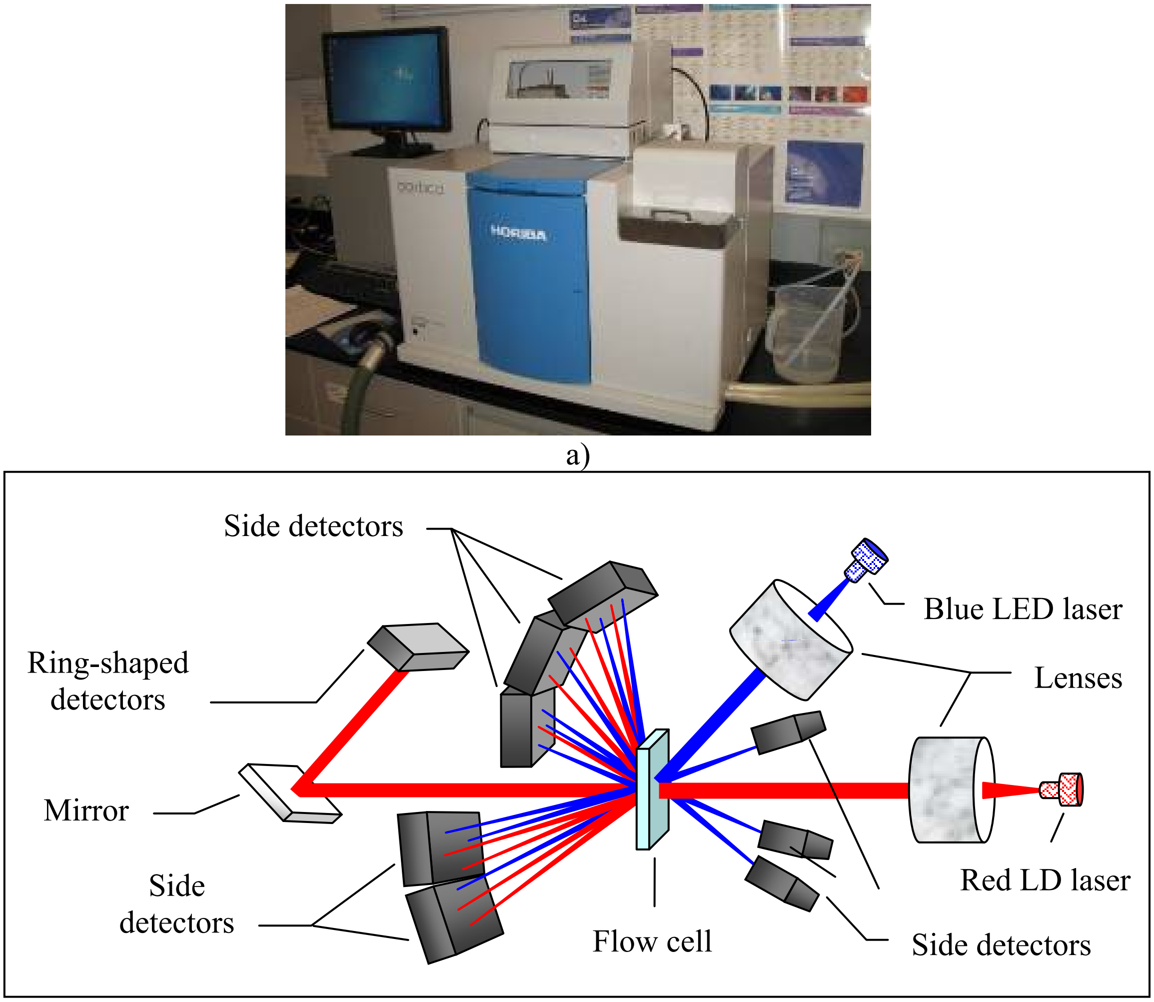

a)

b)

Figure 21: (a) Horiba LA-950 Laser Scattering Particle Size Distribution Analyzer for particle size analysis utilizing (b) a folded Reverse Fourier optical technique with two solid-state light sources. (Illustration adapted from [93].)

The analyzer uses multiple high-angle and back-scatter detectors to capture scattered light signals over a wide range of angles from the two different wavelength laser sources [93]. The software of the instrument is configured to calculate particle size data using the Mie-scattering theory (the Gustav Mie solution to Maxwell's equations). For this particular experiment, the scattering correlations were completed using a refractive index of $2.2 + 0.1i$. Where “i” denotes the imaginary component of the refractive index and accounts for irregularities (deviations from spherical) and opaqueness of the powders.

1.3.2. Results of Synthesizing Uranium Nitride via Reactive Milling

The uranium metal flakes (Figure 19b) obtained from uranium metal ingot (Figure 19a) were a silvery metallic. After nitriding in the ball mill, the uranium metal flakes dramatically reduced in size and turned to a dark gray or blackish color indicating the formation of the nitride (Figure 22).

Figure 22: Photograph of the uranium nitride formed from ball-milling the flakes for 24 hours at room temperature in a nitrogen atmosphere.

XRD results confirmed that the ball-milling synthesis route produced phase pure U_2N_3 powder from the pure uranium metal particles by comparison with the data given by the JCPDS (Figure 23). These results were repeated on five different occasions. According to the literature [17, 19, 57, 61, 62, 64] and by looking at the binary phase diagram for the U-N system (Figure 24), the decomposition of pure U_2N_3 above 1350°C results in pure UN. EDS analysis confirmed that there was no appreciable residual oxygen in the resultant powder. Oxygen concentration was found to be less than the detectable limits of the EDS system used. Based on the XRD and EDS results, it is presumed that the reaction of uranium metal with nitrogen at room temperature proceeded to completion. This is a very exciting finding due to the fact that this is the first time this method has been used to synthesize U_2N_3 or any other actinide nitride.

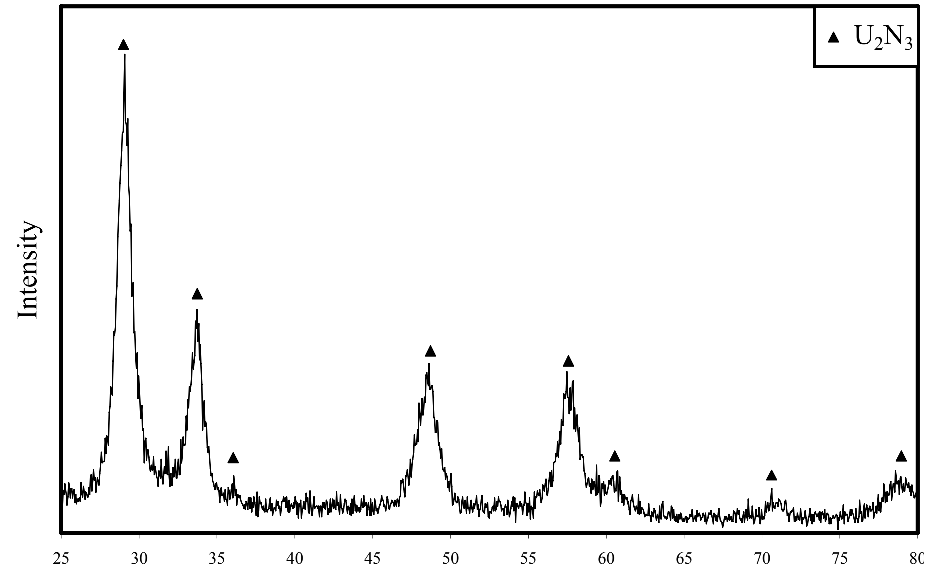

Figure 23: X-ray diffraction spectrum of U_2N_3 powder produced by reactive milling uranium metal in an UHP N_2 atmosphere at room temperature.

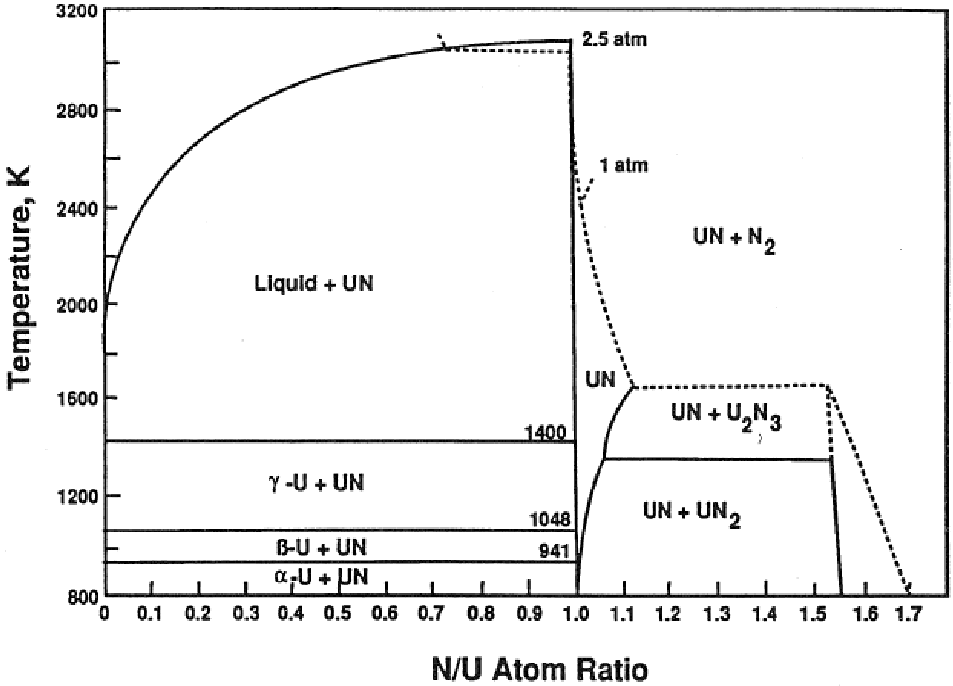

Figure 24: Uranium-nitrogen binary phase diagram from Matthews, *et al.* [11].

Further analysis of the XRD data using Lorentzian fits of the 29.1° ((222) plane) and 33.7° ((400) plane) diffraction peaks was used to find the lattice constant and average crystallite size of the body-centered cubic U_2N_3. The lattice constant was found as 10.63 ± 0.01Å using Bragg's equation (Equation 1) by assuming a first order diffraction peak (n=1) and the incident Cu-K_α x-rays had a wavelength of 1.5418Å. This calculated d-spacing is in good agreement with the published value of 10.657Å [94]. The average crystallite size was found to be approximately 8 nm using the Scherrer relation (Equation 2)

Optical images of the pure metal particles and the resulting U_2N_3 particles were obtained by suspending the particles in an aqueous solution prior to imaging them with an inverted stage optical microscope. The pure metal particles were observed to have irregular and elongated shapes with approximate lengths of a few hundred microns (Figure 25a). An optical micrograph showing the spherically shaped U_2N_3 powders resulting from the reaction ball-milling is shown in Figure 25b. Particle size analysis measured the mean and median particle size of U_2N_3 to be 6.3 µm and 7.2 µm, respectively, with a particle size distribution from 0.5 to 45 µm, as seen in Figure 26. It is worthwhile to note that the particle distribution is represented in volume percent, as opposed to number percent.

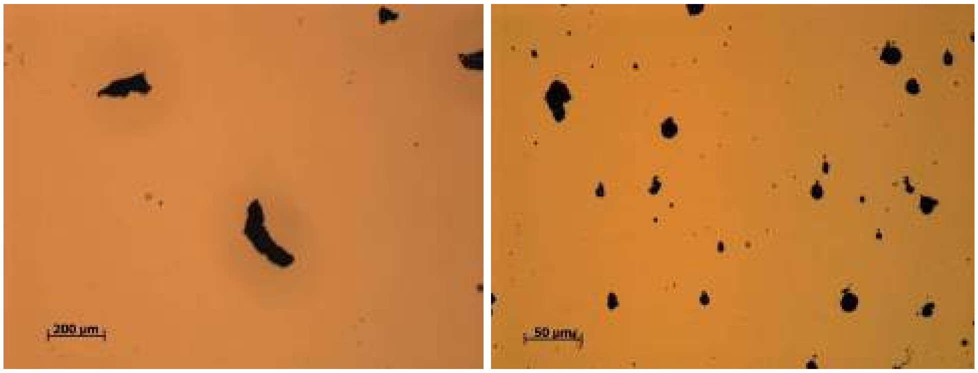

a) b)

Figure 25: Optical micrograph of (a) uranium metal flakes prior to reactive ball-milling in N_2 at 50X magnification showing the irregular, ellipsoidal shape. Optical micrograph of (b) U_2N_3 powder resulting from the reaction ball-milling at 200X magnification showing the spherical shape. Particle size analysis measured the median particle size of U_2N_3 to be 6 µm with a particle size distribution from 0.5 to 45 µm.

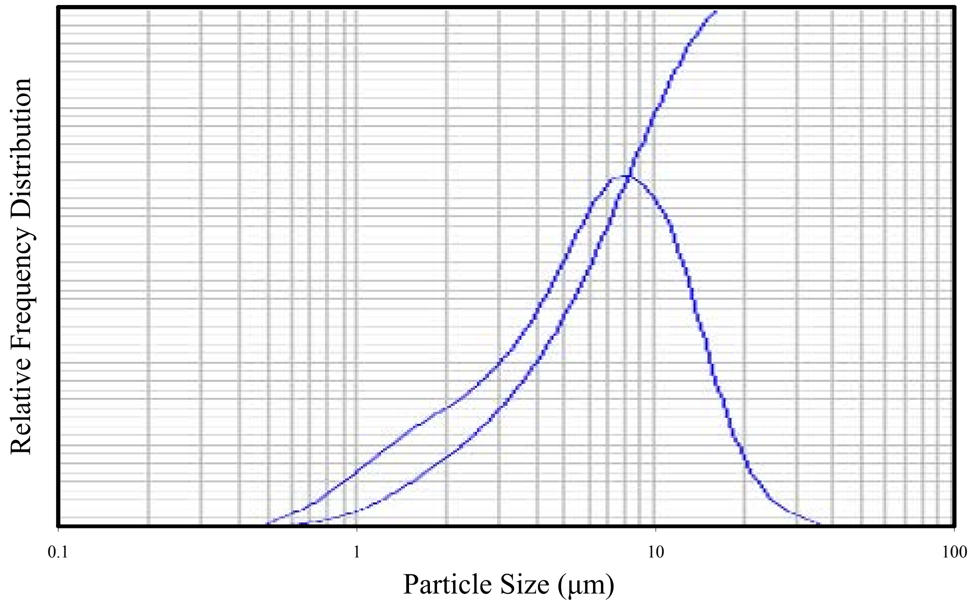

Figure 26: Resulting particle distribution (based on volume percent) of U_2N_3 synthesized by a mechanically induced gas-solid reaction (ball-milling) method in a high purity nitrogen atmosphere at room temperature.

1.4. Discussion of Uranium Nitride Synthesis Routes

The work presented in this report demonstrates the synthesis of phase pure uranium nitride via three methods, namely;

- Carbothermically reducing UO_2 prior to nitridation at 1400°C,
- Hydriding uranium metal prior to nitridation at 320°C, and
- Ball-milling of uranium metal in nitrogen at room temperature [91].

The first synthesis route to UN that was investigated in these studies, the carbothermic reduction of UO_2 prior to nitridation, is a traditional and well documented synthesis route that has been the main source of large-scale UN production in the past. As previously stated, the total reaction of the carbothermic reduction of UO_2 to form UN is described by Reaction 5 [11].

$$UO_2 + 3C + \frac{1}{2}N_2 + 2H_2 \rightarrow UN + 2CO + CH_4 \qquad \text{(Rxn. 5)}$$

Pautasso *et al.* [95] suggests that the total reaction (Reaction 5) of the carbothermic reduction of UO_2 prior to nitridation has four primary steps: (1) The formation of a carbonitride ($UN_{1-x}C_x$) layer at the carbon-oxide interface, (2) the reaction of free carbon and $UN_{1-x}C_x$ with oxygen and nitrogen until a near equilibrium condition is reached, (3) reaction of nitrogen with free carbon and residual oxide present in $UN_{1-x}C_x$ to form a nitride, (4) reaction of $UN_{1-x}C_x$ with nitrogen and hydrogen to form a nitride. Pautasso *et al.* [95] found that the results of steps 1-3 fit a first order rate equation with an activation energy of 307 $^{kJ}/_{mol}$. However, a rate equation was not obtained for step 4 due to the competing reactions between the removal of free carbon and the substitution of carbon by nitrogen in $UN_{1-x}C_x$. Pautasso *et al.* [95] also postulated that the rate controlling step in the carbothermic reduction of UO_2 prior to nitridation is the carbon diffusion through the product layer. The work presented by Pautasso *et al.* [95] cannot be used as a direct comparison to the work presented in this report because Pautasso's work omits the initial vacuum step of the synthesis route.

Further analysis of the thermodynamics of the intermediate reactions of Reaction 5 shows a large dependence on the vapor pressures of the reactant and product gases. The furnace profile for the carbothermic reduction prior to nitridation synthesis route (Figure 27) shows that the first thermal step initiates the reaction between the UO_2 and the carbon forming a uranium oxy-carbide. This uranium oxy-carbide is a precursor to uranium monocarbide (UC), according to Reaction 6. Using the Thermochemical Software and Database version 5.5 [96] and the data provided by Barin [97], the free energy of the carburization reaction at 1773 K would be $140.5^{kJ}/_{mol}$, suggesting that the reaction would not occur at CO equilibrium partial pressures. However, because the conversion is completed in a 10^{-3} vacuum, the evolved CO is immediately removed from the system so that its partial pressure is less than 10^{-3} Torr which allows the reaction to take place.

$$UO_2 + 3C \rightarrow UC + 2CO \qquad \text{(Rxn. 6)}$$

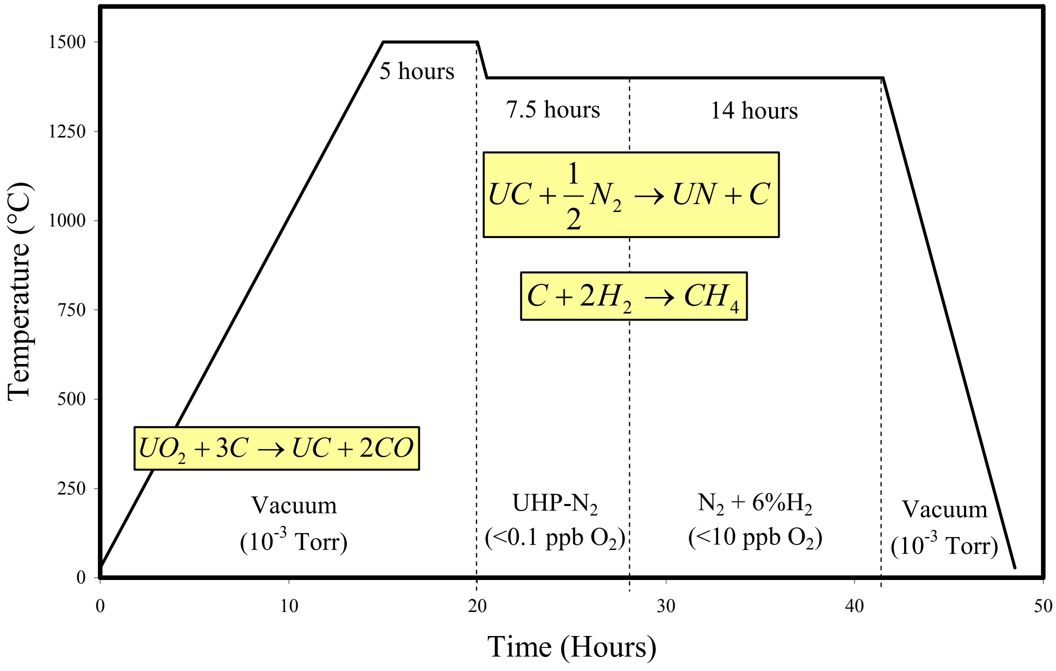

Figure 27: Furnace profile for producing high purity UN from a carbothermic reduction of the oxide prior to nitridation at 1400°C.

After the UO_2 is carburized, the hyperstoichiometric UC is then subjected to 1673 K in a nitrogen gas stream (Figure 27). When nitrogen is introduced into the system, the carbon dissociates from the uranium as a free species as shown in Reaction 7. Assuming the uranium metal and free carbon each have an activity of one, FactSage version 5.5 [96] and the data by

Barin [97] was used to calculated the free energy of the reaction. The free energy of the dissociation reaction (Reaction 7) at 1673 K was calculated to be -49.3 $^{kJ}/_{mol}$, suggesting that there is a thermodynamic driving force for this reaction to occur. A few authors used thermogravimetric techniques to study the reaction kinetics of Reaction 7 and report that the reaction follows a first order rate law according to Equation 3 [69, 74, 95], where α_0 is the reaction ratio and k_0 is the reaction rate. Following these results, the data was plotted on an Arrhenius plot to determine an activation energy, which was found to be between 300 – 360 $^{kJ}/_{mol}$, depending on the author and the study [69, 74, 95].

$$UC + \frac{1}{2}N_2 \rightarrow UN + C \qquad \text{(Rxn. 7)}$$

$$-\ln(1-\alpha_0) = k_0 t \qquad \text{(Eqn. 3)}$$

Although Reaction 7 suggests that the formation of uranium mononitride is complete, there is still a large amount of residual carbon in the specimen. Accordingly, a hydrogen gas is introduced into the system. A N_2 – 6.28% H_2 gas stream is flowed over the sample at 1400°C to remove the residual carbon according to Reaction 8. Assuming there is a stoichiometric amount of hydrogen in the reaction and the CH_4 has an equilibrium partial pressure as it would in a static system, the free energy of this reaction was found to be 94.1 $^{kJ}/_{mol}$ [96]. This positive free energy value suggests that the reaction would not proceed. The reaction does, in fact, proceed due to the fact that there is an infinite hydrogen source (from the flowing gas atmosphere) which also reduces the partial pressure of the resulting CH_4. This removal of carbon via hydrogen step of the synthesis technique has been investigated by Muromura *et al.* [74] who were able to derive a rate equation (according to Equation 3) to determine an activation energy of 175-185 $^{kJ}/_{mol}$ in a NH_3 stream and 285 $^{kJ}/_{mol}$ in a 75% H_2 – 25% N_2 stream. From these results, it is presumed that the activation energy increases with the hydrogen content in the process gas. Accordingly, it can be assumed that due the low hydrogen content of the processing gas used in the experiments presented in this document (N_2 – 6.28% H_2) that the activation energy is higher than the reported 285 $^{kJ}/_{mol}$ reported for a 75% H_2 – 25% N_2 gas stream.

$$C + 2H_2 \rightarrow CH_4 \qquad \text{(Rxn. 8)}$$

$$1-(1-\alpha_0)^{\frac{1}{3}} = k_c t \qquad \text{(Eqn. 3)}$$

The carbothermic reduction prior to nitridation synthesis route is not the most economical synthesis route considered for these studies because it requires an oxide (rather than a metal) as the starting material. However, the carbothermic route was used to produce the large amount of powder needed for the sintering studies. This is primarily due to the commercial availability of high purity UO_2 powder and graphitic carbon for use as the starting materials. The carbothermic reduction method typically produces a phase pure UN powder with high concentrations (500 – 1000 ppm [11])of carbon impurities. However the introduction of the hydrogen gas into the system removes a majority of the residual carbon. For the studies presented in this report, the impurities were below the detectable limits of the performed XRD analysis, but as previously discussed, further chemical analysis was not performed.

The second nitride synthesis route considered for the studies presented in this document is the hydride prior to nitridation synthesis technique of uranium metal to form UN. As previously noted, the hydride prior to nitridation route was the primary source of UN synthesis throughout the 1960s but only a few authors report it [17, 57, 60-62, 71]. The reported documents tend to be brief and report very little on the the properties of UN and the effects of varying the temperature, time, or atmosphere on the kinetics and thermodynamics of the reaction. The work that was presented by Bauer *et al.* [57] suggests that the hydride step was primarily to provide a high surface area powder to increase the kinetics of the reaction. Bauer reported using temperatures in the range of 500-525 K to complete form the hydride prior to nitriding any where from 675 K to 1125 K in a pure nitrogen stream. The subsequent reduction of the sesquinitride was completed in a temperature above 1075 K but below 1775 K.

In the work presented here, the hydride step was completed at a lower temperature than suggested by Bauer *et al.* [57]. The temperature for the hydride reaction was reduced to 435 K and the reaction presumed to proceed according to Reaction 9.

$$U + \frac{3}{2}H_2 \rightarrow UH_3 \qquad \text{(Rxn. 9)}$$

Assuming that the uranium metal and uranium hydride do not exhibit a pressure contribution, it is presumed that the hydride reaction proceeded to completion with a calculated free energy of reaction of -47.6 $^{kJ}/_{mol}$ at 435 K. The temperature of the nitridation step of the reaction was dramatically reduced from what Bauer *et al.* [57] reported as sufficient (675 – 1125 K). In fact, it was found in this work that the nitridation reaction (Reaction 10) proceeded to completion at 595 K with a calculated free energy of reaction of -575 $^{kJ}/_{mol}$. The thermodynamic calculations for U_2N_3 were performed using the thermochemical database of Outokumpu HSC Chemistry version 5.11 [98] with data provided by Knacke [99] due to the fact that the FactSage Thermochemical Software and Database version 5.5 [96] did not contain a database for U_2N_3. The calculation was performed assuming stoichiometric amounts of nitrogen and hydrogen gas as well as neglecting the activity, if any, of the hydride and sesquinitride.

$$2UH_3 + \frac{3}{2}N_2 \rightarrow U_2N_3 + 3H_2 \qquad \text{(Rxn. 10)}$$

The final step to produce UN using the hydride prior to nitridation technique is the reduction of the U_2N_3 phase to UN by subjecting the sample to temperatures above 1350 K (according to the U-N phase diagram of Figure 24) in a reduced nitrogen atmosphere. To increase the kinetics of Reaction 11, the sesquinitride was subjected to 1650 K in a 10^{-3} Torr vacuum. The free energy of the reaction was calculated to be 22.6 $^{kJ}/_{mol}$ using Outokumpu HSC Chemistry database version 5.11 [98] and the data from Knacke [99], suggesting that the reaction would not occur. However, the reaction does proceed because the calculation does not account for the pressure of the evolving nitrogen being equal to or less than 10^{-3} Torr. Although the resulting powder was not phase pure UN, it exhibited very promising aspects due to the fact that no U_2N_3 phase was detected using XRD. The UO_2 phase detected was likely due to handling and transporting the powder between the furnace, glovebox, and diffractometer.

$$U_2N_3 \rightarrow 2UN + \frac{1}{2}N_2 \qquad \text{(Rxn. 11)}$$

Although the hydride prior to nitridation of pure uranium metal was only performed one time (and therefore not optimized) it is still considered as a feasible candidate for producing large quantities of high purity UN by using a product received from one of the aforementioned separations techniques. It is therefore considered an economical and logical synthesis method. However, due to the fact that uranium metal was not commercially available, the hydride prior to nitridation synthesis route was not used as the primary powder synthesis method to UN for the sintering studies.

When assessing the most economical synthesis route with regards to advanced nuclear fuels, the most logical solution is to use the products directly from one of the aforementioned pyroprocessing/electrochemical separation techniques (Table 1, Section 1.1). The novel ball-milling and the hydride-nitride synthesis techniques that were presented in this section use pure uranium metal to form a phase pure nitride at room temperature and 320°C, respectively. It should be noted that the ball-milling route has never been demonstrated with any other lanthanide or actinide prior to this work [91, 92] and is thus a novel synthesis route. The ball-milling route reduces the number of handling and processing steps thereby minimizing the time and risks associated with handling the nitrides. It is also seen as advantageous because it is conducted entirely within a closed system at room temperature (thus reducing the amount of material lost to evaporation and handling) and because of the fact that it requires significantly less infrastructure when compared to the traditional thermal synthesis routes. The success of this low temperature mechanical route for producing UN should have profound implications on the advance fuel cycle because it potentially offers the advantages of a simple, inexpensive method for producing nitride fuels for use in fast-spectrum reactors in a closed system where all of the materials will be retained.

It is presumed that the nitridation induced from the reactive ball-milling process is somewhat dependant on the elastic or plastic properties of the metal being milled. A couple of authors have postulated that brittle and ductile materials respond differently in the ball-milling process [82, 86]. Initially, ductile materials tend to cold-weld together forming larger particles prior to being broken down into smaller particles. In both cases, it is presumed that the nitrogen molecules are adsorbed (chemisorbed) to the highly energetic surface as fresh surfaces are exposed (due to collisions with the media). From a macroscopic point of view, the nitrogen is then diffused through the outer layer of the metal particle forming a ceramic. Once the outer layers of the particles become nitrided (and thus a brittle ceramic), the outer layer is then broken off of the metal particle from subsequent collisions with the media forming a bulk nitride. As the nitride breaks off of the metal, more fresh surfaces are created with high energy and exposed bonds. Due to the high surface energy (also increasing surface area) and exposed bonds, more nitrogen is preferentially adsorbed to the surface and the nitriding process continues until the reaction is completed and bulk, phase pure nitride is formed.

The mechanism by which the nitridation of relatively brittle materials using the ball-milling technique is ill defined. However, it is presumed that the reaction is rate limited by the dissociation of diatomic nitrogen molecules due to the very high dissociation energy (E_{diss} in Figure 28) of the nitrogen-nitrogen bond, which is reported as approximately 950 $^{kJ}/_{mol}$ [100]. As in typical molecular gas adsorption processes, the chemisorption of nitrogen is an activated process by which nitrogen molecules are firstly physisorbed before becoming chemisorbed to fresh, highly reactive metal surfaces created from collisions between the media and the metal. The energy by which the reaction is activated is likely due to the very high energy of the free surface of the fractured metal. It is also presumed that the reaction kinetics are increased via a general and localized temperature increase caused by milling friction and induced at the point of collision between the media and metal, respectively. The kinetics are also presumed to increase from the constant plastic and elastic deformations causing internal strains as well as many new defects. In any case, the nitrogen has to dissociate to form covalent bonds with the uranium metal to form the nitride. Figure 28 shows the potential energy of the system plotted against the distance of the nitrogen molecule from the metal surface (commonly referred to as a Leonard-Jones potential energy curve). The blue dashed curve represents the potential of nitrogen atoms, the black dotted curve represents the potential of molecular nitrogen, and the bold red curve depicts the path that is followed throughout the adsorption process (from right to left).

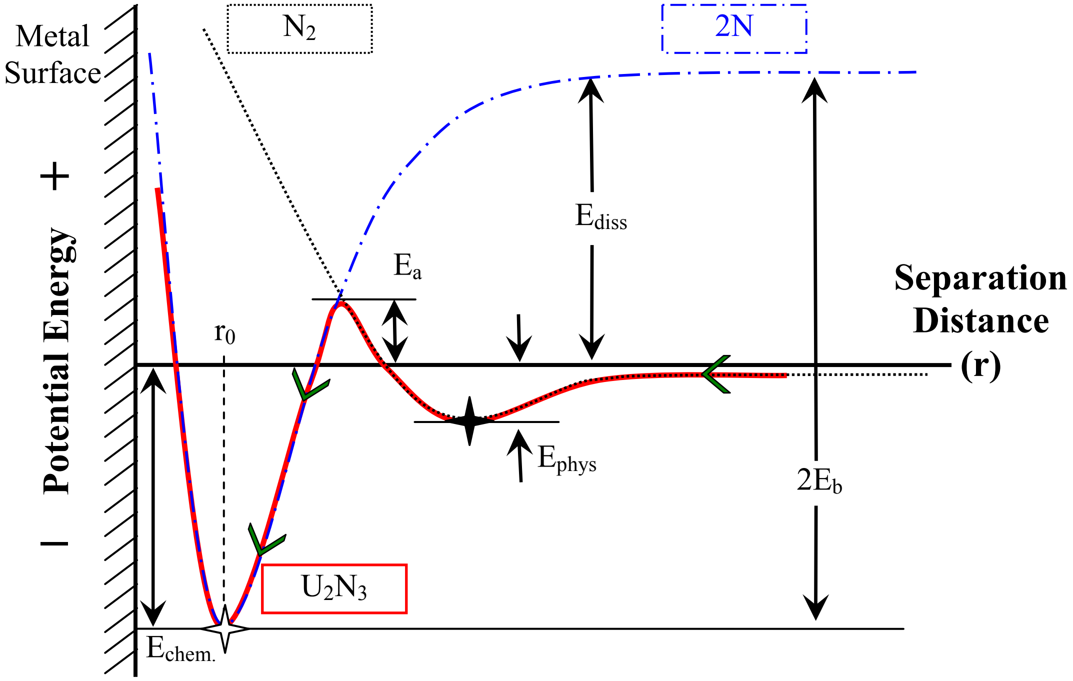

Figure 28: Leonard-Jones potential energy diagram qualitatively showing activated chemisorption of nitrogen on a uranium metal surface. The dashed blue curve corresponds to nitrogen atoms, the dotted black curve corresponds to molecular nitrogen, and the bold red line depicts that path that is taken to adsorb nitrogen into uranium to form uranium nitride (from right to left).

If one were to follow the bold red curve from the right to the left, the sequence of events would be as follows: Molecular nitrogen is attracted to the fresh uranium metal surfaces and finds a shallow potential energy well due to weak van der Waals-type bonding, which is also referred to as the energy of physisorption (E_{phys}). As molecular nitrogen is forced closer to the metal surface and the molecular nitrogen potential line intersects with that of the atomic nitrogen, dissociation of the molecule occurs (in this case it is an activated process with an activation energy of E_a). The system then preferentially falls to the left into the much deeper potential well of the chemisorbed species (E_{chem}) resulting in covalent bonding between the nitrogen and the uranium forming a uranium nitride film. The uranium-nitrogen bond energy is represented by E_b.

2. Synthesis of Dysprosium Mononitride (DyN)

Nitride materials have been considered as advanced nuclear fuels for a select few nuclear reactors for many years due to their desirable properties, including their: High melting points, high thermal conductivities, and high actinide densities. Recent investigations have indicated that the properties of DyN show similarities with those of the transuranics used for transmutation fuel fabrication for such fast spectrum reactors. As mentioned in previous sections, DyN has been identified in this work to serve as a surrogate for AmN in the fabrication of the transmutation fuels [6, 8, 30, 45-47]. After a detailed literature review, the earliest noted documentation found on the synthesis of DyN was in 1993 by Fitzmaurice, *et al.*, who documented a novel synthesis route to DyN through the chloride for applications such as coatings, catalysts, abrasives, and semi/super-conductors [101]. More recently, Takano, *et al.* and the Japan Atomic Energy Research Institute (JAERI), have published work describing the synthesis of DyN via two different routes; a carbothermic reduction of Dy_2O_3 prior to nitriding and a hydride-nitride method [6, 8, 46, 47]. A brief review of these routes is presented in the following text.

Fitzmaurice, *et al.* [101] found that the solid state reaction of anhydrous dysprosium chloride ($DyCl_3$) with lithium nitride (Li_3N) produced crystalline dysprosium nitride with a relatively high yield (Approximately 90%). The reaction was initiated by thoroughly mixing and grinding 0.76 grams of $DyCl_3$ (2.85 mmol) and 0.1 grams of Li_3N (2.85 mmol) together in a controlled atmosphere prior to being sealed in a glass ampoule. The ampoule was placed in a tube furnace and the temperature was raised to 400°C where the following reaction occurred:

$$Li_3N + DyCl_3 \rightarrow DyN + 3LiCl \qquad \text{(Rxn. 12)}$$

This solid state reaction was extremely rapid and exothermic and produced a solid that contained both nitride and chloride phases (identified via XRD techniques). However, when the chloride phases were removed via tetrahydrofuran (THF) titration, a non-stoichiometric nitride powder with a 3 % oxygen impurity was left behind.

Nearly a decade later, Takano, *et al.* [47] synthesized DyN via a carbothermic reduction and subsequent nitridation. Dysprosium oxide (Dy_2O_3, 99.9% pure) was combined with graphite at various molar ratios and ground with a mortar and pestle prior to being cold-pressed into to small disks. The handling of these materials was performed in a glovebox under a purified argon atmosphere to prevent hydrolysis. The reaction was initiated by ramping the furnace temperature to 427°C in vacuum (at approximately 10^{-3} Pa) prior to the oxide reduction at 1717-1822°C in purified nitrogen. To measure the conversion of the oxide to nitride, an infrared spectrometer was placed on the exhaust of the furnace to measure the CO gas release. The typical behavior of the CO gas release is shown in Figure 29. Once the CO gas release subsided, the furnace atmosphere was changed to N_2 + 4% H_2 which caused the formation of HCN (according to Reaction 13) which was presumed to have converted the residual oxygen and residual carbon, as shown in Reaction 14. The total carbothermic reduction prior to nitridation reaction is expressed in Reaction 15.

$$2C + N_2 + H_2 \rightarrow 2HCN \qquad \text{(Rxn. 13)}$$

$$Dy_2O_3 + 3HCN \rightarrow 2DyN + 3CO + \frac{3}{2}H_2 + \frac{1}{2}N_2 \qquad \text{(Rxn. 14)}$$

$$Dy_2O_3 + 3C + N_2 \rightarrow 2DyN + 3CO \qquad \text{(Rxn. 15)}$$

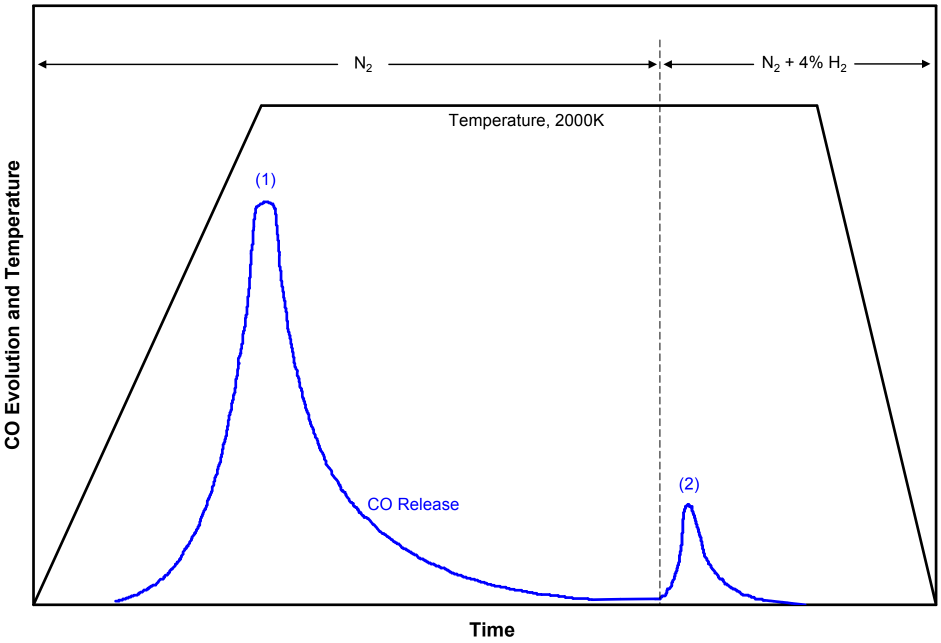

Figure 29: Typical behavior of CO gas release during heating; (1) Carbothermic reduction, (2) Removal of residual carbon and oxygen. Adapted from Takano, *et al*. [47].

As previously mentioned, using the metal (similar to what is produced from pyro-chemical separations techniques) as the initial material for synthesizing nitrides is arguably the most economical synthesis route. A very simple route of synthesizing DyN is provided by the Los Alamos National Laboratory (LANL) group, who demonstrated the ability to synthesize DyN by reacting pure dysprosium metal with pure nitrogen gas [43]. Although there are very little details describing this synthesis technique, it was mentioned that the dysprosium metal (-40 mesh) was reacted with a flow of pure nitrogen gas at 1200°C for 24 hours to form DyN, as characterized by powder X-ray diffraction [43].

Using slight variations of the aforementioned synthesis route, Takano *et al*. [6, 46] has published a few articles describing different methods for synthesizing DyN using metallic dysprosium as the starting material. The first technique reviewed describes the synthesis of DyN by reacting dysprosium metal flakes with a N_2 + 4% H_2 mixed-gas flow at 800°C followed by heating at 1300-1500°C in a nitrogen gas flow as per Reaction 16 [6, 46]. The DyN produced was of high quality and was later used to form a solid solution with ZrN.

$$Dy + \frac{1}{2}N_2 + 4\%H_2 \rightarrow DyN + 4\%H_2 \qquad \text{(Rxn. 16)}$$

However, it should be noted that these articles provide rather sparse details on the furnace dwell times in the different atmospheres and the final purity of the powder that was obtained.

In another article by Takano, *et al.* [8], the synthesis of DyN is described using a metallic dysprosium rod and a helium-hydrogen mixed gas prior to nitridation. The dysprosium metal rod was cut into pieces and placed in a He + 8% H_2 mixed gas stream at 410°C for 20-30 hours to form a dysprosium di-hydride (DyH_2). The hydride was removed from the furnace and crushed in a mortar and pestle prior to being placed back into a furnace, where it was then subjected to purified nitrogen gas stream at 1400°C. The completion of the nitridation process was confirmed with x-ray diffraction and the weight gain of the samples.

As demonstrated in the previous paragraphs, only a select few authors have studied approaches to synthesizing DyN [6, 8, 46, 47, 101], including; a direct nitridation method, a hydride prior to nitridation method, and a carbothermic reduction prior to nitridation method. However, this work focuses on synthesizing phase pure DyN via five routes including: a novel ball-milling synthesis route, a direct nitridation of dysprosium metal, hydriding prior to the nitridation of dysprosium metal, a carbothermic reduction prior to nitridation of Dy_2O_3, and a solution route analogous to Sol-Gel processing. The direct nitridation, hydride prior to nitridation, and the reactive ball milling synthesis routes to DyN are considered to be highly economical because they all start with pure dysprosium metal. They are seen as economical due to the fact that the direct products (metal) of the pyro-chemical separations technologies can be used as the starting materials.

2.1. Carbothermic Reduction Prior to Nitridation Synthesis Route to DyN

After an extensive literature review, one primary investigation described the synthesis of DyN via a carbothermic reduction of the oxide prior to nitridation. This work was performed by Takano, *et al.* [47] and was adapted and used for the initial studies presented in this work.

2.1.1. Experimental Procedures for the Carbothermic Reduction Prior to Nitridation Synthesis Route to DyN

The starting materials for the synthesis of DyN using a carbothermic reduction of a mixture of Dy_2O_3 and graphitic carbon was glassy carbon spherical powder (Alfa Aesar, Ward Hill, MA, USA) and 99.995% pure Dy_2O_3 powder (HEFA Rare-Earth Canada Co. Ltd., Richmond, BC, Canada). Both of these materials can be seen in Figure 30 below. The powders were combined using a molar powder ratio suggested by Takano, *et al.* [47] ($^{C}/_{Dy} = 3$) and were blended for 15 minutes in the Retsch planetary ball mill to obtain a homogenous mixture. The mixture was placed in a niobium-lined alumina boat and transferred to the high temperature alumina tube CM furnace (Figure 4). The furnace profile took approximately 30 hours and began with a 2 hour dwell at 425°C in a 0.6 Pa vacuum (Takano *et al* [47] used 10^{-3} Pa). Following the dwell at 425°C, an oxygen-gettered nitrogen atmosphere was introduced and the furnace was ramped to 1500°C and held for 15 hours. After holding under the nitrogen atmosphere for 5 hours, a N_2 + 6.28% H_2 atmosphere (1 atm (101 kPa)) was introduced for the remainder of the cycle, as shown in Figure 31.

a) b)

Figure 30: The starting materials of the carbothermic reduction prior to nitridation synthesis route to produce DyN are a) Glassy carbon spherical powder mixed with b) Dy_2O_3 powder.

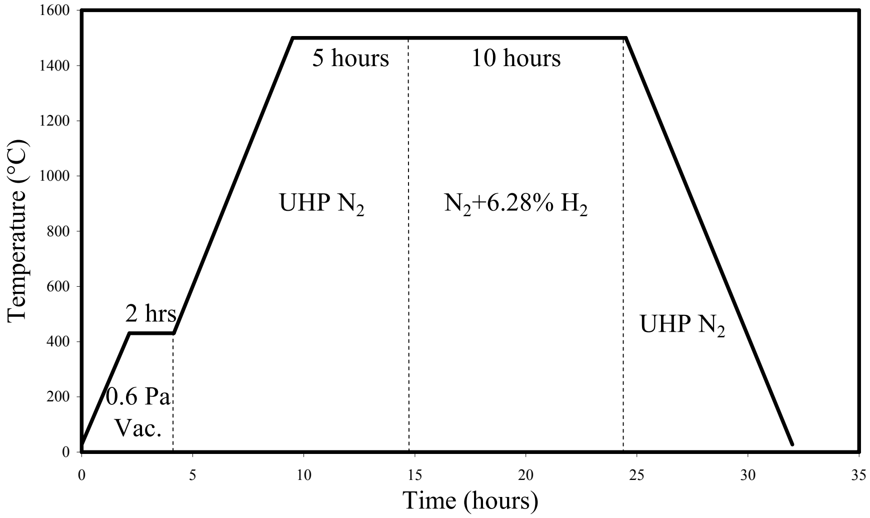

Figure 31: Furnace profile used for preliminary synthesis studies for producing DyN via a carbothermic reduction prior to nitridation synthesis route at 1500°C.

The synthesized powder was sealed in the stainless steel XRD sample holder and XRD was performed using a Philips X'pert XRD with a Cu-Kα source (λ=1.5418 Å) and a 4°/min scan rate in Bragg-Brentano geometry at room temperature.

2.1.2. Results of the Carbothermic Reduction Prior to Nitridation Synthesis Route to DyN

Dysprosia powder is typically a white or off-white color and carbon is typically a black powder (Figure 30). After mixing the powders and subjecting them to the carbothermic reduction prior to nitridation synthesis technique, the powder turned to a dark brown or black color (Figure 32), indicating the formation of DyN.

Figure 32: DyN powder produced via a carbothermic reduction prior to nitridation of a Dy_2O_3 and carbon powder mixture at 1500°C.

The resultant powder was analyzed for phase content using XRD. Figure 33 shows the XRD spectrum which clearly depicts the presence of the DyN phase when compared with the accepted data given by the JCPDS. However, an estimation received from this diffraction pattern suggests that the powder obtained was 80% DyN and 20% Dy_2O_3. Due to the presence of the Dy_2O_3, further optimization of the carbothermic reduction route is needed.

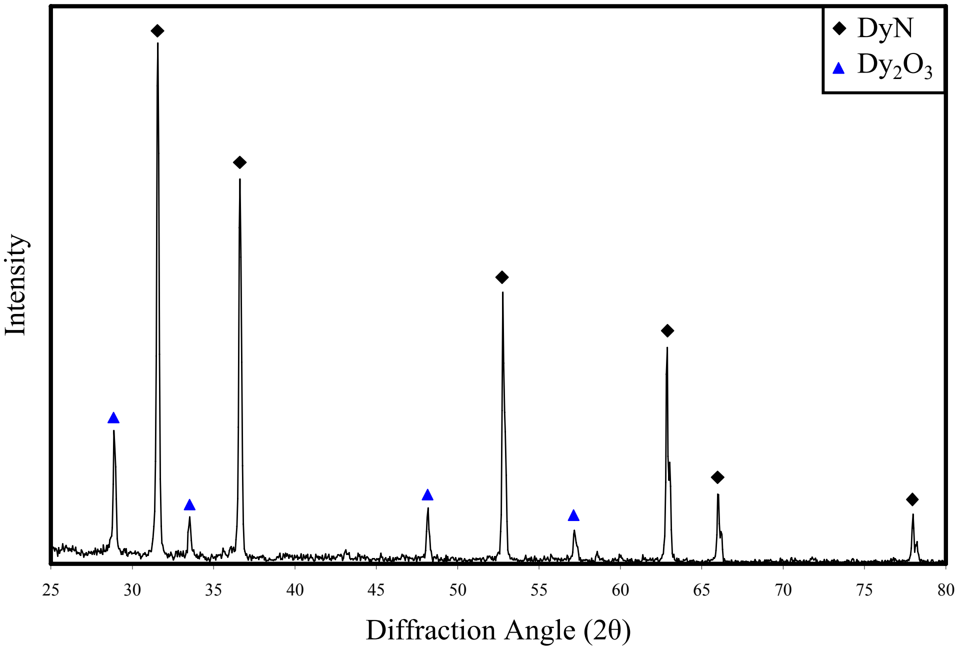

Figure 33: XRD spectrum of DyN powder synthesized by carbothermic reduction of Dy_2O_3 powder at 1500°C prior to nitridation.

2.2. Hydride prior to Nitridation Synthesis Route to DyN

As with the previous two methods of synthesizing DyN (the direct nitridation synthesis route and the ball-milling synthesis route), the hydride prior to nitridation synthesis technique used pure dysprosium metal as the starting material. The experimental procedures for this route have been modified multiple times throughout this work in attempts to increase the quality and purity of the synthesized nitride. Again, this method provides an economical synthesis route that requires very few processing steps and starts with pure dysprosium metal. One primary reason that it is considered as economical is due to the fact that the direct products (metal) of the pyro-chemical separations technologies can be used as the starting materials.

As previously described, Takano, *et al*. [6, 8, 46] is the only author to have published articles describing the synthesis of DyN from dysprosium metal using a hydride prior to nitridation technique. The work presented in this section of the report has been adapted from the work of Takano, *et al*. [6]. Takano reacted dysprosium metal flakes with a N_2 + 4% H_2 mixed-gas at 800°C followed by heating at 1300-1500°C in a nitrogen gas.

2.2.1. Experimental Procedures of the Hydride prior to Nitridation Synthesis Route to DyN

Approximately 15 grams of 99.9% pure dysprosium metal flakes (ESPI, Ashland Oregon) were used in this experiment. The pure dysprosium metal flakes were set in a niobium foil-lined alumina boat and positioned in the high temperature alumina tube CM furnace. The reaction (shown in Reaction 17) was carried to completion by flowing ultra high purity N_2 + 6.28% H_2 over the metal flakes for 4.5 hours at 800°C prior to nitridation in oxygen-gettered ultra high purity nitrogen with approximately 30 ppm H_2O and 1 ppm O_2 at 1500°C over the metal for 3 hours, as shown in the furnace profile of Figure 34.

$$Dy + \frac{1}{2}N_2 + 6.28\%H_2 \rightarrow DyN + 6.28\%H_2 \qquad \text{(Rxn. 17)}$$

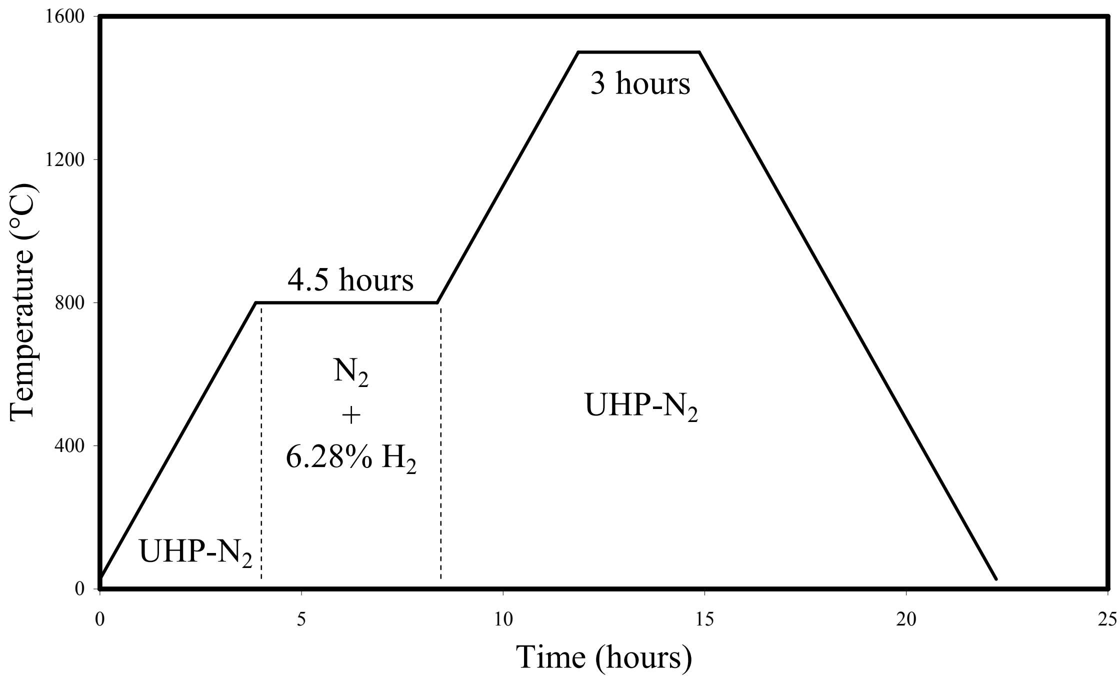

Figure 34: Furnace profile for producing DyN from 99.9% pure dysprosium metal flakes via a hydrogen reduction at 800°C with a N_2 + 6.28% H_2 gas followed by nitridation at 1500°C in very pure nitrogen gas.

As with the previous sample, a sample of the synthesized powder was prepared for x-ray diffraction by sealing it in a stainless steel XRD sample holder (Figure 40). The XRD spectrum was obtained using a Philips X'pert XRD with a Cu-K_α source (λ=1.5418 Å) and a 4°/min scan rate in Bragg-Brentano geometry at room temperature. The powder was further characterized via a Dumas combustion technique coupled with gas chromatography to quantify the composition of the resulting powder. This analysis was completed with a CE Elantech FlashEA 1112 Nitrogen and Carbon Analyzer (Lakewood, NJ, USA).

2.2.2. Results of Synthesizing DyN via a Hydride prior to Nitridation Synthesis Route

Prior to nitridation, the dysprosium metal flakes were a metallic grey color, as seen in Figure 35a. After nitridation, the color of the dysprosium became black (Figure 35b), indicating the formation of DyN.

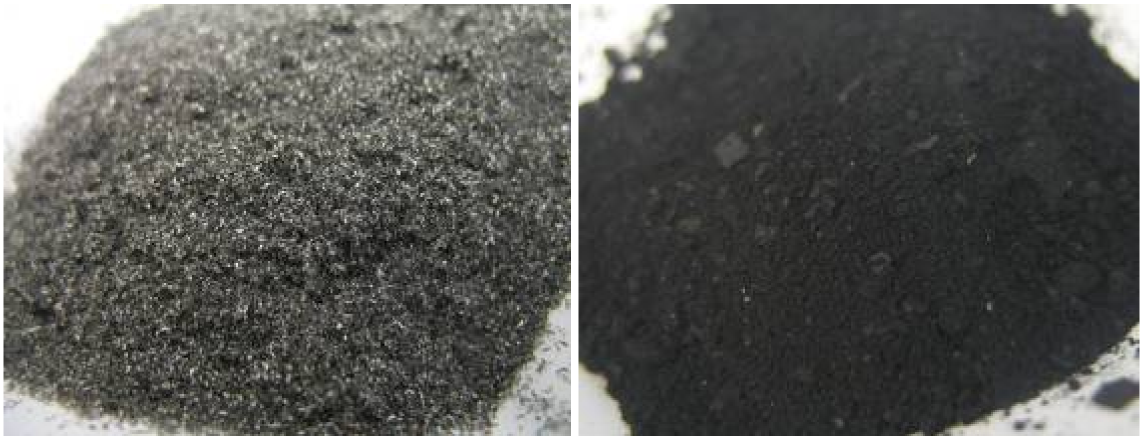

Figure 35: (a) 99.9% pure dysprosium metal flakes (-40 mesh) used as the starting materials in synthesizing (b) DyN via a thermal synthesis route by flowing a N_2 + H_2 mixed gas at 800°C prior to pure nitrogen at 1500°C.

When compared with the accepted data given by the JCPDS, the XRD spectrum in Figure 36 confirmed that phase pure DyN was synthesized. Analysis of the XRD data using Lorentzian fits of the 31.7° ((111) plane) and 36.9° ((200) plane) diffraction peaks was used to find the lattice constant of the face-centered cubic DyN. The lattice constant was found as 4.93 ± 0.01Å using Bragg's equation (Equation 4) by assuming a first order diffraction peak (n=1) and the incident Cu-K_α x-rays had a wavelength of 1.5418Å. This calculated d-spacing is in good agreement with the published value of 4.905Å [102]. Further analysis of the diffraction pattern using Scherrer's relation (Equation 2) suggests an average crystallite size of approximately 49 nm. Characterization of the oxygen content of the resultant powder suggests that the DyN sample contained only 0.043 ± 0.43% oxygen (i.e. below the detectable limits of the system). The hydride prior to nitridation of dysprosium metal was used to duplicate these results on numerous occasions.

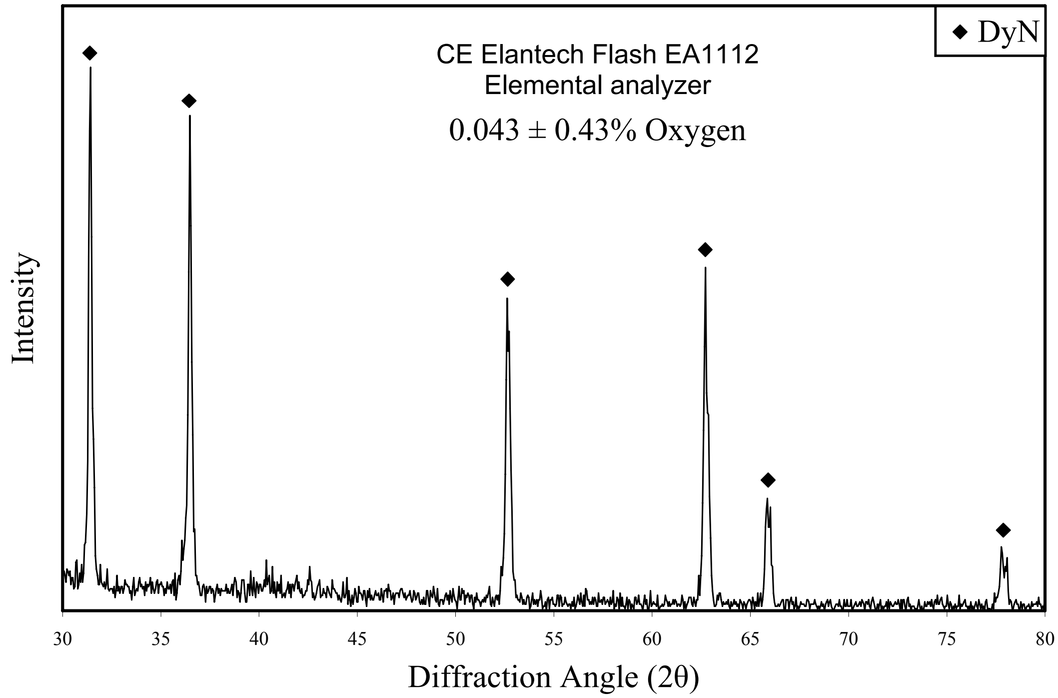

Figure 36: XRD pattern of very high purity DyN powder produced from 99.9% dysprosium metal. The dysprosium metal was heated to 800°C in a N_2/H_2 mixed gas flow prior to 1500°C in UHP nitrogen gas. Further analysis suggests that there is only 0.043% oxygen in the sample.

This modified hydride-nitride route has demonstrated the feasibility of synthesizing very high purity DyN from pure dysprosium metal flakes in two primary steps; at lower temperatures (800°C) in the presence of hydrogen-nitrogen mix gas, and at higher temperatures (1500°C) in the presence of high purity nitrogen.

2.3. Direct Nitridation Synthesis Route to DyN

The direct nitridation of dysprosium metal to DyN is a simple thermal route that uses only an oxygen-gettered ultra high purity nitrogen processing gas. As previously discussed, there has only been one document found that presents this direct nitridation synthesis route to form DyN, and it contains very little information on the synthesis procedures [43]. This section of the report demonstrates the direct nitridation of dysprosium metal to form DyN and presents a detailed procedure so that this work is able to be reproduced.

2.3.1. Experimental Procedures of Synthesizing DyN via a Direct Nitridation Synthesis Route

Approximately 5 grams of 99.9% pure dysprosium metal flakes (ESPI, Ashland Oregon) were used in this experiment. The pure dysprosium metal flakes were set in a niobium foil-lined alumina boat and positioned in the high temperature alumina tube CM furnace. The reaction (shown in Reaction 18) was carried to completion by flowing oxygen-gettered ultra high purity nitrogen with approximately 30 ppm H_2O and 1 ppm O_2 at 1300°C over the metal for 11 hours, as shown in the furnace profile of Figure 37.

$$Dy + \frac{1}{2} N_2 \rightarrow DyN \qquad \text{(Rxn. 18)}$$

After nitridation, a powder sample was prepared for x-ray diffraction by sealing it in a stainless steel XRD sample holder (Figure 40). An XRD spectrum was obtained using a Philips X'pert XRD with a Cu-Kα source (λ=1.5418 Å) and a 4°/min scan rate in Bragg-Brentano geometry at room temperature. The powder was further characterized via a Dumas combustion technique coupled with gas chromatography to quantify the final oxygen content of the powder. This analysis was completed with a CE Elantech FlashEA 1112 Nitrogen and Carbon Analyzer (Lakewood, NJ, USA).

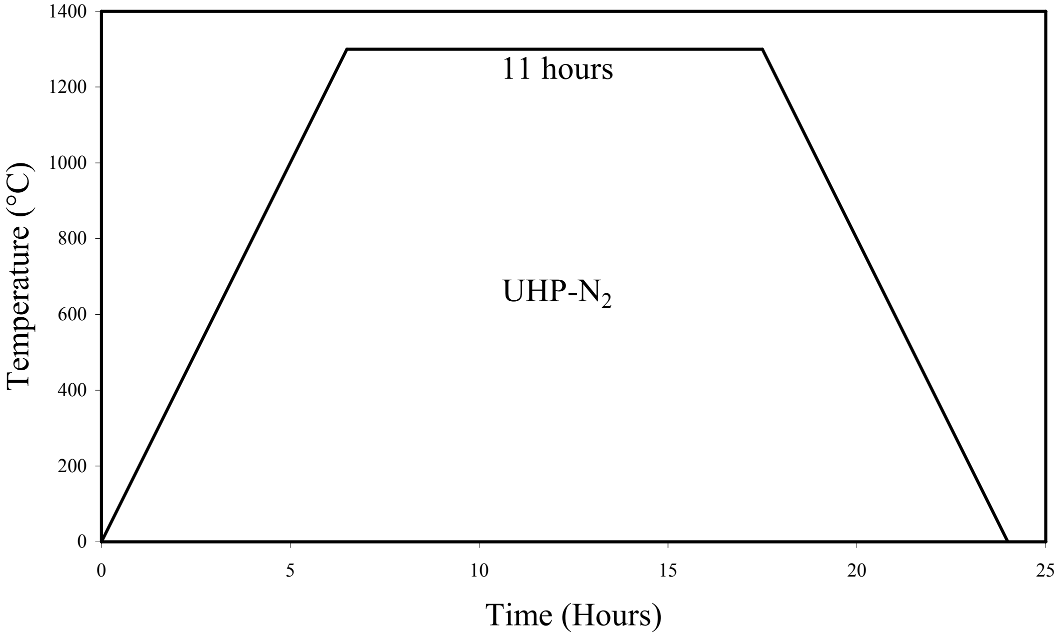

Figure 37: Furnace profile for direct nitridation of pure dysprosium metal flakes producing phase pure DyN at 1300°C for 11 hours.

2.3.2. Results of Synthesizing DyN via a Direct Nitridation Synthesis Route

A typical solid dysprosium ingot is a metallic grey color, as shown in Figure 38a. After nitridation, the dysprosium became a dark gray or black color (Figure 38b), indicating the formation of DyN. Comparison of the XRD spectrum of the resulting powder with the accepted data given by the JCPDS confirmed that a phase pure DyN was synthesized (Figure 39). Further analysis of the XRD data using Lorentzian fits of the 31.6° ((111) plane) and 36.7° ((200) plane) diffraction peaks was used to find the lattice constant of the face-centered cubic DyN. The lattice constant of the DyN was determined to be 4.90 ± 0.01Å using Bragg's equation (Equation 4) by assuming a first order diffraction peak (n=1) and the incident Cu-K_α x-rays had a wavelength of 1.5418Å. This calculated d-spacing is in very good agreement with the published value of

4.905Å [102]. Further analysis of the diffraction pattern using Scherrer's relation (Equation 2) suggests an average crystallite size of approximately 50 nm. Characterization of the oxygen content of the resultant powder suggests that the DyN sample contained only 0.33 ± 0.42% oxygen. However, this value was below the detectable limits of the analyzer used.

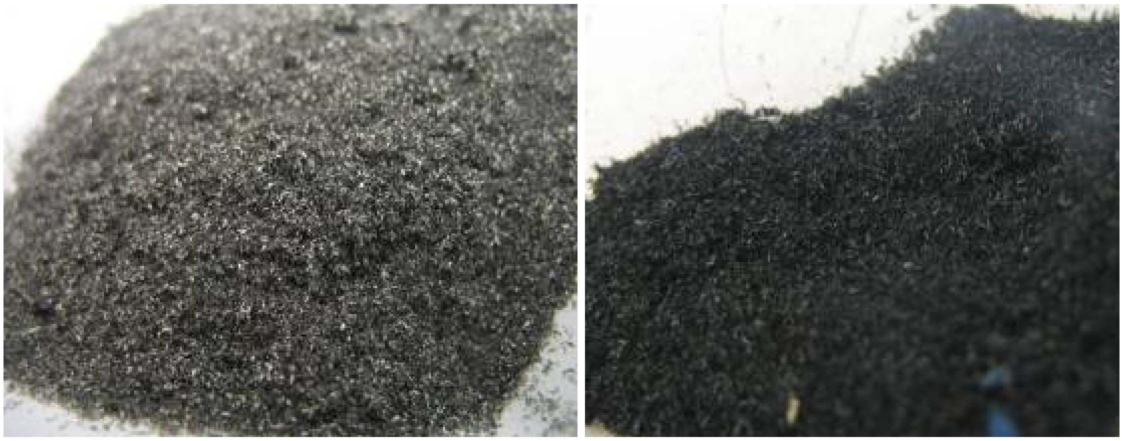
a) b)

Figure 38: (a) 99.9% pure dysprosium metal flakes (-40 mesh) used as the starting materials in synthesizing (b) DyN via a direct nitriding synthesis. Route at 1300°C.

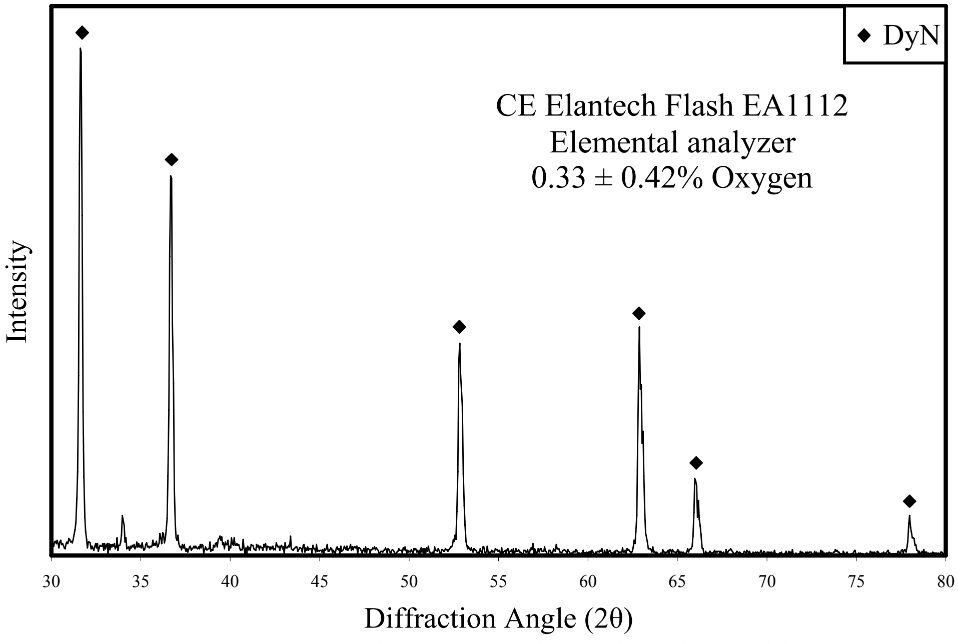

Figure 39: XRD pattern of DyN powder produced by directly nitriding 99.9% pure dysprosium metal flakes at 1300°C. Further analysis suggests that there is only 0.33% oxygen in the sample.

2.4. Novel Reactive Milling Synthesis Route to DyN

This section of the report demonstrates a novel and economical mechanically induced gas-solid reaction (ball-milling) synthesis route for synthesizing high purity DyN at room temperature. The success of this low temperature, mechanical route for producing DyN (as a surrogate for AmN) should have profound implications on the advanced fuel cycle because it potentially offers the advantages of a simple, inexpensive method for producing nitride fuels for use in fast-spectrum reactors. Also, due to the high vapor pressures of DyN and AmN, this route offers a "closed-system" synthesis route preventing the loss of material via the evolution of the vapor. The results of this work have been published in the Journal of Nuclear Materials [91, 92].

After a detailed literature review, the work of synthesizing any lanthanide or actinide (including DyN and UN) at room temperature using a reactive milling technique has never been reported. However, as previously stated, TiN, BN, ZrN, and Fe_3N have been produced by reactive ball milling the respective metals in a nitrogen or ammonia milling atmospher [79-90].

2.4.1. Experimental Procedures for DyN Synthesis via Reactive Milling

Approximately 5 grams of 99.9% pure dysprosium metal flakes (ESPI, Ashland, Oregon, USA) were used in these experiments. The flakes (-40 mesh, < 420 μm) were placed in a 250 mL chrome steel milling vessel along with the milling media prior to sealing and removing from the argon atmosphere glovebox. The milling vessel contained 70 grams of 5 mm diameter yttria stabilized zirconia (YTZ, TOSOH, Tokyo, Japan) milling media providing an optimum metal to media mass ratio of 1:14.

The vessel, seen in Figure 41a, was sealed prior to purging and charged with oxygen-gettered ultra-high purity N_2 to approximately 3.45 atm (350 kPa). The nitrogen gas contained less than 0.1 ppb oxygen content as measured by a Ntron Model OA-1 (Exton, PA, USA) oxygen analyzer. The vessel was fixed in the planetary ball mill (Figure 41b) and the dysprosium was milled for 24 hours at 500 rpm with intermittent nitrogen purges and recharges. The intermittent purges occurred after 2 hours, after an additional 4 hours, and after an additional 8 hours of milling. There is approximately 80% excess nitrogen to complete the metal to mononitride conversion when the 250 mL vessel is charged to 3.45 atm (350 kPa). However, the multiple purge cycles were used to ensure near isobaric nitrogen conditions throughout the milling process.

After milling, the powder was separated from the milling media in the Plas-Lab inert atmosphere glovebox (Figure 1) and prepared for XRD analysis. The XRD system used for this analysis did not have inert atmosphere capabilities and therefore the resultant powder had to be protected from oxidation during transportation to, and during XRD analysis. Therefore, the powder was loaded into a stainless steel powder holder of Figure 40 and sealed with an x-ray transparent film prior to diffraction analysis. The XRD data was collected in air at room temperature using a Philips X'pert XRD with a Cu-K_α source (λ=1.5418 Å) and a 4°/min scan rate in Bragg-Brentano geometry. For particle size distribution data, the DyN powder was dispersed in de-ionized water and analyzed with a Horiba LA-950 Laser Scattering Particle Size Distribution Analyzer. This was done using a refractive index of $2.2 + 0.1i$. Where "i" denotes the imaginary component of the refractive index and accounts for irregularities (deviations from spherical) and opaqueness of the powders.

Figure 40: Stainless steel sample holder used for obtaining XRD patterns. The powder sample is placed and leveled in the center (10 mm diameter by 1 mm deep) and covered with an x-ray transparent film to temporarily protect it from oxidation during transportation to and during XRD analysis.

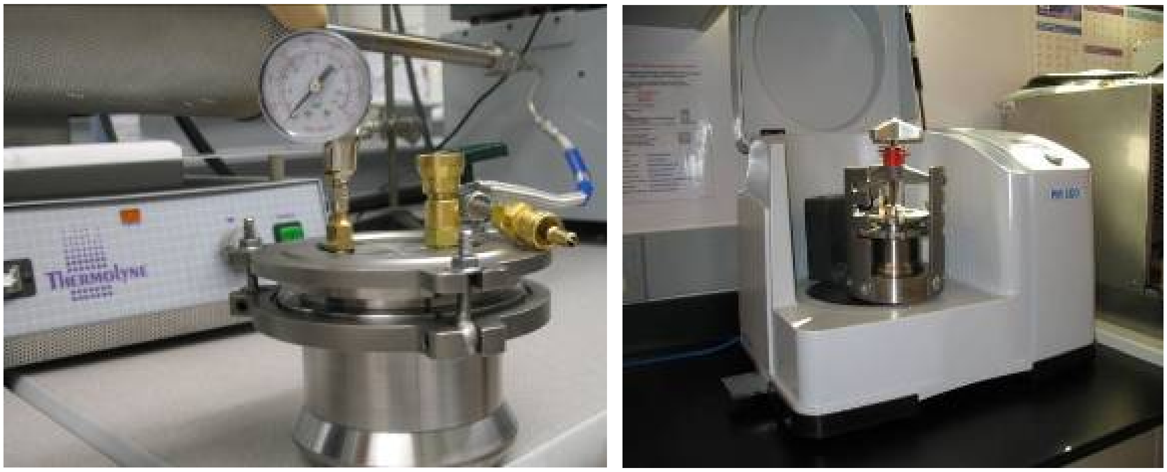

a) b)

Figure 41: a) Planetary ball mill vessel and b) Retsch planetary ball mill (PM100) used for the synthesis of U_2N_3, DyN, and CeN via reactive milling at room temperature. The milling vessel allows for multiple charges/purges with UHP N_2 during the reactive milling process.

2.4.2. Results of the Synthesis of DyN via Reactive Milling

The as received dysprosium metal flakes were very coarse and had a shiny grey color (Figure 42a). After ball-milling the powder became much finer, darker, and lost all luster as shown in Figure 42b and 42c.

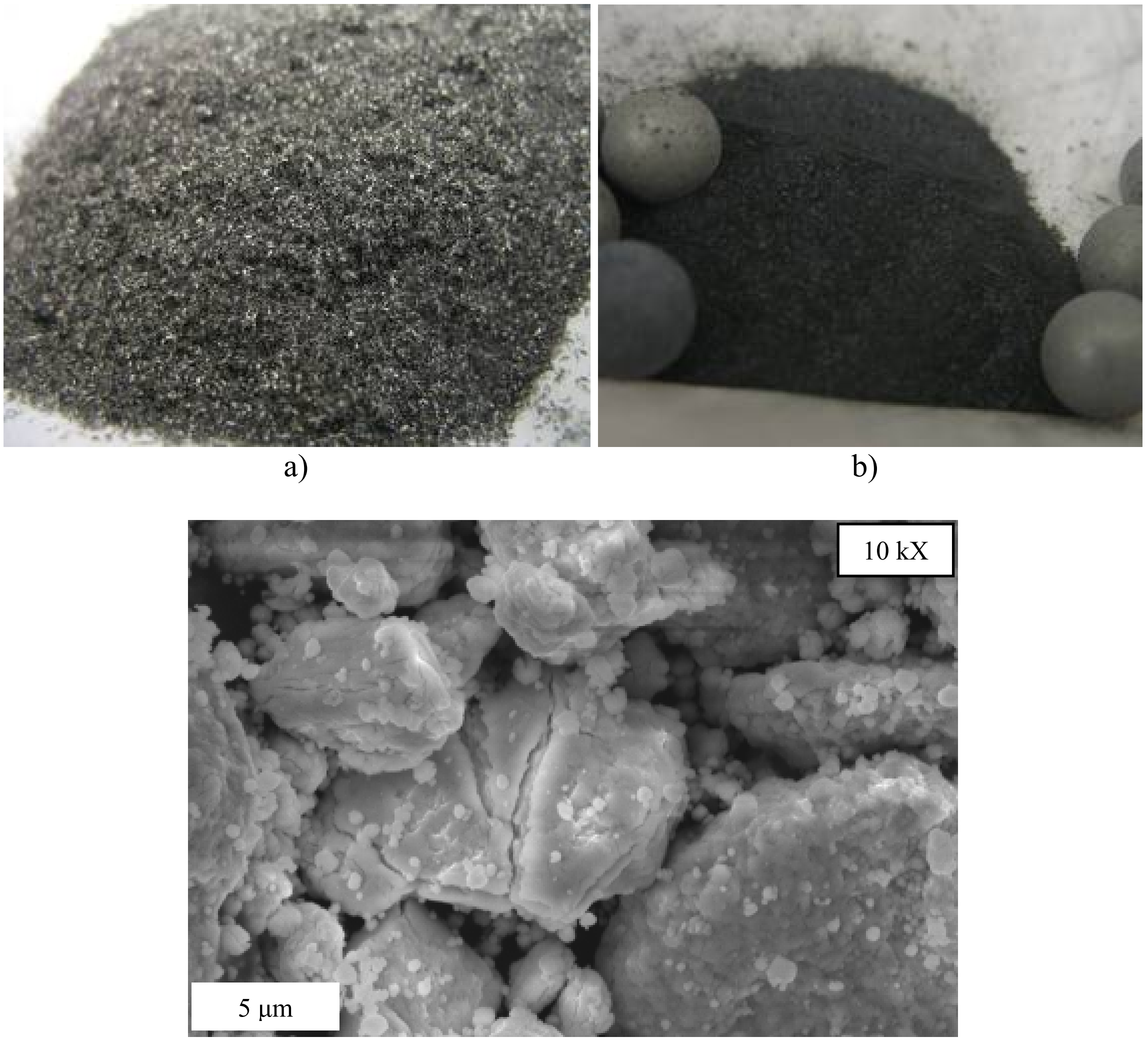

a) b)

c)

Figure 42: Shown are the (a) 99.9% pure dysprosium metal flakes (-40 mesh) that were used as the starting materials in reactive milling for 24 hours in a nitrogen atmosphere at room temperature forming phase pure (b) DyN. The high deformation of the material from milling is seen in the SEM image c).

The XRD spectrum of the DyN which had been milled for 24 hours at room temperature with a metal to media mass ratio of 1:14 is shown in Figure 43. The only peaks present in the XRD spectrum are the DyN peaks (by comparison with the accepted data given by the JCPDS), indicating that the ball-milling route produced a phase pure DyN powder. Further analysis of the XRD data using Lorentzian fits of the 31.7° ((111) plane) and 36.9° ((200) plane) diffraction peaks was used to find the lattice constant of the face-centered cubic DyN. The lattice constant was found as 4.88 ± 0.01Å using Bragg's equation (Equation 4) by assuming a first order diffraction peak (n=1) and the incident Cu-K_α x-rays had a wavelength of 1.5418Å. Further analysis of the diffraction pattern using Scherrer's relation (Equation 2) suggests an average crystallite size of approximately 8 nm. This calculated d-spacing is in good agreement with the published value of 4.905Å [102]. A plot of particle size distribution obtained with the Horiba (Figure 21) laser scattering particle size analyzer is shown in Figure 44. The median particle size of the bi-modal particle distribution was approximately 4 μm and the mean was approximately 3.6 μm (base on volume percent) after 24 hours of milling. It is worth noting that the diffraction pattern also exhibited broad diffraction peaks with low intensities and relatively large peak to noise ratios. These characteristics are attributed to two primary factors: the first being very small crystallites and the second being the amorphization of the solids. The average crystallite sizes were estimated through the Scherrer relation (Equation 2) in the preceding paragraphs. The amorphization of the materials is expected to be due to the high energy impacts between the milling media and the metal/nitride that is endured throughout the milling process. It is presumed that the large mechanical energy provided to the system produces large internal stresses and strains in the crystal structure of the materials, which is seen in the SEM image of the DyN powder (Figure 42c).

$$n\lambda = 2d_{hkl}\sin\theta \qquad \text{(Eqn. 4)}$$

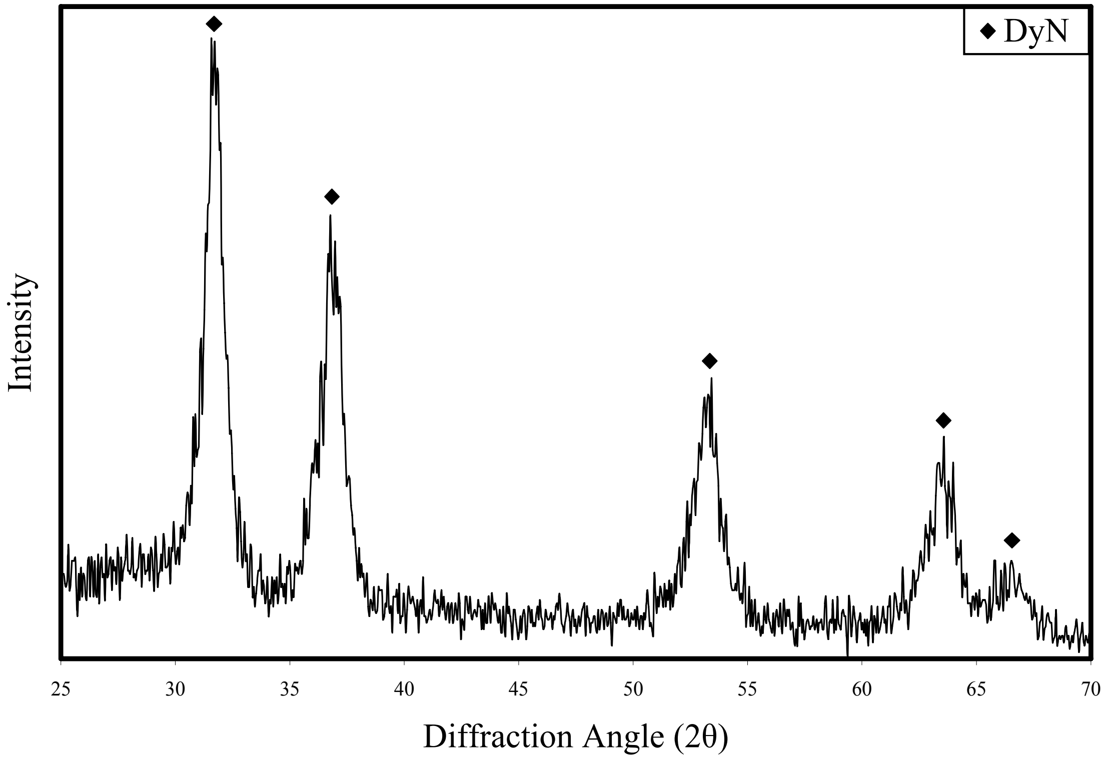

Figure 43: X-ray diffraction spectrum of DyN powder synthesized via a mechanically induced gas-solid reaction (ball-milling) synthesis route at room temperature for 24 hours. The only peaks present are characteristic DyN peaks.

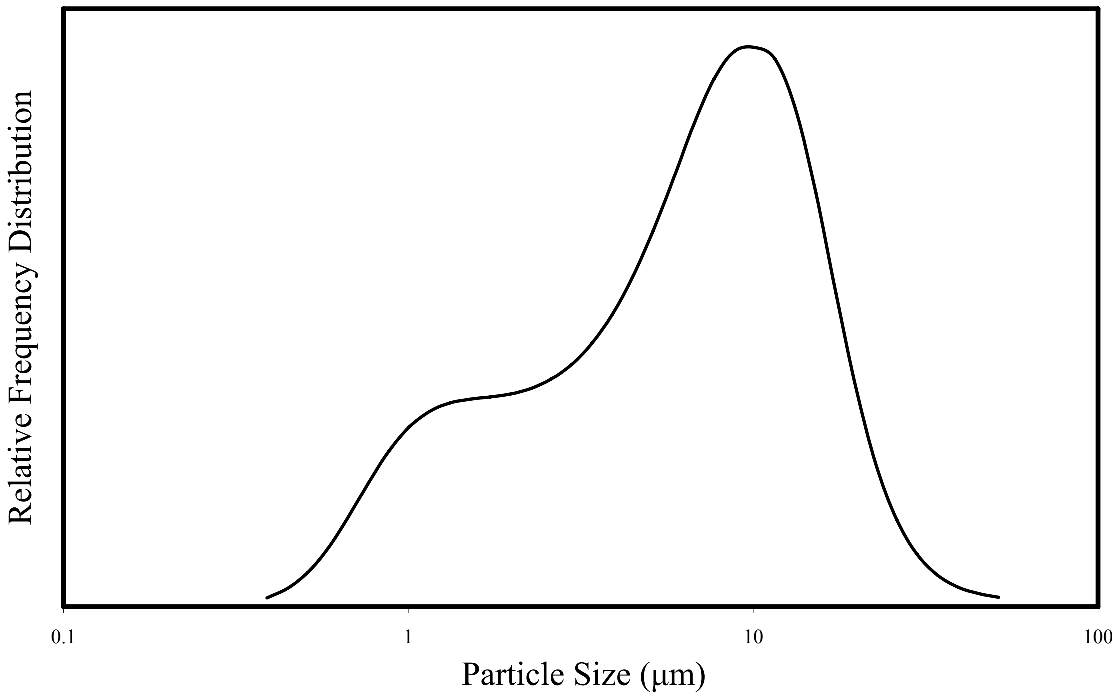

Figure 44: Particle size distribution of DyN powder synthesized via a mechanically induced gas-solid reaction (ball-milling) synthesis route at room temperature for 24 hours. The median particle size is approximately 4 μm and the mean particle size is approximately 3.6 μm.

2.5. Solution Synthesis Route Analogous to Sol Gel Processing for Synthesizing DyN

The University of Florida (UF) investigated solution routes to actinide nitrides. A solution route, such as sol/gel processing that is performed at lower temperatures, would allow for mixing on a molecular level and, therefore, yield more homogenous fuels. Solution processing of ceramics has generally been restricted to metal oxide ceramics with metal-organic compounds as precursors. The most obvious example is sol-gel processing. Metal alkoxides are hydrolyzed to form metal hydroxides, which subsequently condense to form the metal oxides. Non-aqueous systems have been described where the condensation reaction involves formation of stable organic molecules. Thus, a metal ethoxide can be reacted with a metal acetate to form the metal oxide and ethyl acetate. Other stable condensation products are acid anhydrides and ethers. When metal halides are reacted with metal alkoxides, volatile organohalides are formed. The organic group can also be a triorganosilyl group in the case of the formation of alkyhalides. Metal hydrides can be reacted metal hydroxides to form hydrogen and a metal oxide. The condensation reactions are all equilibrium type reactions where the driving forces to form the oxides the high vapor pressure of the condensation product and the high thermodynamic stability of the metal oxides. Mixed oxides (MOX) can also be prepared in this way.

Little has been reported on the formation of metal nitrides by analogous chemistries. The =NH group is isoelectronic to the -O- group, therefore one might expect analogous reactions. With the exception of lithium nitride, most metal oxides are more stable than their nitrides, making it necessary to avoid water or any other -OH containing solvent when attempting to form actinide nitrides. Although many of the reactions discussed above are reported for reactions containing when silicon or titanium metals, not much has been reported for the actinides. It is this “by analogy” approach that has driven the UF research. The nature of the ligand bound to the metal precursor must also be considered. It would be difficult to avoid introduction of oxygen to the actinide nitrides if the ligands are bound through an oxygen atom to the actinide metal ion. For organic solubility, “soft” (*Pearson HSAB concept*) anion legends are required. Some of the soft legends are sulfides, hydrides, and iodides. To date, the UF research has focused on iodide precursors.

2.5.1. Experimental Procedures for DyN Synthesis via an Hexamethyldisilazane (HMDZ) (with Liquid Ammonia Solvent) Synthesis Route

The high reactivity of cerium iodide (presented in Chapter IV, Section 3) prompted the UF to try dysprosium to first prove the approach without the necessity of the very time consuming process of rigorous moisture and air free setup in all steps of the characterization process.

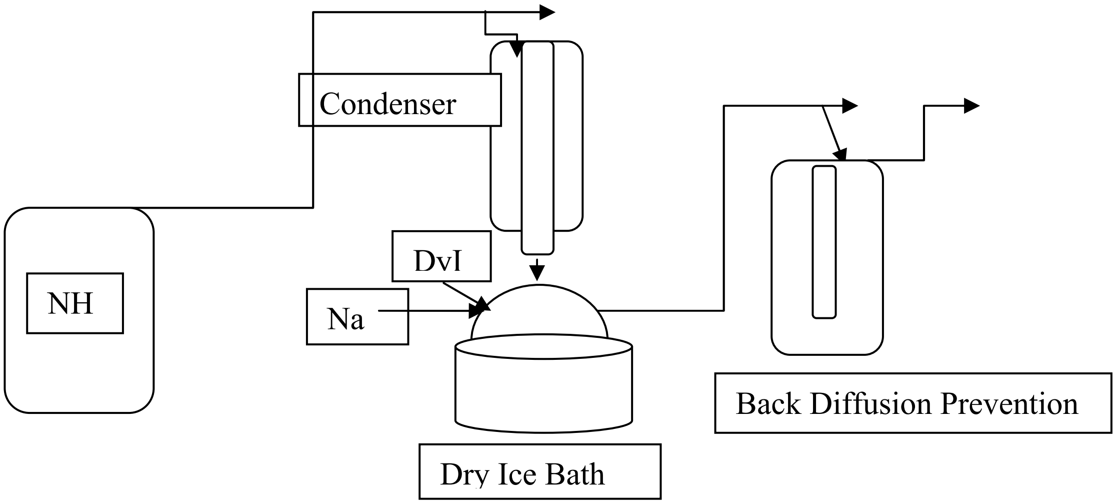

Figure 45: Setup of the apparatus for dysprosium iodide with liquid ammonia experiments

In lieu of the difficulties encountered by the extreme sensitivity of cerium iodide to moisture, dysprosium iodide was chosen for the reaction. Samples of dysprosium (II) Iodide and dysprosium (III) Iodide were purchased. It was found from previous experiments that dysprosium (III) Iodide is a chunky solid, which is very difficult to disperse. Even though dysprosium (II) Iodide is less moisture sensitive compared to cerium (III) iodide, precautions were still taken to avoid moisture by allowing ammonia to run through the system for a few minutes before the start of liquefaction. Once the ammonia was liquefied, sodium was added and the solvated electron was successfully removed by using the rusty nail catalyst in about three and a half hours. Following this, dysprosium (II) iodide was added to the system to carry out the reaction. The dysprosium (II) iodide dispersed immediately in solution forming a deep purple color. The reaction was carried out for about one hour. The proposed reaction is shown in Figure 46.

$$\mathbf{2Na + 2NH_3\,(liquid) \longrightarrow 2NaNH_2 + H_2\uparrow \qquad (1)}$$

$$\mathbf{DyI_2 + 3NaNH_2 \rightleftarrows Dy(NH_2)_2 + 3NaI\downarrow \qquad (2)}$$

$$\mathbf{Dy(NH_2)_2 \xrightarrow{\Delta} (Dy\text{-}N) + 2NH_3\uparrow \qquad (3)}$$

Figure 46: The proposed reaction route to dysprosium nitride in liquid ammonia

After the proposed reaction, the ammonia was allowed to evaporate in an argon purge. The color changed from a purple solution to a mix of white and black powder on the surface of the round bottom flask. The round bottom flask was then put in a heating mantle and was allowed to heat for nearly 8 hours at 400 °C. The powder looked grayish black and is shown in Figure 47.

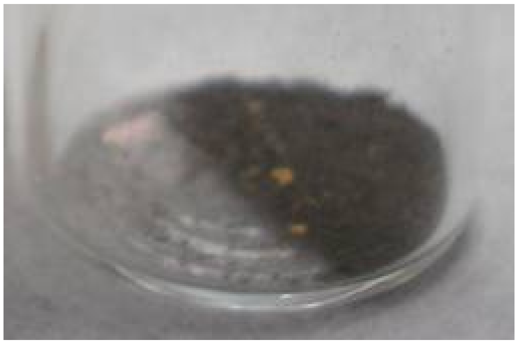

Figure 47: Powder sample from heating a dysprosium iodide mixed with ammonia sample in a heating mantle for 8 hours at 400°C.

2.5.2. Results of the Synthesis of DyN via an Hexamethyldisilazane (HMDZ) (with Liquid Ammonia Solvent) Synthesis Route

XRD analysis this powder left over from the heat treatment showed only amorphous features as shown in Figure 48. Further heat treatment of the powder to 1000°C in argon resulted in a rust like appearance, as shown in Figure 49.

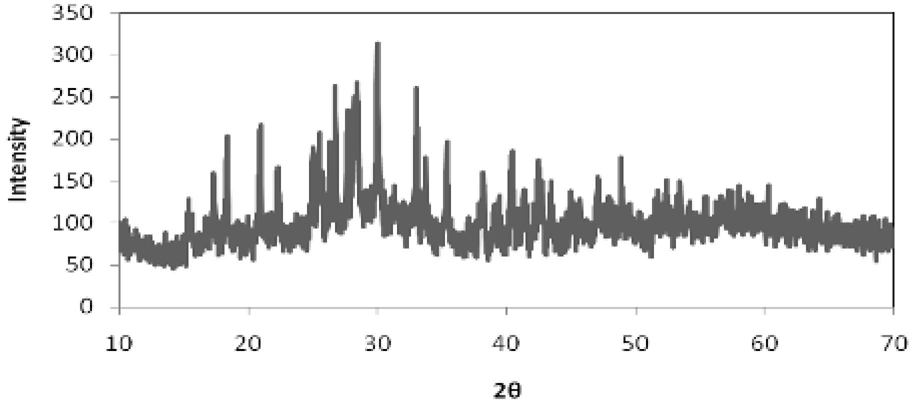

Figure 48: X-ray diffraction results of a powder sample from heating a dysprosium iodide mixed with ammonia sample in a heating mantle for 8 hours at 400°C.

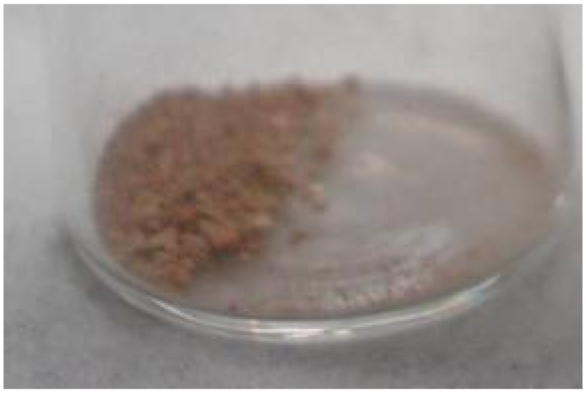

Figure 49: Powder sample from heat treating an amorphous dysprosium-containing powder in a tube furnace for 20 hours at 1000°C in pure argon.

XRD of the heat treated sample showed sharp peaks (Figure 50), but the peaks did not fit any of the materials listed in the JCPDS XRD library. At this point, it is not clear what oxidation state the dysprosium is in, particularly in the presence of the Fe0/FeIII catalyst used to prevent the formation of the solvated electron. In view of the apparent solubility, this route looks promising, though much characterization and improvement in handling these very air and moisture sensitive intermediates.

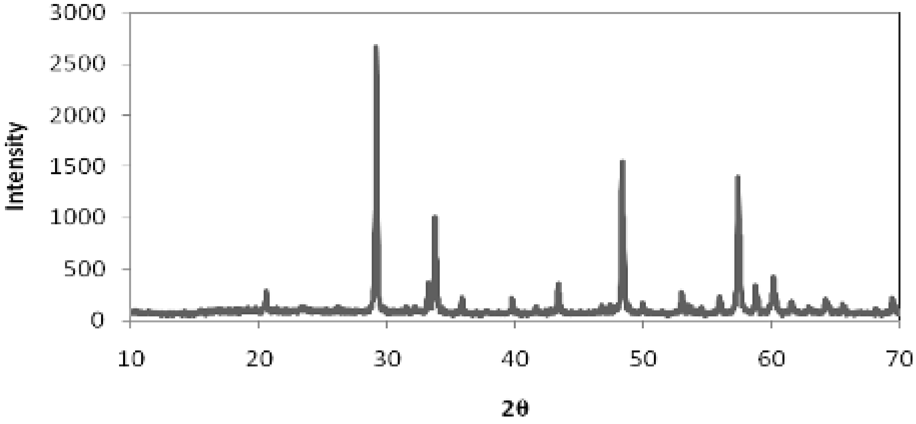

Figure 50: X-ray diffraction results of a sample from heat treating an amorphous dysprosium-containing powder in a tube furnace for 20 hours at 1000°C in pure argon.

2.6. Discussion of the Dysprosium Nitride Synthesis Routes

The work presented in this document has demonstrated the feasibility of synthesizing phase pure DyN via three methods, namely; the simultaneous hydride and nitride formation in a nitrogen hydrogen mixed gas prior to full conversion to DyN in pure nitrogen, directly nitriding dysprosium metal at 1300°C, and reactive milling of dysprosium metal in nitrogen at room temperature. A carbothermic reduction of Dy_2O_3 prior to nitridation at 1500°C was also attempted but resulted in a poor quality product. A solution route was also attempted but the reported results were inconclusive. The focus of the work presented in this document was to use and characterize the routes that used pure dysprosium metal as the starting material. Pure dysprosium metal is not only easily obtained via commercial sources, but it also depicts the products received from pyro-chemical separations technologies. Therefore, when it is used as the starting material for the synthesis of DyN (such as 3 of the 4 routes presented in this report), the route is considered as an economical alternative. However, as demonstrated in the paragraphs at the beginning of Section 2.2, very few authors have studied various approaches to the synthesis of DyN and the most detailed route was by Takano *et al.* [47] who discussed the carbothermic reduction prior to nitridation synthesis route. It seems as though each of the other publications are feasibility studies because of the lack of detail and the lack of thermodynamic and kinetic assessments [6, 8, 46, 47, 101]. The synthesis routes presented in this document can also be considered feasibility studies due to the fact that the mechanisms by which the nitrides form were not fully investigated and the synthesis steps were not optimized.

The discussion of the reactive milling of dysprosium metal is very similar to that presented in Section 1.3 for the synthesis of uranium nitride. It is postulated that the mechanism by which the nitridation of the dysprosium metal occurs at room temperature is due to the high energy free surface that is created from cleavage of the dysprosium metal. It is presumed that it is an activated process when the nitrogen is first physisorbed to the surface of the metal prior to dissociating and chemisorbing to the dysprosium metal.

It is difficult to assess the thermal synthesis techniques presented in these studies due to the lack of data regarding the thermodynamics of DyN. Neither of the two accessible thermodynamic databases (FactSage [96] nor HSC Chemistry [98]) nor the reviewed literature for these studies have any information on the dysprosium-nitrogen system. Also, there exists no complete dysprosium-nitrogen binary phase diagram in the literature. The literature also lacks thermodynamic or kinetic data to be used for analyzing the different thermal synthesis techniques.

The first question about our failure of the solution synthesis route is the feasibility of synthesis of DyN via non-aqueous, sol-gel route. In earlier reported studies, various nitrides have been successfully synthesized using similar non-aqueous routes. For example, plutonium and uranium nitrides have been directly prepared from the liquid ammonia and the corresponding iodides in liquid ammonia [60, 103]. Lanthanide nitride precursors such as Trisbistrimethylsilylamidolanthanides ($((SiMe_3)_2)_3$) (where the metals include: La, Ce, Pr, Nd, Sm, Eu, Gd, Ho, Yb, Y and Lu) have been prepared by the reaction between iodides and lithiumhexamehtyldisilazane in THF at room temperature [104]. Lanthanide nitrides such as YN, LaN, PrN, NdN, SmN, EuN, TbN, ErN, and YbN have also been reported to have been prepared by ammonolysis of the aforementioned lanthanide nitride precursors in ammonia gas at high temperature [105]. However, when the literature was critically reviewed, several issues related to our failure could be rationalized. The first issue is the solubility of the starting iodides that we selected. Plutonium and uranium iodides have been observed to dissolve in the liquid ammonia [60, 103]. However, in the studies presented in this report, dissolutions of dysprosium iodide in liquid ammonia was not observed. The solubility of cerium iodide has been reported to be extremely low in THF, consistent with our observations that cerium iodide and dysprosium iodide cannot dissolve in the relative non-polar hexamethyldisilazane, as well as with various ether co-solvents.

A second concern is the propensity of dysprosium compounds to oxidize. In the studies cited above, many lanthanide precursors have been prepared in a rigorously controlled dry oxygen free environment. However, cerium was an exception [104], as it was pointed out by the researchers. The cerium compound was readily oxidized by even minute traces of air. Lastly, extensive measures were attempted to improve the atmosphere control of the reaction environment. Measures included assembling Schlenk-type glassware and the handling of the reactants in an oxygen-free glovebox, and utilizing an inert argon gas line with vacuum pump. However, the target processing conditions were never achieved. In the previously published study for preparing plutonium and uranium nitrides, the authors pointed out that the liquid anhydrous ammonia could have up to a maximum 5,000 ppm water because of the low reaction temperature (liquid ammonia temperature) [60, 103], the expected nitrides still could be prepared by this one-step reaction.

3. Synthesis of Cerium Mononitride (CeN)

The published studies of the synthesis procedures producing CeN and cerium hydride (CeH_2) are quite limited [15, 59, 76, 106-110]. Samsonov *et al* [109] compiles the work of many authors but many of them cited are Russian articles dating to the early 1900's and were not available. The work of Samsonov reports a broad range of synthesis techniques of CeN, namely; reducing CeO_2 with magnesium or aluminum in nitrogen, heating metallic cerium in nitrogen at 850°C where the nitrogen is quickly absorbed (Note: this was not able to be reproduced by another author), and heating CeH_2 in nitrogen at 800-900°C. Samsonov [109] also reports that another author attempted to make CeN by the reduction of ceria (CeO_2) with carbon in a N_2 atmosphere, but CeN could not be obtained in the temperature range $1250 \leq T \leq 1600$°C. However, CeN is formed upon heating CeC_2 in N_2 or NH_3 at 1250°C, with the reaction being more rapid in N_2 than in NH_3.

This work focuses on synthesizing CeN via four routes including: A novel ball-milling synthesis route, a hydride prior to nitridation synthesis route, a carbothermic reduction prior to nitridation synthesis route, and an iodide synthesis route analogous to sol-gel processing. It should be noted that CeN has a very high propensity for oxidation and thus extra precautions were taken to reduce the amount of oxygen the sample was exposed to.

3.1. Carbothermic Reduction Prior to Nitridation Synthesis Route to CeN

As with the DyN experiments, very little work has been published discussing the carbothermic reduction of CeO_2 prior to nitridation [15, 76, 108, 109]. Work by Nakagawa *et al* [15, 76] served as the basis for carbothermic reduction route reported in this report. Nakagawa performed studies on preparing CeN by starting with CeO_2, reducing it to CeC_2, and then to CeN in various thermal treatments. Nakagawa prepared a CeO_2 and graphite (amorphous carbon) powder mixture in the desired proportions in an agate mortar and pestle. Polyvinyl alcohol was added as a binder and the powder was compacted into green pellets of 10.2 mm OD and 1.6 mm thick under a pressure of about 250 MPa. The pellets were sintered up to 1400°C in a vacuum furnace to convert the CeO_2 to CeC_2. After the heat treatment, the furnace was cooled to room temperature and argon gas was introduced to prevent the oxidation of the samples. The pellet was then placed on a quartz boat was in the center of a quartz reaction tube and provided with a NH_3 or $H_2 + N_2$ stream at 900°C.

3.1.1. Experimental Procedures for the Carbothermic Reduction Prior to Nitridation Synthesis Route to CeN

The starting materials were glassy carbon spherical powder (Alfa Aesar) and 99.9% pure CeO_2 powder (Alfa Aesar) (Figure 51).


a) b)

Figure 51: a) Photograph of glassy carbon spherical powder and b) Photograph of CeO_2 powder prior to being mixed together to initiate the carbothermic reduction prior to nitridation synthesis route to produce CeN.

All work with this material was performed under inert atmosphere. The powders were combined with a molar ratio ($^{C}/_{Ce} = 3$) and blended for 15 minutes in the Retsch planetary ball mill to obtain a homogeneous mixture. The mixture was placed in a niobium-lined alumina boat before being transferred to the high temperature alumina tube CM furnace. The furnace profile took approximately 40 hours and began with a 12 hour dwell at 1400°C under a 0.6 Pa vacuum (Nakagawa [76] used 10^{-4} Pa). The profile then dwelled at 900°C for another 12 hours with a $N_2 + 6.28\%\ H_2$ atmosphere (Nakagawa [76] used ammonia). Figure 52 shows the furnace profile.

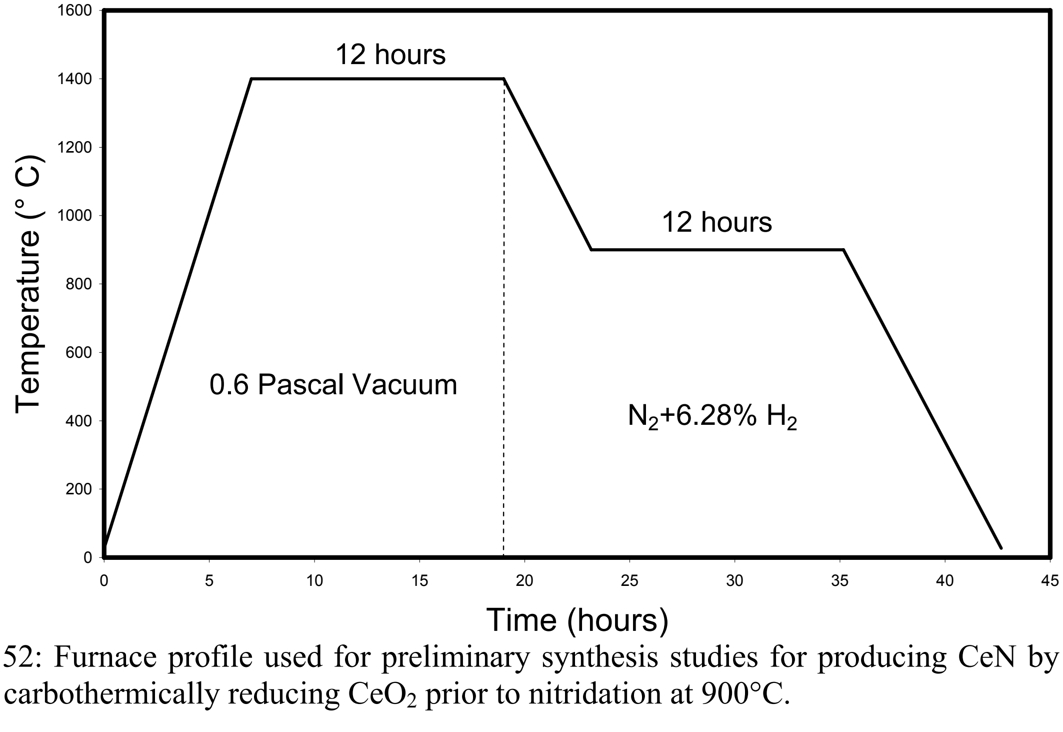

Figure 52: Furnace profile used for preliminary synthesis studies for producing CeN by carbothermically reducing CeO_2 prior to nitridation at 900°C.

3.1.2. Results of the Carbothermic Reduction Prior to Nitridation Synthesis Route to DyN

Ceria powder is typically a white or off-white color and carbon is typically a black powder (Figure 51). After mixing the powders and subjecting them to the carbothermic reduction synthesis technique, the powder turned to a dark brown or black color (Figure 53), predicting the formation of CeN.

Figure 53: Photograph of CeN powder produced via a carbothermic reduction prior to nitridation of a CeO_2 and carbon powder mixture. The thermal processing was carried out at a maximum temperature of 1400°C.

The CeN powder was sealed in the stainless steel XRD sample holder and a XRD pattern was obtained using a Philips X'pert XRD with a Cu-Kα source (λ=1.5418 Å) and a 4°/min scan rate in Bragg-Brentano geometry at room temperature. Figure 54 shows the XRD pattern which clearly depicts the presence of the CeN phase when compared with the excepted data given by the JCPDS. However, the presence of CeO_2 and CeC_2 indicates that further optimization of the carbothermic reduction route is needed. The fact that cerium carbide is present suggests that the final dwell temperature of 900°C may be too low or the 12 hour dwell may be too short.

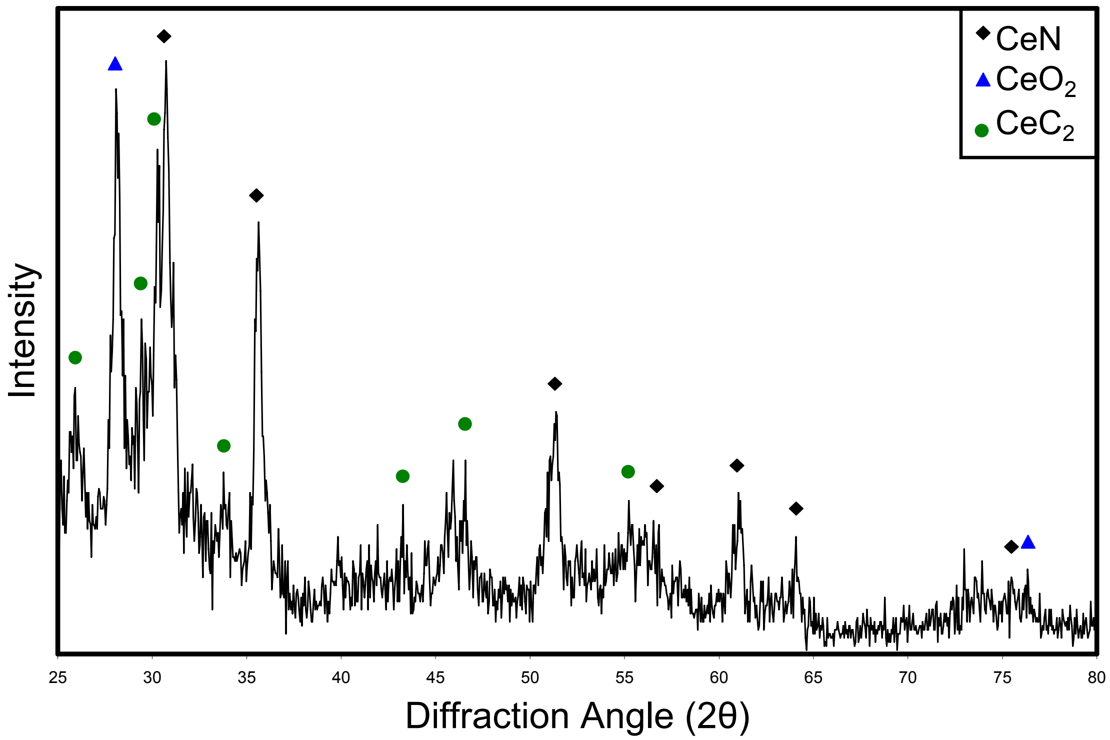

Figure 54: XRD spectrum of CeN powder synthesized by carbothermic reduction of CeO_2 powder at 1400°C. (Philips X'pert XRD with a Cu-Kα source (λ=1.5418 Å) and a 4°/min scan rate in Bragg-Brentano geometry).

3.2. Hydride prior to Nitridation Synthesis Route to CeN

One of the most simple routes for CeN synthesis was that of Hirota *et al* [108] who demonstrated that low-quality CeN could be synthesized by reacting cerium metal with a $N_2 + H_2$ mixed gas at slightly elevated temperatures (200 – 300°C). It is well known that cerium metal will hydride at these lower temperatures. However, if higher temperatures are used to nitride this hydride, a higher quality nitride powder should be produced [108]. Based on these principles and statements, high purity CeN was produced and characterized.

3.2.1. Experimental Procedures of the Hydride prior to Nitridation Synthesis Route to CeN (Route 1)

Approximately 5 grams of 99.9% pure -40 mesh cerium metal flakes (ESPI) were used in the experiment. The pure cerium metal was placed in a niobium foil-lined alumina boat and positioned in the high temperature alumina tube CM furnace (Figure 4). The total reaction (shown in Reaction 21) was carried to completion by flowing UHP N_2 + 6.28%H_2 over the metal for 5 hours at 850°C, as shown in the furnace profile of Figure 55.

$$Ce + H_{2+x} + \frac{1}{2}N_2 \rightarrow CeN + \frac{x}{2}H_2 \qquad \text{(Rxn. 21)}$$

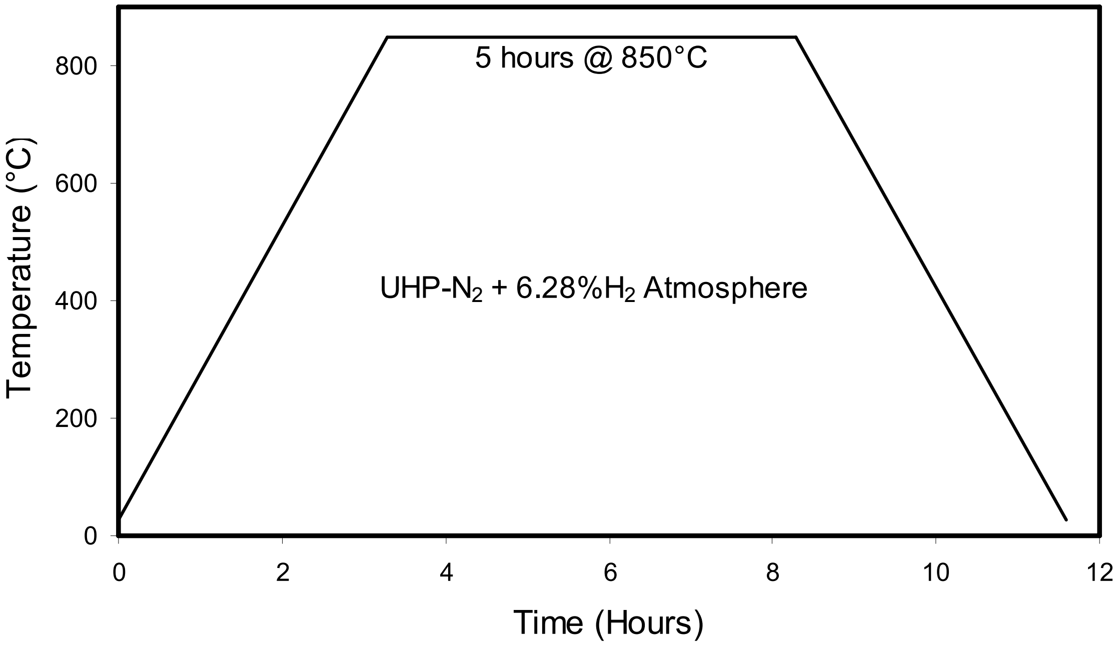

Figure 55: Furnace profile for producing CeN from 5 grams of pure cerium metal flakes.

3.2.2. Results of Synthesizing CeN via a Hydride prior to Nitridation Synthesis Route (Route 1)

The typical color of cerium metal flakes is a silvery grey/brown. After nitridation, the color changed to a very dark brown or black color and became a very fine powder, indicating the formation of CeN (Figure 56). The CeN powder was sealed in the stainless steel XRD sample holder and a XRD pattern was obtained using a Philips X'pert XRD with a Cu-Kα source (λ=1.5418 Å) and a 4°/min scan rate in Bragg-Brentano geometry at room temperature. The diffraction pattern shown in Figure 57 identified the formation of CeN and some CeO_2, as compared to the excepted data given by the JCPDS.

a) b)

Figure 56: a) Photograph of cerium metal flakes used for thermal synthesis routes to CeN. b) Photograph of CeN/CeO_2 powder produced via a thermal synthesis in a $N_2 + H_2$ mixed gas flow at 850°C for 5 hours.

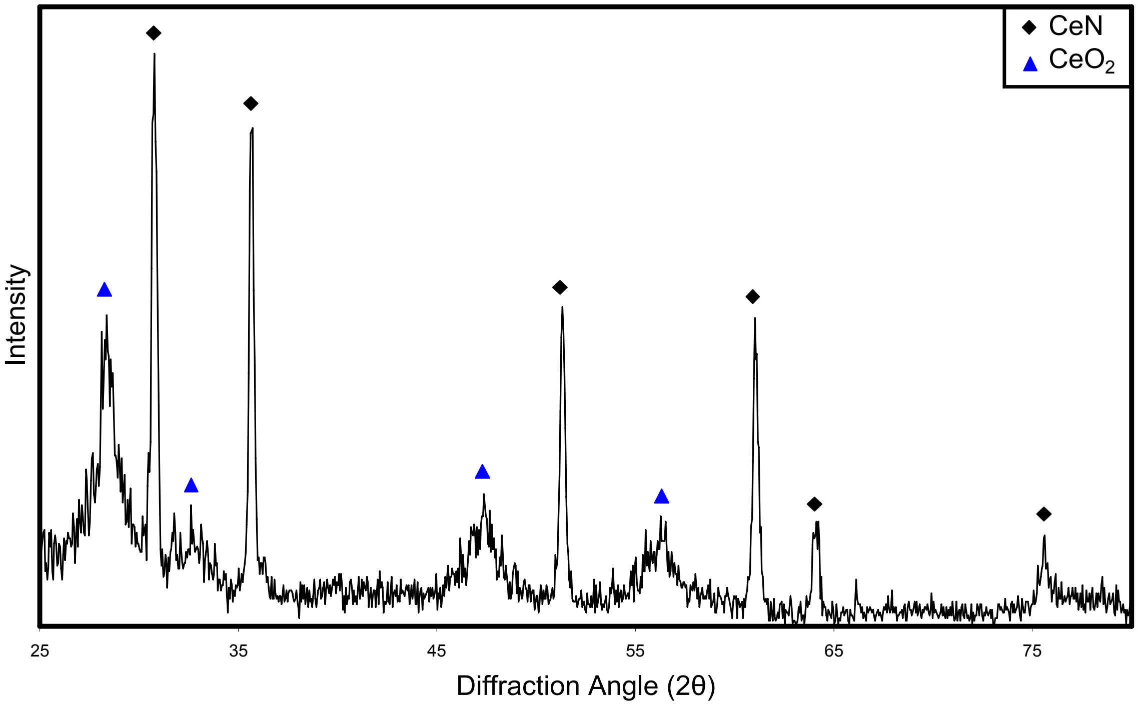

Figure 57: XRD pattern of an attempt to synthesize high purity CeN powder by a hydride-nitride route at 850°C for 5 hours in a N_2 + 6.28%H_2 mixed gas. (Philips X'pert XRD with a Cu-Kα source (λ=1.5418 Å) and a 4°/min scan rate in Bragg-Brentano geometry).

An estimation received from this diffraction pattern suggests that the powder obtained was only 65% CeN and 35% CeO_2. This hydride/nitride route shows promise as a method for synthesizing high quality CeN from pure cerium metal ingot in a hydrogen-nitrogen mixed gas with a minimal amount of handling steps. Further work will confirm the validity of synthesizing high purity CeN using this method.

3.2.3. Experimental Procedures of the Hydride prior to Nitridation Synthesis Route to CeN (Route 2)

Approximately 20 grams of 99.9% pure cerium ingot, obtained from ESPI, was used as a starting material. Before the reaction was initiated, the metal ingot was cleaved into 1-5 gram pieces with a uni-axial hydraulic press inside the argon atmosphere glove box shown in Figure 1a.

The cerium metal was loaded into a copper crucible inside an argon filled glovebox, loaded into a sealable container, and transported to the argon atmosphere glove box containing the hydrogen furnace that is shown in Figure 1b. The hydrogen furnace, a 21100 Barnstead Thermolyne tube furnace, was used to prepare the cerium hydride from the cerium metal ingot according to

Reaction 20. Figure 58 shows the furnace profile that was used in the successful synthesis of CeH_x from pure cerium metal.

$$Ce + H_{2+x} \rightarrow CeH_{2+x} \qquad \text{(Rxn. 20)}$$

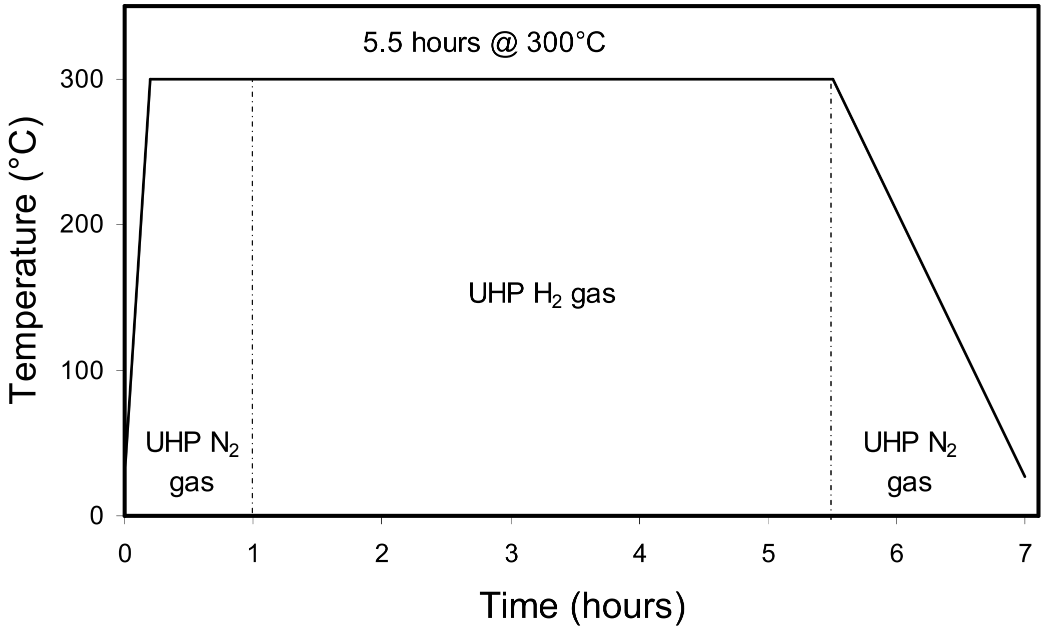

Figure 58: Furnace profile for producing cerium hydride from 1-5 gram solid pieces of 99.9% pure cerium metal ingot.

Due to the instability of cerium hydride and its tendency to oxidize, the sample was placed in a niobium-lined alumina boat inside the argon atmosphere glovebox. The boat was then placed in a sealable container to avoid any reactions with air during transfer to nitridation furnace. The boat was inserted into the nitridation furnace of Figure 3a using an inflatable glovebag filled with argon to further reduce any oxygen contamination. Nitridation was initiated by evacuating and purging the tube of the furnace multiple times to remove any residual oxygen. The tube was then purged with nitrogen for 10 minutes before ramping the temperature of the furnace (Figure 59). The sample was heated at $12.5^{\circ C}/_{min}$ to 900°C, held for 4 hours and then cooled at 12.5°C/min to room temperature. The reaction presumably occurs according to Reaction 21:

$$CeH_{2+x} + \frac{1}{2}N_2 \rightarrow CeN + \frac{x}{2}H_2 \qquad \text{(Rxn. 21)}$$

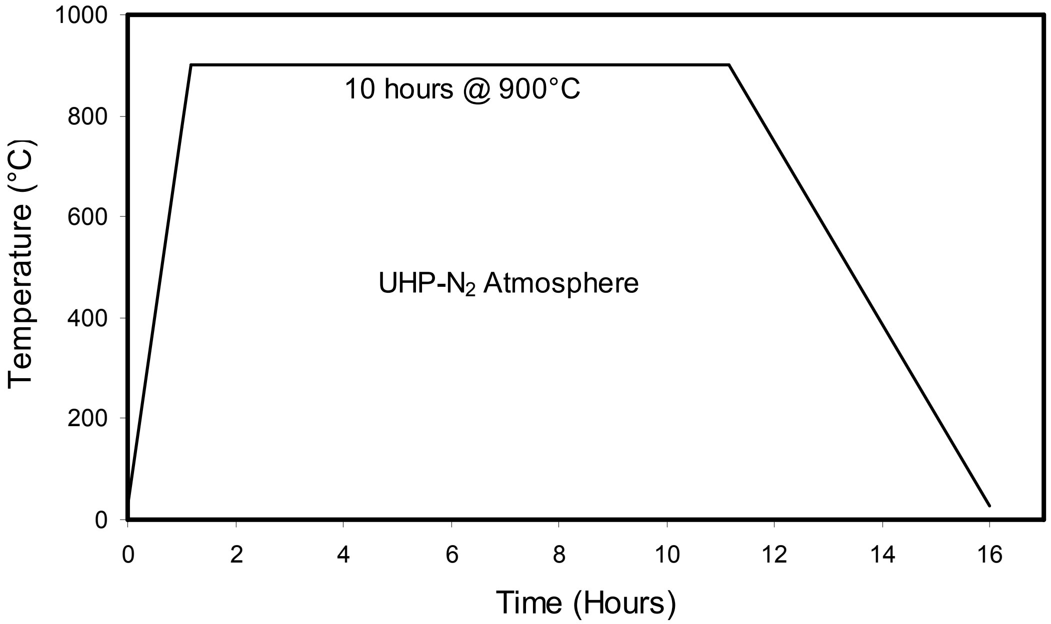

Figure 59: Furnace profile for producing cerium nitride from cerium hydride, as proposed in reaction 10.

3.2.4. Results of Synthesizing CeN via a Hydride prior to Nitridation Synthesis Route (Route 2)

The typical color of solid cerium ingot is a silvery grey. After hydriding, the color changed to dark brown or black and the solid pieces easily broke down to form a powder, indicating the formation of a hydride. After nitridation the color changed to a brown color indicating the formation of CeN. A visual inspection of the powders (shown in Figure 60) shows the relative color changes as the cerium metal is synthesized into cerium hydride and then into cerium nitride, which was confirmed with XRD analysis.


a) b) c)

Figure 60: a) Macroscopic image of cerium metal (left) used for synthesis of cerium hydride (right) in the copper boat shown. b) Photograph of cerium hydride produced with hydrogen gas at 300°C from cerium ingot. c) Photograph of cerium nitride powder synthesized from cerium hydride powder at 900°C in UHP nitrogen gas.

The CeN powder was sealed in the stainless steel XRD sample holder and a XRD pattern was obtained using a Philips X'pert XRD with a Cu-Kα source (λ=1.5418 Å) and a 4°/min scan rate in Bragg-Brentano geometry at room temperature. The diffraction pattern shown in Figure 61 identified the formation of high quality CeN, as compared to the excepted data given by the JCPDS. The powder was further characterized via a Dumas combustion technique coupled with gas chromatography to characterize the actual composition of the powder. The analysis confirmed that the CeN sample contained 1.4 ± 0.42% oxygen. This analysis was completed with a CE Elantech FlashEA 1112 nitrogen and carbon analyzer in the Geosciences Department at BSU.

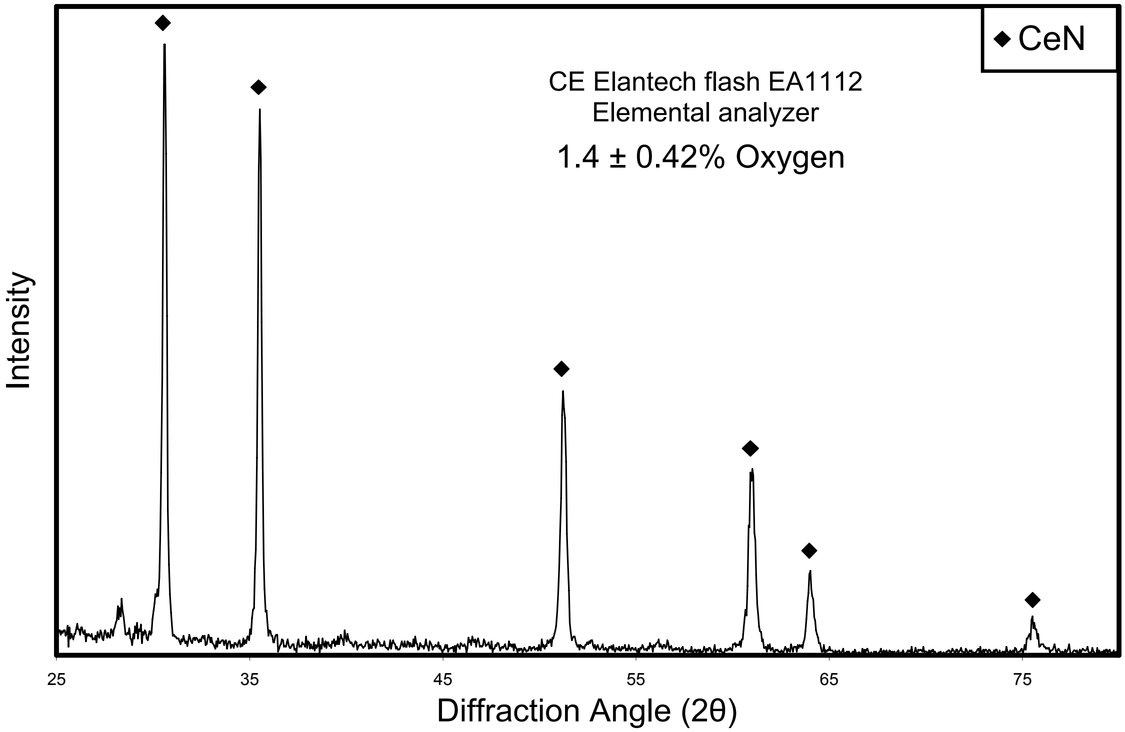

Figure 61: XRD pattern of cerium mononitride powder produced by hydride-nitride synthesis route at 900°C for 4 hours. (Philips X'pert XRD with a Cu-Kα source (λ=1.5418 Å) and a 4°/min scan rate in Bragg-Brentano geometry).

3.3. Novel Reactive Milling Synthesis Route to CeN

This section of the report demonstrates a novel and economical mechanically induced gas-solid reaction (ball milling) synthesis route for synthesizing high purity CeN at room temperature. The success of this low temperature, mechanical route for producing CeN (as a potential surrogate for NpN and PuN) should have profound implications on the advanced fuel cycle (assuming that it is applied to the actinides) because it potentially offers the advantages of a simple, inexpensive method for producing nitride fuels for use in fast-spectrum reactors.

As previously discussed, there are a few published methods for synthesizing nitrides from metals and oxides of dysprosium and cerium [6, 47, 101, 108, 109]. However, these routes can require:

relatively long synthesis times, multi-steps, excessive handling, production of waste from intermediate synthesis steps, and high cost due to the required infrastructure. The mechanical synthesis route presented in this section is an economic alternative to existing thermal routes that require high purity atmospheres, high temperature furnaces, and expensive infrastructures. It is also an economic due to the fact that its starting materials (pure metal) can be obtained directly from the products of spent fuel separations techniques such as electrochemical refining. The mechanical route is viewed as advantageous because it converts a metal to a nitride at room temperature with a reduced number of handling/processing steps thereby minimizing the time and risks typically associated with handling the nitrides. This mechanical synthesis technique is also conducted within a closed system, thus reducing the amount of material lost to evaporation and handling.

No publications have been obtained discussing the synthesis of any of the actinides or lanthanides at room temperature by the use of a ball mill. The only reports found for nitriding metals are those discussing the synthesis of TiN, BN, ZrN, and Fe_3N in a nitrogen or ammonia milling atmosphere [79-83, 85-90]. The work presented in this report is the first that has been documented demonstrating the direct nitridation of dysprosium and cerium metal via a mechanical ball milling route [92]. This work was conducted in parallel with successful efforts to develop economical nitride synthesis methods for uranium nitride [91]. The results suggest direct nitridation of plutonium and americium as well as other actinides may be possible by this method, offering a relatively inexpensive, closed system for processing.

3.3.1. Experimental Procedures for CeN Synthesis via Reactive Milling

Approximately 5 grams of 99.9% pure -40 mesh cerium metal flakes (ESPI) were used in the experiment. The flakes were placed in a 250 mL chrome steel milling vessel along with the milling media under prior to sealing and removing from the glovebox. The milling container contained 70 grams of 5 mm diameter YTZ milling media providing an optimum metal to media mass ratio of 1:14. The vessel was sealed prior to purging and charged with oxygen-gettered UHP N_2 to approximately 350 kPa. The nitrogen gas contained less than 0.1 ppb oxygen content as approximated by a Neutronics OA-1 oxygen analyzer. The vessel (Figure 41a) was fixed in a Retsch planetary ball mill (Figure 41b) and the cerium was milled for 24 hours at 500 rpm with a single purge and recharge after 2 hours of milling.

3.3.2. Results of the Synthesis of CeN via Reactive Milling

The as received cerium metal flakes (Figure 62a) were coarse and had a shiny grey/brown color. After ball milling the powder became much finer, lost its entire luster, and became black, as shown in Figure 62b.

a) b)

Figure 62: Photographs of (a) -40 mesh cerium metal flakes (ESPI, 99.9% pure) and (b) CeN synthesized via a mechanically induced gas-solid reaction at room temperature for 24 hours in nitrogen using a metal to milling media mass ratio of 1:14.

The x-ray diffraction pattern of the CeN produced from 24 hours of milling cerium metal in a nitrogen atmosphere at room temperature with a metal to milling media ratio of 1:14 is shown in Figure 63. The dominant peaks are CeN peaks but small CeO_2 peaks still exist in the sample, which is presumably due to its reactive nature and susceptibility to oxidation. As previously stated, the CeN is very difficult to handle and transporting it to the diffractometer is the most likely source of oxygen. However, the results show that CeN can be produced by this mechanically induced gas-solid reaction of cerium metal in a nitrogen atmosphere.

Analysis of the CeN diffraction pattern using Lorentzian fits of the first four characteristic CeN peaks indicate a lattice constant of 5.04Å ± 0.01Å using Bragg's law, which is in agreement with the published value of 5.02Å [111]. Further analysis of the diffraction pattern using Scherrer's equation indicates that the average resultant crystallite size is 9.4 nm. It is worth noting that the diffraction pattern also exhibited broad diffraction peaks with low intensities and relatively large peak to noise ratios. These characteristics are attributed to two primary factors: the first being very small crystallites and the second being the amorphization of the solids. The average crystallite sizes were estimated through the Scherrer relation (Equation 2) in the preceding paragraphs. The amorphization of the materials is expected to be due to the high energy impacts between the milling media and the metal/nitride that is endured throughout the milling process. It is presumed that the large mechanical energy provided to the system produces large internal stresses and strains in the crystal structure of the materials.

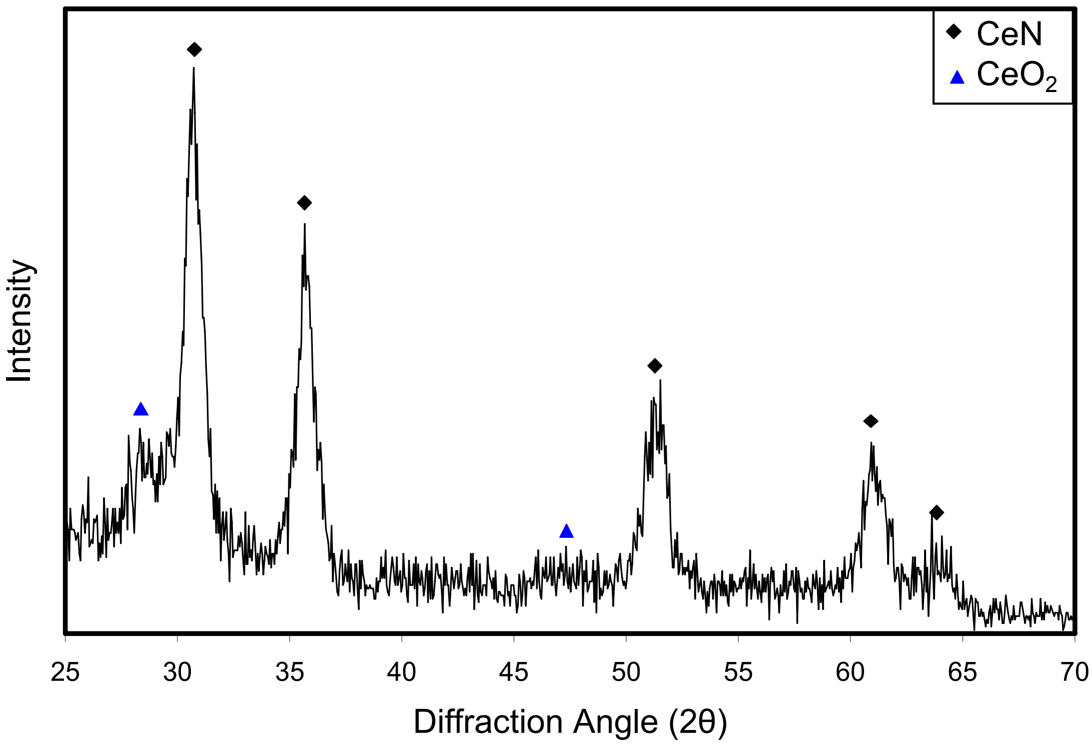

Figure 63: XRD pattern of CeN powder synthesized using -40 mesh cerium metal flakes with a metal to milling media mass ratio of 1:14 after 24 hours of milling at room temperature. The main peaks present are characteristic CeN peaks along with weak CeO_2 peaks.

3.4. Solution Synthesis Routes Analogous to Sol Gel Processing for Synthesizing CeN

UF is investigating solution routes to actinide nitrides. A solution route, such as sol/gel processing that is performed at lower temperatures, would allow for mixing on a molecular level and, therefore, yield more homogenous fuels. Solution processing of ceramics has generally been restricted to metal oxide ceramics with metalorganic compounds as precursors. The most obvious example is sol-gel processing. Metal alkoxides are hydrolyzed to form metal hydroxides, which subsequently condense to form the metal oxides. Non-aqueous systems have been described where the condensation reaction involves formation of stable organic molecules. Thus, a metal ethoxide can be reacted with a metal acetate to form the metal oxide and ethyl acetate. Other stable condensation products are acid anhydrides and ethers. When metal halides are reacted with metal alkoxides, volatile organohalides are formed. The organic group can also be a triorganosilyl group in the case of the formation of alkyhalides. Metal hydrides can be reacted metal hydroxides to form hydrogen and a metal oxide. The condensation reactions are all equilibrium type reactions where the driving forces to form the oxides the high vapor pressure of the condensation product and the high thermodynamic stability of the metal oxides. Mixed oxides (MOX) can also be prepared in this way.

Little has been reported on the formation of metal nitrides by analogous chemistries. The =NH group is isoelectronic to the -O- group, therefore one might expect analogous reactions. With the exception of lithium nitride, most metal oxides are more stable than their nitrides, making it necessary to avoid water or any other -OH containing solvent when attempting to form actinide nitrides. Although many of the reactions discussed above are reported for reactions containing when silicon or titanium metals, not much has been reported for the actinides. It is this "by analogy" approach that has driven the UF research. The nature of the ligand bound to the metal precursor must also be considered. It would be difficult to avoid introduction of oxygen to the actinide nitrides if the ligands are bound through an oxygen atom to the actinide metal ion. For organic solubility, "soft" (*Pearson HSAB concept*) anion legends are required. Some of the soft legends are sulfides, hydrides, and iodides. To date, the UF research has focused on iodide precursors.

3.4.1. Experimental Procedures for CeN Synthesis via an Iodide Synthesis Route

The general concept consists of two steps as shown in Figure 64. The first step is the dissolution of an actinide iodide into hexamethyldisilazane (HMDZ) used here as both a solvent and a reactant. In this scheme, one reaction product is distilled out shifting the condensation equilibria to the right. In the second step, the remaining solution is heated to a selected temperature, yielding a nitride compound and the stable condensation product, HMDZ. The chemical reactions that describe the process are illustrated in Figure 64.

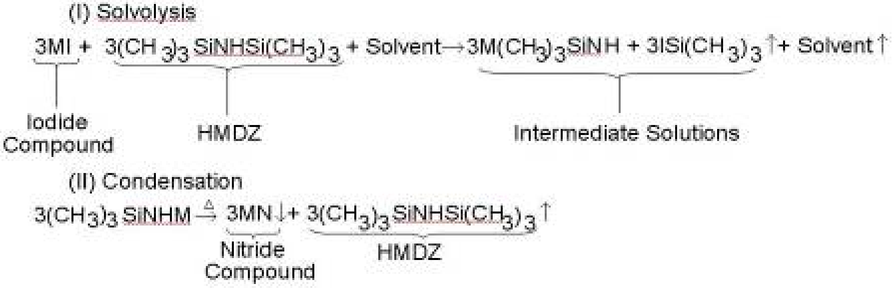

Figure 64: The chemical scheme for the HMPZ / metal iodide approach.

One gram of CeI_3 or DyI_3 and 25g of hexamethyldisilazane (HMDZ) were assembled in a flask with a 3-way adaptor in a glove box with less than 10 ppm oxygen and moisture content. The flask was taken out in an oil bath; the Argon gas line and vacuum line were connected to the 3-way adapter. After 3-cycles of gas purge/evacuation for the gas and vacuum lines, the 3-way adaptor was switched to the gas line and flask (within the argon atmosphere). After the temperature in the oil bath was raised to 100°C, the reaction was continued for 24 hours. The oil bath then was cooled down to 80°C. The vacuum line was under vacuum and the 3-way adaptor was switched to the flask and vacuum line to vacuum distills off the remaining HMDZ. Once the HMDZ was completely removed, the 3-way adaptor was switched back to the gas line and flask. The flask was transferred to a heating element and heated at 400°C for another 24 hours under an argon atmosphere.

3.4.2. Results of the Synthesis of CeN via an Iodide Synthesis Route

The reaction product was taken into a vial in the glove box for XRD analysis. No color change and no indication of dissolving iodides were observed in the reaction at 100°C for either the CeI_3 or the DyI_3. Free iodide was observed by color when the CeI_3 or DyI_3 was heated at 400°C. X-ray diffraction analysis was performed on the reaction products (cerium or dysprosium compound powders) using a Phillips APD 3720 XRD. Lines for cerium or dysprosium oxides or nitrides were always absent. After numerous attempts using multiple configurations and conditions, the planned reaction occur would not occur. For this reason, this viable synthesis route was abandoned.

3.4.3. Experimental Procedures for CeN Synthesis via an Hexamethyldisilazane (HMDZ) and Co-Solvents Synthesis Route

A literature survey was completed on the solubility of CeI_3 in an organic solvent and on the stability of intermediate reactions products. The solvent often used for CeI_3 dissolution is tetrahydrofuran (THF). The solubility of CeI_3 in THF is 0.14g/dm^3 at 20°C. Also, in a study of the reaction involving the dissolution of anhydrous lanthanide chloride and lithium hexamethyldisilazide in THF to form the nitride precursor $Ln(N(SiMe_3)_2)_3$, the cerium compound was reported to be quickly oxidized by even minute trace of air.

An experiment was performed to determine if CeI_3 would dissolve in a solvent mixture of 1,4-dioxane and HMDZ. The solution was analyzed by FTIR to determine what the compositions of the intermediate solutions are, but the results were inconclusive for the sample hydrolyzed during transport to the FTIR.

Two trials were conducted in which 1g CeI_3 was dissolved in a solvent mixture of 25g of HMDZ and 30ml of 1,4-dioxane. The glassware set-up was assembled inside the glove box and the chemical introduced into the assembled glassware. The glassware with the chemicals was removed from the glove box and placed inside a chemical hood were it would be heated to initiate the chemical reaction. The highest temperature selected for the two trials was 140°C instead of the higher temperature of 300°C. This is due to the temperature limitation of the glassware and accessories used for the trial runs. After removing the liquid by distillation for 5 hours, the glassware with the solid product was returned to the glove box. The solid product was dried within the glove box and placed within a closed vial for XRD analysis.

3.4.4. Results for CeN Synthesis via an Hexamethyldisilazane (HMDZ) and Co-Solvents Synthesis Route

Due to the limited solubility of HMDZ in CeI_3, low boiling ethers were used to try to increase the solubility of CeI_3. Among these solvents were diethyl ether, THF, 1,2-dimethoxyethane (monoglyme), and 1,4-dioxane. The first three ethers showed limited solubility of CeI_3. The 1,4-dioxane displayed the highest solubility. FTIR analysis was performed on the CeI_3, 1,4-dioxane and HMDZ mixture. One gram of CeI3 was mixed with 1.2 mL of HMDZ and 1,4-dioxane in excess. The results were inconclusive due to contamination during transport. The solution that was previously sealed inside a glass vial, immediately started to hydrolyze once removed from the glove bag. Upon arrival at the FTIR the solution had turned from yellow to a black color. No prior reaction, in this time scale, has occurred with these results while inside the glove bag, indicating moisture from the atmosphere must have reacted with the solution. Further measures need to be taken to ensure a moisture free environment during transport and data collection.

Several challenges have been encountered during this research, the chief among them is the limited solubility of the CeI_3 even with HMDZ and co-solvents led the UF team to abandon the HMDZ routes.

3.4.5. Experimental Procedures for CeN Synthesis via an Hexamethyldisilazane (HMDZ) (with Liquid Ammonia Solvent) Synthesis Route

HMDZ was selected as the reactant/solvent in earlier trials. However, due to the very low solubility of cerium iodide in the HMDZ, even with co-solvents, none of the previous trials were successful. A new solvent system, liquid ammonia, was chosen to replace the HMDZ. The reaction route is shown in the Figure 65.

$$\mathbf{2Na + 2NH_3\,(liquid) \rightarrow 2NaNH_2 + H_2\uparrow \quad (1)}$$

$$\mathbf{CeI_3 + 3NaNH_2 \rightleftarrows Ce(NH_2)_3 + 3NaI\downarrow \quad (2)}$$

$$\mathbf{Ce(NH_2)_3 \xrightarrow{\Delta} CeN + 2NH_3\uparrow \quad (3)}$$

Figure 65: The proposed reaction route to cerium nitride in liquid ammonia

Several problems arose with this route. We successfully liquidized ammonia gas by dry ice – acetone bath as shown in the Figure 66. Once the liquid ammonia was condensed, sodium was added (3:1 molar ratio to the planned amount of cerium iodide).

(a) (b)


(c) (d)

Figure 66: Dry ice-acetone bath to liquefy ammonia gas. (a) Clear liquefied ammonia solution (b) Solution turns pale blue after addition of Sodium chunk (c) Same solution turns deep blue after some stirring due to greater dispersion of Sodium atoms (d) Solution turns clear due to the catalytic action of the rusty nail.

However, avoiding the undesirable side reaction of the formation of solvated electrons proved difficult. Rusty iron catalysis had been employed previously by Baney, *(reported in unpublished research as a catalyst to accelerate the sodium amide formation and prevent this side reaction).* Even in the presence of a rusty nail as the catalyst, the dark blue color of the solvated electron was still present as can be seen in the Figure 66. The blue color indicated the formation of the solvated electrons, instead of the $NaNH_2$. This situation can be hazardous, since a thin film of highly reactive sodium metal coats all internal surfaces once the ammonia has evaporated.

In a second attempt, more rusty iron catalysts were added to the liquid ammonia. Sodium metal was cut into several small pieces, and added slowly piece by piece to the clear liquid ammonia solution. Once the clear solution was formed, 1 gram of cerium iodide was added into the solution. The reaction was kept for 30 minutes before the dry ice condenser was replaced by the glass stopper to evaporate the ammonia gas under the argon atmosphere. After the ammonia gas was gone, the flask, still under the argon atmosphere, was heated to 360°C and kept over night. The temperature was then cooled to room temperature. A sample of the powders was removed for X-ray diffraction analysis (labeled as reaction-product). The remaining powders were heated to 600°C for 18 hours in the furnace under the argon atmosphere. These powders (labeled as heat-product) were also analyzed by the X-ray diffraction. The colors of both powders were yellowish, but no free iodide release was observed during the heating.

3.4.6. Results of the Synthesis of CeN via an Hexamethyldisilazane (HMDZ) (with Liquid Ammonia Solvent) Synthesis Route

X-ray diffraction analysis was performed on the reaction powders (reaction-product and heat-product). The results indicated that both of the products were not cerium oxide or nitride. According to Reaction 2 in Figure 65, sodium iodide would be formed during the reaction. The melting point of sodium iodide is 660°C and the highest temperature in our current route was 600°C. If sodium iodide were formed, it should remain crystalline in the reaction powders as well as heat-treatment powders. However, based on the XRD results, sodium iodide was not detected in either case. Sodium iodide has a substantial solubility of 162g/100g of liquid ammonia. It was hoped that the high crystal energy of the sodium iodide over cerium iodide would drive Reaction 2. This was apparently not the case.

This test was done to observe whether all of the cerium iodide dissolves in NH_3 (l). The liquid ammonia was condensed into the flask until it was nearly two-thirds full. Cerium iodide was added and the contents were stirred for one hour. The yellow cerium iodide powder formed a cloudy solution, which suggests that some inadvertent hydrolysis may have occurred. However, the solution cleared upon additional stirring. This was contrary to the expectation of a transparent yellow solution formed by dissolving cerium iodide in clear liquid ammonia. The color remained white for quite a while after which it became colorless. Therefore, the tests were stopped and the ammonia was allowed to evaporate. Afterward, we observed some yellow colored residue which suggested that the cerium iodide had dissolved (Figure 67). Techniques still need to be developed for transfer of and characterizing the cerium iodide by a more rigorous oxygen free and dry process.


a) b)

Figure 67: (a) Initially clear solution turned colorless (b) Yellow and brown residue after NH_3 evaporation.

The first question about our failure of the solution synthesis route is the feasibility of synthesis of CeN utilizing non-aqueous, sol-gel routes. In earlier reported studies, various nitrides have been successfully synthesized using similar non-aqueous routes. For example, plutonium and uranium nitrides have been directly prepared from the liquid ammonia and the corresponding iodides in liquid ammonia [60, 103]. Lanthanide nitride precursors such as Trisbistrimethylsilylamido-lanthanides ($(SiMe_3)_2)_3$) (where the metals include: La, Ce, Pr, Nd, Sm, Eu, Gd, Ho, Yb, Y and Lu) have been prepared by the reaction between iodides and lithiumhexamehtyldisilazane in THF at room temperature [104]. Lanthanide nitrides such as YN, LaN, PrN, NdN, SmN, EuN, TbN, ErN, and YbN have also been reported to have been prepared by ammonolysis of the afore-mentioned lanthanide nitride precursors in ammonia gas at high temperature [105]. However, when the literature was critically reviewed, several issues related to our failure could be rationalized. The first issue is the solubility of the starting iodides that we selected. Plutonium and uranium iodides have been observed to dissolve in the liquid ammonia [60, 103]. However, in the studies presented in this report, dissolutions of cerium iodide in liquid ammonia was not observed. The solubility of cerium iodide has been reported to be extremely low in THF, consistent with our observations that cerium iodide and dysprosium iodide cannot dissolve in the relative non-polar hexamethyldisilazane, as well as with various other co-solvents.

A second concern is the propensity of cerium compounds to oxidize. In the studies cited above, many lanthanide precursors have been prepared in a rigorously controlled dry oxygen free environment. However, cerium was an exception [104], as it was pointed out by the researchers. The cerium compounds were readily oxidized by even minute traces of air. Lastly, extensive measures were attempted to improve the atmosphere control of the reaction environment. Measures included assembling Schlenk-type glassware and the handling of the reactants in an oxygen-free glovebox, and utilizing an inert argon gas line with vacuum pump. However, the target processing conditions were never achieved. In the previously published study for preparing plutonium and uranium nitrides, the authors pointed out that the liquid anhydrous ammonia could have up to a maximum 5,000 ppm water because of the low reaction temperature (liquid ammonia temperature) [60, 103], the expected nitrides still could be prepared by this one-step reaction.

The UF reaction processes required a rather high laboratory skill level which is acquired over time as one works his way up the learning curve. The UF effort was plagued by ongoing inexperienced student researchers. Two of the student dropped from the program and from the university, two other students switched to other research. In conclusion, it is believed that with diligent care a solution process similar to the one pursued by UF might be possible. However, the practicality and cost of maintaining such a process might outweigh any purity benefits that could be realized.

CHAPTER V: SINTERING OF NITRIDE MATERIALS

Actinide nitrides have multiple characteristics (as discussed in Chapter 1) that deem them as desirable fuel candidates for fast spectrum nuclear reactors. Accordingly, the sintering of actinide nitrides has been studied by many authors in support of research related to previous reactor work [5, 6, 8, 9, 11-14, 43, 44, 46-48, 53-57, 60, 61, 63, 65, 67, 68, 71, 112-125]. Such previous reactor work relates to various breeder reactors (liquid-metal-fast-breeder reactors (LMFBRs)), space power reactors, and fast reactors considered for the advanced fuel cycle such as: the gas-cooled fast reactor (GFR), the sodium-cooled fast reactor (SFR), and the lead-cooled fast reactor (LFR)) [15, 24, 56, 64, 65]. It is apparent that the density of nitride fuel pellets for minor actinide transmutation has yet to be optimized from the reviewed literature. However, it has been stated that a minimum of 80 percent of the theoretical density (%TD) must be obtained to maintain the structural integrity of the pellet and to retain the fission products during irradiation [13].

Previous space reactor programs have used a cold-pressing and sintering process because it is seen as a relatively well understood and reliable technique [11, 125]. The cold-pressing and sintering technique is also used due to its economic advantage in large scale production when compared to other consolidation techniques. It was thus chosen as the sintering technique for this work. The cold-pressing and sintering technique (for this investigation) was completed in a custom designed high temperature alumina tube CM furnace (Figure 4) that was previously described. The use of an alumina tube furnace is an economical alternative for sintering when compared to a refractory metal furnace, which is commonly used for sintering nitrides [11]. This is because refractory metal furnaces are typically very expensive and require much infrastructure when compared to high temperature alumina tube furnaces.

1. Sintering of Pure Zirconium Nitride (ZrN)

Zirconium nitride (ZrN)has been proposed as an inert matrix fuel (IMF) in the advanced fuel cycle to burn plutonium and transmute long-lived actinides [126]. It was chosen primarily based on its crystal structure (cubic-NaCl) and its high thermal conductivity. The initial experiments discussed in this section report the effect of sintering atmosphere, sintering time, sintering temperature, and oxygen absorbing foils. This set of experiments is used to create base data for future sintering studies involving the effects of sintering aides and additives.

1.1. Experimental Procedures for Sintering Pure ZrN

Commercially available ZrN powder (Alfa Aesar, 99.5% pure, -325 mesh) was used for these experiments. ZrN powder was weighed and cold-pressed in air at 250 MPa for approximately 10 minutes. The green body was wrapped with oxygen-absorbing foils, namely niobium and carbon were used. The wrapped green body was then placed in an alumina crucible and loaded into the same furnace system as is used for nitride powder synthesis, a Barnstead Thermolyne 59300 high temperature tube furnace. The current study focused on two main parameters: atmosphere effects, and sintering temperatures. The two atmospheres studied were high purity Ar gas and a N_2 + 6.28% H_2 mixed gas. Dunwoody *et al* [127] found that sintering temperature of 1600°C favored a high density ZrN pellet. Accordingly, we based our temperature variations from this. Five different samples were sintered with variations of the preceding parameters. The sample details and the parameters employed in their sintering are given in Table **4**.

Table 4: Sample identification and the respective process parameters for sintering of 99.5% pure ZrN.

Sample ID	**Atmosphere**	**Sintering Temperature / Time**	**Wrapping Details**
ZrNArNb1	**Pure Argon**	**1600°C / 10 hrs**	**Nb Foil**
ZrNArNb	**Pure Argon**	**1650°C / 6 hrs**	**Nb Foil**
ZrNArC	**Pure Argon**	**1650°C / 6 hrs**	**Carbon Foil**
$ZrNH_2N_2C$	**$N_2 + 6.28\%H_2$**	**1650°C / 6 hrs**	**Carbon Foil**

The parameters for the samples ZrNArNb1 and ZrNArNb are designed to study the effect of sintering temperature and time, whereas the atmosphere (Ar) and wrapping foils (Nb Foil) are the same for both the samples. The samples identified as ZrNArC and $ZrNH_2N_2C$ were sintered at the same temperatures and times (1650°C for 6 hours) with the same wrapping foil (carbon foil) while the sintering atmosphere was varied.

1.2. Results of Sintering Pure ZrN

Both geometric density and immersion density (using Archimedes principle) measurements were used to calculate the density of the sintered pellets. It should be noted that the percent theoretical density (%TD) was calculated using the theoretical density of ZrN, which is reported as 7.09 g/cm^3 [128]. The geometric density and the corresponding %TD of the samples are listed in Table 5. It was found that the geometric density method is not as reliable and accurate as we had hoped and does not yield reproducible results, particularly for low density materials such as ZrNArC and $ZrNH_2N_2C$.

Table 5: Geometric density measurements obtained from the sintered ZrN pellets by varying parameters such as temperature, time, atmosphere, and wrapping material.

Sample ID	**Geometric Density ($^{g}/_{cm^3}$)**	**% TD**
ZrNArNb1	**4.78**	**67 %**
ZrNArNb	**5.07**	**72 %**
ZrNArC	**4.69**	**66 %**
$ZrNH_2N_2C$	**4.68**	**66 %**

The immersion density (using Archimedes' Principle) was also used to measure the density of the above mentioned samples. Table **5** lists the immersion density with %TD. It was found that the results are reproducible to ± 1 %TD and comparatively much more reliable than the geometric density measurements.

Table 6: Immersion density measurements obtained using the principle of Archimedes' principle. The measurements are obtained from sintered ZrN pellets sintered with varying processing parameters such as: temperature, time, atmosphere, and wrapping material.

SampleID	**Immersion Density ($^{g}/_{cm^3}$)**	**% TD**
ZrNArNb1	**6.59**	**83 %**
ZrNArNb	**5.29**	**75 %**
ZrNArC	**4.9**	**69 %**
ZrNH2N2C	**5.3**	**76 %**

According to Table 6, the sample ZrNArNb1 showed the highest density value, approximately 83% of the theoretical density whereas the geometric density shows a value of 67%. Conclusively, the density measurements obtained by the geometric density method vary considerably while repeating the measurement while the values from immersion density were very repeatable. This result is in agreement with the results of Dunwoody *et al* [127] in which they found that a sintering temperature of 1600°C for 10 hours yielded the highest density pellet.

The ZrNArNb and $ZrNH_2N_2C$ samples have approximately the same density value s (~75%TD). This suggests that varying the atmosphere does not affect the density as much as varying the sintering temperature and time. This is seen in the ZrNArNb1 and ZrNArNb samples in which the parameters are the same except for the sintering temperature and time. The comparison of the samples ZrNArNb and ZrNArC show that the niobium foil wrap is more effective than carbon foil. This could be attributed to the relatively inert nature of the niobium foil when compared to the carbon foil. It is also clear from the photographs of the sintered samples (Figure 68) that the samples ZrNArNb and ZrNArNb1 have the native color of ZrN whereas the samples wrapped with carbon foil ($ZrNH_2N_2C$ and ZrNArC) have a very dark tint, indicating a reaction between the ZrN and the carbon foil.

XRD analysis was performed to identify the phases present after sintering revealed presence of only ZrN phase for all samples. Although the optical observation of the ZrNArC sample shows a different color (indicative of a reaction) than the native ZrN powder, the XRD analysis did not identify any other phases besides ZrN. This suggests that the reaction layer may be present as very thin film that is beyond the detection limit of the diffraction system used.

Sample	Macro Picture
ZrNArNb	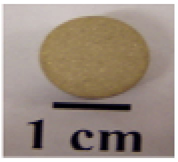
ZrNArNb1	
$ZrNH_2N_2C$	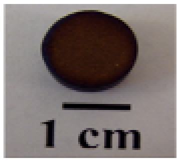
ZrNArC	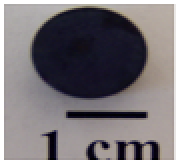

Figure 68: Photographs of ZrN pellets sintered with varying processing parameters such as: temperature, time, atmosphere, and wrapping material.

2. Sintering of Zirconium and Dysprosium Nitride (Zr, Dy)N

There is a need for understanding the thermodynamics and kinetics of nitride fuel sintering including the effects of americium additives. According to Minato, Ogawa, and Chauvin [16, 129, 130], much work needs to be done with americium to better understand its effects on sintering. In 2003, Minato demonstrated a mutual solubility of AmN in YN for IMF applications. Minato also demonstrated the formation of solid solutions of (Am, Zr)N by the carbothermic reduction and nitriding method of the oxide powders in a N_2 gas flow at 1573 K. DyN is a candidate surrogate for AmN. However, no published DyN sintering studies are found in the literature, but there has been a few studies conducted on both americium and dysprosium oxide sintering.

In a pulsed electric currents sintering (PECS) study conducted by Ho Jin Ryu *et al* [21], Dy_2O_3 (used as a surrogate for Am_2O_3) was used as a sintering aid in processing of oxide-dispersed IMF pellets. From this study, the addition of the Dy_2O_3 increased the percent theoretical densities of ZrC, TiC, and ZrN, but lowered it for TiN.

Matzke [20], who was continuing some of the work of Burghartz [19], studied the effects of doping new candidate IMF materials such as: $MgAl_2O_4$, $ZrSiO_4$, CeO_2, SiC, and Si_3N_4. The IMF materials were doped with ^{241}Am using the soaking method, as described by Matzke [18] in a previous work. This method of doping involves suspending the ^{241}Am dopant in a solution and allowing the green pellet (approximately 50 %TD) to absorb it prior to sintering. The final product contained 10-20 wt% americium. This work by Matzke and Burghartz focused on the thermal properties, irradiation effects, and the compatibilities of the ^{241}Am with the candidate IMF materials.

In the work presented in this document, DyN and ZrN powders were hot-pressed at Ceramatec Inc. to determine the sinterability of this binary mixture. However, it should be noted that due to the volatility of DyN, the molar ratio of DyN/ZrN was not increased beyond 1.

2.1. Experimental Procedures for Sintering (Zr, Dy)N

The same ZrN powder used in the previous sintering experiments (supplied by Alfa Aaser (99.5% pure, - 325 mesh)) and a DyN powder supplied by Hefa Rare Earth Canada LTD were combined and hot-pressed for these studies. A compositional range of $(Zr_x, Dy_{1-x})N$ $(1 \leq X \leq 0.5)$ samples were prepared at the correct ratios and mixed with a planetary ball mill to obtain a thorough mixture. The prepared samples were sent to Ceramatec Inc. for hot pressing where they were pressed in a nitrogen atmosphere at 2000°C for 2 hours with an applied pressure of 26 MPa.

2.2. Results of Sintering (Zr, Dy)N

The most important result of this study was that DyN forms a second phase in ZrN and does not form a complete solid solution. The two phases have only been observed using an optical microscope, a scanning electron microscope, and x-ray diffraction. It should be noted that the ionic mismatch of the zirconium to dysprosium elements is approximately 19%, which would indicate that no solid solution would form (according to the Hume-Rothery rules which suggest a maximum mismatch of 15%). It is worth noting that the $(Zr_{0.5}, Dy_{0.5})N$ sample shattered during the hot-pressing. This had been attributed, by the research engineers of Ceramatec, to not relaxing the force ram during cooling of the sample. This inherently caused the formation of micro-cracks throughout the sample, possibly skewing the density measurements.

The density measurements were performed via Archimedes principle of buoyancy. The samples were heated in an inert atmosphere tube furnace to 215°C and held for 30 minutes, according to ASTM standard C830. The samples were immediately weighed after removal from the furnace. The average of five measurements was recorded. The samples were then placed in vials of Norpar 13® manufactured by ExxonMobil, which is a highly hydrophobic paraffin oil with a density of 0.762 $^{g}/_{cm\char`^3}$. The vials containing the samples were placed in a vacuum chamber and evacuated five times to 28 inches of water (gauge) before they were sustained for 2 hours in the evacuated chamber. The samples were removed and blotted with a dampened, lint free towel before the saturated weight was recorded. The value recorded was the average of 8 measurements. The samples were then placed in the basket immersed in the de-ionized water and the immersed weight was recorded. The final value recorded was the average of 8 measurements. All of these values were obtained and used in Equation 5 to calculate the experimental densities.

$$\rho_{\text{experimental}} = \frac{W_{\text{Dry}} * \rho_{\text{DI-water}}}{W_{\text{Saturated}} - W_{\text{Immersed}}} \qquad \text{(Eqn. 5)}$$

The experimental density values were then divided by the theoretical densities of the respective mixtures to obtain the percent theoretical densities (%TD). The theoretical densities of the mixtures were calculated from the reported theoretical densities of ZrN and DyN, which were 7090 [131] and 9930 [128] kg/m^3, respectively. Table 8 shows that all of the samples obtained very high densities predicting that the sintering procedure allowed the samples to enter into the final stages of sintering.

Table 7: Experimental density results of hot-pressed ZrN-DyN samples subjected to 2000°C and 26 MPa

Specimen	**$\rho_{\text{Experimental}}$ ($^{g}/_{cm^3}$)**	**$\rho_{\text{Theoretical}}$ ($^{g}/_{cm^3}$)**	**%TD**
100% ZrN	6.919	7.090	97.6 %
90% ZrN	7.352	7.424	99.0 %
80% ZrN	7.617	7.744	98.4 %
50% ZrN	8.330	8.638	96.4 %

XRD analysis was performed on the different samples to identify the phases present. As shown in Figures 69-72, an oxide peak of either dysprosium or zirconium or both is present in each of the patterns. This can be attributed to handling techniques of the powders before the hot-pressing occurred. The DyN has a very high oxygen affinity contributing to a quickly forming oxide. It also appears that the $(Zr_{0.8}, Dy_{0.2})N$ and $(Zr_{0.5}, Dy_{0.5})N$ samples have formed a secondary phase. This conclusion is drawn from the fact that the peak intensities have a weak correlation to the JCPDS data they were compared to and that there were a few minor peaks that were not able to be identified by any of the suspected JCPDS files.

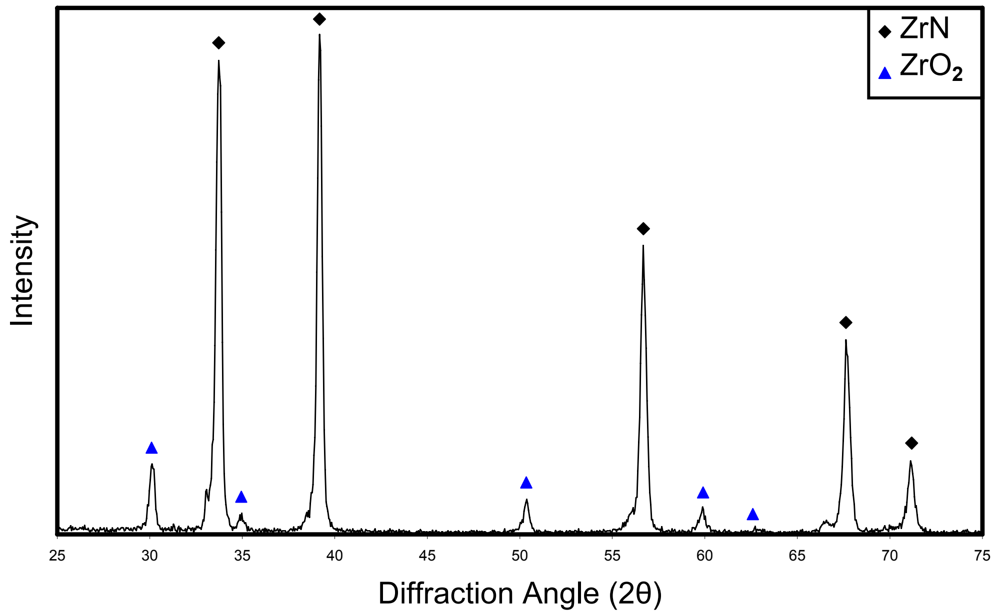

Figure 69: XRD pattern for the 100% ZrN hot-pressed sample. The XRD results suggest that the 99.5% pure ZrN oxidized from processing techniques as the sample was sent to Ceramatec Inc. for hot pressing.

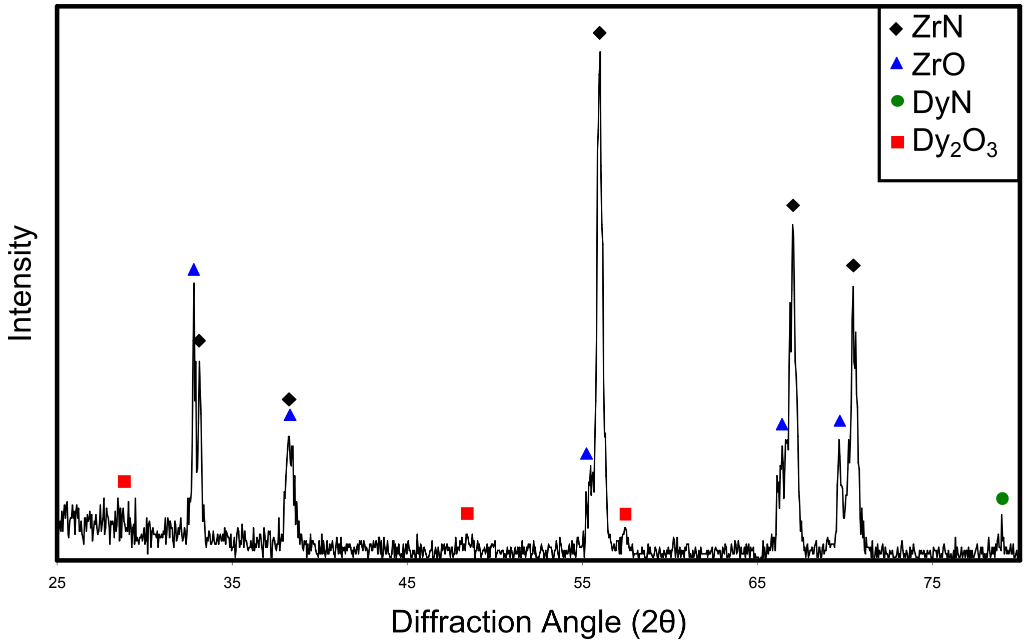

Figure 70: XRD pattern for the $(Zr_{0.9}, Dy_{0.1})N$ hot-pressed sample that was processed at Ceramatec Inc.

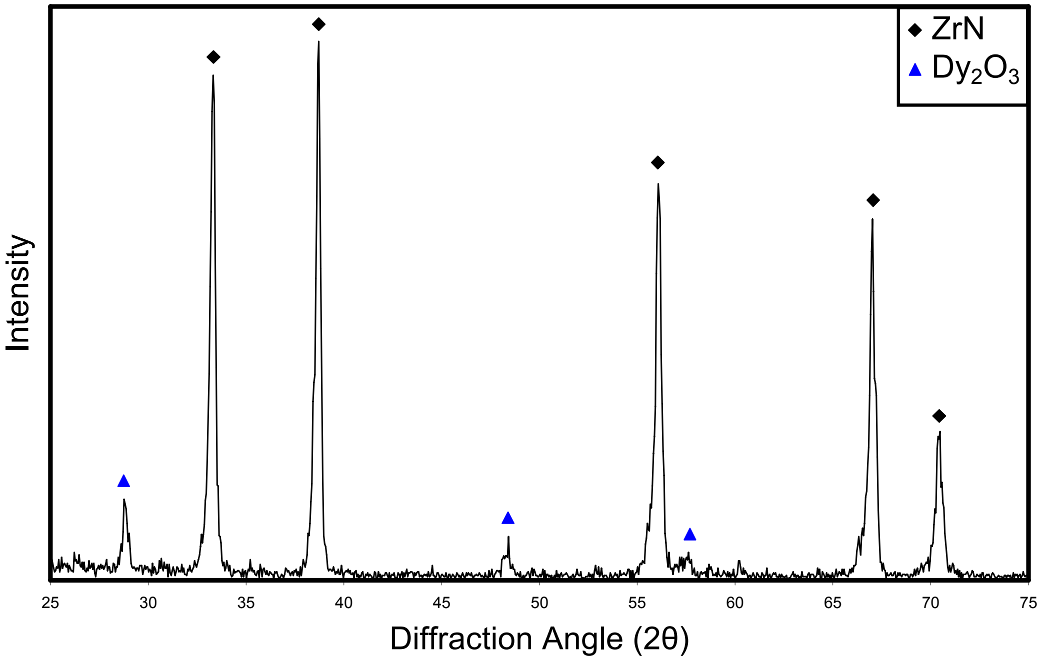

Figure 71: XRD pattern for the ($Zr_{0.8}$, $Dy_{0.2}$)N hot-pressed sample that was processed at Ceramatec Inc.

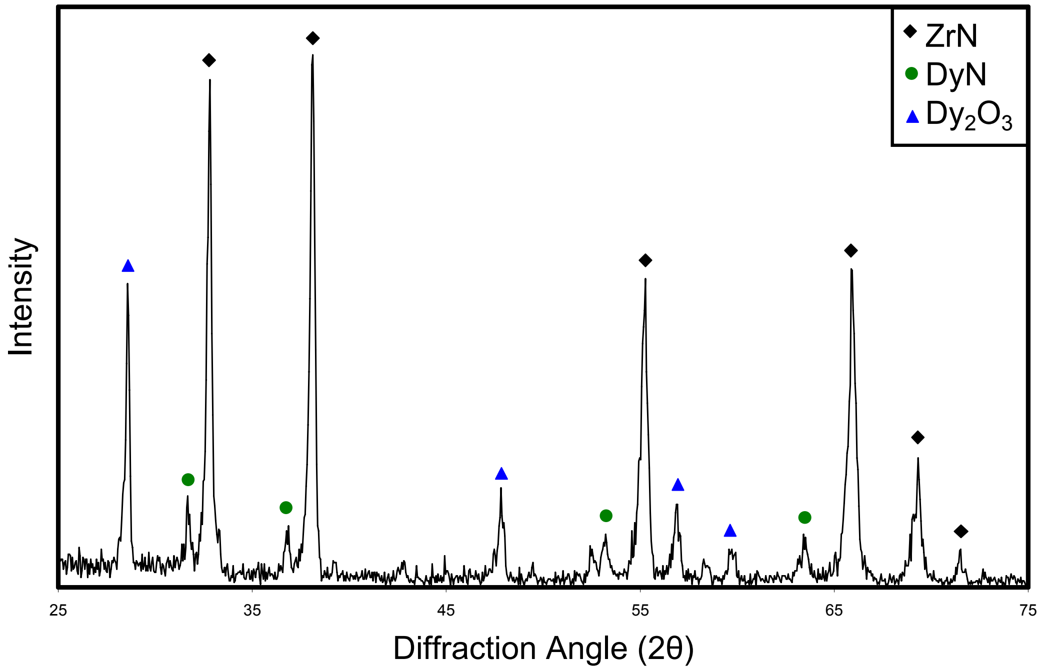

Figure 72: XRD pattern for the ($Zr_{0.5}$, $Dy_{0.5}$)N hot-pressed sample that was processed at Ceramatec Inc.

Optical microscopy was initially used to characterize these samples. Figure 73 shows the respective images of all the samples which were captured at 200X magnification.

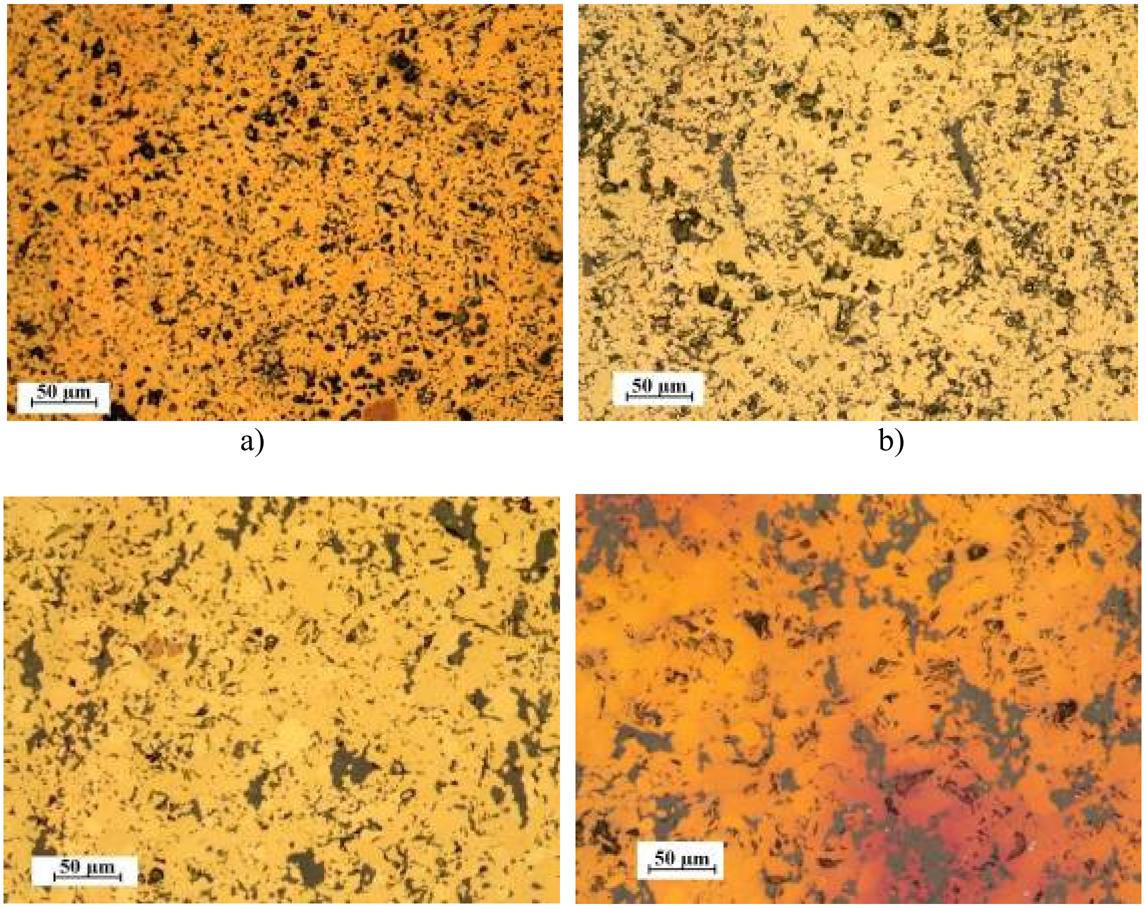

a) b)

c) d)

Figure 73: Optical microscopy images of the hot-pressed samples of (Zr_x, Dy_{1-x})N sintered plates from optical microscopy at 200X. The hot-pressing occurred at Ceramatec Inc. where they were pressed in a nitrogen atmosphere at 2000°C for 2 hours with an applied pressure of 26 MPa. (a) 100%ZrN, (b) ($Zr_{0.9}$, $Dy_{0.1}$)N, (c) ($Zr_{0.8}$, $Dy_{0.2}$)N, and (d) ($Zr_{0.5}$, $Dy_{0.5}$)N.

The next analysis step was to perform scanning electron microscopy (SEM) to look closer at the porosity and grain structure of the different specimens. The four reported images were captured at 10kX and can be seen in Figure 74. The hot-pressed microstructures indicate that complete solubility was not achieved even at this very elevated temperature and high pressure. Further analysis on these hot-pressed samples will be performed to determine the compositions of these phases, but it is presumed that the two phases are zirconium saturated DyN and dysprosium saturated ZrN. Unfortunately, a phase diagram for this system is not available. This is an important finding due to the lack of information in the literature regarding the equilibrium conditions for these compounds.

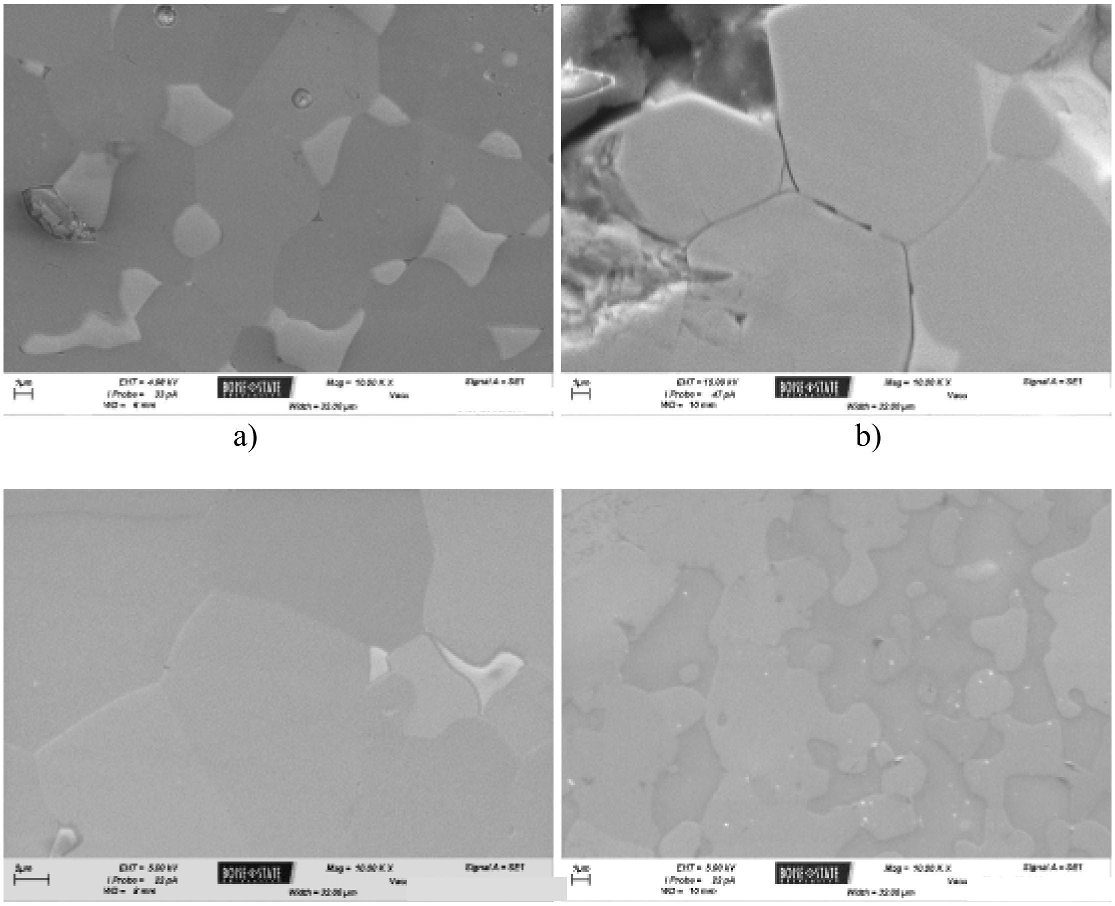

a) b)

c) d)

Figure 74: SEM images of the hot-pressed samples of (Zr_x, Dy_{1-x})N sintered plates at 10kX. The hot-pressing occurred at Ceramatec Inc. where they were pressed in a nitrogen atmosphere at 2000°C for 2 hours with an applied pressure of 26 MPa. (a) 100%ZrN, (b) ($Zr_{0.9}$, $Dy_{0.1}$)N, (c) ($Zr_{0.8}$, $Dy_{0.2}$)N, and (d) ($Zr_{0.5}$, $Dy_{0.5}$)N.

Further studies of these materials included a heat-treatment of the ZrN-DyN specimens for 24 hours in argon at 1400°C. This heat treatment was performed to determine if the volatility of the DyN in these mixtures affects the microstructure at high temperatures over time.

The four samples subjected to the heat treatment were polished prior to being loaded into the furnace to remove oxide layers or residual carbon from graphite dies used during the original hot pressing. The samples were placed in a niobium-lined alumina boat and loaded into the high temperature CM furnace. They were subjected to 1400°C for 24 hours in oxygen-gettered argon gas (< 1 ppm oxygen).

The experimental density values were found by using a similar approach as previously described. These experimental values were then divided by the theoretical densities of the respective mixtures to obtain the percent theoretical densities (%TD). Table 9 shows a side-by-side comparison of the %TD of the samples before and after the heat treatment at 1400°C in argon. When comparing these values, there is statistically no change in the percent theoretical densities partially due to the experimental error in the measuring techniques. However, the general trend of the effects of the heat treatment shows that the percent theoretical densities decrease, but only by a small amount. The largest change was exhibited in the 90% ZrN sample and was only a change of 1%.

Table 8: Experimental density results of hot-pressed ZrN-DyN samples subjected to 2000°C and 26 MPa before and after a 24 hour heat treatment in argon at 1400°C.

Specimen	**$\rho_{Experimental}$ ($^{g}/_{cm\^3}$)**	**$\rho_{Theoretical}$ ($^{g}/_{cm\^3}$)**	**%TD (Before H.T.)**	**%TD (After H.T.)**
100% ZrN	6.877	7.090	97.6 %	97.0%
90% ZrN	7.276	7.424	99.0 %	98.0%
80% ZrN	7.590	7.744	98.4 %	98.0%
50% ZrN	8.333	8.638	96.4 %	96.5%

SEM was performed to determine if there is a significant change in the porosity and grain structure of the different specimens after the heat treatment at 1400°C. The four reported images were captured at 5kX and can be seen in Figure 75 below. When compared to the images in Figure 74 of the as-received samples, there does not seem to be a significant change in grain morphology or porosity.

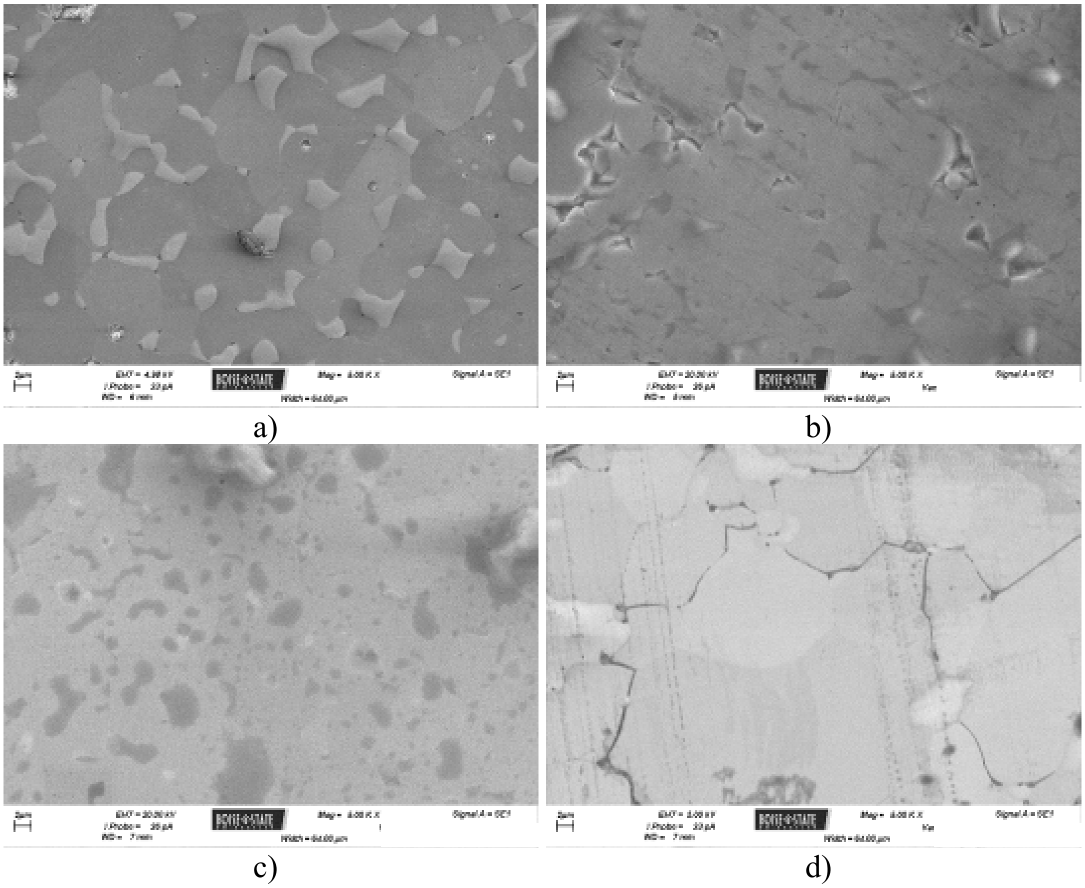

Figure 75: SEM images of the$(Zr_x, Dy_{1-x})N$ hot-pressed samples at 5kX after a 24 hour heat treatment in argon at 1400°C. The hot-pressing occurred at Ceramatec Inc. where they were pressed in a nitrogen atmosphere at 2000°C for 2 hours with an

applied pressure of 26 MPa. (a) 100%ZrN, (b) ($Zr_{0.9}$, $Dy_{0.1}$)N, (c) ($Zr_{0.8}$, $Dy_{0.2}$)N, and (d) ($Zr_{0.5}$, $Dy_{0.5}$)N.

3. Sintering of Pure Uranium Mononitride (UN)

Many authors have reported the feasibility of sintering UN via methods such as: cold-pressing prior to sintering, arc-melting and casting, hot isostatic pressing, spark plasma sintering (also known as a field assisted sintering technique (FAST) or pulsed electric current sintering (PECS)), and reaction sintering of mixtures of metal and higher nitrides (also known as combustion synthesis) [11, 35, 44, 56, 57]. However, a full understanding of the effects of varying process variables on pellet properties such as the density, stoichiometry, and microstructure is needed regardless of the sintering technique. The properties of the pellets must be characterized and well understood prior to conduct further studies on the irradiation performance of the fuel.

The goal of the work presented in this section was to provide preliminary processing procedures using UN prior to studying the effects of adding DyN, which adds an order of complexity to the studies. The effects of sintering time, sintering temperature, compaction pressure, atmosphere, and morphology of the initial UN powder on the density, microstructure, and mass loss of the sintered pellets was studied.

To gain a perspective of initial sintering parameters that have been previously investigated for actinide nitrides, a literature review was completed [5, 6, 8, 9, 11-14, 43, 44, 46-48, 53-55, 57, 63, 65, 67, 71, 112-124]. In 1965, McLaren *et al.* [71] studied the effects of milling time, compaction pressure, sintering temperature, and sintering time on the final sintered density of UN. The powders were initially synthesized using a route that hydrided uranium metal prior to nitridation (similar to that presented Section 2.1.2 of this document). 50 gram batches of powder were milled in a high energy tungsten carbide vibratory mill. McLaren *et al.* [71] reported particle sizes ranging from 0.01 to 3.0 μm and 0.01 to 0.5 μm after 8 and 128 hours of milling, respectively. However, the particle sizes were determined using optical techniques. The powders that were milled for longer periods of time (i.e. had a smaller average particle size) pressed into pellets with lower green densities than those of larger particle sizes, as seen in Figure 76. The pellets were then subjected to 1550°C or 1700°C (for constant times) and it was observed that the pellets with the smaller particle sizes exhibited greater densification than those pellets composed of the larger particles. In fact, the same final sintered densities were achieved despite variations in the particle size distribution.

McLaren *et al.* [71] also showed that there is a slight relation between the compaction pressure and the final sintered density of the UN pellets in further studies. The final sintered density increased by approximately 2.5% as the compaction pressure increased from 275 MPa to 1100 MPa, However, pellets that were pressed at 1100 MPa exhibited de-laminations resulting in poor structural integrity of the sintered pellets. Using the gathered data, UN powder was then milled for 20 hours (arbitrary optimum) prior to being pressed at 550 MPa and sintered in a tungsten mesh furnace in argon for 2 hours at various temperatures, ranging from 1450°C to 1700°C. The results are shown in Figure 77. From McLaren's investigations, there appears to be a linear relationship between the sintering temperature and the final sintered density of the UN pellets.

Further studies show the effects of sintering time on the final sintered densities of the pellets made from powders that were milled for 18 hours prior to being pressed at 550 MPa and sintered at 1700°C (Figure 77).

The results that McLaren *et al.* [71] present on varying the milling time, compaction pressure, and sintering temperature on the sintered density of UN suggests that: Higher green densities are achieved with larger particle size powders, particle size has little (if any) effect on the final sintered density, compaction pressure has a minute effect on the sintered density (although higher compaction pressures caused de-laminations of the green pellet), the final density has a linear dependence on the sintering temperature, and that a majority of the densification takes place in the first 2 hours of sintering [71]. However, as will be seen in the succeeding reviews and the investigations presented in this report, McLaren's [71] claims are not consistent with other published findings. It seems as though the data may be intrinsically flawed for two primary reasons: The first reason being that the results presented by McLaren *et al.* [71] suggest that there is little, if any, dependence of particle size on the sintering kinetics of the pellets. However, a majority of the sintering models compiled in APPENDIX B show a large dependence of the radius of the powder sphere on densification, especially in the initial stages of sintering. The second reason that the data presented by McLaren *et al.* [71] seems flawed is that they found a linear dependence between the sintered density and the temperature of sintering. Again, when compared to the sintering models compiled in APPENDIX B, no model would predict a linear relationship between the temperature of sintering and the densification rate of the compact.

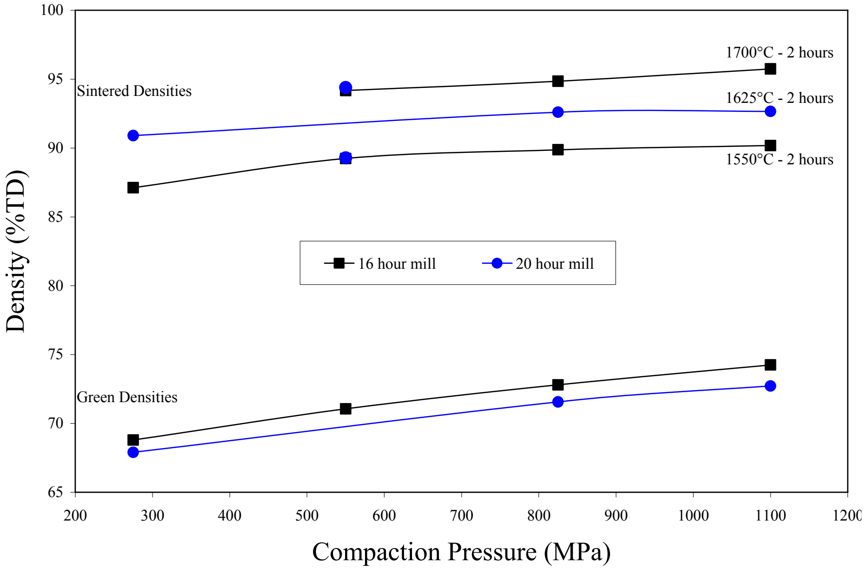

Figure 76: The effects of ball-milling time, compaction pressure, and sintering temperature on the final sintered density of pure UN powders. The compacts were sintered for 2 hours at their respective temperatures. Figure adapted from McLaren *et al.* [71].

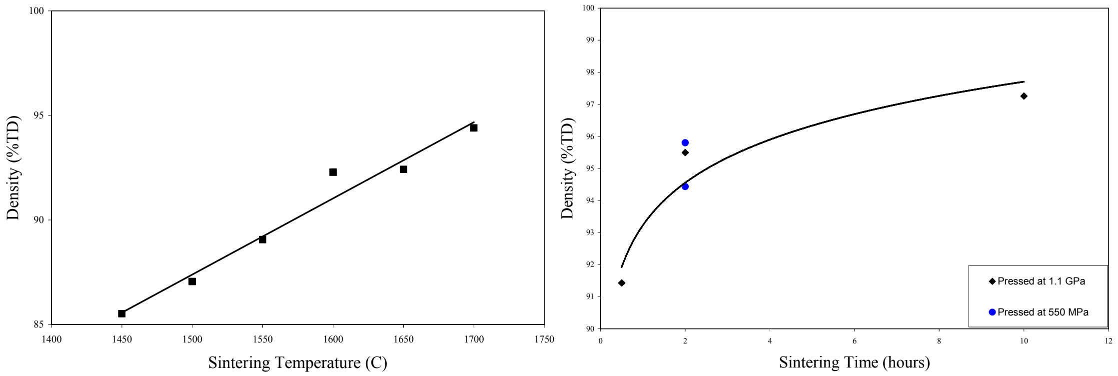

Figure 77: The effects of sintering temperature (sintered for 2 hours) and sintering time (at 1700°C) on the final densities of UN pellets that were milled for 18 hours prior to pressing at 550 MPa. The sintering occurred in high purity argon. Figures adapted from McLaren *et al.* [71].

As UN became more recognized as a feasible candidate for nuclear fuel applications, the kinetics and thermodynamics of its processing procedures needed to be better understood. A limited number of publications have been found that discuss the dependence of nitrogen pressure on the sintering of UN. In 1971, Tennery *et al.* [123] published one of the first investigations that suggested the sintering of UN depends on not only time, temperature, and particle size, but also the nitrogen pressure maintained over the nitride throughout the sintering process. Tennery *et al.* [123] synthesized UN powder using a hydride prior to nitridation method (similar to section 2.1.2 of this report) prior to compacting at 825 MPa into 9.5 mm diameter by 25 mm long green pellets. The pellets were sintered for two hours at a specified temperature (1600 – 2100°C) in varying nitrogen pressures (Figure 78) and the corresponding weight loss was documented. The weight loss results are shown in Table 9. It was determined that the initial powder contained some U_2N_3 phase based on the results of nitrogen analysis. Nitrogen analysis on the initial powder showed a 6.9 wt% nitrogen content when stoichiometric UN and U_2N_3 would have 5.5 wt% and 8.1 wt% nitrogen, respectively. Due to the presence of U_2N_3 in the initial powder, a 1.4% weight loss was also expected for each sintered sample due to the decomposition of the U_2N_3 phase to UN at the higher temperatures. Weight loss of the pellets that was in excess of the 1.4% was attributed to the loss of small fragments of the pellets during transferring to and from the furnace.

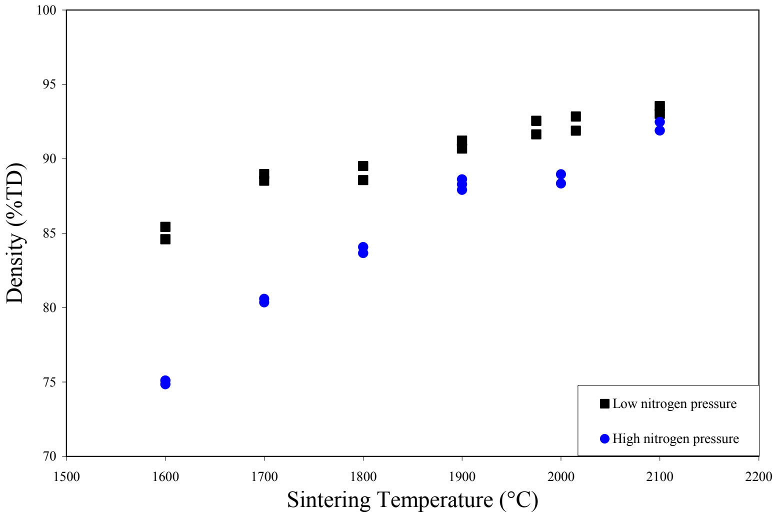

Figure 78: The effect of nitrogen pressure and sintering temperature on the final sintered density of UN. The pellets were isostatically pressed and sintered for 2 hours. Figure adapted from Tennery *et al.* [123].

Further microstructural evaluation of the pellets from the studies in Figure 78 showed a general correlation between the grain size and nitrogen pressure in the sintering atmosphere. The grains tended to be larger as the nitrogen pressure was decreased. Conversely, smaller grains were observed at higher nitrogen pressures. It was also found using optical micrographs that a minute amount of free uranium existed as an intergranular phase in the sample sintered at 2100°C in the low nitrogen atmosphere. The results of the work presented by Tennery *et al.* [123] demonstrate that a minimum nitrogen atmosphere of 10^{-4} torr ($1.3 \cdot 10^{-8}$ MPa) and 1 torr ($1.3 \cdot 10^{-4}$ MPa) was needed when sintering UN at 1600°C and 2200°C, respectively, in order to prevent the dissociation of the UN into liquid uranium metal and nitrogen gas.

Table 9: The effect of nitrogen pressure on the weight loss of pure UN samples sintered for 2 hours at the respective temperatures [123].

N_2 Pres. (torr)	**Sinter Temp. (°C)**	**Weight Loss**
1140	**2100**	**1.7 %**
	2000	**1.8 %**
	1900	**1.6 %**
	1800	**1.6 %**
	1700	**1.5 %**
	1600	**1.6 %**
$4.5 \cdot 10^{-1}$	**2100**	**8.4 %**
$1.0 \cdot 10^{-1}$	**2000**	**4.6 %**
$3.2 \cdot 10^{-2}$	**1900**	**2.4 %**
$5.6 \cdot 10^{-3}$	**1800**	**2.0 %**
$1.2 \cdot 10^{-3}$	**1700**	**1.8 %**
$2.0 \cdot 10^{-4}$	**1600**	**1.6 %**

In 1972, Bauer *et al.* [57] reviewed the properties and irradiation behavior of (U, Pu)N for fast breeder reactors, with an emphasis on UN. The review includes thermodynamic, physical, and mechanical properties such as; crystal structure, heat capacity, thermal conductivity, thermal expansion, diffusivity of nitrogen in UN, elastic modulus, Poisson's ratio, hot hardness, and creep. The data was included as a precursor for presenting work on fuel synthesis (nitride synthesis and sintering), compatibility studies, and irradiation performance.

Bauer *et al.* [57] initially studied the effects of temperature and particle size on the final sintered density of UN using the cold-pressing and sintering technique. The UN powder was ball milled from 0 – 64 hours prior to sintering for 3 hours as various temperatures (1300 – 2000°C). The experimental results of Bauer's sintering investigations suggested that an average particle size of less then 2 μm was needed to achieve a sintered density of 95 %TD or greater. Bauer *et al.* [57] reported that ball-milling UN for 32 hours was sufficient to reach the 2 μm particle size threshold. However, the ball-milling method was not specified.

Bauer *et al.* [57] continued their investigations by studying the effects of atmosphere (vacuum, nitrogen, and argon) and temperature (1300 – 2000°C) on the final density of the UN pellets, as shown in Figure 79. The sintering of UN in vacuum was only performed to 1500°C because sintering above 1500°C resulted in the formation of liquid uranium metal which greatly increased the sintering rate. The formation of the uranium metal is more understood now that a uranium-nitrogen binary phase diagram exists (Figure 80). From the phase diagram, it is seen that UN will dissociate into uranium metal and UN when the temperature is increased above 1400 K (1127°C) in hypostoichiometric nitrogen conditions. The dissociation of UN to uranium metal and N_2 is a direct result of the hypostoichiometric nitrogen condition caused by the vacuum sintering atmosphere. One might also expect the results of sintering UN in pure argon (and thus a low nitrogen partial pressure) to be similar to sintering in vacuum because of the low partial pressure of nitrogen within the process gas. However, the results presented by Bauer *et al.* [57] suggest that this is not the case and that sintering in argon will produce very similar results to sintering in nitrogen. Further evaluation of the binary phase diagram (Figure 80) shows that sintering in nitrogen will force the UN into a hyperstoichiometric region of the phase diagram resulting in the formation of an undesirable U_2N_3 phase which hinders sintering.

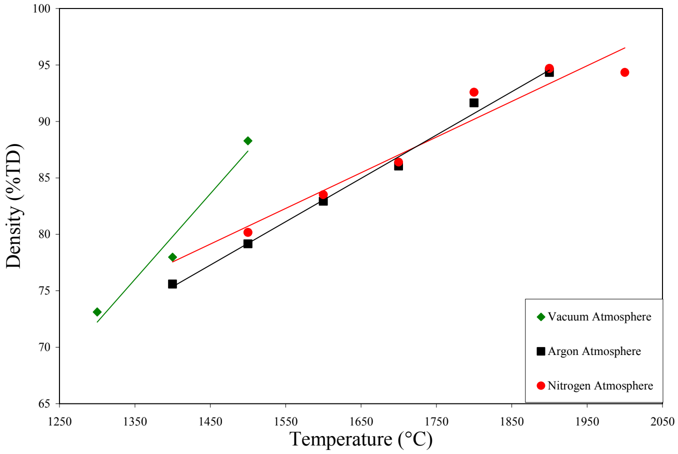

Figure 79: The effects of atmosphere and temperature on the sintered density of pure UN powders with an average particle size less then 2 μm. Figure adapted from Bauer *et al.* [57].

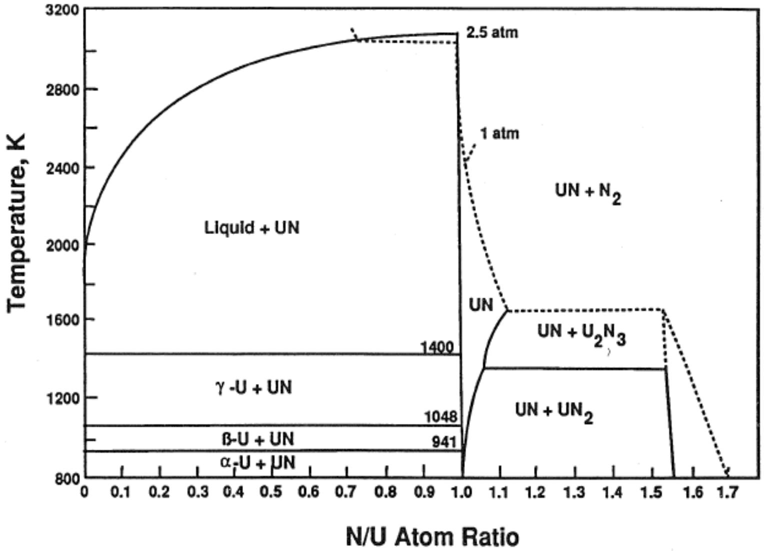

Figure 80: Uranium-nitrogen binary phase diagram from Matthews, *et al.* [11].

Over a decade after Bauer's work [57], and as nuclear power again began to prosper in the United States, Matthews *et al.* [11] reviewed and reported on UN for the SP-100 project. The LANL and Matthews *et al.* [11] specified the desired attributes of a space nuclear nitride fuel as the following: (1) 87% ± 2%TD with 37% U^{235} to meet power requirements, (2) 20 μm grains, open porosity, and no cracks to control swelling and fission-gas release, and (3) < 500 ppm carbon, < 500 ppm oxygen, and 1.0 ± 0.02 deviation from stoichiometric UN to control cladding and coolant compatibility. In the work presented by Matthews *et al.* [11], the final sintered density and grain sizes of the UN pellets was reported as a function of milling time (0-80 minutes) to reduce UN particle size and increase sinterability, sintering time (0-24 hours) to increase grain size, and sintering temperature (1800, 1950, and 2100°C) to increase density. The left plot in Figure 81 shows the dependence Matthews *et al.* [11] found between the densification of UN and milling time. The milling was performed in a high energy vibratory ball mill. From Figure 81 it is seen that the pellet density increases with milling time but additional milling was detrimental because the powder became difficult to press into solid pellets. However, it was stated by Matthews *et al.* [11] that the final sintered density was nearly independent of the green density. The plot on the right of Figure 81 shows the densification of pure UN (milled for an unspecified amount of time) as a function of the sintering time and the sintering temperature.

Four years later in 1992, Matthews *et al.* [55] published another article on the development of processes for fuel fabrication. However, sparse details were given on the success of the presented sintering variables for sintering approximately 44,000 individual 97%-enriched UN fuel pellets, but the basics of processing were given in the previous reveiew [11].

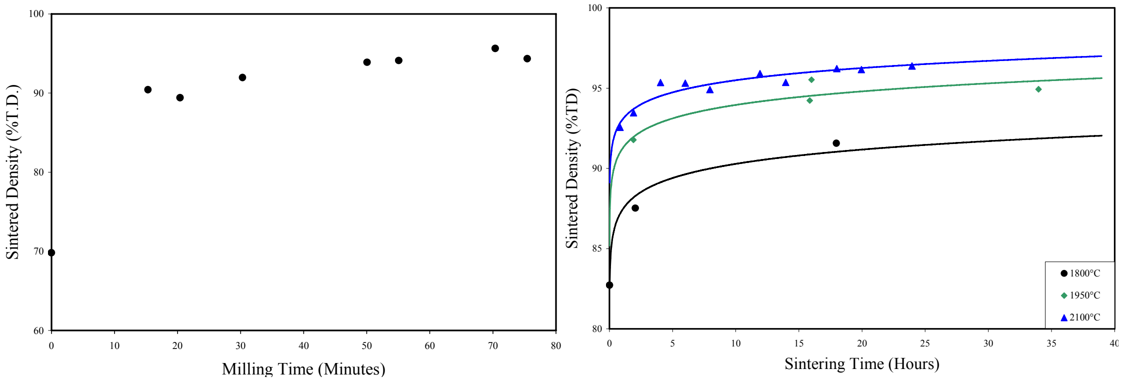

Figure 81: The effect of high energy vibratory ball-milling time, sintering time, and temperature on the final sintered density of pure UN. Figures adapted from Matthews *et al.* [11].

The JAERI also contributed to the advancement of nitride fuels. Their work focused on the (U, Pu)N system. Arai *et al.* [9, 67, 115, 116] reports studying the effects of milling time (0 – 48 hours), green pellet compaction pressure (20 – 400 MPa), sintering temperature (1650 – 1775°C), and sintering atmosphere (Ar, Ar – 8% H_2, and N_2 – 8% H_2) on the sintered density of (U, Pu)N pellets. According to Arai *et al.*, longer milling times resulted in greater sintered densities, which is also seen in the first plot of Figure 82. The second plot in Figure 82 shows the effects of compaction pressure on the green and sintered densities of (U, Pu)N pellets. The pellets were synthesized from powder that had been ball milled for 48 hours prior to being sintered for 5 hours in Ar – 8% H_2 (all compaction pressures resulted in green pellets with good structural integrities). The second plot in Figure 82 shows that the compaction pressure has very little impact on the final sintered density of the pellets but the green densities slightly increase with greater compaction pressures.

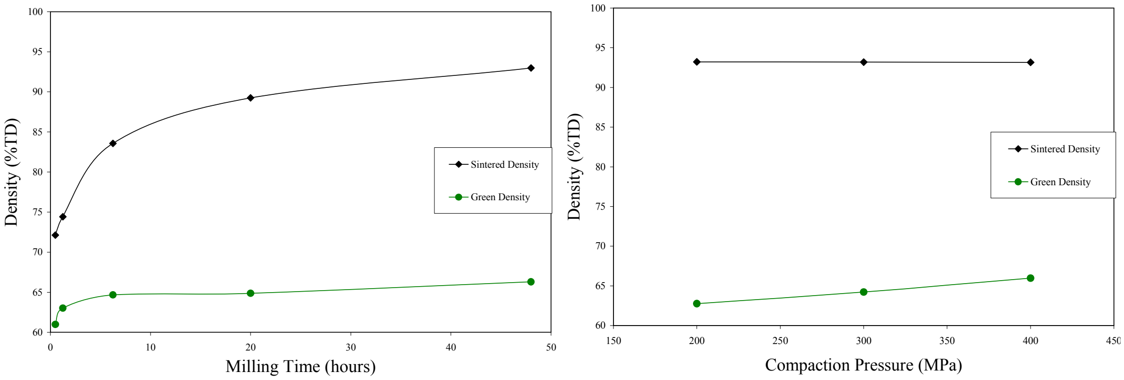

Figure 82: The effect of ball-milling time and compaction pressure (on powders milled for 48 hours) on the green and sintered densities of (U, Pu)N pellets that were sintered for 5 hours in Ar – 8%H_2 . Figures adapted from Arai *et al.* [9, 67].

(U, Pu)N powders were milled for 48 hours prior to pressing into pellets and sintering for 5 hours in various atmospheres (Ar, Ar – 8% H_2, and N_2 – 8% H_2) and temperatures ranging from 1650 °C to 1775°C (shown in the first plot of Figure 83). The final density of the nitride pellets increased with lower nitrogen partial pressure gases (i.e. Ar and Ar – 8% H_2 gas). Further observation of the microstructures of these pellets lead the authors to believe that the diffusion of the heavy metal atoms is suppressed when the nitrogen partial pressure is high (thus resulting in smaller grain sizes) [9, 67]. However, conventional kinetics would suggest that an increase in grain boundary area would increase the rate of diffusion which is contradictory to the observations made by Arai *et al.* [9, 67].

Due to the fact that the densities reached were typically greater than 90%TD, the use of wax-type pore formers was also studied (0 to 2 wt%) in order to achieve the desired density of 85%TD. The second plot shown in Figure 83 shows the effects of pore former concentration on the sintered density of (U, Pu)N pellets that were sintered for 5 hours at 1750°C. A linear dependence between the pore former content and the sintered density was observed.

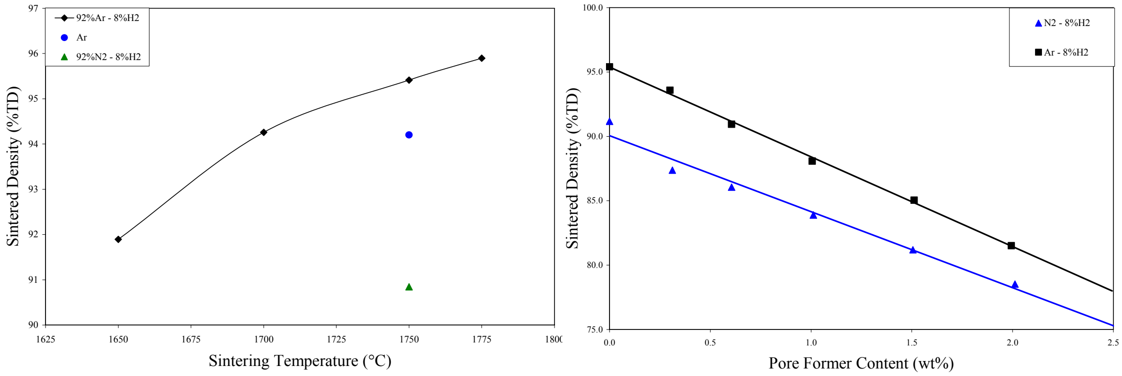

Figure 83: The effects of sintering atmosphere, temperature, and pore former content on the final sintered densities of (U, Pu)N pellets that were milled for 48 hours and pressed at 400 MPa prior to sintering for 5 hours. Figure adapted from Arai *et al.* [9, 67].

Zirconium nitride (ZrN) was studied by a few authors as a candidate inert matrix for advanced nuclear fuels as well as a surrogate for actinide nitrides. In 2001 and 2002, Margevicius *et al.* [43, 112] investigated the effects of sintering aids such as palladium (Pd), binders such as polyethylene glycol (PEG), die lubricants such as zinc stearate, milling conditions, and sintering atmospheres on the sintering of ZrN pellets. Margevicius *et al.* [112] conducted preliminary studies by sintering ZrN in air and in argon for 24 hours at various temperatures (1400 – 1700°C). The resultant ZrN that was sintered in air was less dense (by approximately 12%TD) than that sintered in an argon atmosphere. The samples sintered in air were covered by a loose ZrN powder as a barrier from oxygen. Furthermore, increasing the sintering temperature from 1400°C to 1700°C in argon resulted in a minimal 3% increase in the sintered density.

Further work consisted of milling ZrN in a SPEX mill with 0.2 wt% of each of PEG and zinc stearate for various durations (0 – 45 minutes) with and without Pd powder (0.3 vol%). The pellets were pressed at 500 MPa and fired in an argon atmosphere for 20 hours at 1400°C. The effect of milling time on the final sintered density of the ZrN compacts was documented and plotted (Figure 84). Accordingly, the final sintered density of the pure ZrN was increased by approximately 15% when it was milled for 45 minutes without the addition of the Pd powder. Both experiments (with and without the Pd powder) were co-milled with PEG and zinc stearate. Further examination of the powders using SEM revealed that after 30 minutes of milling the powder began to agglomerate and there was a significant reduction in the number average particle size.

Further investigations of the sintering of ZrN as a surrogate for actinide bearing nitrides by Dunwoody *et al.* [114] and Wheeler *et al.* [48] (also with the LANL group) were conducted. The effects of atmosphere (N_2, N_2 – 6%H_2, Ar, and Ar – 6% H_2) and temperature (1100 – 1700°C) on the final sintered density and nitrogen stoichiometry of ZrN was reported. ZrN, 0.2 wt% zinc stearate (as a die lubricant), and 0.2 wt% PEG (as a particle binder) were SPEX milled with one milling media for 45 minutes. The pellets were then compacted at 250 MPa and sintered for 10 hours at the previously mentioned temperatures and atmospheres. It was observed that the pellets sintered at 1400°C and 1500°C in pure argon had much higher densities than those sintered in pure nitrogen (by approximately 17% TD). It was also observed that the pellets sintered under hydrogen containing atmospheres sintered to lower densities than in pure argon and pure nitrogen, respectively (Figure 85). The density measurements of the sintered nitride pellets were completed using immersion techniques. The observed dependence on sintering atmosphere suggests that the kinetics of sintering is strongly influenced by the sintering atmosphere. It was also found that the lattice parameters of the pellets sintered in nitrogen were higher than those sintered in argon. It is speculated that the larger lattice parameter in the pellets sintered in nitrogen is attributed to the hyperstoichiometric conditions of the pellets (assuming that excess nitrogen adsorbed into the lattice).

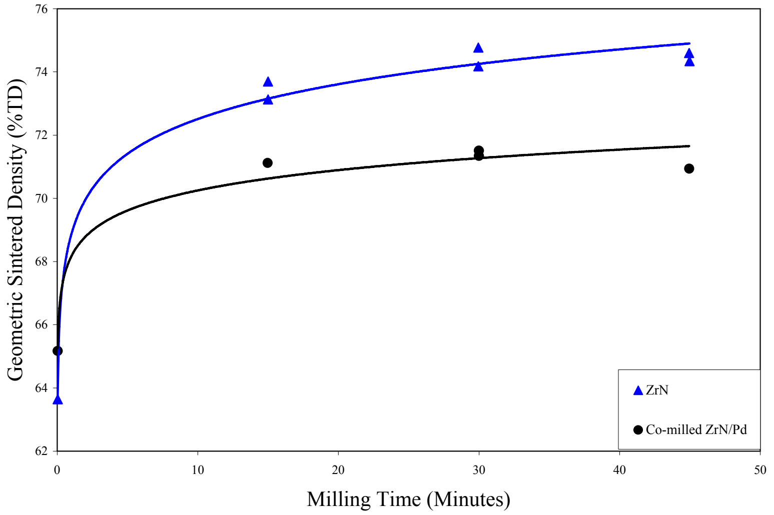

Figure 84: The effect of SPEX milling time on the sintered density of ZrN with and without Pd powder (0.3 vol%) and 0.2 wt% of each of PEG and zinc stearate. The mixtures were sintered for 20 hours at 1400°C in argon. Figure adapted from a LANL report [43].

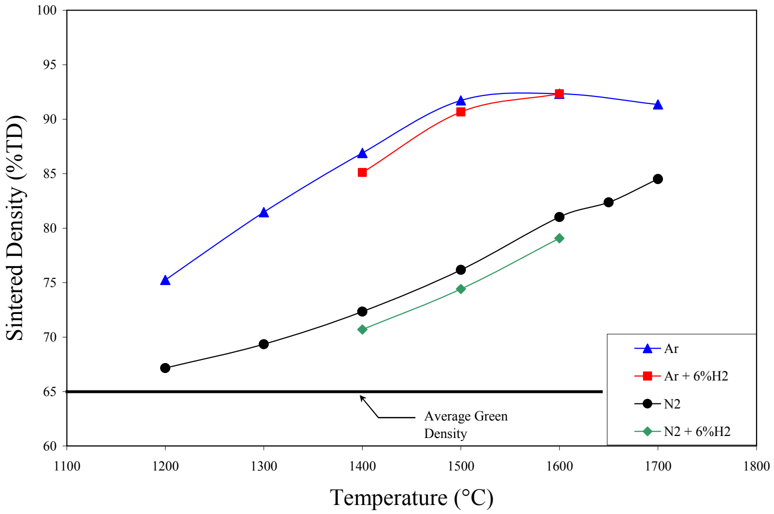

Figure 85: The effects of sintering temperature and atmosphere on the final density of ZrN pellets. Adapted from Dunwoody *et al*. [114] and Wheeler *et al.* [48].

Many authors have studied various effects of processing parameters on the sintered densities and microstructures of nitride materials, as demonstrated in the preceding literature review. The reviewed literature provided insight into the characteristics that define a ‘desirable’ fuel pellet for advanced nuclear fuel applications as well as providing an idea of initial processing parameters to help guide the direction of the work presented in this report.

However, the literature review provides a poor benchmark standard to compare with the work presented in this report to. It is a poor standard for this work due to two primary reasons. The first reason being that all of the reviewed articles used different types of mills, media, powder synthesis techniques, furnaces, processing gases, and other processing variables that would effect the sintered nitride product and would be difficult to duplicate and compare to the work presented in this document. The second factor that makes the reviewed literature a poor standard to compare the work presented in this report to is the fact that specific processing details were left out in almost every reviewed article. It is therefore an objective of the next section of this report to understand and optimize processing parameters using pure UN. Once the processing parameters are defined and understood, DyN additives will be introduced.

3.1. Experimental Procedures for Sintering Pure UN

The focus for this section of the report is to use the sintering parameters gained from the previously reported literature review (Section 3.1), as well as the insight gained from practical lab experience to determine feasible sintering parameters for the remainder of these studies. Through the literature review presented in Section 3.1, many of the studies used PEG or poly vinyl butyral (PVB) and zinc stearate when pressing green pellets. However, there was no mention of a solvent to dissolve the particle binder and/or die lubricant. Studies were then conducted using toluene to dissolve PVB to demonstrate the effects of compaction pressure (300 – 415 MPa) and milling time (0 – 24 hours) on the green density of UN powder (Figure 86). The UN powder was wet-milled in a solution of 0.15 wt% PVB dispersed in toluene (0.3 $^{mL}/_{gm\ powder}$). The milling was completed in the Retsch planetary ball mill (Figure 20b) at 500 RPM for 0.5, 5, 10, and 20 hours prior to cold-pressing (300 – 415 MPa) in a 0.2500 inch diameter carbide pellet die (Figure 87). It is seen that greater green densities are achieved with higher compaction pressures and less milling.

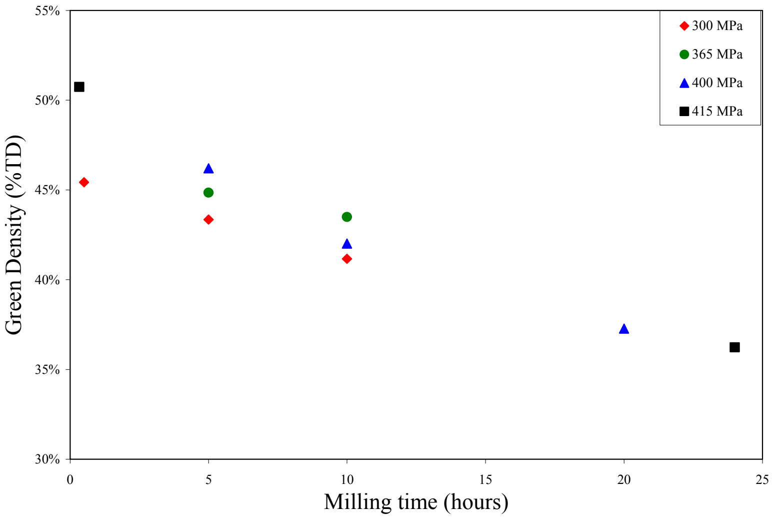

Figure 86: The effects of high energy milling time and compaction pressure on the green density of pure UN powder wet-milled in a solution of 0.15 wt% PVB dispersed in toluene (0.3 $^{mL}/_{gm\ powder}$).

Figure 87: Photograph of a 0.2500” diameter carbide pellet die and pellet punch used for pressing UN pellets.

As seen in Figure 86, the highest green density achieved was approximately 50%TD of pure UN and that was using a powder that was compacted at high pressures and milled for very little time. The literature suggests that a green density of at least 60%TD should be obtained in order to achieve the final sintered density of 85 ± 5%TD [11]. The structural integrity of these pellets was relatively poor and further investigations were needed to improve the structure of the green pellet. In the meantime, the 43%TD green pellet that was milled for 5 hours and pressed at 300 MPa was sintered at 1500°C for 10 hours in an ultra high purity argon atmosphere. The sintered pellet shown in Figure 88b had a final density of approximately 68%TD and the laminations from cold-pressing can be seen.

Figure 88: 68%TD sintered UN pellet after cold pressing wet-milled UN (in toluene with zinc stearate and PVB) at 300 MPa. The 45%TD green pellet was sintered in very pure argon at 1500°C for 10 hours.

In attempts to increase the integrity of the green pellets and to achieve higher sintered densities, processing parameters such as milling time, compaction pressure, and sintering atmosphere were investigated. This section of the report focuses on pressing and sintering pure UN without the addition of binders, lubricants, or dispersants. The initial powder used was phase pure UN synthesized via the carbothermic reduction of the oxide prior to nitriding again for this study (described in great detail in Section 2.1.1). When the powder is removed from the furnace after synthesis, it is removed as an extremely brittle consolidated mass that is relatively easy to break down in an agate mortar and pestle. It is presumed that the powder is partially sintered at the temperatures endured during sintering (1500°C) but due to the lack of close contact, only weak bonds are formed. The particle morphology of the as-synthesized powder after it was broken down in a mortar and pestle is shown in the SEM image of Figure 89. It is seen in this image that the as-synthesized powder is primarily composed of agglomerates of sub-micron particles.

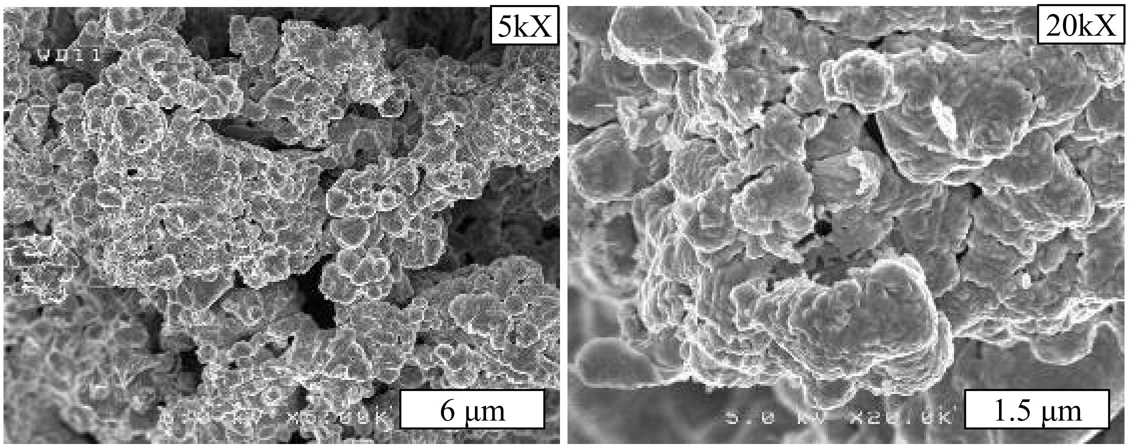

Figure 89: SEM images of UN powder prepared by the carbothermic reduction of UO_2 prior to nitridation at 1500°C.

After the UN powder was synthesized, it was grinded with an agate mortar and pestle prior to being ball-milled (using a 10:1 milling media to powder mass ratio) in the Retsch planetary ball mill (Figure 20a) with no binder, solvent, or die lubricant. The pellets were pressed at 420 MPa using the 0.2500 inch diameter carbide pellet die (Figure 87) and a hydraulic press inside the PlasLab argon atmosphere glovebox (Figure 1a). In the first study, the pellets were ball-milled for different lengths of time (0-24 hours) prior to being sintered in oxygen-gettered ultra-high purity argon for 5 hours at 1550°C. The oxygen content of the argon gas was measured as less than 0.1 ppb by an Ntron Model OA-1 (Exton, PA, USA) oxygen analyzer for all of the experiments. As seen in Figure 90, the pellets with larger particle sizes (less milling time) pressed to a greater green density, as shown as the gray portion of the columns. However, the densification observed in the pellets with the smaller particle sizes (milled for the longer times) was far greater than that of the other pellets with larger particle sizes (as shown by the black portions of the columns). The green densities were measured using a geometrical approach and the sintered density was found using Archimedes technique. The error for both the green and sintered densities was calculated as approximately 2%TD. A sample calculation of the error propagation is provided in APPENDIX C for both the green and sintered densities.

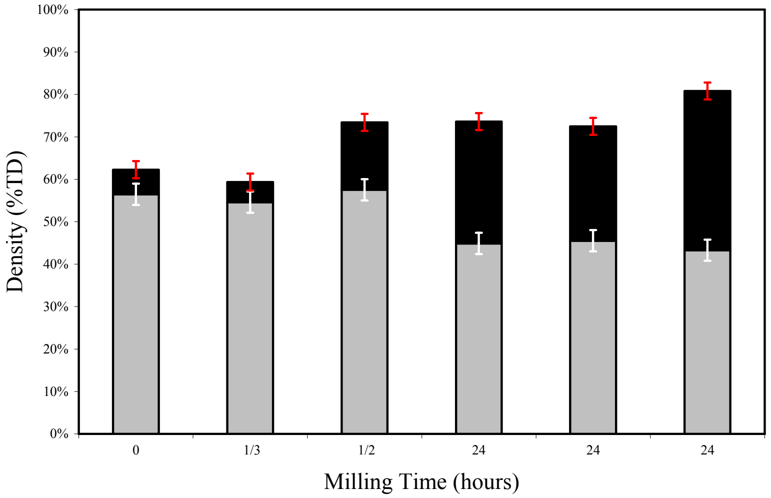

Figure 90: The effects of dry milling time on the green and sintered density of UN pellets. The pellets were cold-pressed at 420 MPa prior to being sintered at 1550°C for 5 hours in very high purity argon. The green density is shown in gray and the densification is shown in the black.

From Figure 90, it is seen that the pellet that was fabricated from the as-synthesized powder (no ball-milling) sintered very poorly. In fact, this pellet only exhibited a 6% densification to reach a final density of 61%TD. The pellet was sectioned and polished (Figure 91). However, due to the porous structure of the pellet, it experienced “particle pull-out” when polishing resulting in a poor finish.

Figure 91: UN pellet sintered at 1550°C for 5 hours in very pure argon using as-synthesized powder (i.e. no milling, binder, or lubricant). The pellet was pressed at 420 MPa to 56%TD and only reached a sintered density of 61%TD.

It is also seen from Figure 90 that the pellets that were dry milled for 24 hours pressed to a lower green density than the pellets that were milled for shorter times but experienced greater densification (5%TD versus 35%TD). The pellet that sintered to the highest density (approximately 81%TD) was sectioned with a slow speed diamond saw prior to polishing with SiC to 1200 grit and a 1 μm diamond suspended solution on a polishing pad. An optical image as well as a SEM image are shown in Figure 92. As seen in these images, there exists a distinct ring around the outer diameter of the pellet. It is presumed that this ring is a result of the sintering atmosphere and can be explained by studying the uranium-nitrogen binary phase diagram.

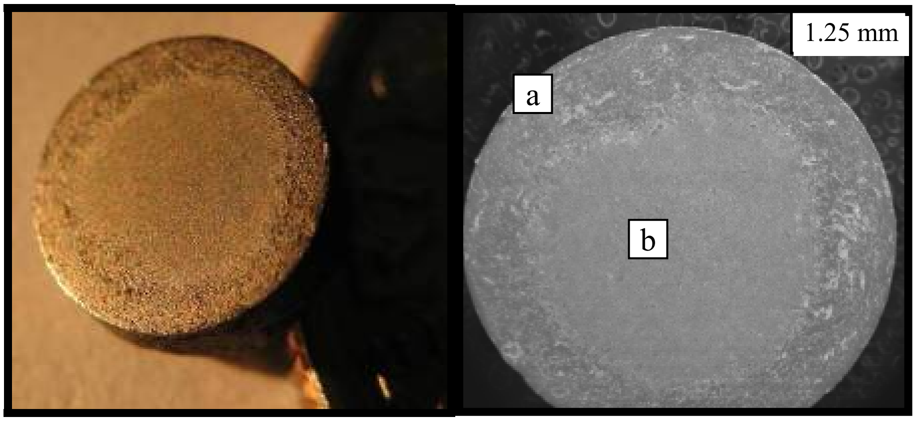

Figure 92: UN pellet sintered at 1550°C for 5 hours in oxygen-gettered UHP argon using powder that was ball milled for 24 hours to reduce the particle size. The pellet was pressed at 420 MPa to 43%TD and reached a sintered density of 81%TD.

The dense ring around the perimeter of the pellet shown in Figure 92 is likely due to hypostoichiometric nitrogen conditions during sintering in pure argon that caused a nitrogen depleted region. The UN likely dissociated into UN and uranium metal as represented by the left star in the uranium-nitrogen binary phase diagram in Figure 93. When the liquid uranium formed, the sintering kinetics were increased and the region became more dense. Further analysis of the pellet was conducted to investigate its microstructure in the regions of interest. Figure 94 shows SEM images of the sectioned and polished UN pellet. The image on the left, designated as ‘a,’ is the outer portion of the pellet (corresponding to Figure 92) where it is presumed that liquid uranium formed and enhanced sintering. It is seen that the outer ring of the pellet is much denser where it is presumed that the liquid uranium formed. There are also has dark regions that appear in the images that likely correspond to the free uranium, however, further analysis using electron probe micro analysis (EPMA) techniques would be useful. The image on the right of Figure 94, designated as 'b,' is the inner portion of the pellet where it is presumed to be stoichiometric UN where no liquid phase formed. From the image of the center of the pellet, it is seen that the pellet is much more porous, but still shows evidence of the intermediate phase of sintering.

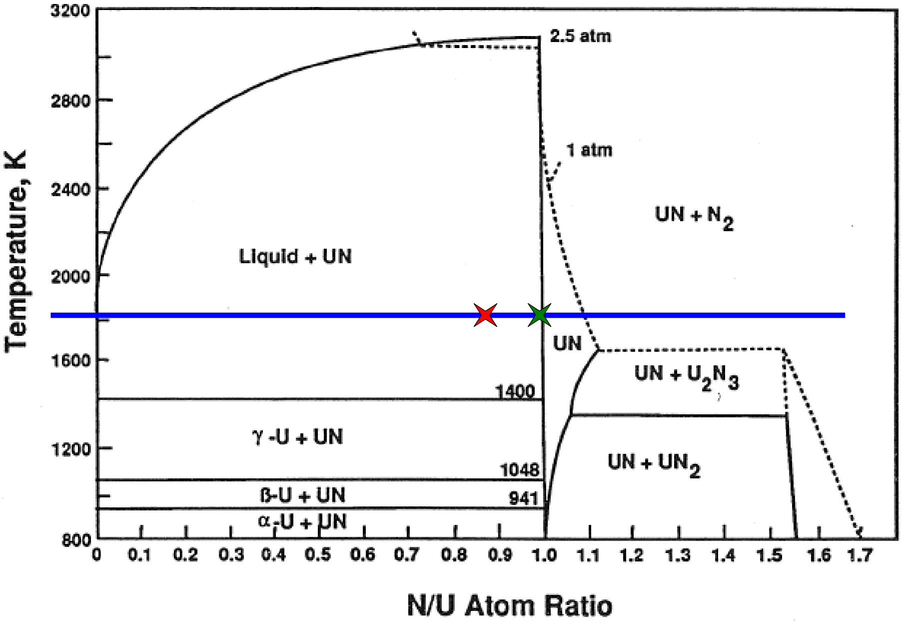

Figure 93: Uranium-nitrogen binary phase diagram from Matthews *et al.* [11]. The stars shown in red and green (left and right) represent reactions that occur at 1550°C depending on the nitrogen pressure in the sintering atmosphere.

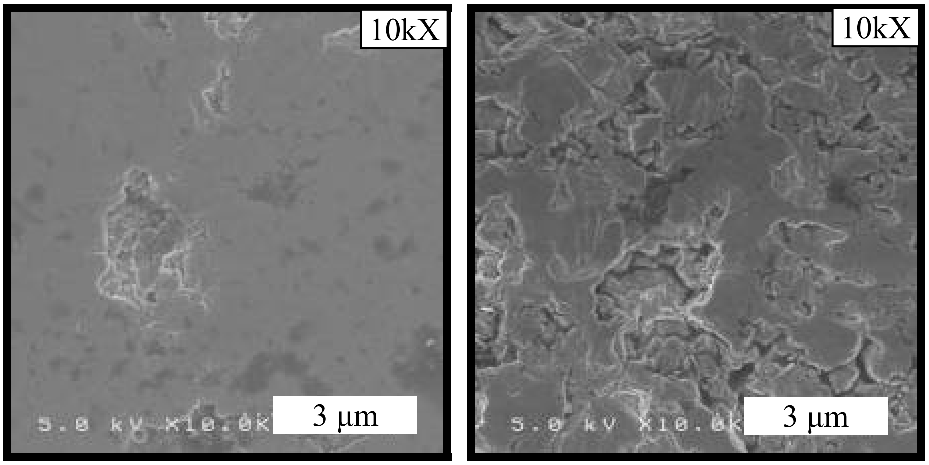

a) b)

Figure 94: SEM images of the sectioned and polished UN pellet shown in Figure 92. The image on the left, designated as ‘a’ is the outer portion of the pellet where liquid uranium formed during sintering. Image ‘b’ is the inner portion of the pellet showing no evidence of liquid uranium formation.

Although the pellet of Figure 92 had a final density in the desired range for fuel pellet applications, the existence of free uranium will likely cause the fuel to swell, creep, and react with the cladding when heated and irradiated. This is therefore an undesirable property for fuel pellet applications and more work was done to study the atmospheric effects on sintering.

Thermodynamic calculations based on the dissociation reaction shown in Reaction 22 suggest that for the liquid phase to form at 1550°C, the partial pressure of nitrogen would have to be less than $1.404 \cdot 10^{-8}$ atm ($1.423 \cdot 10^{-6}$ kPa). The calculation was completed using the FactSage Thermochemical Software and Database version 5.5 [96] and is presented in its entirety in APPENDIX D. However, the kinetics of nitrogen diffusion in uranium plays a large role in the dissociation reaction. Due to the fact that the kinetics of nitrogen diffusion in uranium metal is beyond the scope of this report, a discussion and review of nitrogen diffusion in uranium is presented in APPENDIX E.

$$UN \rightarrow U + \frac{1}{2} N_2 \tag{Rxn. 22}$$

Further investigations were completed to study the effects of varying nitrogen content in the processing atmospheres on the stoichiometry of the sintered pellet. In an ideal atmosphere, stoichiometric UN could be sintered resulting in a stoichiometric UN pellet. Such an atmosphere would exhibit a low nitrogen partial pressure to prevent the formation of a sesquinitride, but a high enough nitrogen partial pressure to prevent the formation of liquid uranium. All of the pellets used in this study were fabricated using phase pure UN powders synthesized by the carbothermic reduction of UO_2 prior to nitridation synthesis route. Prior to sintering, the powders were milled in a planetary ball-mill with a 10:1 media to powder mass ratio for 24 hours with no solvent, binder, or lubricant prior to being cold-pressed at 420 MPa in an argon atmosphere glovebox.

The pellets were sintered in ultra high purity processing gases in the high temperature CM alumina tube furnace (Figure 4) at 1550°C for different lengths of time (5, 10, or 20 hours, as noted on the individual experiments shown in Figure 95). The ultra high purity gases were further purified from oxygen and moisture prior to entering the furnace. In order to increase and measure the purity of the already high purity processing gases the gases flow into a Drierite (Xenia, OH, USA) $CaSO_4$ desiccant to remove moisture, a Restek Thermal Gas Purifier (Bellefonte, PA, USA) to remove oxygen, a ppm range Ntron Model OA-1 (Exton, PA, USA) oxygen analyzer, and an Ametek 303B Moisture Monitor (Pittsburgh, PA, USA) prior to being introduced into the tube of the furnace. The processing gas usually has less then 1 ppb oxygen and less than 50 ppm moisture.

The first experiments examined the effects of sintering time on the densification of the pellets in a pure argon atmosphere. The densification results can be seen in Figure 95 in the blue shaded columns. Of the three fabricated pellets, the green densities were statistically equivalent and the sintering time had very little effect on the densification of the pellets. In fact, the densification of the pellets sintered at 5, 10, and 20 hours are all statistically the same. The next set of experiments investigated the sintering of UN pellets in a pure nitrogen atmosphere and is shown in the gray shaded columns of Figure 95. The first pellet shown was sintered in pure nitrogen for the entire sintering process. The pellet only exhibited 11% densification, assuming that the pellet had remained pure UN. However, further phase analysis using XRD techniques showed that U_2N_3 formed at the surface of the pellet. The U_2N_3 phase is considered as an undesirable phase for nuclear fuel applications because upon heating, it dissociates into to UN and N_2 (according to Reaction 23), causing the fuel pin to pressurize. The dissociation of U_2N_3 can also lead to nitridation and embrittlement of the cladding. The reaction is represented by the right star on the uranium-nitrogen binary phase diagram in Figure 93. The rapid formation of N_2 also presumably causes the fuel to crack during sintering and/or irradiation [11].

$$U_2N_3 \rightarrow 2UN + \frac{1}{2}N_2 \qquad \text{(Rxn. 23)}$$

It is also seen in the uranium-nitrogen phase diagram (Figure 93) that U_2N_3 is not a stable phase at the sintering temperatures studied here. The binary phase diagram suggests that the formation of the sesquinitride will only form upon heating and/or cooling a UN sample through the hyperstoichiometric nitrogen region that occurs at approximately 1070°C – 1350°C. Thermodynamic calculations of the dissociation of U_2N_3 into UN and nitrogen gas are shown in APPENDIX D (as per Reaction 23). Using the upper boundary of the U_2N_3 phase (assuming a cooling reaction), the equilibrium partial pressure of nitrogen is calculated to be $2.37 \cdot 10^{-5}$ atm ($2.40 \cdot 10^{-3}$ kPa). Accordingly, in attempts of preventing the formation of the sesquinitride, the same profile (1550°C for 10 hours) was run in a high purity nitrogen atmosphere and ramped down in different atmospheres trying to reduce the U_2N_3 phase to UN. The difference between the three sintering experiments in pure nitrogen is that one was ramped down in pure nitrogen, one was ramped down in a 10^{-3} Torr vacuum, and one was ramped down in high purity argon. It was thought that the U_2N_3 that formed during the sintering in nitrogen would reduce to UN by cooling the sample in an atmosphere containing a low partial pressure of nitrogen. However, cooling the sample in a low nitrogen partial pressure atmosphere showed no significant difference from cooling the sample in pure nitrogen, as seen in the gray and black columns in the center of Figure 95. The three studies yielded very similar amounts of densification and final densification that leads to the presumption that the U_2N_3 phase is still present.

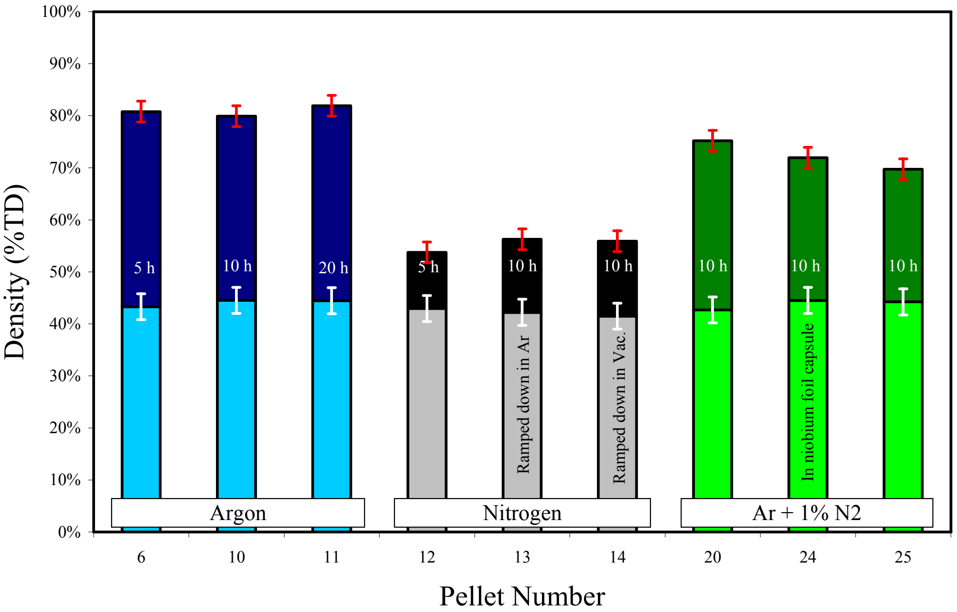

Figure 95: UN pellets sintered in different atmospheres at 1550°C for different lengths of time (listed on the column of the individual data sets). All of the pellets were ball milled for 24 hours with no binder, solvent, or lubricant prior to being cold-pressed at 420 MPa. The green density is shown in the lighter shades and the densification in the darker shades.

Based on the previous thermodynamic calculations, an Ar – 1% N_2 mixed gas was used in the final three preliminary experiments presented in Figure 95 (in shades of green on the right). The resulting pellets exhibited an approximate 33% densification to reach approximately 75%TD. Pellets 24 and 25 were prepared, processed, and sintered in the same furnace run, the only difference being that pellet 24 was wrapped in a niobium foil as an extra barrier from oxidation. The two pellets exhibited very a similar amount of densification and they had similar appearances as seen in Figure 96. However, pellet 24 (wrapped in niobium foil), seemed to have a slightly more metallic luster than the pellet that was exposed to the process gas. The densification data obtained from these studies was also compared to the data obtained from Bauer *et al.* [57] in Figure 97. It is seen in Figure 97 that the data obtained from the investigations presented in this report varies from what Bauer reported.

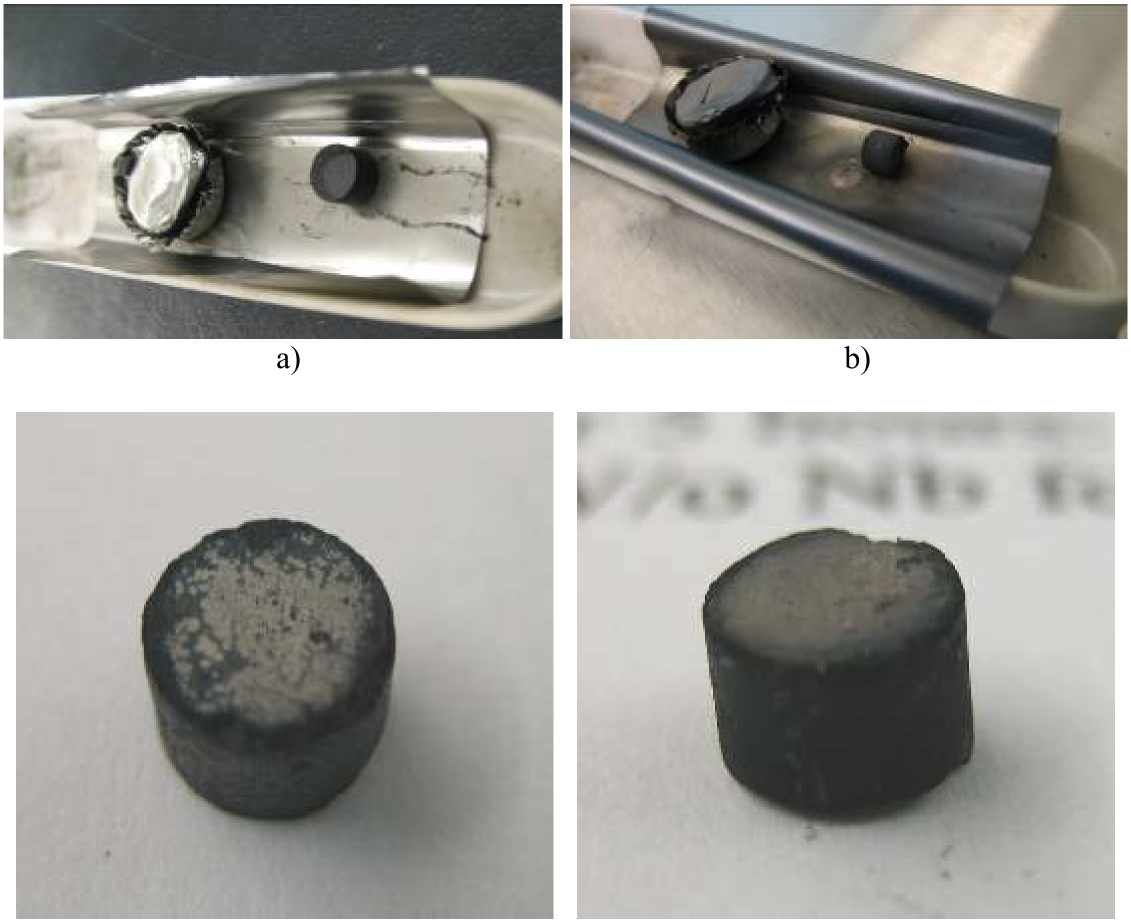

a) b)

c) d)

Figure 96: UN pellets sintered at 1550°C for 10 hours in an Ar – 1%N_2 mixed gas. Images of the pellets in the niobium foil-lined alumina boat (a) prior to and (b) after the sintering profile. It is seen that the encapsulated pellet (c) had slightly more metallic luster than the pellet that was exposed to the Ar – 1%N_2 process gas (d).

To better understand the kinetics of the sintering processes, the effects of processing parameters (particle size, time, temperature, and atmosphere) on the grain sizes and particle-particle interaction must also be studied. One of the best ways to obtain microstructural information is by optical and electron microscopy. From information obtained using optical and electron microscopy, the kinetics of sintering can be modeled according to predetermined models. A list of initial stage, intermediate stage, and final stage sintering models can be found in APPENDIX B. Once microstructural data (grain size and particle necking measurements) is obtained as a function of time, temperature, and initial particle size, the models presented in APPENDIX B can be used to determine the rate limiting sintering mechanism.

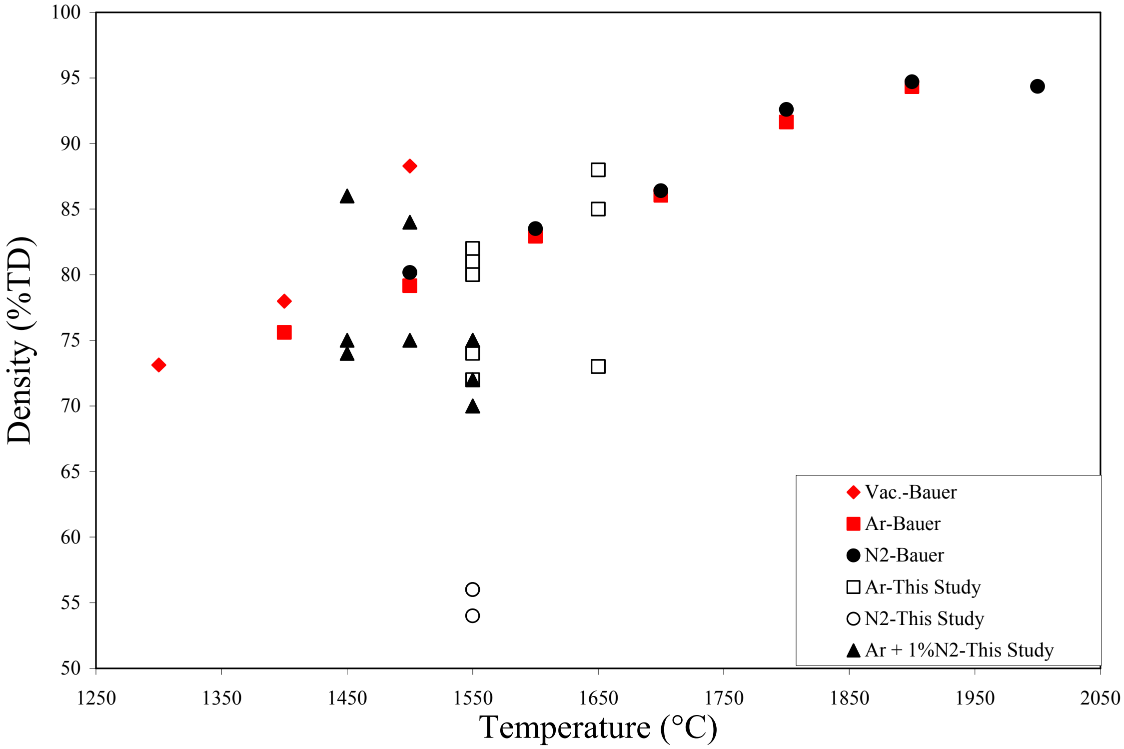

Figure 97: The effects of atmosphere and temperature on the sintered density of pure UN powders. Data from the sintering experiments presented in this document compared to the data provided by Bauer *et al.* [57].

Using the sintered pellet number 25 (processing conditions described above), the pellet was first cut in air using a low speed saw in a petroleum-based cutting fluid. The pellet was polished in a petroleum-based cutting fluid with SiC paper to 1200 grit. However, the sample resisted polishing and very little useful data on the microstructure of the pellet was able to be extracted from the optical and SEM images. In attempts to gain a further understanding of microstructure and the mechanisms of sintering of this same pellet (pellet #25), it was fractured and the fracture surface was observed using electron microscopy. Figure 98 shows the SEM images obtained of the fracture surface. It is speculated that a possible evaporation-condensation mass transport mechanism (which is a coarsening effect and not a desired densification effect) has taken place due to the very distinct faceted features in the 50X images. However, much more work needs to be completed to validate this assertion.

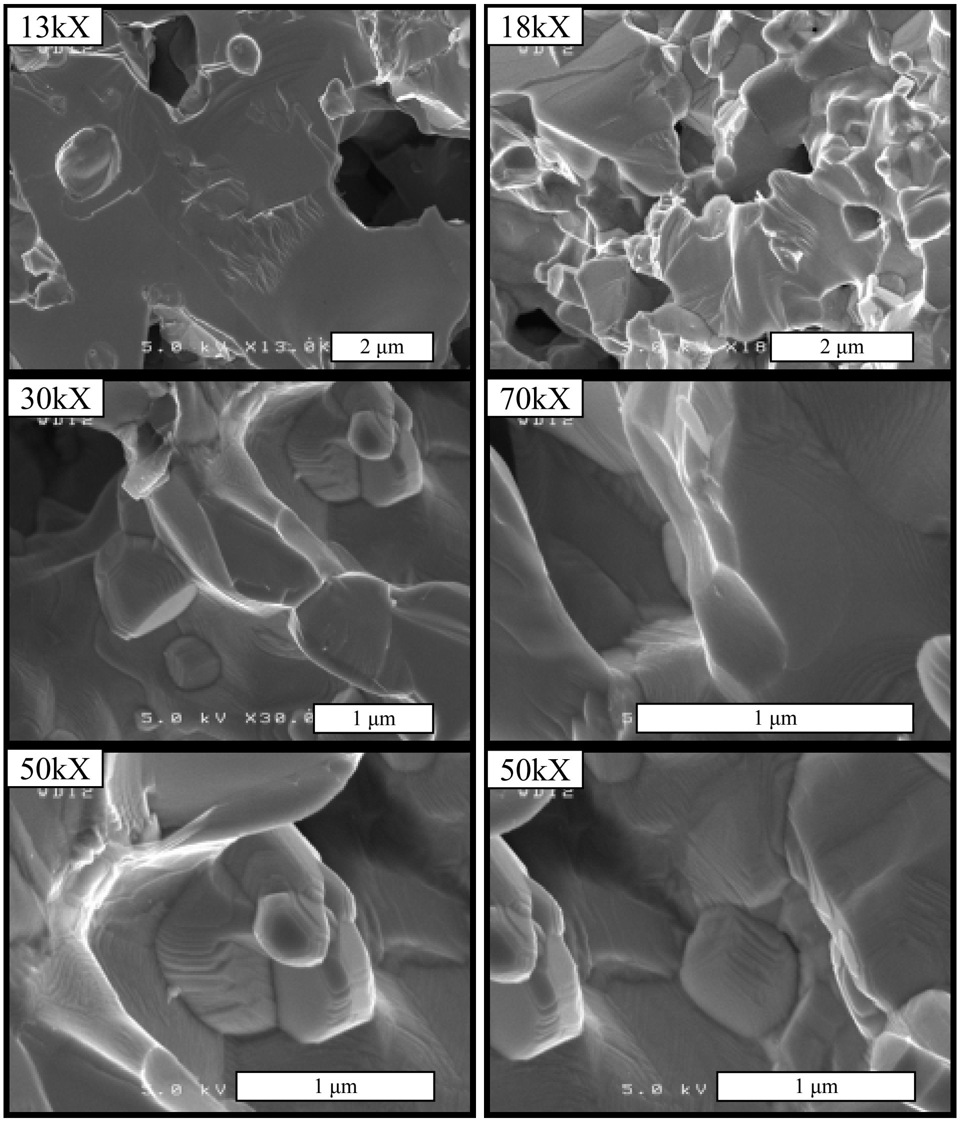

Figure 98: SEM images of a fracture surface of a UN pellet that was sintered at 1550°C for 5 hours in an Ar – 1%N_2 mixed gas.

3.2. Results of Sintering Pure UN

The following parameters have been chosen to further study the effects on sintering UN with DyN additives:

- Sintering method: Cold pressing and sintering
- Pellet dimension ratio: $1.0 \leq {}^{\text{Length}}/_{\text{Diameter}} \leq 1.2$
- Binder/Die lubriacant: None
- Milling time: 24 hours
- Compaction pressures: 280 MPa
- Desired green density: 45-55 %TD
- Sintering aides: None
- Compositional range: 0 – 30 mol% DyN in UN matrix
- Sintering atmosphere: Ar – 1%N_2
- Sintering temperature: 1450 – 1650°C
- Sintering times: 5-40 hours
- Desired sintered density: 85%TD
- Ramp rate: $200^{\circ\text{C}}/_{\text{hour}}$

4. Sintering of Uranium and Dysprosium Nitride (U,Dy)N

Until recently DyN has been studied very little due to its lack of applications. However, since its discovered properties show similarities with those of the transuranics used for transmutation fuel fabrication for the fast spectrum reactors, more research has been conducted to better understand its thermophysical properties. As mentioned in previous sections, it is speculated that DyN may be a suitable surrogate for AmN in the fabrication of the transmutation fuels [6, 8, 30, 45-47]. However, there is very little published data to confirm this. Due to the fact that the dysprosium-nitrogen system has not been thoroughly studied, very little is known about its sintering properties and additive effects. There are a few authors who have reported sintering of DyN in as a solid solution with ZrN, with ZrN being a feasible inert matrix candidate for advanced fuels. Takano *et al.* [6, 8, 46] and the LANL group [43] both focused on the (Zr, Dy)N solid solutions with DyN as a surrogate to AmN. However, the status report from the LANL group was brief and only a few experimental details were discussed. The main details gained from the LANL groups was that solid solutions of (Dy, Zr)N were sintered in an alumina tube furnace for 24 hours at 1400°C.

Further studies of adding dysprosium to an inert matrix was studied by Takano *et al.* [6] who prepared $(Zr_{0.8}, Dy_{0.2})N$ and $(Zr_{0.5}, Dy_{0.5})N$ solid solutions by subjecting the compacts to 1773 K for 20-50 hours. The resulting compacts were used to study hydrolysis reactions as a function moisture and processing atmosphere. However, no data was presented on the effects of DyN content on sintering or the densification achieved. More work by Takano *et al.* [8, 46, 47] documents the lattice thermal expansions of (Dy, Zr)N solid solutions, the stability of (Dy, Zr)N solid solutions in air and in moist environments, and the oxygen solubility of Dy(N, O) solid solutions. However, no data was presented discussing the sintering of the compacts.

According to Minato, Ogawa, and Chauvin [16, 129, 130], much work needs to be completed with AmN to better understand its effects on sintering. Accordingly (as stated in the objectives of this work), this section of the report investigates the effects of DyN content on the sintered density and mass loss of the UN and (U, Dy)N pellets. The sintering procedures were developed and optimized in Section 3.1 with the work of UN.

4.1. Experimental Procedures for Sintering (U, Dy)N

The final experiments presented in this report investigate the effects of sintering time, sintering temperature, and DyN content in a UN matrix on the final sintered product. The parameters varied in this investigation include: DyN content (0 – 30 mol%), sintering temperature (1450 – 1650°C), and sintering time (10 – 40 hours). The sintered pellets were analyzed for density and mass loss. The UN used in these investigations was synthesized via a carbothermic reduction of UO_2 prior to nitridation and the DyN used was synthesized via a hydride prior to nitridation of dysprosium metal. Both of the methods are described in great detail in Chapter IV, Sections 1.1 and 2.2., respectively. The two powders were combined in the argon atmosphere glovebox prior to sealing in a chrome steel milling vessel and mixed at ratios from 0 – 30 mol% (according to Table 10). The milling vessel was then placed in the planetary ball for 24 hours at 500 RPM with no die lubricant or particle binder. The powders were milled using 5 mm diameter ytrria stabilized zirconia in a 10:1 media mass to nitride mass ratio.

After preparing the powders, the pellets were then cold-pressed in the argon atmosphere glovebox using a carbide pellet die as seen in Figure 87. The green densities of the pellets were found using a geometric approach (the propagation of error through the calculations is presented in APPENDIX C). The pellets were then sealed in niobium foil capsules (Figure 99) prior setting in an alumina boat and loading into the alumina tube CM furnace. Once the pellets were removed from the furnace (Figure 99), they were immediately weighed to determine the mass loss prior to measuring the density using an immersion technique.

Table 10: Molar ratios of UN-DyN powders that were blended and milled for 24 hours in a pure argon atmosphere with a 10:1 YSZ milling media to powder mass ratio. These powders are ready for pressing and sintering.

UN (mol%)	**100%**	**99%**	**95%**	**90%**	**80%**	**70%**
DyN (mol%)	**0%**	**1%**	**5%**	**10%**	**20%**	**30%**
Mass UN (gm)	**9**	**8.937**	**8.685**	**8.350**	**7.659**	**6.922**
Mass DyN (gm)	**0**	**0.063**	**0.315**	**0.650**	**1.341**	**2.078**

Figure 99: Photographs of the (U, Dy)N pellets encapsulated in Nb foil before and after a typical sintering profile in Ar – 1%N_2.

4.2. Results of Sintering (U, Dy)N

Figure 100 shows the results of varying DyN content on the mass loss during sintering. From this plot it is seen that as the DyN content is increased, the less mass is lost during sintering. It is also seen in this plot that the sintering of pure UN resulted in the greatest mass loss. One possible explanation for this is that nitrogen gas is being evolved during the sintering process and causes the formation of a hypostoichiometric UN compound (UN_2 or U_2N_3). It can be concluded from these results that DyN is retained to temperatures less then 1700°C, which is expected.

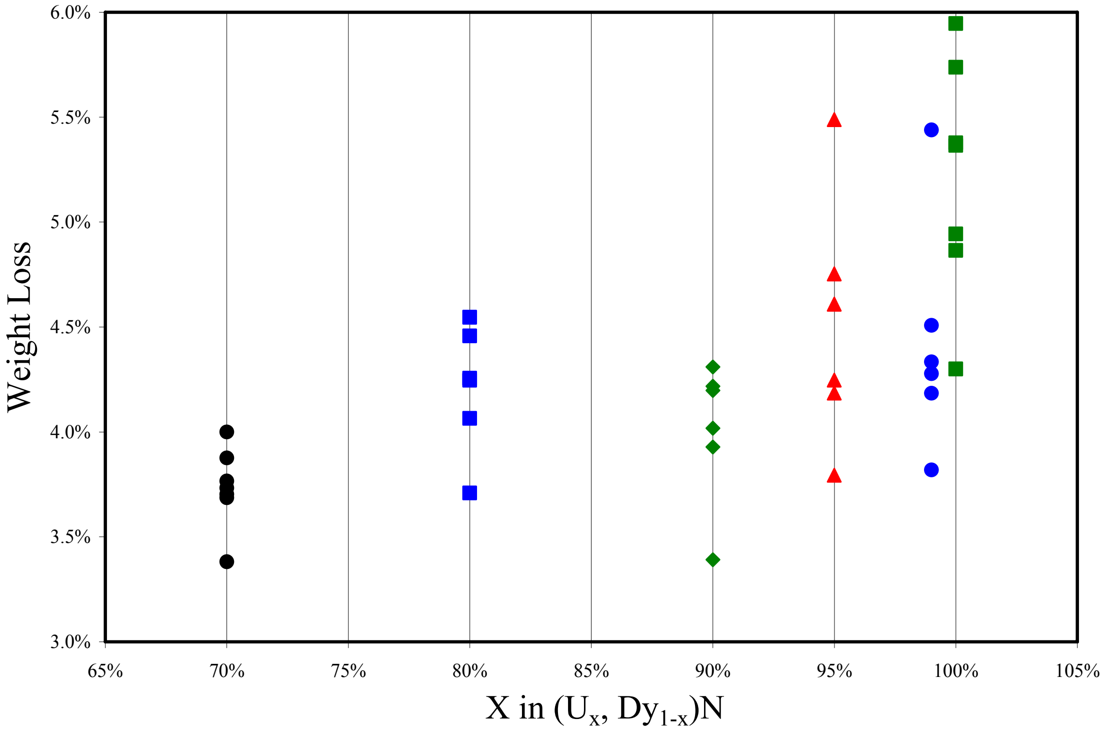

Figure 100: The effects of DyN content on the mass loss of (U, Dy)N pellets when sintered at temperatures ranging from 1450 to 1650°C for durations ranging from 10 to 40 hours.

Figure 101 shows the effects of sintering temperature, sintering time, and DyN content on the green and sintered densities of the (U, Dy)N pellets. The yellow region across the middle of the plot depicts the desired green density range. All of the pellets fell into the desired range. The blue dashed line at 85%TD represents the target sintered density for nuclear fuel applications. Although only a number of the pellets reached the desired density range, it is fairly remarkable that any of the pellets reached the desired density due the fact that the studies were completed at such low sintering temperatures.

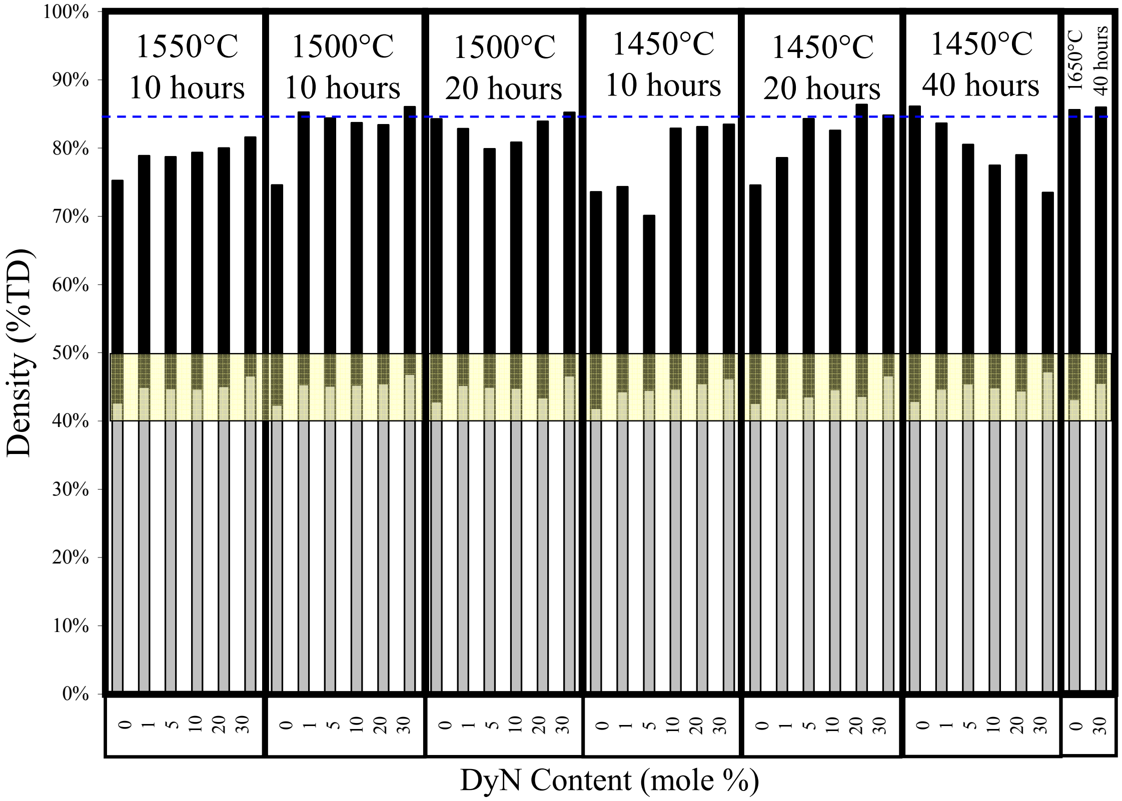

Figure 101: The effects of DyN content, sintering time, and sintering temperature on the green and final densities of (U, Dy)N pellets. The green density is the gray shaded region of the column plot and the densification is shown in black.

CHAPTER VI: OXIDATION STUDY OF DYSPROSIUM MONONITRIDE

One of the main concerns when working with nitride fuels is the propensity for oxidation during handling, synthesis, and sintering. It is critical to understand the oxidation of DyN to better understand the conditions that cause oxide formation and to optimize these handling, sintering, and synthesis conditions. After a detailed literature review, there have been no reported studies regarding the oxidation properties of DyN. The work reported here is intended to establish a knowledge database to better understand of the oxidation behavior of DyN. The data gained will be used to identify a rate law that most accurately describes the kinetics of oxidation. This rate law will then be used to identify the rate controlling mechanism (and therefore the reaction rate constants), the activation energy for oxidation, and the effects of oxygen partial pressure.

1. Characterization of the DyN Powder used for the Oxidation Studies

The starting material for this sintering study is phase pure DyN produced via the hydride prior to nitridation synthesis route of dysprosium metal, as presented in great detail in Chapter IV, Section 2. After synthesis, the sample was milled in the planetary ball mill for 20 minutes with YTZ milling media to obtain a homogeneous particle size distribution.

To properly assess the kinetics of oxidation, the specific surface area and particle size needs to be accurately characterized. Therefore, optical micrographs were obtained to gain insight to the size and morphology of the powder. Valuable data was difficult to obtain from interpretation of the optical micrographs because the particles are very densely packed. The images obtained (Figure 102) are at 50X magnification in reflective mode and 20X in transmission mode, respectively. The dark spots are the particles. As a general observation, the particles appear to be spherical.

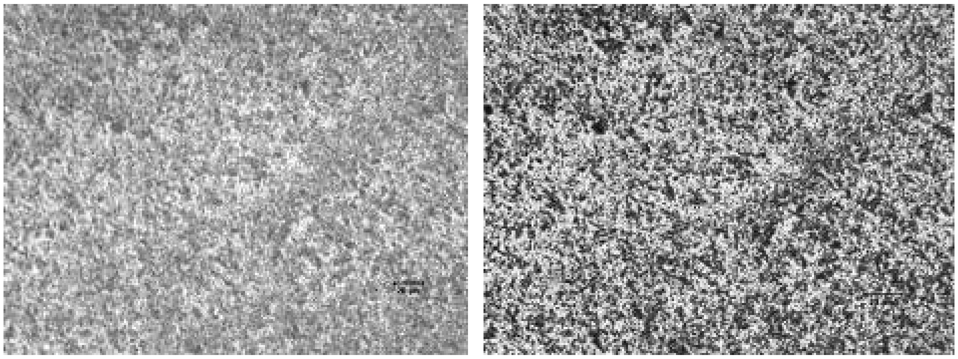

a) b)

Figure 102: Optical micrographs of the DyN powder prior to BET surface area analysis at a) 50X magnification in reflective mode and b) 20X in transmission mode.

To gain further insight to the particle morphology, the particles were also imaged using electron microscopy, more specifically, scanning electron microscopy (SEM). The resulting images (shown in Figure 103) indicate that the particles are larger agglomerates composed of very small, spherical particles.

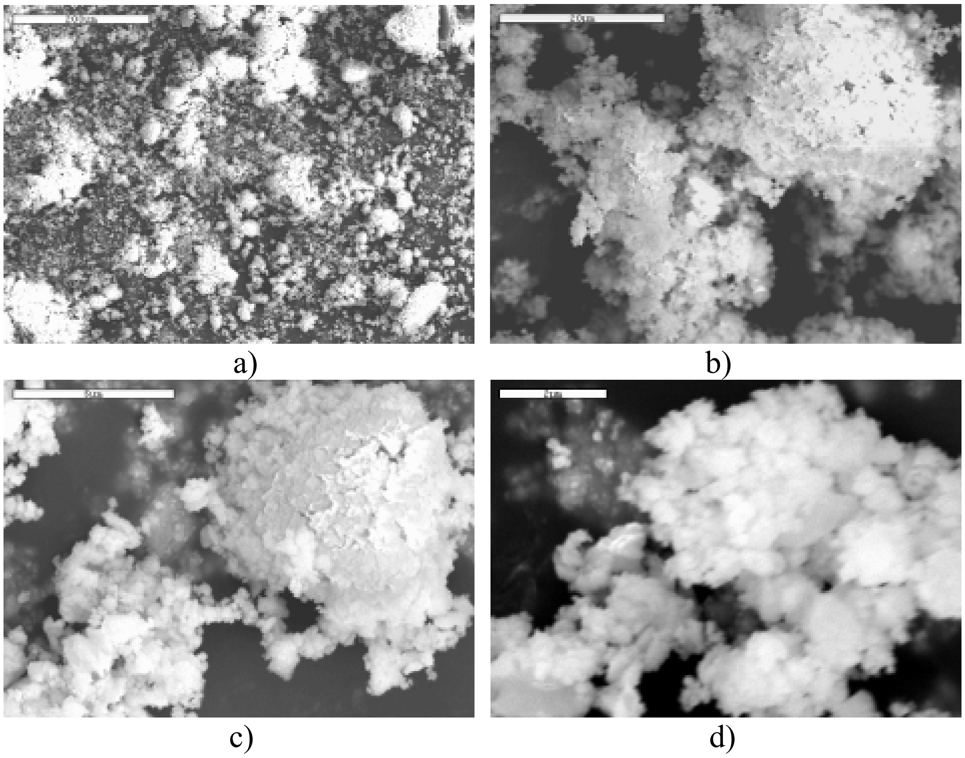

a) b)

c) d)

Figure 103: SEM images of the DyN powder used in the oxidation studies. The SEM images are at a) 500 X (200 µm scale bar), b) 1 kX (20 µm scale bar), c) 10 kX (5 µm scale bar), d) 20 kX (2 µm scale bar).

2. Experimental Procedures for the Oxidation of DyN

As previously stated, the starting material for this oxidiation study is phase pure DyN produced via the hydride prior to nitridation synthesis route of dysprosium metal. After synthesis, the sample was milled in the planetary ball mill for 20 minutes with YTZ milling media to obtain a homogeneous particle size distribution. The DyN powder was then analyzed for specific particle size and surface area using a Brunauer – Emmett –Teller (BET) technique at the UF. All analyses were performed with caution against moisture and oxygen by retaining the sample in an argon atmosphere glove box until such a time it was possible to perform the analyses. These experiments were conducted at the Particle Engineering Research Center with technical guidance from Mr. Gill Brubaker at the UF.

The TGA work presented in this report was performed using the TA Instruments SDT 2960 Simultaneous DSC/TGA, previously described in this report (Figure 9). To better understand the temperature range over which the oxidation of DyN occurs with the given particle size, the first step was a non-isothermal gravitational analysis study from room temperature to 800°C. The experiment was run with approximately 42.0 mg of the high purity DyN powder. The sample was ramped to 800°C at $1^{\circ C}/_{min}$ in a certified N_2 – 20.00% O_2 atmosphere. To better understand this phenomenon and to properly identify the governing rate laws, isothermal DSC/TGA experiments were performed at 200°C, 250°C, 300°C, 325°C, 350°C, 375°C, 400°C, 450°C, 500°C, and 600°C. It should be noted that all of the runs above 350°C have been duplicated to validate the results, which show good agreement. The isothermal TGA experiments were each run individually causing the mass of each run to be slightly different. Table 10 shows the initial mass of DyN at the corresponding isothermal temperature.

Table 11: Isothermal oxidation temperatures and the corresponding initial DyN masses used for the isothermal oxidation data of DyN powder synthesize via a hydride prior to nitridation synthesis route.

Temperature (°C)	**Initial DyN Mass (mg)**
200	**48.34**
250	**42.56**
300	**42.22**
325	**46.55**
350	**39.75**
375	**46.07**
400	**40.37**
450	**44.86**
500	**48.89**
600	**45.04**

For each isothermal run, it took approximately 5 minutes for the system to reach the desired temperatures and equilibrate. In this initial time, the system was purged with a high purity argon gas that was gettered for oxygen. Once the system was in thermal equilibrium, the gas was switched to a certified N_2 – 20.00% O_2 and the reaction was monitored for 6 hours.

Using the data that was collected from the isothermal oxidation studies and the BET analysis of the DyN powder, efforts were put forth in identifying a suitable rate law that most accurately describes the kinetics of oxidation. The isothermal experiment at 450°C was arbitrarily selected to fit different oxidation models to. In fact, 26 different models have been selected to fit against the acquired data, including; diffusion controlled, Avrami-Erofeev, zero order, first order, second order, geometric, power law, autocatalysis, as well as many others.

3. Results of the Oxidation of DyN

The results of the Autosorb instrument display a specific surface area of 0.0653 m^2/g that corresponds to a bimodal particle size distribution, as seen in Figure 104. The mean particle size of the 0.1 – 300 μm particle size distribution was found to be approximately 2.0 μm, as displayed in Table 12.

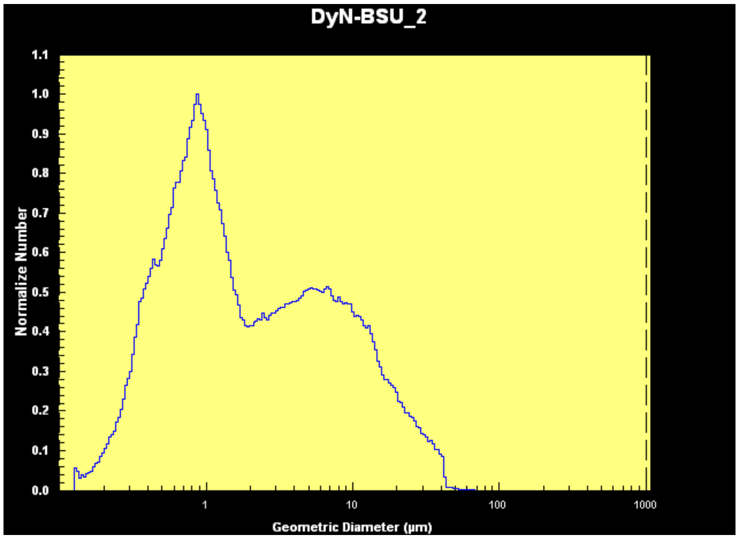

Figure 104: Particle size distribution plot of DyN powder obtained using a BET surface analysis technique.

Table 12: Particle size distribution statistics of the DyN powder used for oxidation studies. This data was obtained using a BET surface analysis technique.

Geometric Mean	1.99 µm
Geometric Standard Deviation	3.69
Mode (linear scale)	0.851 µm
D(4,3)	28.4 µm
D(3,2)	22.7 µm
Specific Surface Area	6.53e-02 m²/g
Size Range	0.100 - 100 µm

From the non-isothermal TGA plot in Figure 105, it is seen that the active oxidation region occurs from approximately 150°C to 400°C. The TGA results of this non-isothermal run show a weight gain of approximately 6% between the temperatures of 200°C and 500°C. Also, as observed using the DSC results, an exothermic reaction occurs at approximately 375°C. Therefore, the conditions for the succeeding experiments were set as isothermal TGA experiments at 200°C, 250°C, 300°C, 325°C, 350°C, 375°C, 400°C, 450°C, 500°C, and 600°C. The resulting isothermal oxidation experiments are shown in Figure 106.

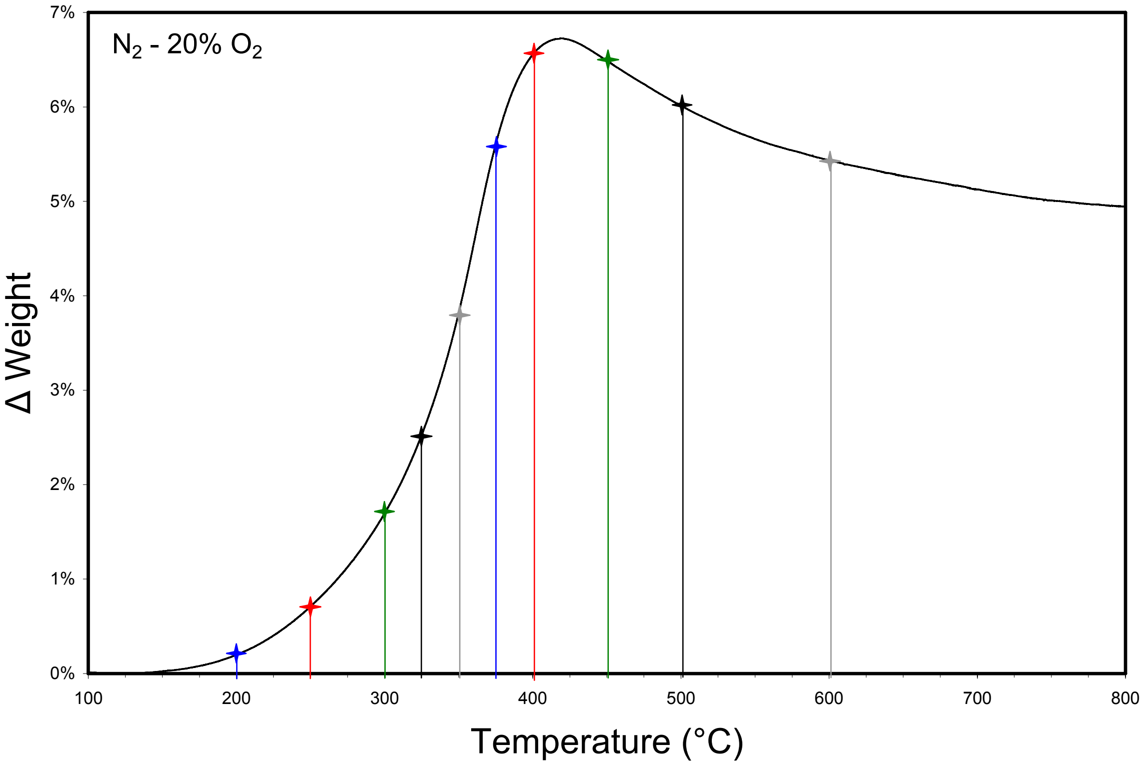

Figure 105: Thermal Gravitational Analysis of the oxidation of high purity DyN powder. The DyN powder was ramped to 800°C at $1^{\circ C}/_{\min}$ in ultra high purity $N_2 - 20\% \ O_2$ reactant gas. The vertical lines on the graph indicate the temperatures at which isothermal analysis was performed in the succeeding section.

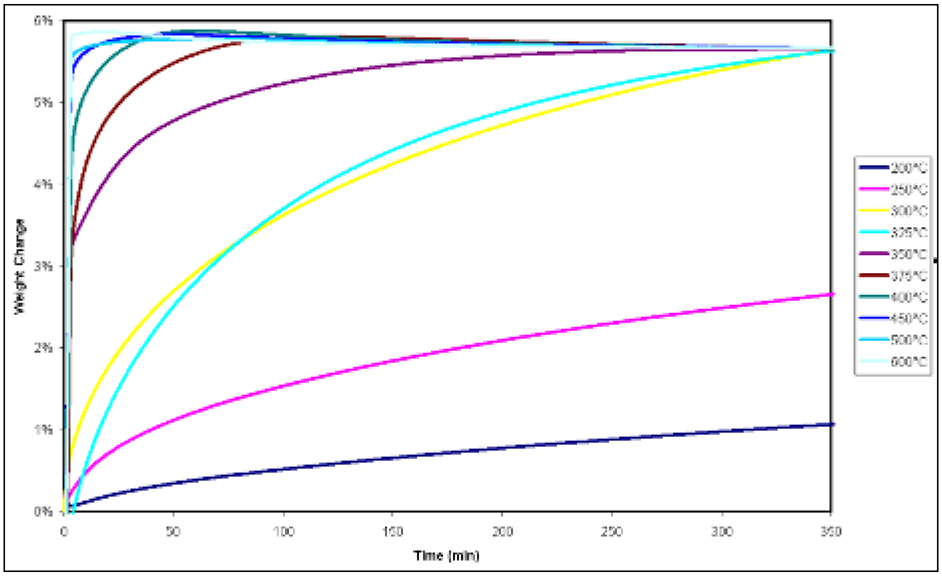

a)

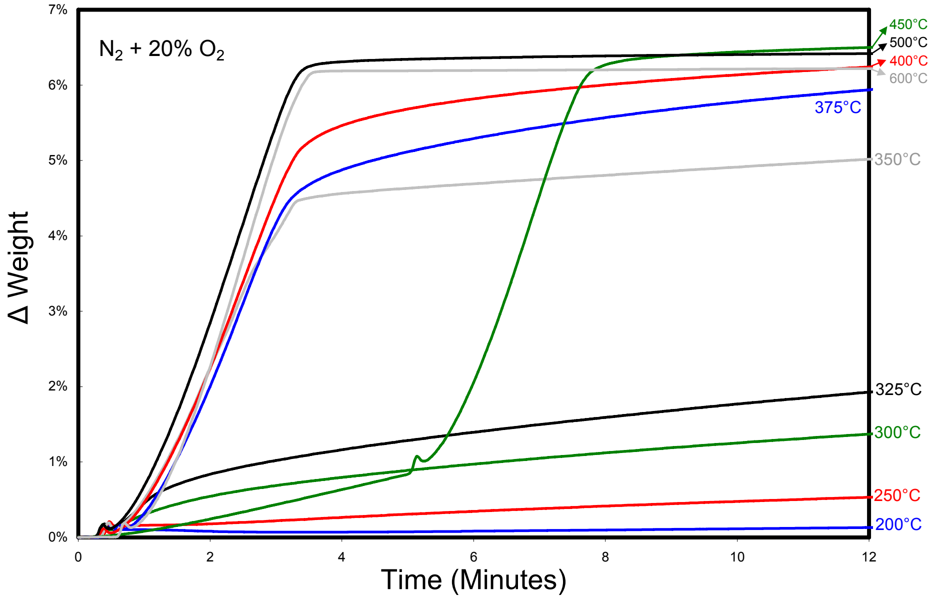

b)

Figure 106: Isothermal TGA measurements of the oxidation of high purity DyN powder a) for the entire 6 hours of oxidation, and b) for the first 12 minutes of oxidation to show the initial linear trend. The oxidation was completed in a N_2 + 20% O_2 process atmosphere and shows a convergence at approximately a 5.66% weight change. The DyN powder was ramped to the respective temperatures in ultra high purity oxygen-gettered argon in approximately 5 minutes prior to introducing the N_2 + 20% O_2 reactant gas flow, where the samples were reacted for 6 hours.

The isothermal experiment at 450°C was arbitrarily selected to fit different oxidation models to. As previously stated, 26 different models have been selected to fit against the acquired data. Initially, the reaction appears to be autocatalytic with most of weight change occurring within the first three minutes of the reaction and by fitting the autocatalytic model to the data it is shown that it fits fairly well. The autocatalytic model has an r^2 value of 0.9497, but three other models fit it better, as seen in Figure 107. The geometric-interface model fits with a r^2 value of 0.9741, the half-power law fits with an r^2 value of 0.9745, and the best fitting model is zero order model with an r^2 value of 0.9979.

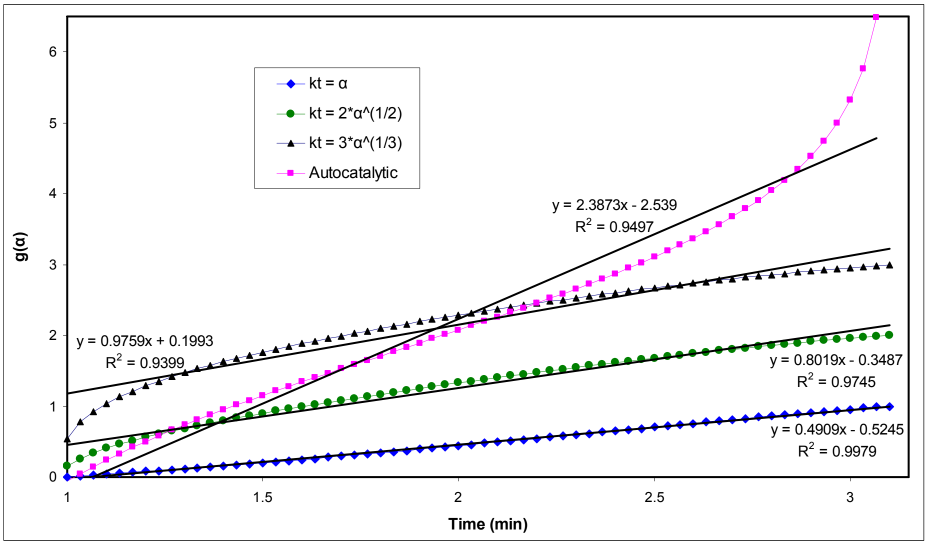

Figure 107: Plot showing the data obtained from DyN oxidation studies fit using well-understood oxidation models. The models fit here are the zero order, the half-power law, the geometric-interface model, and the autocatalytic model.

CHAPTER VII: ECONOMIC ANALYSIS

This section of the report is to compare the cost of synthesizing actinide nitrides using the traditional carbothermic reduction of the oxides (presented in Chapter IV, Sections 1.1, 2.1, and 3.1 for UN, DyN, and CeN respectively) and the novel reactive milling technique (presented in Chapter IV, Sections 1.3, 2.4, and 3.3 for UN, DyN, and CeN, respectively). Although it is known that an actual fuel processing plant would likely use a continuous process, the associated costs for this analysis are based on batch processing techniques for nitride fuel developments experienced in the Advanced Materials Laboratory at Boise State University. It should be noted that although the batch processing technique is different than what would likely be used in full-scale nuclear fuel processing facility, the cost analysis can be scaled to represent any processing scale.

When analyzing a process on the order of a full-scale nuclear fuel processing facility, a few assumptions need to be clear to ensure that the estimations can accurately represent the actual processing costs. For instance, an assumption to this analysis is that the maximum size batch that can be made with the equipment prices listed in Figures 108, 109, and 110 will produce enough material for 100 fuel pellets (which equates to approximately 150 grams of nitride powders) with dimensions of 0.25 inch diameter and a 0.25 inch height. It is assumed that each synthesis and sintering process yields approximately 95% powder to form sintered pellets. However, given the stringent tolerances that must be maintained for the pellets to bond together and fit properly inside the fuel cladding, it is assumed that only approximately 80% of the pellets are suitable for fuel pin development. The remaining 20% can be crushed, milled, and re-sintered, but that is also not accounted for in this analysis. It is also assumed that 50,000 individual fuel pellets are required for a 100 kWe thermo-electric fuel core (such as that used in the SP-100 project [14]). Therefore, each batch would need to be repeated 650 times (including the 70% yield rate). One can image how a few minuscule costs can be magnified when looked at on a larger scale.

Further assumptions made to ensure an accurate analysis include:

- The analysis of the batch processing is indicative of the cost of a continuous process.
- The cost of the starting materials is the same, the difference being how they are obtained (i.e. Pyro-chemical vs. electrochemical, or metal vs. oxide)
- Each batch will produce 100 fuel pellets with 0.25 inch diameter by 0.25 inch height (~150 grams of nitride powder).
- Each of the synthesis processes yield approximately 95% powder.
- The final sintered product yield is 80%.
- 50,000 quality fuel pellets are required for a 100 kWe thermo-electric fuel core.
- Costs of maintenance and replacement parts have been neglected.
- The installation costs of all facilities have been neglected.
- The infrastructure for nuclear materials handling is neglected.
- The cost per square foot of active processing space is estimated at \$500/ft^2/year.
- The amount (and cost) of processing waste production is considered as an invariant.

- The man-power required to operate each process is considered an invariant with the exception that the thermal routes require one extra engineer with an assumed salary of $100,000 annually.
- A compressed gas cylinder (50 L at 16 MPa) containing $^{15}N_2$ costs approximately $1200.

The associated cost of batch processing the fuels using a carbothermic reduction synthesis route and a novel reactive ball milling route are seen in Figures 108, 109, and110. Due to the fact that the pressing and sintering of the nitride materials will be the same regardless of how the nitrides are synthesized, the steps, time, equipment required, and the cost of the equipment for the pressing and sintering of the nitride materials is assumed to be invariant. Figure 108 shows the process flow steps required to synthesize a nitride starting with metal oxide and carbon powders (similar to what is obtained from a chemical separation technique). The time, required equipment, and approximate equipment costs of each associated process step is also listed. From this process chart, it would take approximately 55 hours per batch and a capital equipment cost of approximately $111,500 (neglecting the invariants between the different processing techniques). Figure 109 shows the process flow starting with metal flakes (similar to what is obtained from a pyroprocessing separation technique). From this process chart, it would take approximately 27 hours per batch and a capital equipment cost of approximately $43,700 (neglecting the invariants between the different processing techniques). Figure 110 is similar to Figure 109 except for the synthesis of uranium nitride at room temperature forms a sesquinitride (U_2N_3) which has to be heat treated in an argon – nitrogen mixed gas to form the mononitride, which requires an extra step with associated costs. As shown in Figure 110, it would take approximately 41 hours per batch and a capital equipment cost of approximately $79,900 (neglecting the invariants between the different processing techniques).

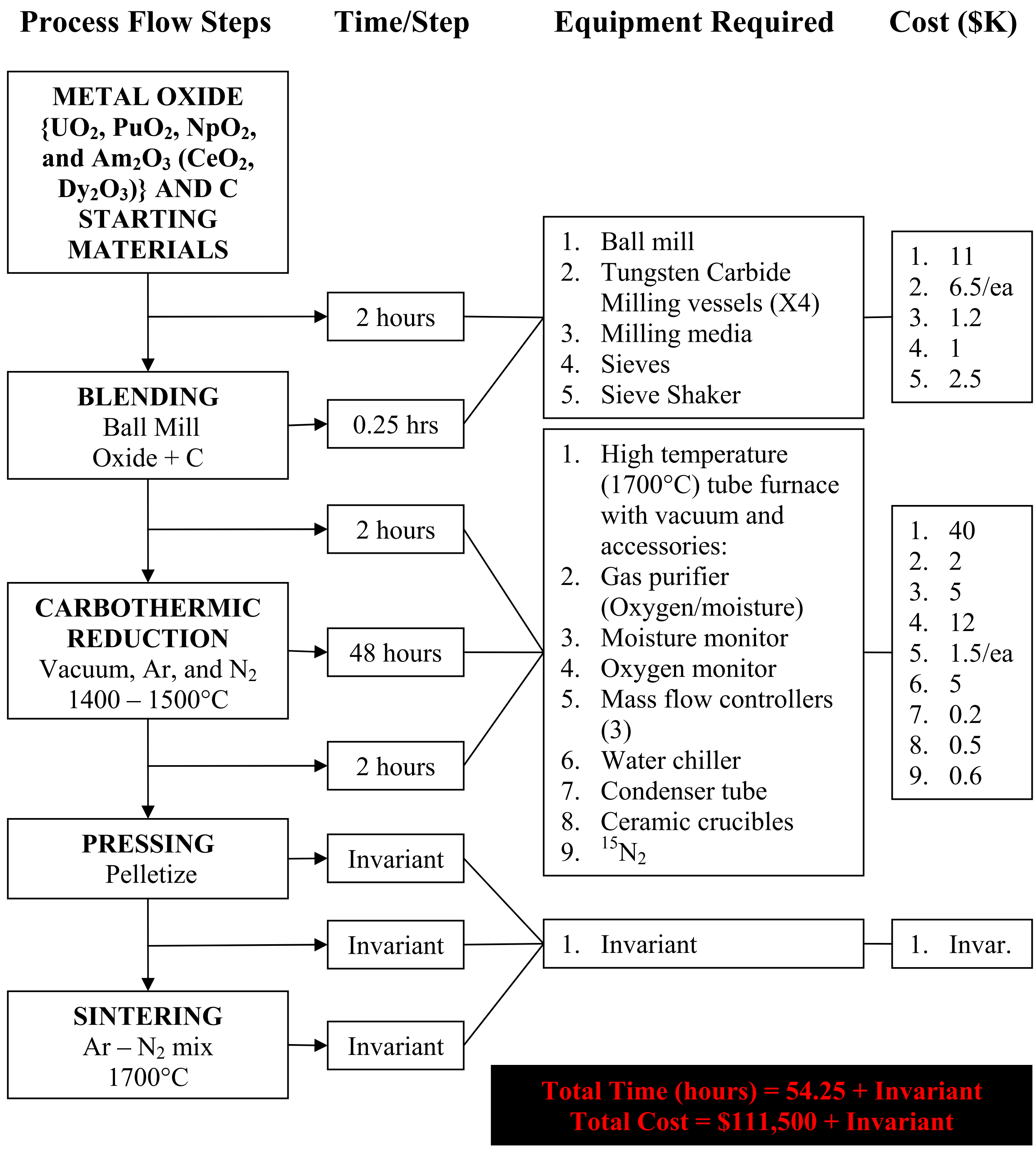

Figure 108: Process flow chart of the batch production of one hundred 0.25” diameter by 0.25” long nitride fuel pellets starting with metal oxide and carbon powders (similar to what is obtained from a chemical separation technique). The time, required equipment, and approximate capital equipment costs of each associated process step is also listed. From this process chart, it would take approximately 55 hours per batch and a capital equipment cost of approximately $111,500 (neglecting the invariants between the different processing techniques).

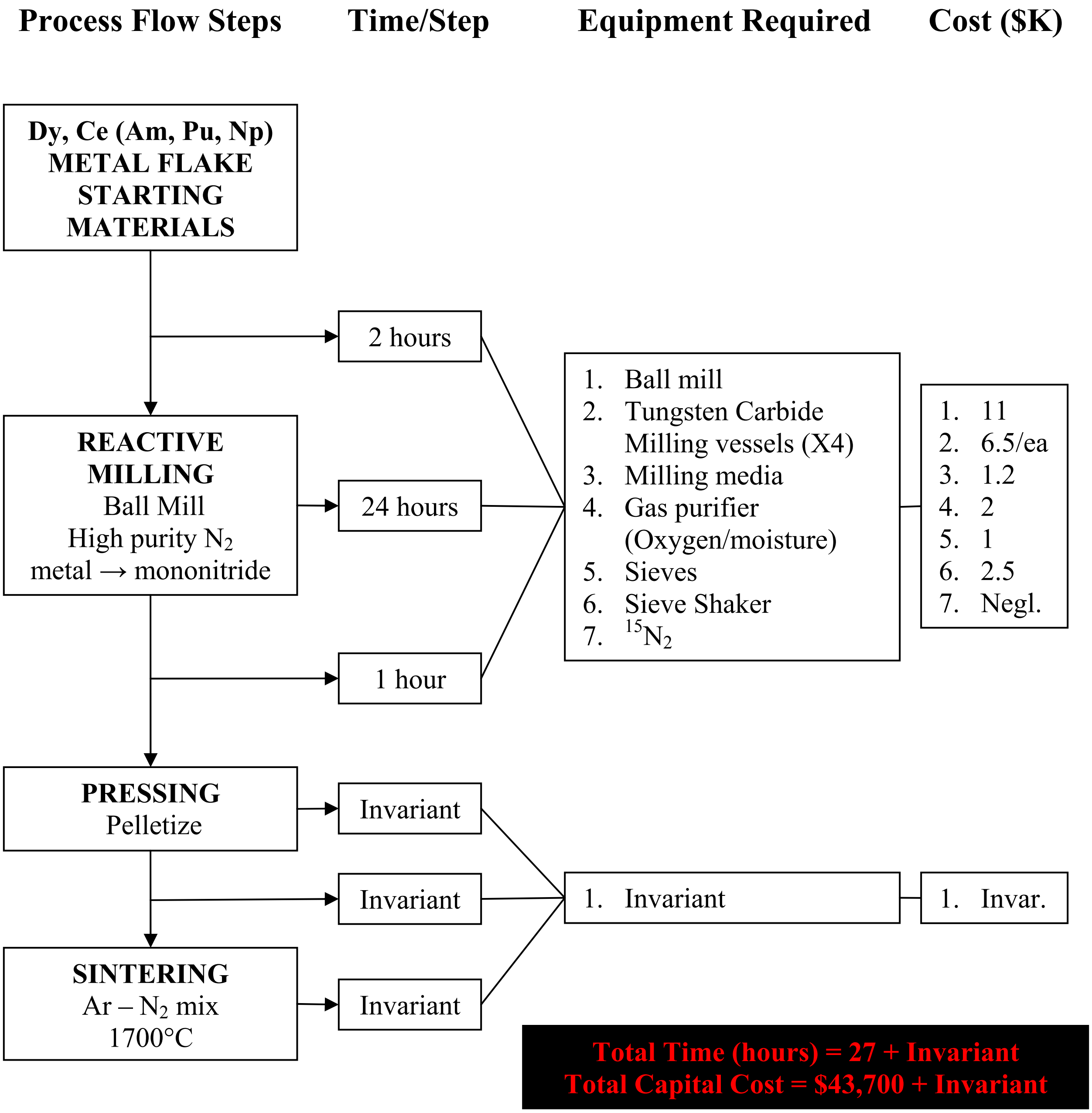

Figure 109: Process flow chart of the batch production of one hundred 0.25” diameter by 0.25” long nitride fuel pellets starting with metal flakes (similar to what is obtained from a pyroprocessing separation technique). The time, required equipment, and approximate capital equipment costs of each associated process step is also listed. From this process chart, it would take approximately 27 hours per batch and a capital equipment cost of approximately $43,700 (neglecting the invariants between the different processing techniques).

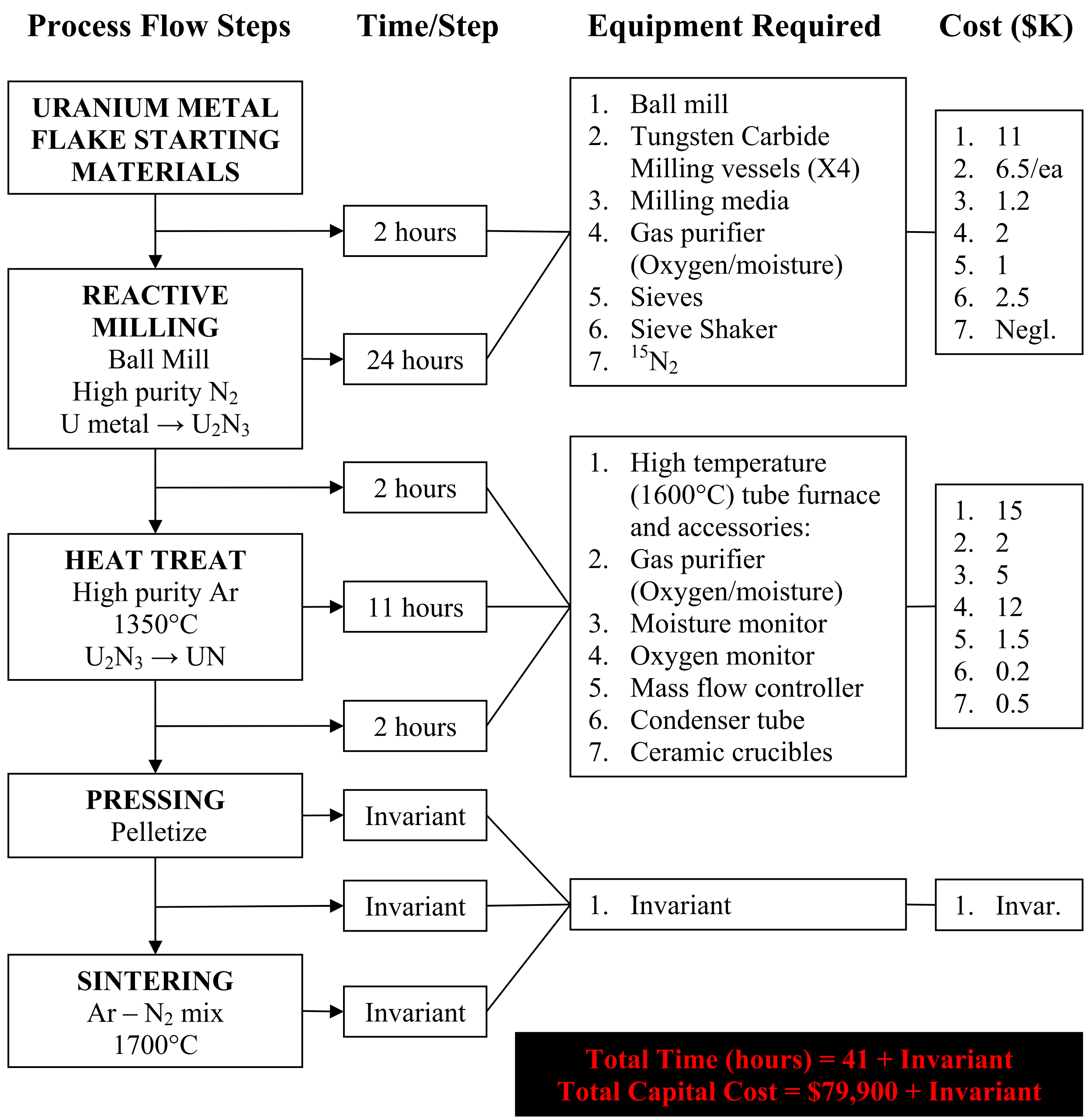

Figure 110: Process flow chart of the batch production of one hundred 0.25” diameter by 0.25” long nitride fuel pellets starting with metal flakes (similar to what is obtained from a pyroprocessing separation technique). The time, required equipment, and approximate capital equipment costs of each associated process step is also listed. From this process chart, it would take approximately 41 hours per batch and a capital equipment cost of approximately $79,900 (neglecting the invariants between the different processing techniques).

By putting this data into perspective in the production of a small, 100 kWe thermo-electric, fuel core (such as that used in the SP-100 project [14]) one can easily see a cost, time, and energy savings associated with the novel reactive milling technique. Table 13 shows the variables used for calculating the number of batches required to synthesize enough fuel for such a reactor. If 50,000 nuclear fuel pellets are required to make the core and each batch is capable of 100 fuel pellets, then it will require approximately 750 batches (by also taking in to account the powder processing and sintered pellet yields, as previously discussed).

Table 13: This table shows the variables used for calculating the number of batches required to synthesize the enough fuel for a 100 kWe (50,000 fuel pellets) thermo-electric fuel core (such as that used in the SP-100 project [14]).

Required fuel pellets	**50,000**
# of fuel pellets per batch	100
Powder yield	95%
Sintered pellet yield	70%
Total # of batches required	**752**

Table 14 shows the economic analysis between the three synthesis routes proposed in detail in Figures 108, 109, and 110. The thermal routes will required a bit more space in order to accommodate the extra furnace and furnace accessories. Using the reactive milling synthesis technique as a baseline footprint, the carbothermic reduction synthesis method will require approximately 300 square feet more active processing space and the extra furnace required for the sesquinitride reduction to mononitride (in the case of UN synthesis using the reactive milling technique Figure 110) will require approximately 200 square feet of extra space. Assuming that the extra space costs $500 per square foot per year to manage, this equates to an estimated $150,000 and $100,000 increased facility costs annually.

From Table 14, it is seen that using the traditional carbothermic reduction technique to produce 50,000 fuel pellets has the largest footprint, takes the longest time, and is the most expensive. Using the carbothermic technique at 100% capacity for 24 hours a day and 7 days a week, it would take approximately 245 days, or two-thirds of a year to produce the required 50,000 fuel pellets and would cost approximately $370,000 dollars more than the proposed reactive milling technique.

Table 14: This table is the economic analysis comparing a traditional carbothermic reduction synthesis route and a novel reactive milling technique in the synthesis of enough fuel for a 100 kWe (50,000 fuel pellets) thermo-electric fuel core (such as that used in the SP-100 project [14]).

	Carbothermic Reduction	**Reactive milling (with heat treat)**	**Reactive milling (without heat treat)**
Fuel Systems	UN, PuN, AmN, NpN	UN	PuN, AmN, NpN
Starting Materials	Metal oxide and carbon powders	Metal flake	Metal flake
Capital costs	$111,500	$79,900	$43,700
Batch time (hours)	54.25	41	27
Batches required		752	
Total time required (hours)	**40,789**	**30,827**	**20,301**
Engineers	4.00	3.00	2.00
Excess active processing space (ft^2)	300	200	0
Total Cost	**$611,279**	**$430,172**	**$243,700**
Total Cost per fuel pellet	**$12.23**	**$8.60**	**$4.87**

CHAPTER VIII: ACCOMPLISHMENTS

1. Project Details

All of the accomplishments are summarized as below. In order to perform this research, necessary laboratory infrastructure was developed; including basic facilities and experimental equipment. Notable accomplishments from this project include: the synthesis of uranium, dysprosium, and cerium nitrides using a novel, low-cost mechanical method at room temperature; the synthesis of phase pure UN, DyN, and CeN using thermal methods; and the sintering of UN and $(U_x, Dy_{1-x})N$ $(0.7 \leq X \leq 1)$ pellets from phase pure powder that was synthesized in the Advanced Materials Laboratory at Boise State University.

- Novel Ball-Milling Synthesis Route:
  This route was demonstrated by nitriding pure uranium, dysprosium, and cerium metal flakes at room temperature for 24 hours and less, yielding phase pure U_2N_3, DyN, and CeN, respectively.
- $(U_x, Dy_{1-x})N$ Pellet Sintering
  Pure UN was sintered using a traditional pressing and sintering technique in order to develop feasible procedures for sintering $(U_x, Dy_{1-x})N$ pellets. The sinterability of UN was studied by sintering 6.5 mm diameter pellets and varying multiple processing parameters including: milling time, binders, lubricants, compaction pressures, compositional range (0 – 30 mol% DyN), sintering atmosphere, sintering time, and sintering temperature.
- Direct Nitridation Synthesis Route:
  This route was demonstrated by nitriding 99.9% pure dysprosium metal flakes at 1300°C yielding a phase pure DyN powder with an oxygen content of 0.33%.
- Hydriding prior to Nitridation Synthesis Route:
  This route was demonstrated by the synthesis of UN, DyN, and CeN. Pure uranium metal ingot pieces produced UN and UO_2, suggesting that pure UN is feasible. Pure dysprosium and cerium metal flakes produced very high purity DyN and CeN with 0.043% and 1.4% oxygen contents, respectively.
- Carbothermic Reduction prior to Nitridation Synthesis Route
  This route was demonstrated by the synthesis of UN, DyN, and CeN. The carbothermic reduction of UO_2 has proven to provide the largest amount of phase pure UN for other related studies. Also, this route has been utilized to produce low quality DyN and CeN.
- Oxidation Kinetics of DyN
  Thermal gravitational analysis has been performed from room temperature to 800°C to identify a suitable oxidation range for isothermal studies. Multiple isothermal gravitational analysis runs have been made for 6 hours to describe the weight change of the DyN as it converts to Dy_2O_3. The data was then fit to a total of 26 oxidation kinetic models. Initially, the reaction appears to be autocatalytic with most of weight change occurring within the first three minutes of the reaction and by fitting the autocatalytic model to the data it is shown that it fits fairly well, with an r^2 value of 0.9497.

- Solution Routes Analogous to Sol-Gel Processing:
  These routes were attempted at the UF in the synthesis of DyN and CeN but resulted in limited success due to the extremely reactive nature of the nitride materials. This route shows promise for synthesizing pure nitrides and may also be used in the future as a synthesis route for UN.
- Sintering/Hot Pressing:
  The optimum conditions for sintering pure ZrN were determined and the maximum density achieved was approximately 83 % theoretical density. Therefore, hot-pressing was used to achieve higher densities. The results of the ZrN-DyN hot-pressing clearly show that DyN does not form a complete solid solution with ZrN.
- Economic Analysis:
  The novel reactive milling technique will require less infrastructure, smaller footprint, lower energy demands, less engineers/operators, and less cost. The reactive milling technique will cost an approximate 60% less than the carbothermic reduction synthesis route.

2. Publications and Presentations

"New Routes to Lanthanide and Actinide Nitrides." B.J. Jaques, D.D. Osterberg, B.M. Marx, A.S. Hamdy, P.G. Callahan, and D. P. Butt, Presented at the Global 2009: The Nuclear Fuel Cycle: Sustainable Options & Industrial Perspectives, Paris, France, September 6-11, 2009.

"The Synthesis of Uranium and Dysprosium Nitride Compounds at Low Temperatures using Reactive Ball Milling." B.J. Jaques, D.D. Osterberg, C.R. Smith, D.P. Butt. To be presented at the Materials Science and Technology 2009 Conference, Pittsburgh, PA. October 25-29, 2009.

"New Routes to Actinide and Lanthanide Nitrides." B.J. Jaques, D. P. Butt, To be presented at the 3rd International Meeting on Developments in Materials, Processes and Applications of Emerging Technologies, Manchester, United Kingdom, July 21-23, 2009. Invited.

"Synthesis of Dysprosium Nitride by Reactive Milling." C.R. Smith, B.J. Jaques, D.P. Butt, Presented at the 6th annual Boise State University Undergraduate Research Conference, Boise, ID, April 20, 2009.

"Co-Nitriding Uranium and Dysprosium Metals by Reactive Milling." D.D. Osterberg, B.J. Jaques, D.P. Butt, Presented at the 6th annual Boise State University Undergraduate Research Conference, Boise, ID, April 20, 2009.

[92] "Synthesis of Dysprosium and Cerium Nitrides by a Mechanically Induced Gas-Solid Reaction." P.G. Callahan, B.J. Jaques, B.M. Marx, A.S. Hamdy, D.D. Osterberg, and D.P. Butt, Journal of Nuclear Materials. In Print. April 2009.

"Synthesis of Dysprosium Nitride by Reactive Milling." C.R. Smith, B.J. Jaques, D.P. Butt, Presented at 138th annual TMS 2009 Conference, San Francisco, CA, February 15-19, 2009.

[91] “Synthesis of Uranium Nitride by a Mechanically Induced Gas-Solid Reaction.” B. J. Jaques, B.M. Marx, A.S. Hamdy, and D.P. Butt, Journal of Nuclear Materials. Vol. 381, (3) 2008, 309-311.

“The Synthesis and Sintering of Nitrides of Uranium and Dysprosium.” B. J. Jaques, Master's Thesis, Boise State University, Boise, ID. December 15, 2008.

“Synthesis and Sintering of UN, DyN, and (U_x, Dy_{1-x})N.” B. J. Jaques, Thesis defense presented to the Boise State University College of Engineering, Boise, ID. October 17, 2008.

“Synthesis of Uranium Nitride at Low Temperatures via Reactive Ball-Milling.” B.J. Jaques, M.F. Hurley, B.M. Marx, D.D. Osterberg, and D.P. Butt, Presented at the Materials Science and Technology 2008 Conference, Pittsburgh, PA, October 6-9, 2008.

“Fabrication of (U, Dy)N Pellets.” B. J. Jaques, D. P. Butt, Presented at the Materials Science and Technology 2008 Conference, Pittsburgh, PA, October 6-9, 2008.

“Synthesis and Sintering of Lanthanide and Actinide Nitrides,” B.J. Jaques, Presented to Boise State University College of Engineering, Boise, ID, March 7, 2008.

“Synthesis of Dysprosium and Cerium Nitrides by a Mechanically Induced Gas-Solid Reaction." P.G. Callahan, B.J. Jaques, B.M. Marx, A.S. Hamdy, D.D. Osterberg, D.P. Butt, Presented at the Materials Science and Technology 2007 Conference, Detroit, MI, September 16-20, 2007.

“Thermodynamics and Kinetics of Nitride Fuel Sintering and the effects of Americium and Dysprosium Nitride Additives.” B. J. Jaques, Presented at the GNEP Annual Review Meeting, Litchfield, AZ, October 2-4, 2007.

“Synthesis of Dysprosium Nitride via Direct Nitridation of Dysprosium Metal.” B.J. Jaques, D. P. Butt, Presented at the Materials Science and Technology 2007 Conference, Detroit, MI, September 16-20, 2007.

"Synthesis of Dysprosium and Cerium Nitrides by a Mechanically Induced Gas-Solid Reaction." P. G. Callahan, B. J. Jaques, B. M. Marx, A. S. Hamdy, D. D. Osterberg, D. P. Butt, Presented at the Materials Science and Technology 2007 Conference, Detroit, MI, September 16-20, 2007.

[132] “Synthesis and Characterization of Actinide Nitrides.” B.J. Jaques, D. P. Butt, Presented at the Global 2007: Advanced Nuclear Fuel Cycles and Systems, Boise, ID, September 9-13, 2007.

“Survey of Nitride Powder Synthesis Techniques.” B.J. Jaques, P.G. Callahan, B.M. Marx, D.D. Osterberg, A.S. Hamdy, G. Balfour, P. Perisamy, M.F. Hurley, and D.P. Butt, Presented at the Idaho University Consortia Academic Center for Excellence Workshop, Boise, ID, May 8, 2007.

“Synthesis and Characterization of Nitride Powders for Use in Surrogate Comparison to Actinide Fuels.” B.J. Jaques, Presented to Boise State University College of Engineering, Boise, ID, February 2, 2007.

REFERENCES

[1] U.S.D.O.E., http://www.energy.gov/print/3150.htm, 2006.

[2] J. S. Choi, B. Ebbinghaus, and T. Meier, "Laboratory Directed Research and Development (LDRD) on Mono-Uranium Nitride Fuel Development for SSTAR and Space Applications," LLNL, U.C. Berkeley 2006.

[3] U.S.D.O.E., "Advanced Fuel Cycle Initiative," 2006.

[4] B. Dixon, "Systems Analysis-Advanced Fuel Cycle Initiative and Global Nuclear Energy Partnership," Washington D.C., 2006.

[5] S. T. Voit, K. J. McClellan, R. Margevicius, C. R. Stanek, and H. Hawkins, "The Design and Production of Actinide Nitride Fuels at the Los Alamos National Laboratory for the Advanced Fuel Cycle Initiative Program," Los Alamos National Laboratory 2006.

[6] M. Takano, A. Itoh, M. Akabori, and K. Minato, "Hydrolysis reactions of rare-earth and americium mononitrides," *Journal of Physics and Chemistry of Solids,* vol. 66, pp. 697-700, 2005.

[7] M. Beauvy, C. Dalmasso, and P. Iacconi, "Irradiation effects of swift heavy ions in actinide oxides and actinide nitrides: Structure and optical properties," *Nuclear Instruments and Methods in Physics Research, Section B: Beam Interactions with Materials and Atoms,* vol. 250, pp. 137-141, 2006.

[8] M. Takano, S. Tagami, K. Minato, T. Kozaki, and S. Sato, "Lattice thermal expansions of (Dy, Zr)N solid solutions," *Journal of Alloys and Compounds,* vol. 439, pp. 215-220, 2007.

[9] Y. Arai, "Fabrication of Actinide Mononitride Fuel," in *Proceedings of the workshop on manufacturing technology and process for reactor fuels*, Tokai, Japan, 1995, pp. 182-193.

[10] T. Nishi, M. Takano, A. Itoh, M. Akabori, K. Minato, and M. Kizaki, "Thermal diffusivity of Americium mononitride from 373 to 1473 K," *Journal of Nuclear Materials,* vol. 355, pp. 114-118, 2006.

[11] R. B. Matthews, K. M. Chidester, C. W. Hoth, R. E. Mason, and R. L. Petty, "Fabrication and testing of uranium nitride fuel for space power reactors," *Journal of Nuclear Materials,* vol. 151, p. 345, 1988.

[12] M. Streit and F. Ingold, "Nitrides as a nuclear fuel option," *Journal of the European Ceramic Society Elecroceramics IX,* vol. 25, pp. 2687-2692, 2005.

[13] Y. Arai and K. Minato, "Fabrication and electrochemical behavior of nitride fuel for future applications," *Journal of Nuclear Materials,* vol. 344, pp. 180-5, 2005.

[14] R. B. Matthews, R. E. Barrs, H. T. Blair, D. P. Butt, R. E. Mason, J. Stark, W.A., E. K. Storms, and S. Wallace, T. C., "Fuels for Space Nuclear Power and Propulsion: 1983-1993," in *A Critical Review of Space Nuclear Power and Propulsion 1984-1993*, M. S. El-Genk, Ed. New York: American Institute of Physics, 1994, pp. 179-220.

[15] T. Nakagawa, H. Matsuoka, M. Sawa, M. Hirota, M. Miyake, and M. Katsura, "Formation of uranium and cerium nitrides by the reaction of carbides with NH3 and N2/H2 stream," *Journal of Nuclear Materials,* vol. 247, p. 127, 1997.

[16] K. Minato, M. Akabori, M. Takano, Y. Arai, K. Nakajima, A. Itoh, and T. Ogawa, "Fabrication of nitride fuels for transmutation of minor actinides," Karlsruhe, Germany, 2003, pp. 18-24.

[17] N. H. Olschewski, J.-P. Glatz, H. Bokelund, and M. J.-F. Leroy, "Fate of nitrogen upon reprocessing of nitride fuels," *Journal of Nuclear Materials,* vol. 188, pp. 244-248, 1992.

[18] H. Matzke, E. Toscano, C. T. Walker, and A. G. Solomah, "Neptunium doping of the crystalline ceramic waste form synroc B," *Advanced Ceramic Materials,* vol. 3, pp. 285-8, 1988.

[19] M. Burghartz, H. Matzke, C. Leger, G. Vambenepe, and M. Rome, "Inert matrices for the transmutation of actinides: Fabrication, thermal properties and radiation stability of ceramic materials," *Journal of Alloys and Compounds,* vol. 271-273, pp. 544-548, 1998.

[20] H. Matzke, V. V. Rondinella, and T. Wiss, "Materials research on inert matrices: A screening study," *Journal of Nuclear Materials,* vol. 274, pp. 47-53, 1999.

[21] R. Ho Jin, L. Young Woo, C. Seung Il, and H. Soon Hyung, "Sintering behaviour and microstructures of carbides and nitrides for the inert matrix fuel by spark plasma sintering," *Journal of Nuclear Materials,* vol. 352, pp. 341-8, 2006.

[22] Y. W. Lee, S. C. Lee, H. S. Kim, C. Y. Joung, and C. Degueldre, "Study on the mechanical properties and thermal conductivity of silicon carbide-, zirconia- and magnesia aluminate-based simulated inert matrix nuclear fuel materials after cyclic thermal shock," Tokai, Japan, 2003, pp. 15-23.

[23] S. Voit, K. McClellan, and M. Stan, "Depleted uranium dioxide (dUO2) feedstock modification and characterization for mixed oxide fuel fabrication at the Los Alamos National Laboratory," Washington, DC, USA, 2004, pp. 492-3.

[24] C. Lopez, X. Deschanels, J. M. Bart, J. M. Boubals, C. Den Auwer, and E. Simoni, "Solubility of actinide surrogates in nuclear glasses," *Journal of Nuclear Materials,* vol. 312, pp. 76-80, 2003.

[25] H.-C. Yang, Y.-J. Cho, H.-C. Eun, J.-H. Yoo, and J.-H. Kim, "Molten salt oxidation of ion-exchange resins doped with toxic metals and radioactive metal surrogates," *Journal of Nuclear Science and Technology,* vol. 42, pp. 123-129, 2005.

[26] M. Ferrandon and T. Krause, "Role of the oxide support on the performance of Rh catalysts for the autothermal reforming of gasoline and gasoline surrogates to hydrogen," *Applied Catalysis A: General,* vol. 311, pp. 135-145, 2006.

[27] Y. Park, D. G. Kolman, H. Ziraffe, C. Haertling, and D. P. Butt, "Gallium removal from weapons-grade plutonium and cerium oxide surrogate by a thermal technique," *Materials Research Society Symposium - Proceedings,* vol. 556, pp. 129-134, 1999.

[28] Y. S. Park, T. N. Taylor, A. Atencio, and D. P. Butt, "Kinetics of and Atmospheric Effects on Gallium Removal from CeO_2 Based Mixed Oxide Surrogate," *Ceramic Trans.,* vol. 93, pp. 69-78, 1999.

[29] T. Advocat, F. Jorion, T. Marcillat, G. Leturcq, X. Deschanels, J. M. Boubals, L. Bojat, P. Nivet, and S. Peuget, "Fabrication of $^{239/238}$Pu-zirconolite ceramic pellets by natural sintering," in *Scientific Basis for Nuclear Waste Management XXVII* Kalmar, Sweden: Materials Research Society, 2004, pp. 267-272.

[30] M. S. S. Brooks, O. Eriksson, and B. Johansson, "From the transition metals to the rare earths-via the actinides," *Journal of Alloys and Compounds,* vol. 223, pp. 204-210, 1995.

[31] D. G. Kolman, M. E. Griego, C. A. James, and D. P. Butt, "Thermally induced gallium removal from plutonium dioxide for MOX fuel production," *Journal of Nuclear Materials,* vol. 282, p. 245, 2000.

[32] J. R. Schoonover, A. Saab, J. S. Bridgewater, G. J. Havrilla, C. T. Zugates, and P. J. Treado, "Raman/SEM chemical imaging of a residual gallium phase in a mixed oxide feed surrogate," *Applied Spectroscopy,* vol. 54, pp. 1362-1371, 2000.

[33] P. A. Lessing and T. A. Hyde, "MOX fuel fabrication for the AFCI program," *Transactions of the American Nuclear Society,* vol. 94, pp. 838-9, 2006.

[34] S. V. Yudintsev, T. S. Ioudintseva, A. V. Mokhov, B. S. Nikonov, E. E. Konovalov, S. A. Perevalov, S. V. Stefanovsky, A. G. Ptashkin, M. Glagovsky, and A. V. Kouprine, "Study of pyrochlore and garnet-based matrices for actinide wastes produced by a self-propagating high-temperature synthesis," Kalmar, Sweden, 2004, pp. 273-8.

[35] H. J. Ryu, Y. W. Lee, S. Cha, and S. H. Hong, "Sintering behaviour and microstructures of carbides and nitrides for the inert matrix fuel by spark plasma sintering," *Journal of Nuclear Materials,* vol. 352, pp. 341-8, 2006.

[36] T. C. Carter, T. W. Knight, and S. Anghaie, "Feasibility of mixed carbide fuels for use in transmutation systems," San Diego, CA, United States, 2003, pp. 124-127.

[37] M. A. Molecke, M. W. Gregson, K. B. Sorenson, M. C. Billone, H. Tsai, W. Koch, O. Nolte, G. Pretzsch, F. Lange, B. Autrusson, O. Loiseau, N. S. Thompson, R. S. Hibbs, F. I. Young, and T. Mo, "Initiation of depleted uranium oxide and spent fuel testing for the spent fuel sabotage aerosol ratio programme," *International Journal of Radioactive Materials Transport,* vol. 15, pp. 131-9, 2004.

[38] T. C. Carter, T. W. Knight, and S. Anghaie, "Development of mixed carbide fuels in support of the AFCI program," Washington, DC, USA, 2004, pp. 501-2.

[39] B. B. Spencer, G. D. D. Cul, and E. D. Collins, "Processing of spent TRISO-coated Gen IV reactor fuels: mechanical head-end processing," *Transactions of the American Nuclear Society,* vol. 92, pp. 319-20, 2005.

[40] J. W. Adams, R. E. Barletta, P. E. Vanier, M. B. Dowell, and J. W. Lennartz, "Preparation, characterization and performance of CVR coatings for PBR fuels," Albuquerque, NM, USA, 1994, pp. 245-51.

[41] S. M. Frank, T. L. Barber, T. DiSanto, K. M. Goff, S. G. Johnson, J. F. Jue, M. Noy, T. P. O'Holleran, and W. Sinkler, "Alpha-decay radiation damage study of a glass-bonded sodalite ceramic waste form," Boston, MA, USA, 2002, pp. 487-94.

[42] T. Arima, K. Idemitsu, K. Yamahira, S. Torikai, and Y. Inagaki, "Application of internal gelation to sol-gel synthesis of ceria-doped zirconia microspheres as nuclear fuel analogous materials," *Journal of Alloys and Compounds,* vol. 394, pp. 271-276, 2005.

[43] "AAA Quarterly Report: Multi-Tier Fuel Cycle Approach to Nuclear Waste Management," 2002.

[44] C. Donohoue, M. Reigel, D. Burkes, J. Moore, and J. R. Kennedy, "Nitride Nuclear Fuel Production Using Combustion Synthesis," *Transactions of the American Nuclear Society,* vol. 96, pp. 695-696, 2007.

[45] T. Ogawa, "Private Conversation," 2006.

[46] M. Takano, A. Itoh, M. Akabori, K. Minato, and M. Numata, "Study on the stability of AmN and (Am,Zr)N," in *Global 2003: Atoms for Prosperity: Updating Eisenhower's Global Vision for Nuclear Energy* New Orleans, LA, United States, 2003, pp. 2285-2291.

[47] M. Takano, A. Itoh, M. Akabori, and T. Ogawa, "Oxygen solubility in dysprosium mononitride prepared by carbothermic synthesis," *Journal of Alloys and Compounds,* vol. 327, p. 235, 2001.

[48] K. Wheeler, P. Peralta, M. Parra, K. McClellan, J. Dunwoody, and G. Egeland, "Effect of sintering conditions on the microstructure and mechanical properties of ZrN as a surrogate for actinide nitride fuels," *Journal of Nuclear Materials,* vol. 366, pp. 306-316, 2007.

[49] Y. S. Park, D. G. Kolman, H. Ziraffe, C. L. Haertling, and D. P. Butt, "Gallium Removal from Weapons-Grade Plutonium and Cerium Oxide Surrogate by Thermal Technique," in *Mater. Res. Soc. Symp. Proceedings*, 1999, pp. 129-234.

[50] M. Stan, T. J. Armstrong, D. P. Butt, T. C. Wallace, Y. S. Park, C. L. Haertling, T. Hartmann, and R. J. Hanrahan, "Stability of the Perovskite Compounds in Ce-Ga-O and Pu-Ga-O Systems," *J. Am. Ceram. Soc.,* vol. 85, pp. 2811-16, 2002.

[51] U.S.D.O.E., "The U.S. Generation IV Fast Reactor Strategy," U.S. Department of Energy Office of Nuclear Energy 2006.

[52] U.S.D.O.E., "A Technology Roadmap for Generation IV Nuclear Energy Systems," U.S. Department of Energy Research Advisory Committee 2002.

[53] R. B. Matthews, "Overview of SP-100 fuel development activities," in *Proceedings of the Seventh Symposium on Space Nuclear Power Systems (CONF-900109).* vol. 2 Albuquerque, NM, USA: University of New Mexico, 1990, pp. 883-888.

[54] R. B. Matthews, "Overview of space reactor fuel development activities," *Transactions of the American Nuclear Society,* vol. 64, pp. 266-267, 1991.

[55] R. B. Matthews, "Ceramic Fuel Development for Space Reactors," *American Ceramic Society Bulletin,* vol. 51, pp. 96-101, 1992.

[56] H. Matzke, *Science of Advanced LMFBR Fuels*. Amsterdam, The Netherlands: Elsevier Science Publishing Company, Inc., 1986.

[57] A. A. Bauer, "Nitride Fuels: Properties and Potentials," *Reactor Technology,* vol. 15, pp. 87-104, 1972.

[58] A. M. Itoh A., Takano M., Ogawa T., Numata M., Itonaga F., "Fabrication of Americium-Based Nitrides by Carbothermic Reduction Method," *Journal of Nuclear Science and Technology,* vol. Suppl. 3, pp. 737-740, 2002.

[59] T. Muromura and H. Tagawa, "Formation of uranium mononitride by the reaction of uranium dioxide with carbon in ammonia and a mixture of hydrogen and nitrogen-- I synthesis of high purity UN," *Journal of Nuclear Materials,* vol. 71, p. 65, 1977.

[60] J. M. Cleveland, G. H. Bryan, C. R. Heiple, and R. J. Sironen, "A new, low-temperature synthesis of plutonium and uranium nitrides," *Nuclear Technology,* vol. 25, pp. 541-5, 1975.

[61] N. Oi, S. Hirayama, I. Tanabe, A. Muramatsu, and T. Kawada, "Preparation of high density uranium nitride and uranium carbonitride fuel pellets," *Journal of Nuclear Science and Technology,* vol. 9, pp. 521-7, 1972.

[62] M. Paljevic and Z. Despotovic, "Oxidation of Uranium Nitride," *Journal of Nuclear Materials,* vol. 57, pp. 253-257, 1975.

[63] B. D. Rogozkin, N. M. Stepennova, G. A. Bergman, and A. A. Proshkin, "Thermochemical stability, radiation testing, fabrication, and reprocessing of mononitride fuel," *Atomic Energy,* vol. 95, pp. 835-844, 2003.

[64] F. Delvoye, J. Larroque, and M. Beauvy, "Synthesis of (U,Pu) Nitrides from the Elements," *Journal of the Less-Common Metals,* vol. 121, pp. 656-657, 1985.

[65] J. T. Dunwoody, Stanek, C.R. , McClellan, K.J., Voit, S.L., Volz H.M., and Hickman, H.M., "Synthesis of uranium nitride and uranium carbide powder by carbothermic reduction," in *Global 2007* Boise, ID, 2007, pp. 586-590.

[66] F. Anselin, "Etude des Nitrures D'Uranium, de Plutonium et de Leurs Solutions Solides," *Journal of Nuclear Materials,* vol. 10, pp. 301-320, 1963.

[67] Y. Arai, S. Fukushima, K. Shiozawa, and M. Handa, "Fabrication of (U, Pu)N Fuel Pellets," *Journal of Nuclear Materials,* vol. 168, pp. 280-289, 1989.

[68] H. Bernard, "Advanced Fuel Fabrication," *Journal of Nuclear Materials,* vol. 166, pp. 105-111, 1989.

[69] W. O. Greenhalgh, "Kinetic Measurements for the Carbothermic Synthesis of UN, PuN, and (U,Pu)N," *Journal of the American Ceramic Society,* vol. 56, pp. 553-557, 1973.

[70] G. Ledergerber, Z. Kopajtic, F. Ingold, and R. W. Stratton, "Preparation of uranium nitride in the form of microspheres," *Journal of Nuclear Materials,* vol. 188, pp. 28-35, 1992.

[71] J. R. McLaren and P. W. M. Atkinson, "The sintering of uranium mononitride," *Journal of Nuclear Materials,* vol. 17, pp. 142-148, 1965.

[72] S. K. Mukerjee, J. V. Dehadraya, V. N. Vaidya, and D. D. Sood, "Kinetics of the carbothermic synthesis of uranium mononitride microspheres," *Journal of Nuclear Materials,* vol. 185, pp. 39-49, 1991.

[73] T. Muromura and H. Tagawa, "Mechanism and kinetics for the formation of uranium mononitride by the reaction of uranium dioxide with carbon and nitrogen," *Journal of the American Ceramic Society,* vol. 61, pp. 30-5, 1978.

[74] T. Muromura and H. Tagawa, "Formation of uranium mononitride by the reaction of uranium dioxide with carbon in ammonia and a mixture of hydrogen and nitrogen. II. Reaction rates," *Journal of Nuclear Materials,* vol. 80, pp. 330-8, 1979.

[75] T. Muromura and H. Tagawa, "Synthesis of high purity uranium mononitride from oxide through carbide," *Journal of Nuclear Science and Technology,* vol. 17, pp. 57-66, 1980.

[76] T. Nakagawa, H. Matsuoka, M. Sawa, K. Idehara, and M. Katsura, "Preparation of lanthanide nitrides by carbothermic reduction using ammonia," *Journal of Nuclear Materials,* vol. 247, p. 147, 1997.

[77] T. Muromura and H. Tagaua, "Lattice parameter of uranium mononitride," *Journal of Nuclear Materials,* vol. 79, pp. 264-6, 1979.

[78] Y. Suzuki and Y. Arai, "Thermophysical and thermodynamic properties of actinide mononitrides and their solid solutions," *Journal of Alloys and Compounds,* vol. 271-273, pp. 577-582, 1998.

[79] Y. Chen, J. Fitz Gerald, J. S. Williams, and S. Bulcock, "Synthesis of boron nitride nanotubes at low temperatures using reactive ball milling," *Chemical Physics Letters,* vol. 299, p. 260, 1999.

[80] Y. Chen, T. Halstead, and J. S. Williams, "Influence of milling temperature and atmosphere on the synthesis of iron nitrides by ball milling," *Materials Science & Engineering A (Structural Materials: Properties, Microstructure and Processing),* vol. 206, pp. 24-9, 1996.

[81] M. S. El-Eskandarany and A. H. Ashour, "Mechanically induced gas-solid reaction for the synthesis of nanocrystalline ZrN powders and their subsequent consolidations," *Journal of Alloys and Compounds,* vol. 313, pp. 224-234, 2000/12/15 2000.

[82] F. J. Gotor, M. D. Alcala, C. Real, and J. M. Criado, "Combustion synthesis of TiN induced by high-energy ball milling of Ti under nitrogen atmosphere," *Journal of Materials Research,* vol. 17, pp. 1655-1663, 2002.

[83] M. Senna and K. Okamoto, "Rapid synthesis of Ti- and Zr-nitrides under tribochemical condition," Princeton, NJ, USA, 1989, pp. 453-60.

[84] C. Zhang, K. Komeya, J. Tatami, and T. Meguro, "Inhomogeneous grain growth and elongation of Dy-α sialon ceramics at temperatures above 1800°C," *Journal of the European Ceramic Society,* vol. 20, pp. 939-944, 2000.

[85] M. S. El-Eskandarany, "Solid state nitrization reaction of amorphous tantalum aluminium nitride alloy powders: the role of amorphization by reactive ball milling," *Journal of Alloys and Compounds,* vol. 203, pp. 117-126, 1994/1/4 1994.

[86] P. Millet and A. Calka, "Ball milling of soft metals: the formation of gallium nitride," *Materials Science Forum,* vol. 179-181, pp. 321-324, 1995.

[87] G. Mulas, L. Schiffini, G. Tanda, and G. Cocco, "Hydriding processes of Mg and Zr alloys by reactive milling," *Journal of Materials Science,* vol. 39, pp. 5251-5254, 2004.

[88] G. Mulas, L. Schiffini, G. Tanda, and G. Cocco, "Hydriding kinetics and process parameters in reactive milling," *Journal of Alloys and Compounds,* vol. 404-406, pp. 343-346, 2005.

[89] F. Zhang, W. A. Kaczmarek, L. Lu, and M. O. Lai, "Formation of Al-TiN metal matrix composite via mechanochemical route," *Scripta Materialia,* vol. 43, pp. 1097-1102, 2000.

[90] F. Zhang, W. A. Kaczmarek, L. Lu, and M. O. Lai, "Formation of titanium nitrides via wet reaction ball milling," *Journal of Alloys and Compounds,* vol. 307, pp. 249-253, 2000.

[91] B. J. Jaques, B. M. Marx, A. S. Hamdy, and D. P. Butt, "Synthesis of Uranium Nitride by a Mechanically Induced Gas-Solid Reaction," *Journal of Nuclear Materials,* vol. 381, pp. 309-311, 2008.

[92] P. Callahan, B. J. Jaques, B. M. Marx, A. S. Hamdy, and D. P. Butt, "Mechanical Synthesis of Dysprosium and Cerium Nitrides," *Journal of Nuclear Materials,* vol. In Print, 2009.

[93] HORIBA, http://www.jp.horiba.com/analy_e/la-950/, 2008.

[94] R. E. Rundle, N. C. Baenziger, A. S. Wilson, and R. A. McDonald, "The structures of the carbides, nitrides and oxides of uranium," *Journal of the American Chemical Society,* vol. 70, pp. 99-105, 1948.

[95] G. Pautasso, K. Richter, and C. Sari, "Investigation of the reaction UO_{2+x}+PuO_2+C+N_2 by thermogravimetry," *Journal of Nuclear Materials,* vol. 158, pp. 12-18, 1988.

[96] C. W. Bale, P. Chanrtrand, S. A. Degterov, R. Ben Mahfoud, J. Melancon, A. D. Pelton, G. Eriksson, K. Hack, and S. Peterson, "FactSage Thermochemical Software and Databases," 2004.

[97] I. Barin, O. Knacke, and O. Kubaschewski, *Thermodynamic Properties of Inorganic Substances*. Berlin: Verlag Stahleisen, 1977.

[98] A. Roine, "Outokumpu HSC Chemistry for Windows," 5.1 ed, 2002.

[99] O. Knacke, O. Kubaschewski, and K. Hesselmann, *Thermochemical Properties of Inorganic Substances*, Second ed. Berlin: Springer-Verlag, 1991.

[100] K. Sieradzki and P. J. Ficalora, "The effect of a partially dissociated nitrogen environment on the fracture toughness of 4340 steel," *Scripta Metallurgica,* vol. 12, pp. 511-512, 1978.

[101] J. C. Fitzmaurice, A. Hector, A. T. Rowley, and I. P. Parkin, "Rapid, low energy synthesis of lanthanide nitrides," *Polyhedron,* vol. 13, pp. 235-240, 1994.

[102] T. Nakagawa, K. Sako, T. Arakawa, and T. A. Yamamoto, "Magnetocaloric effect of mononitride containing gadolinium and dysprosium GdxDy1-xN," *Journal of Alloys and Compounds,* vol. 364, pp. 53-58, 2004.

[103] G. H. Bryan, J. M. Cleveland, and C. R. Heiple, "Method for Preparing Actinide Nitrides." vol. 3923959, U. S. Patent, Ed., 1975.

[104] D. C. Bradley, J. S. Ghotra, and A. F. Hart, "Low co-ordination numbers in lanthanide and actinide compounds. Part I. The preparation and characterization of tris{bis(trimethylsilyl)-amido}lanthanides," *J. Chem. Soc., Dalton Trans.,* pp. 1021-1023, 1973.

[105] R. L. LaDuca and P. T. Wolczanski, "Preparation of Lanthanide Nitrides via Ammonolysis of Molten ((Me3Si)2N)3Ln: Onset of Crystallization Catalyzed by LiNH2 and LiCl," *Inorganic Chemistry,* vol. 31, pp. 1311-1313, 1992.

[106] L. I. Osadchaya, V. V. Sokolov, L. N. Trushnikova, and A. P. Zubareva, "Preparation of Cerium Hydrides," *Inorganic Materials,* vol. 39, pp. 1142-1143, 2003.

[107] R. C. Brown and N. J. Clark, "The cerium-nitrogen-oxygen system--I The equilibrium diagram at 1500[deg]C," *Journal of Inorganic and Nuclear Chemistry,* vol. 36, p. 1777, 1974.

[108] M. Hirota, M. Katsura, and M. Miyake, "Preparation of CeN by reaction of Ce with a N2-H2 mixture," *Journal of Alloys and Compounds,* vol. 207-208, p. 409, 1994.

[109] G. V. Samsonov, "Preparation of Cerium Nitride," *Journal of Applied Chemistry,* vol. 35, pp. 2359-2362, November 1962.

[110] D. Sarussi, I. Jacob, J. Bloch, N. Shamir, and M. H. Mintz, "Kinetics and mechanism of cerium hydride formation," *Journal of Alloys and Compounds,* vol. 191, pp. 91-99, 1993.

[111] S. Q. Xiao, K. Tsuzuki, H. Sugimura, and O. Takai, "Synthesis and properties of CeN thin films deposited by arc ion plating," *Journal of Materials Science,* vol. 33, pp. 3251-3254, 1998.

[112] R. Margevicius, H. T. Blair, K. M. Chidester, K. J. McClellan, and K. Sickafus, "Ceramic Fuel Fabrication Development for the Transmutation of Waste," Los Alamos National Laboratory 2001.

[113] S. P. Willson and R. Margevicius, "Fabrication of Transuranic Actinide Ceramic Fuels," *Transactions of the American Nuclear Society,* vol. 91, pp. 451-452, 2004.

[114] J. T. Dunwoody, C. R. Stanek, K. J. McClellan, S. T. Voit, T. Hartmann, K. Wheeler, P. Manuel, and P. D. Peralta, "Optimization of Sintering Parameters for Nitride Transmutation Fuels," *Ceramic Engineering and Science Proceedings,* vol. 27, pp. 26-38, 2006.

[115] Y. Arai, M. Morihira, and T. Ohmichi, "The Effect of Oxygen Impurity on the Characteristics of Uranium and Uranium-Plutonium Mixed Nitride Fuels," *Journal of Nuclear Materials,* vol. 202, pp. 70-78, 1993.

[116] Y. Arai and K. Nakajima, "Preparation and characterization of PuN pellets containing ZrN and TiN," *Journal of Nuclear Materials,* vol. 281, pp. 244-247, 2000.

[117] Y. Arai, K. Nakajima, and Y. Suzuki, "Thermal conductivity of actinide mononitride solid solutions," *Journal of Alloys and Compounds,* vol. 271-273, pp. 602-605, 1998.

[118] T. J. Davies and P. E. Evans, "The Preparation and Examination of Mixtures of Aluminum Nitride (AlN) and Uranium Mononitride (UN)," *Journal of Nuclear Materials,* vol. 13, pp. 152-168, 1964.

[119] M. Jolkkonen, M. Streit, and J. Wallenius, "Thermochemical modelling of uranium-free nitride fuels," *Journal of Nuclear Science and Technology,* vol. 41, pp. 457-465, 2004.

[120] M. Streit, F. Ingold, L. J. Gauckler, and J. P. Ottaviani, "Annular Plutonium Zirconium Nitride in the Form of Microspheres," *Proceedings of Advanced Reactors with Innovative Fuels,* pp. 81-90, 2001.

[121] M. Streit, F. Ingold, M. Pouchon, L. J. Gauckler, and J.-P. Ottaviani, "Zirconium nitride as inert matrix for fast systems," *Journal of Nuclear Materials,* vol. 319, pp. 51-58, 2003.

[122] V. J. Tennery and E. S. Bomar, "Sintering of (U,Pu)N as a function of Temperature and Nitrogen Pressure," *Transactions of the American Nuclear Society,* vol. 19, pp. 101-102, 1974.

[123] V. J. Tennery, T. G. Godfrey, and R. A. Potter, "Sintering of U N as a function of temperature and N2 pressure," *Journal of the American Ceramic Society,* vol. 54, pp. 327-331, 1971.

[124] A. Ciriello, V. V. Rondinella, D. Staicu, and J. Somers, "Thermophysical characterization of nitrides inert matrices: Preliminary results on zirconium nitride," *Journal of Nuclear Materials,* vol. 371, pp. 129-133, 2007.

[125] P. Bardelle and D. Warin, "Mechanism and kinetics of the uranium-plutonium mononitride synthesis," *Journal of Nuclear Materials,* vol. 188, pp. 36-42, 1992.

[126] M. Streit, F. Ingold, M. Pouchon, L. J. Gauckler, and J. P. Ottaviani, "Zirconium nitride as inert matrix for fast systems," in *8th Inert Matrix Fuel Workshop (IMF-8).* vol. 319 Tokai, Japan: Journal of Nuclear Materials, 2003, pp. 51-58.

[127] J. T. Dunwoody, "Single Gas Sintering Atmosphere Study," D. P. Butt, Ed., 2005.

[128] M. Winter, http://www.webelements.com, 2006.

[129] T. Ogawa, "Transmutation of minor actinides and innovative fuel cycle concepts," Susono, Japan, 2002, pp. 539-46.

[130] N. Chauvin, R. J. M. Konings, and H. Matzke, "Optimization of inert matrix fuel concepts for americium transmutation," *Journal of Nuclear Materials,* vol. 274, pp. 105-111, 1999.

[131] V. Basini, J. P. Ottaviani, J. C. Richaud, M. Streit, and F. Ingold, "Experimental assessment of thermophysical properties of (Pu, Zr)N," *Journal of Nuclear Materials,* vol. 344, pp. 186-190, 2005.

[132] B. Jaques, D. P. Butt, B. M. Marx, A. S. Hamdy, D. Osterberg, and G. Balfour, "Synthesis and characterization of actinide nitrides," Boise, ID, United states, 2007, pp. 591-596.

[133] *CRC Handbook of Chemistry and Physics, Internet Version 2007* 87 ed. Boca Raton, FL: Taylor and Francis, 2007.

[134] R. P. C. Schram, J. G. Boshoven, E. H. P. Cordfunke, R. J. M. Konings, and R. R. van der Laan, "Enthalpy increment measurements of cerium mononitride, CeN," *Journal of Alloys and Compounds,* vol. 252, pp. 20-23, 1997.

[135] T. Ogawa, T. Ohmichi, A. Maeda, Y. Arai, and Y. Suzuki, "Vaporization behaviour of (Pu,Am)N," *Journal of Alloys and Compounds,* vol. 224, pp. 55-59, 1995.

[136] S.-H. Wang, C.-C. Chang, and J. S. Chen, "Effects of substrate bias and nitrogen flow ratio on the resistivity, density, stoichiometry, and crystal structure of reactively sputtered ZrN _x thin films," *Journal of Vacuum Science and Technology A: Vacuum, Surfaces and Films,* vol. 22, pp. 2145-2151, 2004.

[137] H. Kleykamp, "Selection of materials as diluents for burning of plutonium fuels in nuclear reactors," *Journal of Nuclear Materials,* vol. 275, pp. 1-11, 1999.

[138] V. K. Kaul and U. Saxena, "Short-Range Order to Long-Range Order Transition in Rare-Earth-Metal Oxide Thin Crystals," *Acta Crystallographica Section A,* vol. 33, pp. 992-&, 1977.

[139] T. Fluckiger, M. Erbudak, A. Hensch, Y. Weisskopf, M. Hong, and A. R. Kortan, "Structure of Gd₂O₃ films epitaxially grown on GaAs(100) and GaN(0001) surfaces," Avignon, France, 2002, pp. 441-444.

[140] Anonymous, http://www.accuratus.com/zirc.html, 2006.

[141] T. Yamashita, H. Muto, T. Tsuji, and Y. Nakamura, "Thermal expansion of neptunium-plutonium mixed oxides," *Journal of Alloys and Compounds,* vol. 271-273, pp. 404-407, 1998.

[142] K. Bakker and R. J. M. Konings, "On the thermal conductivity of inert-matrix fuels containing americium oxide," *Journal of Nuclear Materials,* vol. 254, pp. 129-134, 1998.

[143] M. Sowwan, "Investigation of solid-solid interface structure using a novel X-ray diffraction method." vol. Doctor of Philosophy: Hebrew University, 2002, p. 84.

[144] M. Yashima and S. Tsunekawa, "Structures and the oxygen deficiency of tetragonal and monoclinic zirconium oxide nanoparticles," *Acta Crystallographica Section B-Structural Science,* vol. 62, pp. 161-164, Feb 2006.

[145] D.-J. Kim, Y.-S. Kim, S.-H. Kim, J.-H. Kim, J.-H. Yang, Y.-W. Lee, and H.-S. Kim, "The linear thermal expansion and the thermal diffusivity measurements for near-stoichiometric (U, Ce)O2 solid solutions," *Thermochimica Acta,* vol. 441, pp. 127-131, 2006.

[146] M. Inoue, "Thermal conductivity of uranium-plutonium oxide fuel for fast reactors," *Journal of Nuclear Materials,* vol. 282, pp. 186-195, 2000.

[147] K. Bakker and R. J. M. Konings, "The influence of americium oxide inclusions on the thermal conductivity of inert-matrix fuel," *Journal of Alloys and Compounds,* vol. 271, pp. 632-635, Jun 1998.

[148] R. D. Baker, S. S. Hecker, and D. R. Harbur, "Plutonium a Wartime Nightmare but a Metallurgist's Dream," Los Alamos Science Winter/Spring 1983 1983.

[149] I. Barin, O. Knacke, and O. Kubaschewski, "Thermodynamic Properties of Inorganic Substances," Verlag Stahleisen, Berlin, 1977.

[150] M. N. Rahaman, *Ceramic Processing and Sintering*. New York: Marcel Dekker, Inc., 1995.

[151] W. D. Kingery and M. Berg, "Study of the initial stages of sintering solids by viscous flow, evaporation-condensation and self-diffusion," *Journal of Applied Physics,* vol. 26, pp. 1205-1213, 1955.

[152] D. L. Johnson and I. B. Cutler, "Diffusion sintering. II. Initial sintering kinetics of alumina," *Journal of the American Ceramic Society,* vol. 46, pp. 545-550, 1963.

[153] R. L. Coble, "Initial sintering of alumina and hematite," *Journal of American Ceramic Society,* vol. 41, pp. 55-62, 1958.

[154] G. C. Kuczynski, "Self-diffusion of in sintering of metallic particles," *Journal of Metals Trans. AIME,* vol. 185, pp. 169-178, 1949.

[155] R. M. German and Z. A. Munir, "Surface area reduction during isothermal sintering," *Journal of the American Ceramic Society,* vol. 59, pp. 379-83, 1976.

[156] H. Jiaping, P. Q. Mantas, and A. M. R. Senos, "Sintering kinetics of undoped and Mn-doped zinc oxide in the intermediate stage," *Journal of the American Ceramic Society,* vol. 88, pp. 1773-8, 2005.

[157] R. M. German, *Sintering Theory and Practice*. New York: John Wiley & Sons Inc., 1996.

[158] D. L. Johnson, "A general model for the intermediate stage of sintering," *Journal of American Ceramic Society,* vol. 53, pp. 574-577, 1970.

[159] R. L. Coble, "Sintering crystalline solids. I. Intermediate and final state diffusion models," *Journal of Applied Physics,* vol. 32, pp. 787-792, 1961.

[160] J. D. Hansen, R. P. Rusin, T. Mao-Hua, and D. L. Johnson, "Combined-stage sintering model," *Journal of the American Ceramic Society,* vol. 75, pp. 1129-35, 1992.

[161] J. Wang and R. Raj, "Estimate of the activation energies for boundary diffusion from rate-controlled sintering of pure alumina, and alumina doped with zirconia or titania," *Journal of the American Ceramic Society,* vol. 73, pp. 1172-5, 1990.

[162] C. May-Ying, M. N. Rahaman, L. C. De Jonghe, and R. J. Brook, "Effect of heating rate on sintering and coarsening," *Journal of the American Ceramic Society,* vol. 74, pp. 1217-25, 1991.

[163] J. Zhao and M. P. Harmer, "Sintering kinetics for a model final-stage microstructure: a study of Al₂O₃," *Philosophical Magazine Letters,* vol. 63, pp. 7-14, 1991.

[164] M. W. Chase, C. A. Davies, J. R. Downey, D. J. Frurip, R. A. McDonald, and A. N. Syverud, *JANAF Thermochemical Tables Part I and I I*, Third ed. vol. 14. New York: American Chemical Society and the American Institute of Physics for the National Bureau of Standards, 1985.

[165] J. B. Holt and M. Y. Almassy, "Nitrogen diffusion in uranium nitride as measured by alpha particle activation of ¹⁵N," *Journal of the American Ceramic Society,* vol. 52, pp. 631-5, 1969.

[166] R. H. Condit, J. B. Holt, and L. Himmel, "Nuclear activation technique for detecting nitrogen-15 tracer in solids," *Journal of the Electrochemical Society,* vol. 114, pp. 1100-1103, 1967.

[167] T. J. Sturiale and M. A. DeCrescente, "Self-Diffusion of Nitrogen in Uranium Mononitride," Pratt and Whitney Aircraft Co., PWAC-477 September 1965 1965.

[168] J. W. Droege and C. A. Alexander, "Progress on Development of Fuels and Technology for Advanced Reactors During July 1969-June 1979," Battelle Memorial Institute, BMI 1886 1970.

[169] S. L. Hayes, J. K. Thomas, and K. L. Peddicord, "Material property correlations for uranium mononitride. III. Transport properties," *Journal of Nuclear Materials,* vol. 171, pp. 289-299, 1990.

[170] H. Matzke, "Atomic mechanisms of mass transport in ceramic nuclear fuel materials," *Journal of the Chemical Society Faraday Transactions,* vol. 86, pp. 1243-56, 1990.

APPENDICES

APPENDIX A:
Physical and Thermodynamic Properties of Various Nitrides, Oxides, and Metals

Table 15: Physical properties and values for pure fuel metals and surrogates.

Property	Element						
	U	Pu	Ce	Am	Dy	Gd	Zr
Atomic Radius (pm) [133]	139	151	183	131	175	179	159
Oxidation States [133]	6,5,4,3	6,5,4,3	3,4	6,5,4,3	3	3	4
Ionic Radii [133]	73	86	114	98	103	105	84
Electronegativity [133]	1.7	1.3	1.12	-	1.22	1.20	1.33
1st Ionization Potential (eV) [133]	6.19	6.06	5.54	5.99	5.94	6.15	6.63
Crystal Structure	Orhor. Cmcm [128]	Monoclin. P21/m [128]	HCP P63/mmc [128]	HCP P63/mmc [128]	HCP P63/mmc [128]	HCP P63/mmc [128]	HCP P63/mmc [128]
Lattice Constant (nm)	a=0.2854 b=0.5870 c=0.4955 [128]	a = 0.6183 b = 0.4822 c = 1.0963 β = 101.79° [128]	a = 0.3620 c = 0.5990 [128]	a = 0.3468 c =1.124 [128]	a = 0.3953 c = 0.5654 [128]	a = 0.3232 c = 0.5147 [128]	a = 0.3636 c = 0.5783 [128]
Density (g/cm^3)	19.05 [128]	19.82 [128]	6.69 [128]	6.93 [128]	8.55 [128]	6.51[128]	7.9 [128]
Thermal Conductivity (W/m-K)	27.6 [128]	6.74 [128]	11.4 [128]	10 [128]	10.7 [128]	22.7 [128]	10.6 [128]
Linear CTE (1/K)	13.9 [128]	-	6.3 [128]	-	9.9 [128]	5.7 [128]	9.4 [128]
$T_{Melting}$ (K)	1405 [128]	912.5 [128]	1068 [128]	1450 [128]	1680 [128]	2128 [128]	1585 [128]

Table 16: Physical properties and values for nitride fuels and surrogates.

Property	**Nitride**						
	UN	**PuN**	**CeN**	**AmN**	**DyN**	**GdN**	**ZrN**
Crystal Structure	**Rock Salt [78]**	**Rock Salt [78]**	**Rock Salt [134]**	**Rock Salt [135]**	**Rock Salt [102]**	**Rock Salt [102]**	**Rock Salt [136]**
Lattice Constant (nm)	**0.4889 [78]**	**0.4905 [78]**	**0.502 [111]**	**0.499 [135]**	**0.49 [102]**	**0.498 [102]**	**0.4577 [6]**
Theoretical Density (g/cm^3)	**14.3 [78]**	**14.4 [131]**	**7.89 [111]**	**13.74**	**9.93**	**9.1**	**7.29 [131]**
Thermal Conductivity (W/m-K)	**25 (1773K) [78]**	**11 (1773K) [78]**	**5 (1073-2273K) [137]**	**-**	**-**	**-**	**17 (773K) 23 (1273K) 26 (1773K) 24 (2273K) [137]**
Linear Thermal Exp. Coefficient (1/K)	**9 (1773K) [78]**	**15 (1773K) [78]**	**30 [134]**	**-**	**-**	**-**	**7.65 (300-2000K) [131]**
Melting Point (K)	**3078 [137]**	**2823 [137]**	**2830 [137]**	**-**	**-**	**-**	**3233 [137]**

Table 17: Physical properties and values for oxide fuels and surrogates.

Property	Oxide						
	UO_2	PuO_2	CeO_2	AmO_2	Dy_2O_3	Gd_2O_3	ZrO_2
Crystal Structure	Fluorite [128]	Fluorite [128]	Fluorite [128]	Fluorite	Cubic [138]	Cubic [139]	Monoclinic 1443K Tetragonal 2643K Cubic 2983K [140]
Lattice Constant (nm)	0.5470 [128]	0.5395 [141]	0.5305 [128]	0.5377 [142]	0.537 [138]	1.0813 [143]	a = 0.5131 b = 0.5182 c = 0.5325 β = 99.34° [144]
Theoretical Density (g/cm^3)	10.97 [145]	11.5 [128]	7.65 [128]	11.68 [128]	7.8 [128]	7.1 [128]	5.68 [128]
Thermal Conductivity (W/m-K)	7.5 (573K) 6 (773K) 3.5 (1273) 2.8 (1573) [145]	5.75 (573K) 4 (773K) 3.2 (1273) 2.5 (1773) [146]	3.02 (1000K) [137]	0.69 (333K) [147]	-	-	2.2 (1273K) 1.5 (1773K) 1.8 (2273K) [137]
Linear Thermal Exp. Coefficient (1/K)	9.02 [145]	6.46 [141]	-	-	-	-	3.1 (298-1443K)
Melting Point (K)	3100 [128]	2673 [128]	2673 [137]	2448 [142]	2681 [128]	2693 [128]	2983 [137]

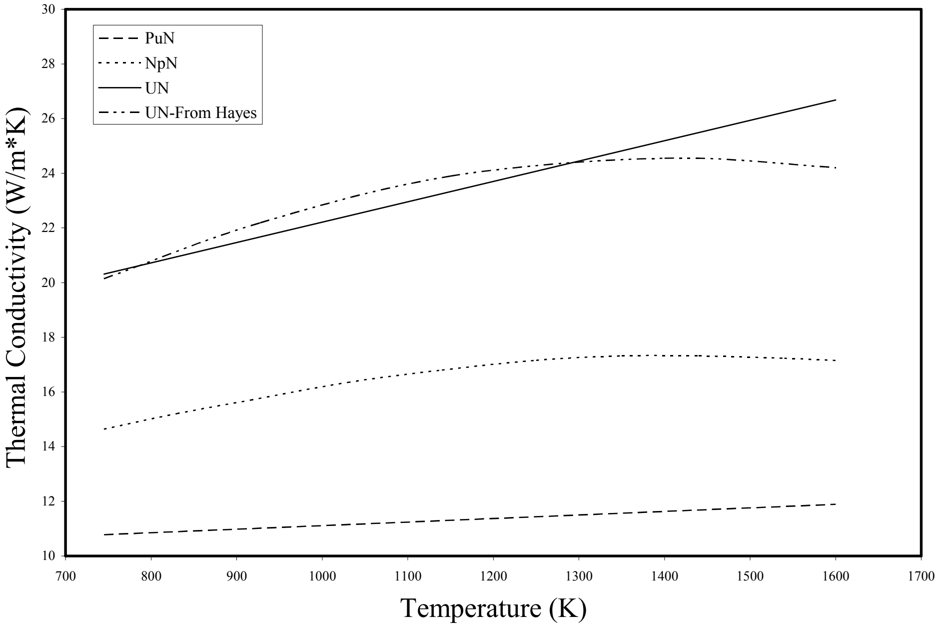

Figure 111: Thermal conductivity as a function of temperature for various actinide mononitrides. Figure adapted from [78].

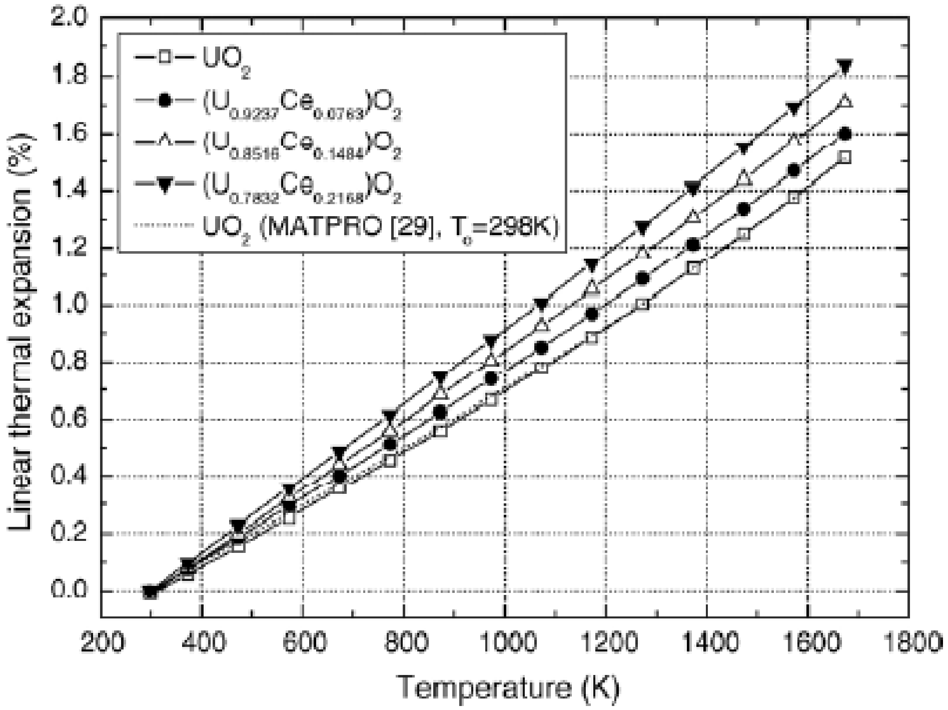

Figure 112: Linear thermal expansion coefficients of cerium doped and undoped uranium oxides measured using the TMA method [145].

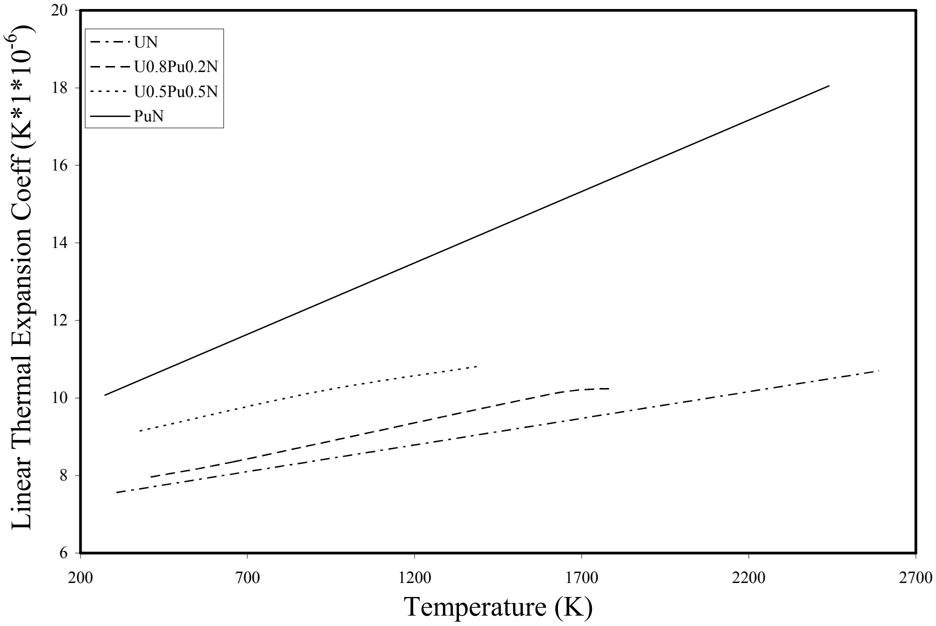

Figure 113: Linear thermal expansion coefficient as a function of temperature for various actinide mononitrides. Figure adapted from [78].

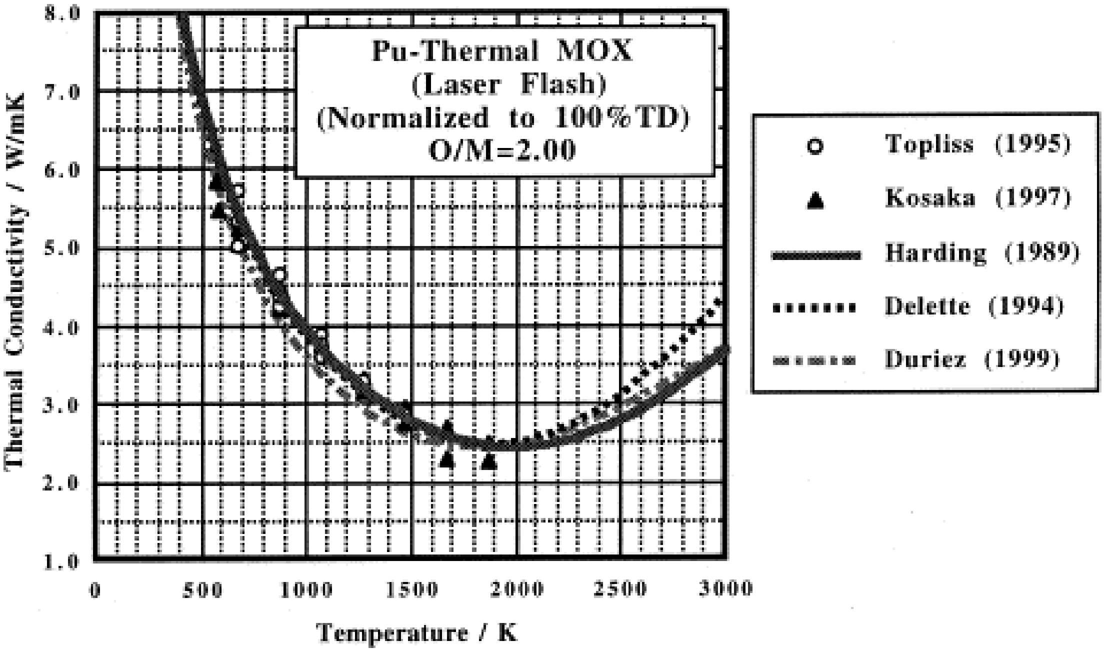

Figure 114: Thermal conductivity of Plutonium Oxide as a function of temperature [146].

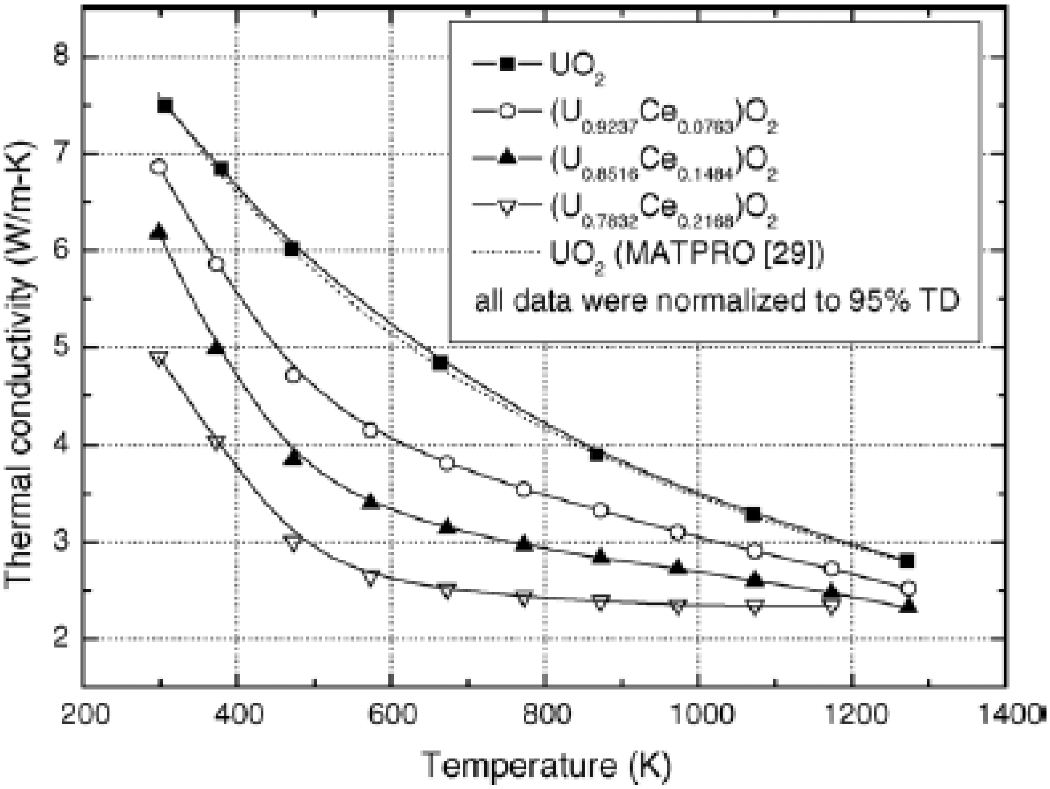

Figure 115: Thermal conductivity of cerium doped and undoped unranium oxides [145].

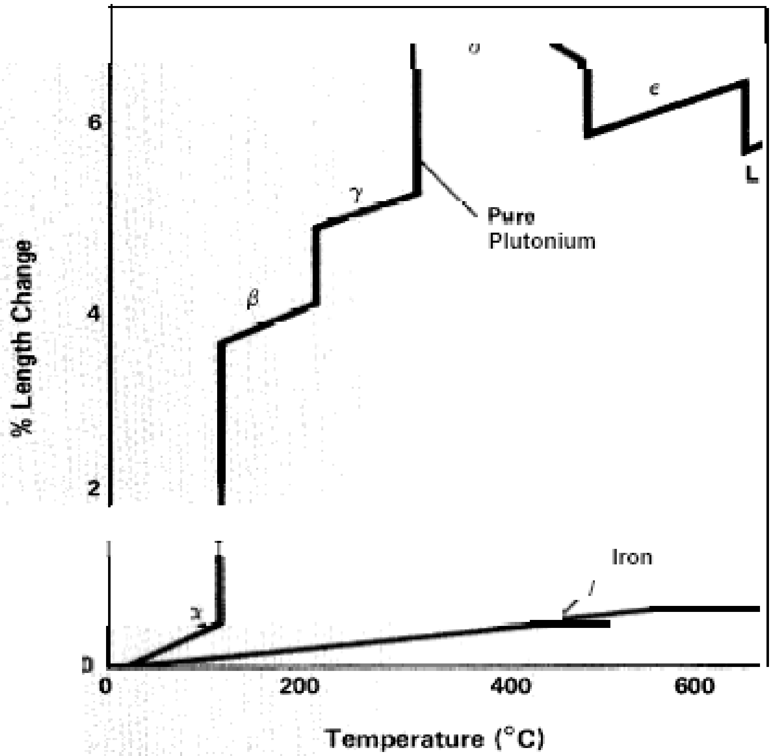

Figure 116: Length changes at phase transitions for plutonium [148].

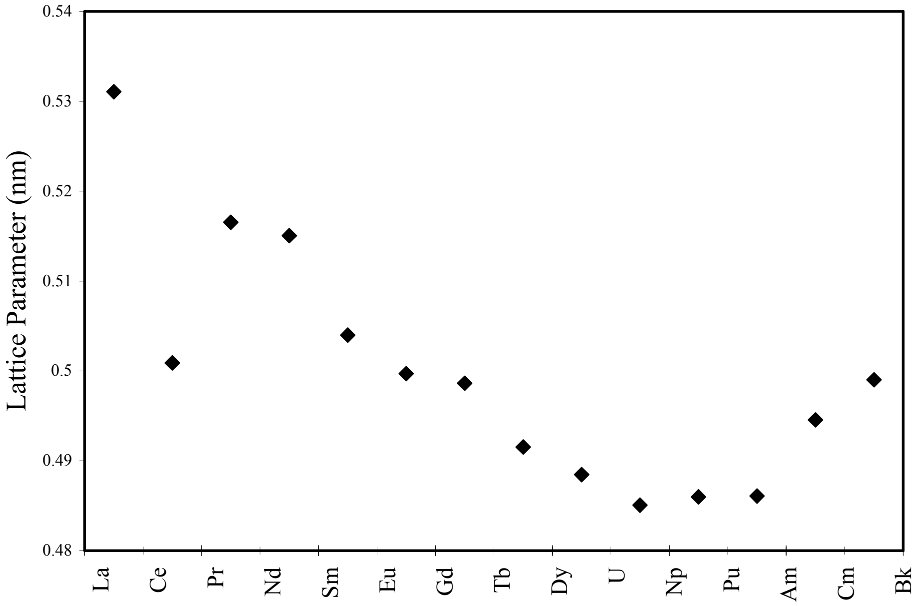

Figure 117: Lattice parameters of various metal nitrides. Figure adapted from [135].

Table 18: Differences in lattice parameters and miscibility in various metal nitride. Table adapted from [135].

	a (nm)	**|UN-MN|**	**|AmN-MN|**
LaN	**0.5305**	**0.0417 Complete miscible. (1973K)**	**0.0314**
CeN	**0.501**	**0.0122**	**0.0019**
PrN	**0.5165**	**0.0277**	**0.0174**
NdN	**0.5151**	**0.0263**	**0.016**
YN	**0.4891**	**0.0003**	**0.01**
UN	**0.4888**	**-**	**0.0103**
NpN	**0.04899**	**0.0011**	**0.0092**
PuN	**0.4905**	**0.0017**	**0.0086**
AmN	**0.4991**	**0.0103**	**-**
CmN	**0.5041**	**0.0153**	**0.005**
BkN	**0.495**	**0.0062**	**0.0041**
ZrN	**0.4576**	**0.0312**	**0.0415 Miscibl. gap**
TiN	**0.4242**	**0.0646 4 mol.% in UN at 2672K**	**0.0749**

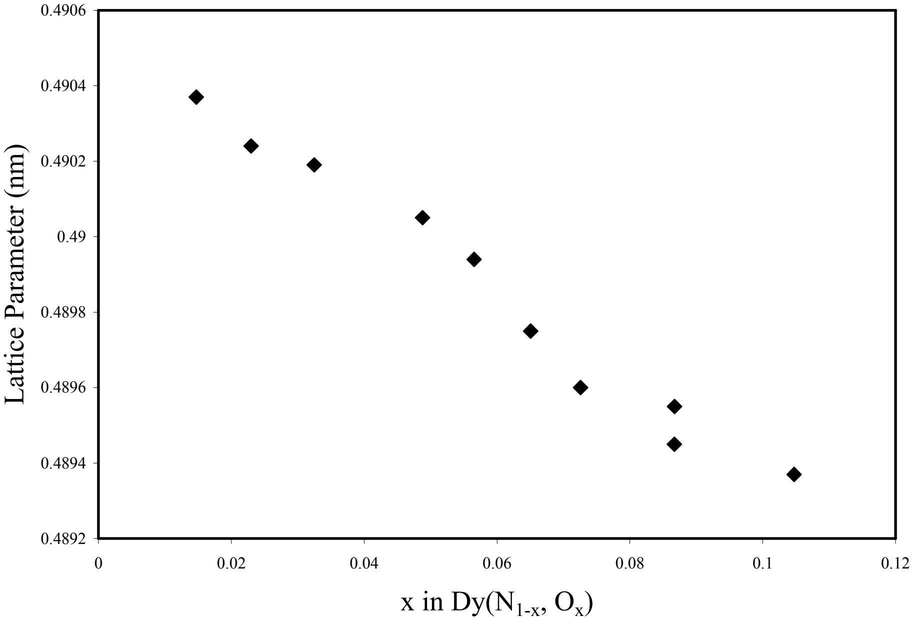

Figure 118: Lattice parameter as a function of nitrogen and oxygen concentration in dysprosium. Figure adapted from [47].

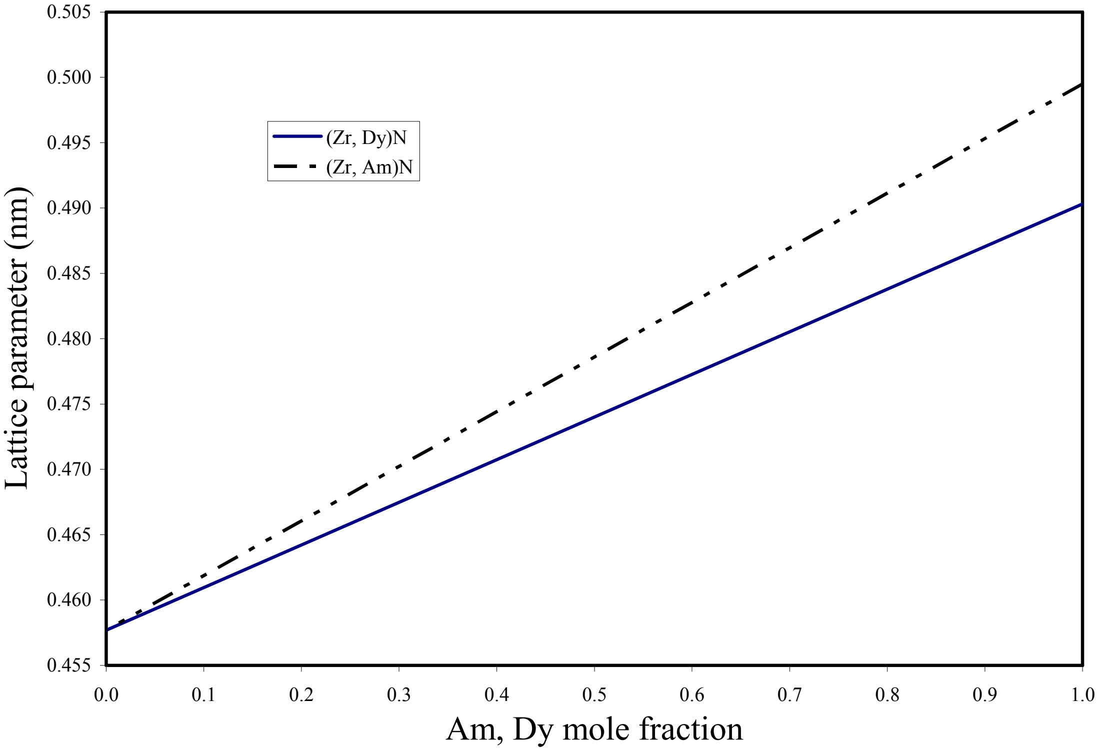

Figure 119: Lattice parameters of Zr doped AmN and DyN. Figure adapted from [6].

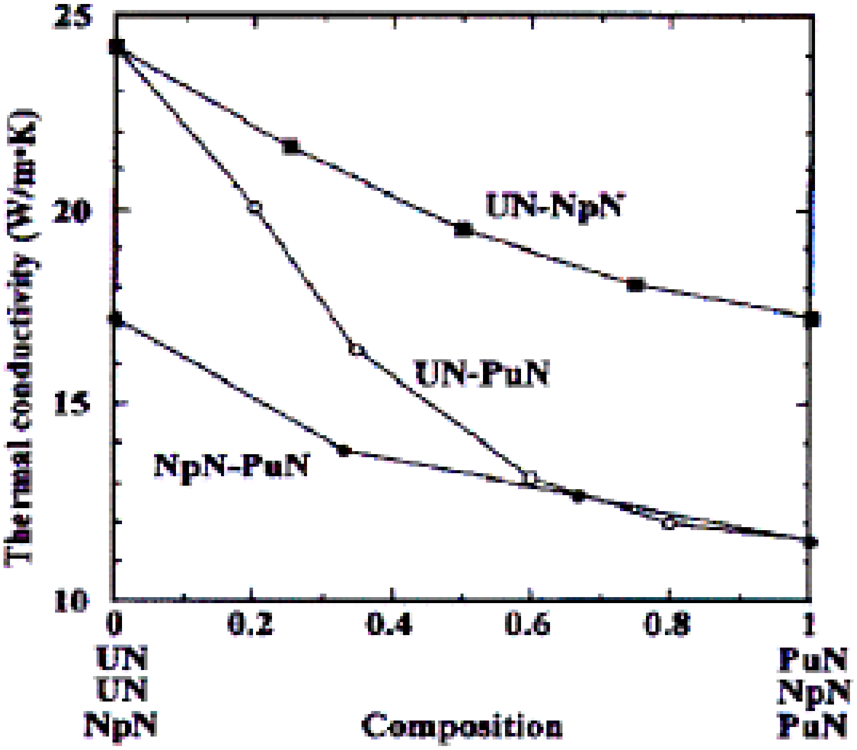

Figure 120: Thermal conductivity of some actinide mononitride solid solutions [45].

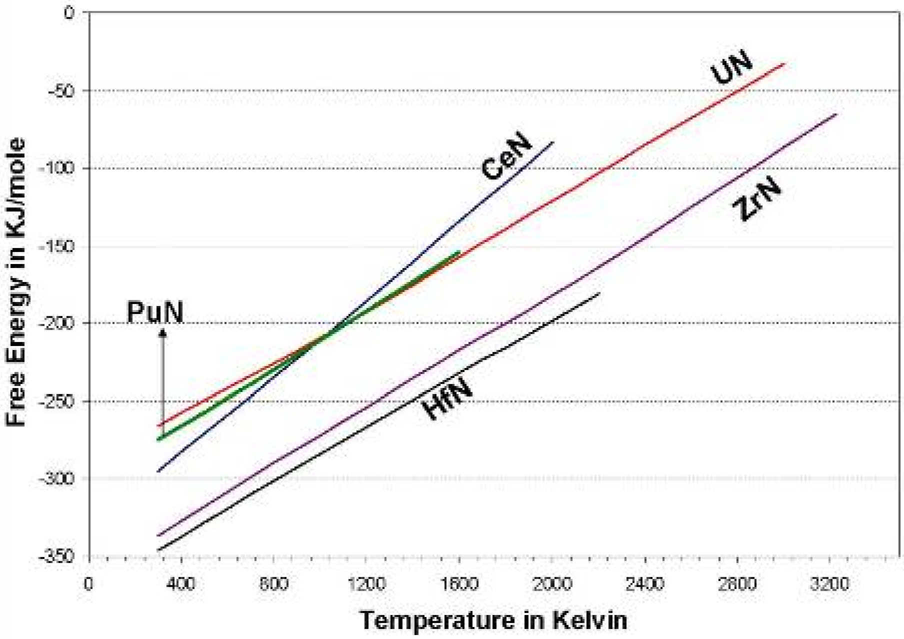

Figure 121: Free energy versus temperature curves for various nitrides. The data points in the plots were collected from Barin [149].

APPENDIX B:

Compilation of Initial, Intermediate, and Final Stage Sintering Models

INITIAL STAGE SINTERING MODELS

Model Description	Neck Growth Models	Volume Change Models
Surface Diffusion (Evaporation-Condensation) [150] (equal spheres)	$\left(\frac{X}{R}\right)^7 = \left(\frac{56 D_s \delta_s \gamma_{sv} \Omega}{kTR^4}\right) t$	$\frac{\Delta L}{L_0} = 0$
Lattice Diffusion from Surface [150] (equal spheres)	$\left(\frac{X}{R}\right)^4 = \left(\frac{20 D_l \gamma_{sv} \Omega}{kTR^3}\right) t$	$\frac{\Delta L}{L_0} = 0$
Vapor Transport [150] (equal spheres)	$\left(\frac{X}{R}\right)^3 = \left(\frac{3 p_0 \gamma_{sv} \Omega}{kTR^2 \sqrt{2\pi mkT}}\right) t$	$\frac{\Delta L}{L_0} = 0$
Vacancy diffusion from neck to surface [151] (equal spheres)	$\left(\frac{X}{R}\right)^5 = \frac{5\pi \gamma_{sv} a^3 D_V}{2kTR^3} t$	$\frac{\Delta L}{L_0} = 0$
Lattice Diffusion from Grain Boundary [150] (equal spheres)	$\left(\frac{X}{R}\right)^5 = \left(\frac{80\pi D_l \gamma_{sv} \Omega}{kTR^3}\right) t$	$\left(\frac{\Delta L}{L_0}\right)^{\frac{5}{2}} = -\left(\frac{5\pi D_l \gamma_{sv} \Omega}{2kTR^3}\right) t$
Viscous Flow (Volume Diffusion) [150] Assumes flow occurs uniformly along axis joining the centers of the spheres. (equal spheres)	$\left(\frac{X}{R}\right)^2 = \left(\frac{3\gamma_{sv}}{2\eta R}\right) t$	$\frac{\Delta L}{L_0} = -\left(\frac{3\gamma_{sv}}{8\eta R}\right) t$
Grain Boundary Diffusion [150] Assumes vacancy concentration throughout neck is constant (equal spheres)	$\left(\frac{X}{R}\right)^6 = \left(\frac{96 D_{gb} \delta_{gb} \gamma_{sv} \Omega}{kTR^4}\right) t$	$\left(\frac{\Delta L}{L_0}\right)^3 = -\left(\frac{3 D_{gb} \delta_{gb} \gamma_{sv} \Omega}{2kTR^4}\right) t$
Bulk vacancy diffusion from neck to grain boundary (equal spheres) [151]	$\left(\frac{X}{R}\right)^5 = \frac{80 \gamma_{sv} a^3 D_V}{kTR^3} t$	$\frac{\Delta L}{L_0} = \left(\frac{20 \gamma_{sv} a^3 D_V}{\sqrt{2} R^3 kT}\right) t^{\frac{2}{5}}$
Bulk diffusion with spherical initial contact [152]	---	$\frac{\Delta L}{L_0} = \left[\frac{31 \gamma_{sv} a^3 D_V}{\pi^2 R^3 kT}\right]^{0.46} t^{0.46}$
Bulk diffusion with paraboloid initial contact [152]	---	$\frac{\Delta L}{L_0} = \left[\frac{20 \gamma_{sv} a^3 D_V}{\pi R^2 kT}\right]^{0.46} t^{0.46}$
Bulk diffusion with 160° cone on a plane initial contact [152]	---	$\frac{\Delta L}{L_0} = \left[\frac{180(\tan^2 10°) \gamma_{sv} a^3 D_V}{\pi^2 R^3 kT}\right]^{0.33} t^{0.33}$

Bulk diffusion with spherical with a grooved neck initial contact [152]	---	$\frac{\Delta L}{L_0} = \left[\frac{23\gamma_{sv}a^3D_V}{\pi^2R^3kT}\right]^{0.46} t^{0.46}$
Grain Boundary diffusion with spherical initial contact [152]	---	$\frac{\Delta L}{L_0} = \left[\frac{50\delta_{gb}\gamma_{sv}a^3D_V}{7\pi R^4kT}\right]^{0.31} t^{0.31}$
Grain boundary diffusion with paraboloid initial contact [152]	---	$\frac{\Delta L}{L_0} = \left[\frac{102\delta_{gb}\gamma_{sv}a^3D_V}{7\pi R^3kT}\right]^{0.31} t^{0.31}$
Grain boundary diffusion with 160° cone on a plane initial contact [152]	---	$\frac{\Delta L}{L_0} = \left[\frac{55\delta_{gb}(\tan^2 10°)\gamma_{sv}a^3D_V}{R^4kT}\right]^{0.25} t^{0.25}$
G. b. diffusion with spherical with a grooved neck initial contact [152]	---	$\frac{\Delta L}{L_0} = \left[\frac{3\delta_{gb}\gamma_{sv}a^3D_V}{2R^4kT}\right]^{0.31} t^{0.31}$
Bulk diffusion to a grain boundary (equal spheres) [152]	$X^{4.7} = \frac{43\gamma_{sv}a^3D_VR^{1.7}}{kT}t$	---
G. b. diffusion to a grain boundary (equal spheres) [152]	$X^7 = \frac{115\delta_{gb}\gamma_{sv}a^3D_VR^3}{kT}t$	---
Grain boundary diffusion to a grain boundary (2 spheres) [153]	$X^6 = \frac{96\gamma_{sv}a^3D_VR^2}{kT}t$	---
Bulk diffusion to the surface (sphere on plane) [154]	$X^5 = \frac{40\gamma_{sv}a^3D_VR^2}{kT}t$	---
Surface diffusion to the surface (sphere on plane) [154]	$X^7 = \frac{56\delta_{gb}\gamma_{sv}a^3D_VR^3}{kT}t$	---
Bulk diffusion to the grain boundary (equal spheres) [153]	$X^4 = \frac{32\gamma_{sv}a^3D_VR^2}{kT}t$	---
Viscous/Plastic Flow [155]	$\left(\frac{\Delta S}{S_0}\right)^{1.1} = Kt$	---
Evaporation-Condensation [155]	$\left(\frac{\Delta S}{S_0}\right)^{1.5} = Kt$	
Lattice/Volume/Bulk Diffusion [155]	$\left(\frac{\Delta S}{S_0}\right)^{2.7} = Kt$	
Grain-Boundary Diffusion [155]	$\left(\frac{\Delta S}{S_0}\right)^{3.3} = Kt$	
Surface Diffusion [155]	$\left(\frac{\Delta S}{S_0}\right)^{3.5} = Kt$	---

X ≡ Radius of the neck
D_s ≡ Surface diffusion coefficient
D_{gb} ≡ Grain Boundary diffusion coefficient
δ_s ≡ Thickness for surface diffusion
δ_{gb} ≡ Thickness for grain boundary diffusion
p_0 ≡ Vapor pressure over flat surface
k ≡ Boltzmann constant
η ≡ Viscosity
t ≡ time
D_l ≡ Lattice diffusion coefficient
D_V ≡ Self diffusion coefficient
a ≡ Atomic radius
γ_{sv} ≡ Specific surface energy
m ≡ Mass of atom
T ≡ Temperature
R ≡ Radius of sphere

INTERMEDIATE STAGE SINTERING MODELS

Model Descr. (Limiting Mechanisms)	**Densification Rate Model**	**Notes**
Lattice/Volume/Bulk Diffusion [156]	$\frac{d\rho}{dt} = \frac{12 D_{0V}\Omega\rho}{g' kTG^2}\exp\left(\frac{-Q_s}{RT}\right)\Sigma\Phi_S^{1.8}$	---
Grain-Boundary Diffusion [156]	$\frac{d\rho}{dt} = \frac{24\delta D_{0b}\Omega}{g' kTG^3}\exp\left(-\frac{Q_s}{RT}\right)\Sigma\Phi_S$	---
Lattice/Volume/Bulk Diffusion [150]	$\frac{1}{\rho}\frac{d\rho}{dt} \approx \frac{4}{3}\frac{AD_l\gamma_{sv}\Omega}{\rho kTG^3}$	---
Grain-Boundary Diffusion [150]	$\frac{1}{\rho}\frac{d\rho}{dt} \approx \frac{4}{3}\frac{\delta_{gb}D_{gb}\gamma_{sv}\Omega}{\rho kTG^4(1-\rho)^{\frac{1}{2}}}$	---
Lattice/Volume/Bulk Diffusion [157]	$\frac{d\rho}{dt} = \frac{g' D_V\Omega\gamma_{sv}}{kTG^3}$	Vacancy sink at center of grain boundary
Lattice/Volume/Bulk Diffusion [158]	$-\ln(1-P) = \frac{378 D_V\Omega\gamma_{sv}}{kTG^3}(t_f - t)$	All grains have same size and shape
Lattice/Volume/Bulk Diffusion [158]	$P = \frac{335 D_V\Omega\gamma_{sv}}{kTG^3}(t_f - t)$	All grains have same size and shape
Lattice/Volume/Bulk Diffusion [158]	$P^{\frac{3}{2}}\left[1 - \frac{3}{2}\ln(1.2P)\right] = \frac{1190 D_V\Omega\gamma_{sv}}{kTG^3}(t_f - t)$	All grains have same size and shape
Lattice/Volume/Bulk Diffusion [159] (formatted by [158])	$P = \frac{720 D_V\Omega\gamma_{sv}}{kTG^3}(t_f - t)$	All grains have same size and shape. Not for use when pore shrinks to zero radius, or discontinuous grain growth, or pore phase becomes discontinuous unless grain-boundary diffusion is the mechanism
Grain-Boundary Diffusion [159] (formatted by [158])	$\frac{2}{3}P^{\frac{3}{2}} = \frac{80 bD_V\Omega\gamma_{sv}}{kTG^4}(t_f - t)$	
Grain-Boundary Diffusion [158]	$\frac{2}{3}P^{\frac{3}{2}} = \frac{860 bD_V\Omega\gamma_{sv}}{kTG^4}(t_f - t)$	---
Grain-Boundary Diffusion [158]	$\int_0^P \frac{P^{\frac{1}{2}}dP}{1-P} = \frac{1000 bD_V\Omega\gamma_{sv}}{kTG^4}(t_f - t)$	---

$D_{s,gb,l}$ ≡ Surface, grain-boundary, lattice diffusion coefficient, respectively
D_{0V} ≡ pre-exponential factor of the vol. diffusion coeff.
G ≡ grain size
Ω ≡ atomic volume
Q ≡ activation energy
Φ ≡ Sintering-stress intensification factor
k ≡ Boltzmann constant
γ_{sv} ≡ Specific surface energy

P ≡ Porosity
D_{0b} ≡ pre-exponential factor of the g.b. diffusion coeff.
T ≡ Temperature
ρ ≡ density
Σ ≡ sintering stress
g' ≡ a geometric factor
δ_{gb} ≡ Thickness for grain boundary diffusion
A ≡ constant

FINAL STAGE SINTERING MODELS

Model Descr. (Limiting Mechanisms)	**Model**	**Notes**
Lattice (Volume, Bulk) Diffusion (concentric sphere model) [150]	$P_S = \frac{6\pi D_l \gamma_{sv} \Omega}{\sqrt{2} l_p^3 kT}\left(t_f - t\right)$	Valid for less than about 2%
Viscous Flow (concentric sphere model) [150]	$\frac{\gamma_{sv} N^{\frac{1}{3}}}{\eta}\left(t - t_0\right) = F_{MS}(\rho) - F_{MS}(\rho_0)$ $where:$ $F_{MS}(\rho) = \frac{2}{3}\left(\frac{3}{4\pi}\right)^{\frac{1}{3}}\left[\frac{1}{2}\ln\left(\frac{1+\rho^3}{(1+\rho)^3}\right) - \sqrt{3}\arctan\left(\frac{2\rho - 1}{\sqrt{3}}\right)\right]$	Amorphous materials
Surface Diffusion [157]	$\frac{dG}{dt} = \frac{4K_f \gamma_{sv} A}{G d_P^4 \left[\frac{A}{d_P^4 M_G} + 1\right]}$	---
Volume Diffusion [157]	$\frac{dG}{dt} = \frac{4K_f \gamma_{sv} A}{G d_P^3 \left[\frac{A}{d_P^3 M_G} + 1\right]}$	---
Evaporation-Condensation [157]	$\frac{dG}{dt} = \frac{4K_f \gamma_{sv} A}{G d_P^2 \left[\frac{A}{d_P^2 M_G} + 1\right]}$	---

$D_{s,gb,l}$ ≡ Surface, grain-boundary, or lattice diffusion coefficient, respectively
γ_{sv} ≡ Specific surface energy
k ≡ Boltzmann constant
l_p ≡ pore length
P_S ≡ porosity
d_P ≡ pore size
M_G ≡ grain mobility
η ≡ viscosity
Ω ≡ atomic volume
T ≡ Temperature
t ≡ time
K_f ≡ geometric constant
A ≡ material parameter conglomeration
G ≡ grain size
ρ ≡ density

GENERAL SINTERING MODELS (FROM BEGINNING TO END OF SINTERING CYCLE)

Model Description (Limiting Mechanisms)	**Model**	**Notes**
Isotropic, linear shrinkage (vacancy and/or grain boundary diffusion) [160]	$-\frac{dL}{Ldt}=\frac{\gamma_{sv}\Omega_a}{kT}\left(\frac{\delta D_b\alpha C_k C_b}{G^4 C_\lambda C_a C_h}+\frac{D_v\alpha C_k C_v}{G^3 C_\lambda C_a C_h}\right)$	D is known as a function of T.
Grain Boundary Diffusion [161]	$-\frac{dL}{Ldt}=\frac{C\gamma_{sv}\Omega_v^{\frac{2}{3}}f(\rho)}{3RTG^4}\exp\left(\frac{-Q}{kT}\right)$	---
Lattice/Volume/Bulk Diffusion [161]	$-\frac{dL}{Ldt}=\frac{C\gamma_{sv}\Omega_v^{\frac{2}{3}}f(\rho)}{3RTG^3}\exp\left(\frac{-Q}{kT}\right)$	---
Grain Boundary Diffusion [162]	$-\frac{dL}{Ldt}=\frac{8\pi\Omega_a\Sigma\delta D_b\phi^{\frac{3}{2}}}{kTx^3}$	---
Lattice/Volume/Bulk Diffusion [162]	$-\frac{dL}{Ldt}=\frac{16\pi\Omega_a\Sigma\delta D_v\phi^{\frac{3}{2}}}{kTx^2}$	---
Grain Boundary Diffusion [163]	$-\frac{dL}{Ldt}=\frac{C_b\gamma_{sv}\Omega_a\delta D_b N}{3kTG^4}$	---
Lattice/Volume/Bulk Diffusion [163]	$-\frac{dL}{Ldt}=\frac{C_v\gamma_{sv}\Omega_a D_v N f(\rho,N)}{3kTG^3}$	---
General for grain boundary and volume/lattice/bulk diffusion [158]	$\frac{N_L l}{2\pi T_{A,net}}\frac{dV}{Vdt}=\frac{\gamma_{sv}\Omega_a D_v N_L}{kTN_A}+\frac{\gamma_{sv}\Omega_a b D_b}{kT}$	Atom geometry is rapid compared with the rate of change of neck geometry

$C_{k,b,v,a,h,\lambda}$ ≡ Constants associated with: curvature, grain boundary diffusion, vacancy diffusion, diffusion area, distance from centroid to face, and distance material is drawn to the pore, respectively

$D_{v,b}$ ≡ Diffusion coefficient associated with vacancy and grain boundary diffusion, respectively

γ_s ≡ Specific surface energy

L ≡ linear dimension

t ≡ time

α ≡ constant of proportionality relating λ and γ

Ω_a ≡ atomic volume

k ≡ Boltzmann constant

T ≡ temperature

δ ≡ grain boundary thickness

Ω_v ≡ molar volume

V ≡ volume of shrinking element

l ≡ mean grain intercept length

N_A ≡ Number of g.b./pore intersections per area of polish plane

$f(\rho)$ ≡ unspecified function of density

R ≡ Gas constant

G ≡ grain size

Q ≡ activation energy

Σ ≡ sintering stress

x ≡ scaling distance (rather than grain size)

φ ≡ Geometrical factor related to DeHoff's efficiency factor

N ≡ the number of pores per grain

$f(\rho,N)$ ≡ ratio of pore size to the grain size

b ≡ width of grain boundary

N_L ≡ Number of intersections per length of test line

$T_{A,net}$ ≡ number of times a test line is tangent to convex solid-pore interfaces minus the number of times it is tangent to concave surfaces per unite area.

APPENDIX C:
Error Propagation Calculations for Density Determinations

Green density error calculations

$$\rho = \frac{m}{\pi * r^2 * L}$$

Scale (dm)	±	0.005	gms
Length (dL)	±	0.005	cm
Radius (dr)	±	0.005	cm

$^{\partial\rho}/_{\partial m} = 1/(\pi*L*r^2) =$ 6.517

$^{\partial\rho}/_{\partial L} = -m/(\pi*L^2*r^2) =$ 13.173

$^{\partial\rho}/_{\partial r} = -2m/(\pi*L*r^3) =$ 39.644

Error $= (\partial\rho/\partial r)dr + (\partial\rho/\partial L)dL + (\partial\rho/\partial m)dm =$ 0.297

m	=	0.9703	gms
L	=	0.48	cm
r	=	0.319	cm
ρ	=	6.323	$^{gms}/_{cm\hat{}3}$
	±	0.297	

$\rho_{theor.}$	=	14.3	$^{gms}/_{cm\hat{}3}$

%TD	=	44.2%
	±	2.1%

Sintered density error calculations (Archimedes)

$$\rho = \frac{m_{dry} * \rho_{H_2O}}{m_{dry} - m_{\text{Im}\,mersed}} = \frac{m_{dry} * \left(1.0017 - \left(0.0002315 * T_{H_2O}\right)\right)}{m_{dry} - m_{\text{Im}\,mersed}}$$

$$\frac{\partial\rho}{\partial m_{dry}} = \frac{-m_{dry} * \left(1.0017 - \left(0.0002315 * T_{H_2O}\right)\right)}{\left(m_{dry} - m_{\text{Immersed}}\right)^2} + \frac{1.0017 - \left(0.0002315 * T_{H_2O}\right)}{m_{dry} - m_{\text{Immersed}}}$$

$$\frac{\partial\rho}{\partial m_{\text{Immersed}}} = \frac{m_{dry} * \left(1.0017 - \left(0.0002315 * T_{H_2O}\right)\right)}{\left(m_{dry} - m_{\text{Immersed}}\right)^2}$$

$$\frac{\partial\rho}{\partial T_{H_2O}} = \frac{0.0002315 * m_{dry}}{m_{dry} - m_{\text{Immersed}}}$$

dm_{dry}	±	0.001	gms
$dm_{immersed}$	±	0.001	gms
dT_{H2O}	±	0.2	°C

$\partial\rho/\partial m\_dry$ =	135.489
$\partial\rho/\partial m\_immersed$ =	148.582
$\partial\rho/\partial T\_H2O$ =	0.003

error = (∂ρ/∂m_dry)dm_dry + (∂ρ/∂m_im)dm_im + (∂ρ/∂T)dT = 0.285

m_{dry}	=	0.8636	gms
$m_{immersed}$	=	0.7875	gms
T_{H2O}	=	23	°C
ρ	=	11.307	gms/cm^3
	±	0.285	

$\rho_{theor.}$	=	14.3	gms/cm^3

%TD	=	79.1%
	±	2.0%

APPENDIX D:
Thermodynamic Calculations of Uranium Nitride Reactions

From Barin *et al.* and Chase *et al.* [149, 164], the free energy of formation for UN at 1823.15 K and 1623.15 K (1550°C and 1350°C) is -137.042 $^{kJ}/_{mol}$ and -150.599 $^{kJ}/_{mol}$, respectively. According to Knacke *et al.* [99], the free energy of formation of U_2N_3 at 1350°C is -319.582 $^{kJ}/_{mol}$.

The calculation for Reaction 1 shows that at 1550°C, UN will dissociate into uranium metal and nitrogen gas if the nitrogen pressure is less then $1.423 \cdot 10^{-3}$ Pa. The calculation for Reaction 2 shows that at 1350°C, U_2N_3 will dissociate into UN and nitrogen at a nitrogen partial pressure of 24 Pa.

Reaction 1

$$UN \rightarrow U(l) + \frac{1}{2}N_2$$

$$\Delta G_f = -RT * \ln(K_{eq})$$

$$= -RT * \ln\left(\frac{a_U * \left(P_{N_2}\right)^{\frac{1}{2}}}{a_{UN}}\right)$$

$$= -\frac{RT}{2} * \ln P_{N_2}$$

$$\Delta G_f = \Delta G_U + \frac{1}{2}\Delta G_{N_2} - \Delta G_{UN}$$

$$= 0 + \frac{1}{2}(0) - (-137042)\left[\frac{J}{mol}\right]$$

$$\therefore P_{N_2} = 1.423 * 10^{-3}[Pa] = 14 ppb$$

$$\text{* At } 1550^{\circ}C$$

Reaction 2

$$U_2N_3 \rightarrow 2UN + \frac{3}{2}N_2$$

$$\Delta G_f = -RT * \ln(K_{eq})$$

$$= -RT * \ln\left(\frac{a_{UN}^2 * \left(P_{N_2}\right)^{\frac{3}{2}}}{a_{U_2N_3}}\right)$$

$$= -\frac{3RT}{2} * \ln P_{N_2}$$

$$\Delta G_f = \Delta G_{UN} + \frac{3}{2}\Delta G_{N_2} - \Delta G_{U_2N_3}$$

$$= -150599 + \frac{3}{2}(0) - (-319582)\left[\frac{J}{mol}\right]$$

$$\therefore P_{N_2} = 24.0[Pa]$$

$$\text{* At } 1350^{\circ}C$$

APPENDIX E:
Discussion and Review of Nitrogen Diffusion in Uranium

This is a review of research conducted in the area of diffusion of nitrogen in the uranium mononitride (UN) system and the difficulties associated with obtaining meaningful kinetics data. UN is a prospective fuel for an advanced fuel cycle because it possesses essential fuel-like properties including: high density, high thermal conductivity, and a high melting temperature. Therefore, knowledge of the kinetic properties for the UN system is important for modeling the chemical phases present over the life of a fuel element, especially at elevated temperatures. Due to the constantly varying composition and the formation of secondary phases at these elevated temperatures, the diffusion paths and diffusion rates vary dramatically making the kinetic analysis difficult.

Only a few authors have published data regarding kinetic studies of the UN system, possibly due to the challenges associated with obtaining diffusion coefficients and meaningful activation energies. One of the first published articles studying the nitrogen diffusion kinetics in the UN system was in 1969 by Holt and Almassy [165]. In their work, nitrogen self-diffusion in UN was measured with α-particle activation of ^{15}N (α-energy degradation method), as described in detail by Condit and Holt in a previous work [166]. The starting material was a 1 x 0.5 x 0.2 cm block of a UN crystal with large grains (~1 cm^2 in area). The two largest faces were surface ground flat to tolerances of ± 2 μm before the samples were annealed at 1673 K in 10^{-6} Torr vacuum for a "few minutes." An equilibrium anneal was then performed in ^{14}N at the same temperatures, pressures, and times as the subsequent diffusion anneal. The diffusion runs were completed in an N_2 atmosphere enriched to 95% ^{15}N with varying temperatures (2053-2273 K), pressures (7-600 Torr), and times (5-92 hours). It should be noted that the temperatures and nitrogen pressures were regulated during heating and cooling of the samples to stay within the narrow UN phase field. After the diffusion runs were completed and prior to irradiation, a shallow bevel (0.5-1.5°) was ground on the edge of the polished surfaces resulting in a 140 μm profile change (Figure 122a). The UN samples were irradiated and the specimen activity was measured from the nuclear reaction of $^{15}\mathrm{N}(\alpha, n)\,^{18}\mathrm{F}$, which produces radioactive ^{18}F when in the presence of ^{15}N. Figure 122b shows microdensitometer traces after successive exposure times of the sample after irradiation. The penetration distances were measured within ± 2 μm. The nitrogen diffusion was measured by correlating the concentration C at some distance y from the surface at some time t. With the surface concentration assumed constant, the following Equation 6 describes the penetration profile of nitrogen in UN:

$$C = C_0 * erfc\left(\frac{y}{2\sqrt{Dt}}\right) \qquad \text{(Eqn. 6)}$$

With this equation, a diffusion coefficient D can be found from knowing the concentration at some depth y and a known time t. Figure 123, adapted from the Holt and Almassy paper [165], shows the diffusion coefficients of nitrogen in UN from their own work compared with the work of Sturiale and DeCrescente [167]. Holt and Almassy state that the diffusion coefficients recorded by Struiale and DeCrescente were measured by a gaseous exchange technique that provided nitrogen diffusion coefficients approximately 5 times higher than their measurements.

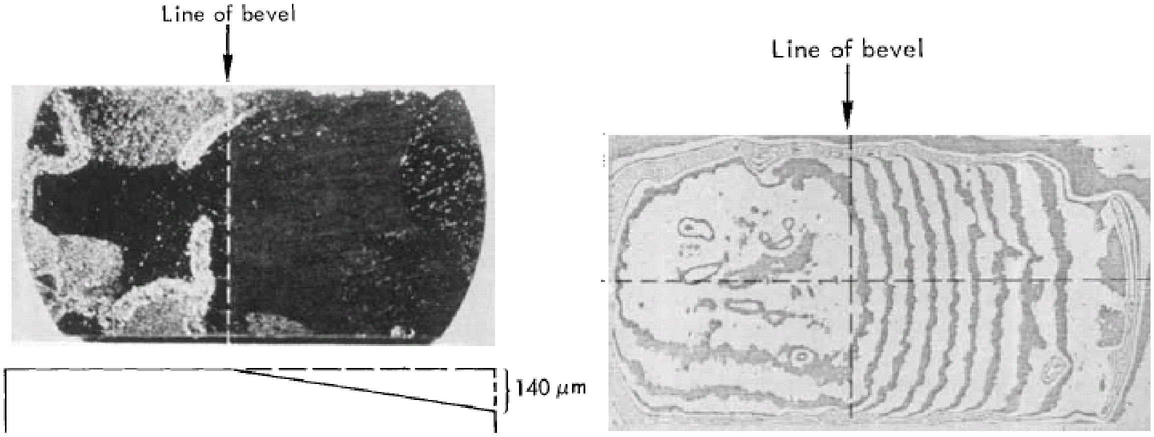

(a) (b)

Figure 122: Photographs from Holt and Almassy [165]. (a) Photograph of the top view and a schematic of the profile of the bevel ground into UN samples to study the diffusion of nitrogen. (b) Isodensitometer scan of the autoradiograph (optical density contour map) after irradiation of the UN samples.

The apparent activation energy of nitrogen diffusion in the UN system can be obtained from the plot in Figure 123. From this figure, the estimated activation energy of nitrogen interstitial diffusion from the work of Holt and Almassy is found to be 235 $^{kJ}/_{mol}$. Holt and Almassy then compared this to the work of Sturiale and DeCrescente, who estimated an apparent activation energy for grain boundary diffusion of 121 $^{kJ}/_{mol}$.

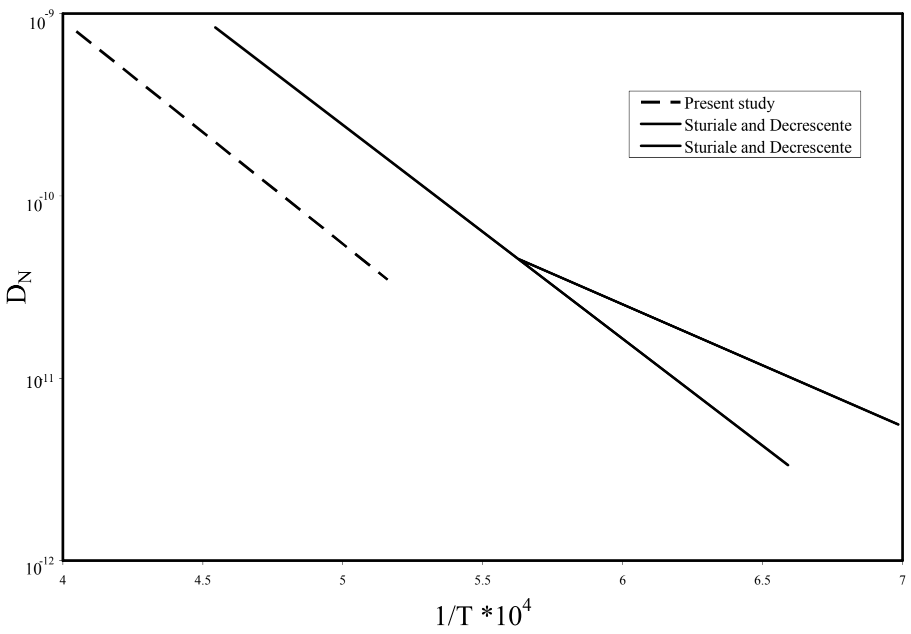

Figure 123: Graph presented by Holt and Almassy [165] comparing the diffusion coefficients of nitrogen in UN. The graph shows the work of Holt and Almassy compared with the data of Sturiale and DeCrescente [167].

The works of Sturiale and DeCrescente [167], Holt and Almassy [165], and Droege and Alexander [168] were compared by Hayes [169] in 1990 (Figure 124). However, the reports by Sturiale and DeCrescente and Droege and Alexander were not available for my review. The data presented in this review is merely data presented by Holt and Almassy [165] and Hayes [169].

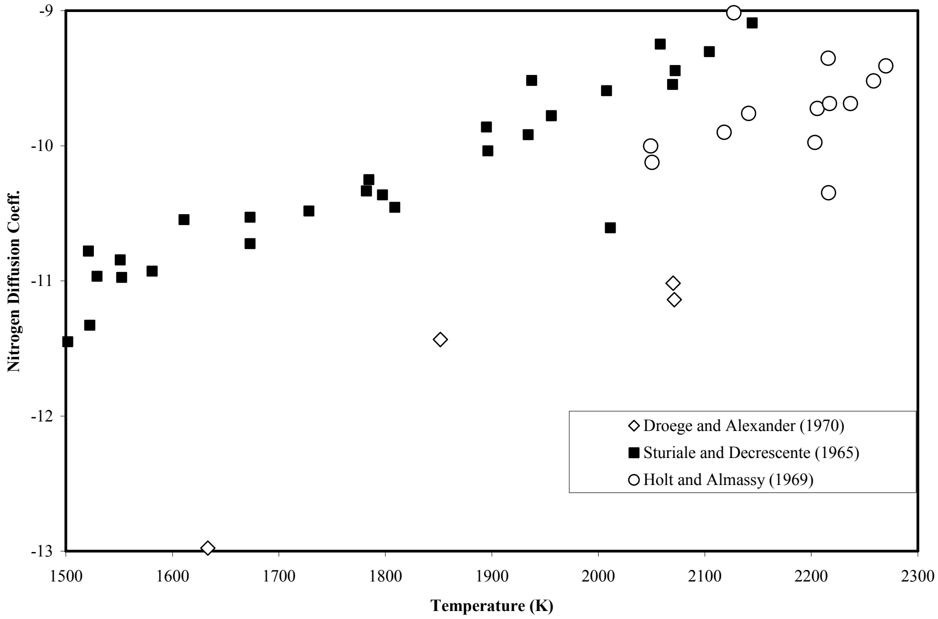

Figure 124: Compilation by Hayes [169] of three independent studies on the self-diffusion coefficient of nitrogen in the UN system. The work of Holt and Almassy and Struiale and DeCrescente were used to derive a temperature, pressure, and grain size dependent nitrogen diffusion coefficient relation.

Hayes states that “significant surface evaporation occurred to the test specimens prior to analysis” in regards to the data of Droege and Alexander [168]. Those four data points were disregarded because the surface evaporation “pulled-out” nitrogen from the crystal giving the appearance of a lower diffusion coefficient. This apparent diffusion coefficient does not represent the kinetics of nitrogen in the UN system well. Hence, Hayes only considered the other two works [165, 167] to obtain a “best-fit” equation for the self-diffusion coefficient of nitrogen, D_N, in the UN system. Hayes obtained Equation 7 as a function of the partial pressure of nitrogen (P, atm), the average grain size (g, μm), and the temperature (T, K).

$$D_{\mathrm{N\ in\ UN}} = 2.2516 * 10^{-5} * P^{0.4134} * g^{-0.737+(2.179*10^{-4}*T)} * \exp\left(\frac{-19214.7}{T}\right) \left[\frac{cm^2}{s}\right] \quad \text{(Eqn. 7)}$$

According to Hayes, Equation 7 is valid for; grain sizes in the range of 25-5000 μm, pressures less than 2.0 atm, temperatures in the range of 1500-2275 K, and substantially hyperstoichiometric UN. It should also be noted that this equation was formulated after two outlier data points were removed from the data set (Holt and Almassy at 2129 K and Sturiale and DeCrescente at 2013 K).

Hansjoachim Matzke is also one of the few authors to study nitrogen diffusion in the UN system. Most of Matzke's work pertains to carbide and oxide actinide fuels and much of it is presented in a textbook published in 1986 [56], although a more recent journal publication [170] will be the focus of this review. Figure 125, obtained from the Matzke paper, shows the Arrhenius plot for nitrogen diffusion in quasi-stoichiometric UN at 0.1316 atm (13.33 kPa) and a nitrogen partial pressure of 0.131 atm. However, sample preparation and experimental techniques used to analyze the kinetics of the UN system are not addressed in either case. It should be noted that the data used to construct this plot was not explicitly cited, but is presumed to also be from the work of Sturiale and DeCrescente [167], Holt and Almassy [165], and Droege and Alexander [168]. The data presented in Figure 125 shows only "some typical data points" and is a possible explanation of why the data in this figure does not appear as scattered as in Figures 123 and 124. This might also be an explanation of why the activation energies of nitrogen diffusion in UN are not the same. In this figure, Matzke was also able to determine the diffusion coefficient of nitrogen in quasi-stoichiometric UN at a constant partial pressure of nitrogen (0.1316 atm (13.33 kPa)). The equation obtained is:

$$D_{\mathrm{N\,in\,UN}} = 3*10^{-4}*\exp\left(\frac{-2.73\,\mathrm{eV}}{\mathrm{kT}}\right)\quad\left[\frac{cm^2}{s}\right] \qquad \text{(Eqn. 8)}$$

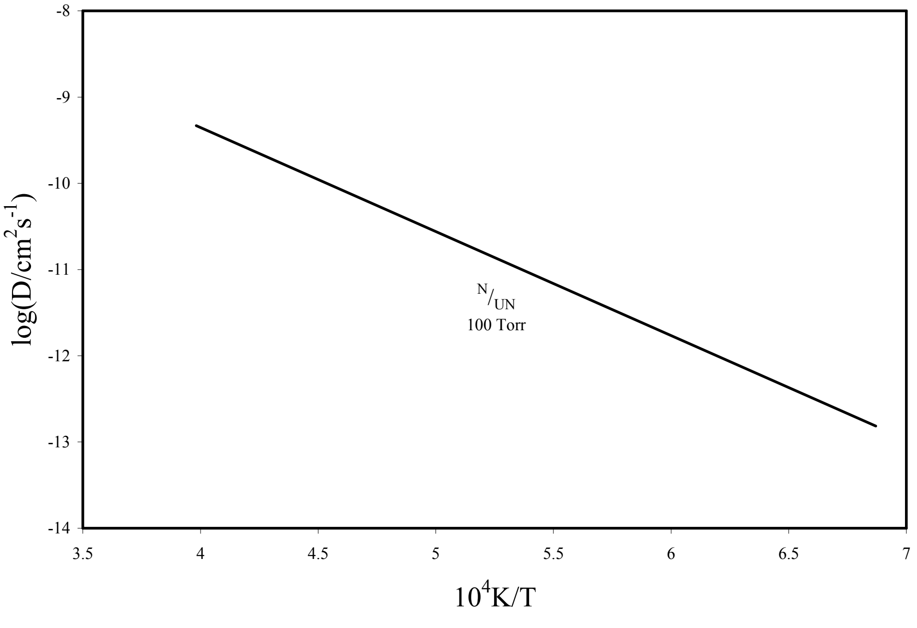

Figure 125: Compilation by Matzke [56, 170] showing an Arrhenius diagram for the nitrogen diffusion coefficient in quasi-stoichiometric UN at 0.1316 atm (13.33 kPa) with a nitrogen partial pressure of 0.131 atm. "Some typical data points" are only shown from the work of Sturiale and DeCrescente [167], Holt and Almassy [165], and Droege and Alexander [168].

The estimated activation energy for nitrogen diffusion in UN is calculated to be 263 $^{kJ}/_{mol}$ from Equation . Matzke also performed work to find the diffusion coefficient of nitrogen in UN by surface and vacancy diffusion. The surface diffusion coefficient D_s, also considered the mass transfer coefficient by Matzke, is generally given as a function of the number of adatoms n (cm^{-2}), the number of adsites N_s (cm^{-2}), and the intrinsic surface diffusion coefficient of adatoms $D_{s,a}$ [170]. The relation is shown in Equation 9.

$$D_s = \left(\frac{n}{N_s}\right) * D_{s,a} \qquad \text{(Eqn. 9)}$$

However, the surface diffusion coefficient in this study was found by measuring the mobility of rare-gas filled bubbles (experimental procedures are not discussed by Matzke). Figure 126 shows the Arrhenius plot of the diffusion of nitrogen via vacancy diffusion D_v^N and via surface diffusion D_s. The activation energy for either of the preceding mechanisms was not presented.

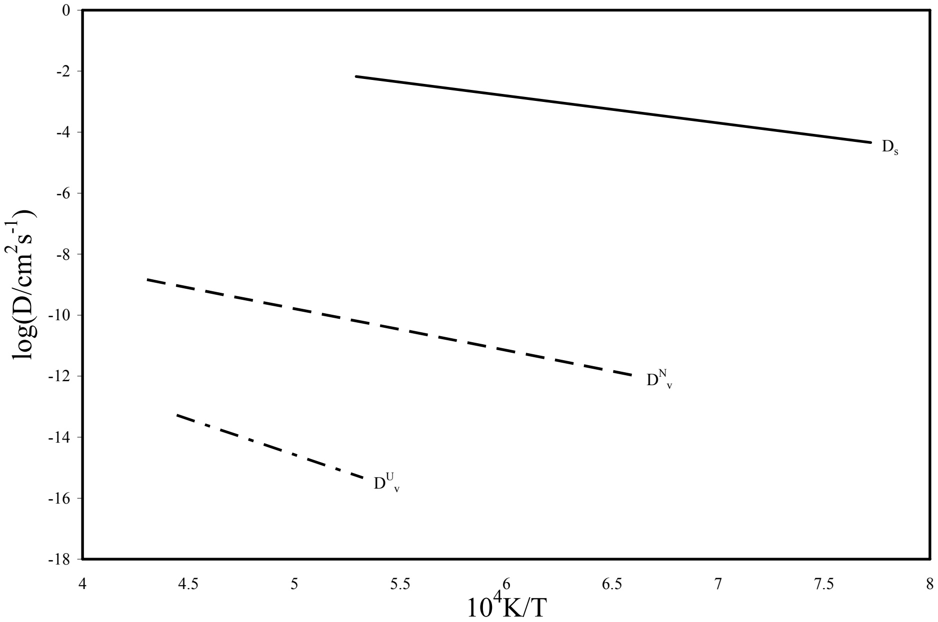

Figure 126: Compilation by Matzke [170] showing an Arrhenius diagram of the nitrogen diffusion coefficient via vacancy diffusion D_v^N and via surface diffusion D_s. Also shown in this figure is the diffusion coefficient of uranium via vacancy diffusion D_v^U.

We know that the rate-limiting mechanism is the slowest species via the fastest path. It is seen in Figure 127 that the diffusion of uranium is much slower than the diffusion of nitrogen in the UN system. This is a strong indication that the diffusion of uranium is the rate-limiting mechanism. Regardless, knowledge of the nitrogen diffusion mechanisms are essential "pieces of the puzzle" when studying the uranium mononitride system.

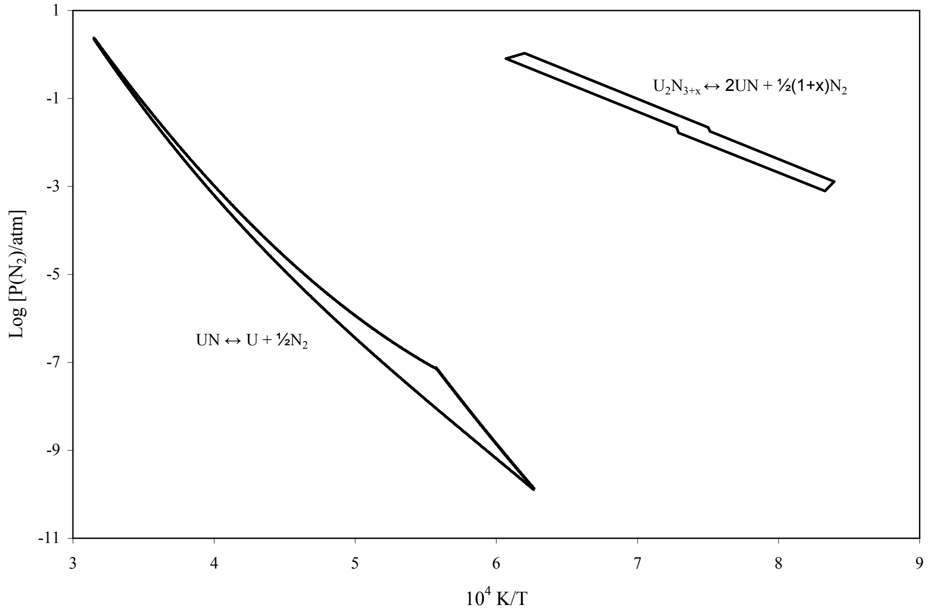

Figure 127: Figure adapted from Matzke [170] showing the decomposition pressures of uranium nitrides: U_2N_3 in equilibrium with UN, and UN in equilibrium with nitrogen-saturated uranium metal, indicating the phase field of the mononitride phase.

An important aspect of the studies reviewed in this work is that the activation energies of diffusion mechanisms are not meaningful since the compositions are not constant within the working parameters. Most of the papers still present an activation energy and propose a mechanism. Table 19 below summarizes the proposed mechanisms and estimated activation energies.

Table 19: Proposed nitrogen diffusion mechanisms and estimated activation energies suggested by individual authors in this review.

Author(s)	**Estimated activation energy for nitrogen diffusion in UN ($^{kJ}/_{mol}$)**	**Proposed diffusion mechanism of nitrogen in UN system**
Sturiale and DeCrescente [167]	121	Grain boundary diffusion
Holt and Almassy [165]	235	Interstitial diffusion
Matzke [170]	263	Interstitial diffusion
Matzke [170]	235-405	Various reports

Activation energies of nitrogen diffusion in UN will be difficult to obtain until a nitrogen partial pressure and composition relation is well understood for the stoichiometric UN system [56, 165, 170]. This is due to the narrow single-phase field of stoichiometric UN, seen when expressed in terms of N/U-ratios. Contrary, when the single-phase field is expressed in terms of nitrogen partial pressure it appears quite large (Figure 127).

Both of the review papers by Hayes [169] and Matzke [170] present the scattered diffusion data from the work of Holt and Almassy [165] and Sturiale and DeCrescente [167] (Figures 123 and 124). From this scattered data, Hayes developed an Equation for the diffusion of nitrogen in UN with up to 6 significant figures. As previously stated, the data is not meaningful because of the lack of a defined relationship between the composition and the partial pressures of nitrogen in the UN system. Adequate data does not seem to be available for Hayes to derive an equation as a function of grain size from only two data sets with scarce grain size analysis. Matzke, on the other hand, recognized multiple times throughout his paper that "no fundamental significance should be attributed to these activation enthalpies" and developed an Equation 8 with a more reasonable accuracy at a constant nitrogen partial pressure. The grain size effects are also neglected. In this work, Matzke identified a range of activation energies for nitrogen diffusion mechanisms from 232-405 $^{kJ}/_{mol}$ that were not explicitly attributed to individual works.

Matzke [170] implied that an interstitial mechanism for nitrogen diffusion occurred because of the dependence of nitrogen diffusion on the square root of the partial pressure of nitrogen. Holt and Almassy [165] assumed that the nitrogen atom is a single, negatively charged, interstitial ion with an accompanying electron hole as shown in Kroeger-Vink notation in Equation 10.

$$\frac{1}{2}N_2 + V_i = N_i' + \dot{h} \qquad \text{(Eqn. 10)}$$

Holt and Almassy stated that some of the discrepancy between data sets with Sturiale and DeCrescente is in the initial preparation. Holt and Almassy used a section of a uranium nitride boule with very large grains (some nearly ~1cm^2 in area) when Sturiale and DeCrescente used small ground particles of UN that "undoubtedly contained many micro-fractures and dislocations which could serve as small channels for the rapid diffusion of nitrogen." This would have provided a larger surface area (assuming the solid was not ground flat) and more grain boundaries leading to increased apparent diffusion. Again, due to the unavailability of the report of Sturiale and DeCrescente, it is not clear how the samples were prepared or how the analysis was performed, except that it was done by the "gaseous exchange technique."

All of the papers seem to conclude with one common diffusion mechanism of nitrogen in UN. The common mechanism of all of the papers is diffusion through nitrogen interstitials. However, as shown in the Table 19, the activation energy for the presumed grain boundary diffusion mechanism is the lowest and would therefore be the likely diffusion mechanism. But, due to the relation of the square root of the partial pressure of nitrogen to the diffusion coefficient, an interstitial mechanism is assumed. Much work still needs to be completed for the mechanisms to be better understood. More work studying micro-structural characterization techniques as well as properly documented and more precise studies are needed to allow other researchers to further analyze and draw valid conclusions from the data. One of the main drawbacks of this topic is the lack of data and the lack of experimental procedure detail.

APPENDIX F:

Standard Operating Procedure for: Synthesis of Depleted-UN Pellets by Carbothermic Reduction from Depleted-UO_2

NOTE: The primary radiological hazard of depleted Uranium compounds is ingestion. Depleted Uranium is a weak alpha-particle emitter and thus cannot penetrate the skin. This procedure is written in a way to "practice" safe handling techniques for more highly radioactive isotopes.

NOTE: The primary physical hazard of these materials is that they are pyrophoric.
BE CAREFUL WHEN HANDLING THE MATERIALS TO AVOID DIRECT EXPOSURE TO AIR!!

Materials/Consumables:	**Equipment:**	**Special Facilities Resource Needs:**
N_2 gas, N_2+ 6.28% H_2 mixed gas, H_2 gas, safety eyewear, latex gloves, laboratory apron/coat, Fantastic cleaner, $H_2$0 (Liquid), carbon powder, UO_2 powder, Graphite Crucible, disposable booties	**Vacuum/Hydrogen furnace with cooling water and moisture/oxygen getterers, Geiger counter, glove box, uni-axial press, pellet die, planetary milling machine and accessories (jars, media, clamps etc.), precise weigh scale**	**208 single phase power (H_2/Vacuum furnace), 110 single phase power (glove box), compressed H_2 gas supply, compressed N_2 gas supply, compressed Ar gas supply, cooling water**

Step	Description	Respirator	Safety Eyewear	Two pair of latex or nitrile gloves	Close-toed Shoes	Laboratory Coat
1	**All personnel authorized to work on this project must obtain Boise State University Radiation Safety Training Certification and abide by the BSU Radioactive Materials Management Manual, section 5: Individual Users.**					
2	**Whenever an area is to be utilized for radioactive material handling it should be marked off with a caution tape bearing "Radioactive Material." These areas include; furnaces, fume-hoods, sinks, bench tops and immediate transportation routes.**					
3	**The "two-person" rule will be followed at all times of radioactive material handling.**					
4	**When radioactive material is obtained from an outside vendor, the procedures listed in the BSU Radioactive Materials Management Manual, section 7: Procurement and Inventory of Radioactive Materials must be followed. In addition to these guidelines the following criteria must be**					

	satisfied: **a. Check that the correct MSDS is in the MSDS binder in Micron Engineering Center room 213. Be sure to read and understand the associated risks of each material.** **b. Check that the correct documents from the Boise State University Radiation Safety Officer are in the Radioactive Material Record binder located in the Micron Engineering Center room 213.** **DO NOT PROCEED unless a and b are both satisfied.**					
	NOTE: Anytime a radioactive material is used or discarded, maintain a log in the Radioactive Material Record binder located in Micron Engineering Center room 213 in accordance with the BSU Radioactive Materials Management Manual, section 7: Procurement and Inventory of Radioactive Materials.					
5	**To begin the experiment, transfer all essential materials into the glove box for blending and milling of the powders.**	**X**	**X**	**X**	**X**	X
6	**Inside the glove box, clear the work area. Cover it with absorbent paper to make clean up easier. Also, mark an area with tape on this piece of paper to place all apparatuses used for handling radioactive materials. (Approximately a 6-inch square.)**		**X**		**X**	X
7	**On all four gloves in the glove box, place a disposable glove on to help prevent future contamination.**		**X**		**X**	X
8	**Open and make readily available the contaminated waste container labeled "Radioactive Waste Material" in the glove box.**		**X**		**X**	X
	NOTE: If any type of spill occurs at any time throughout the experiment, refer to the BSU Radioactive Materials Management Manual, section 10: Emergency Procedures.					
9	**In the glove box, weigh the predetermined amounts of the different powders in each corresponding weigh dish with the corresponding scoopula.** **Place the contaminated scoopula in the marked region and the non contaminated scoopula somewhere on the absorbent paper but away from the contaminated pieces.**		**X**		**X**	X
10	**One at a time, with the UO_2 powder being last, pour each of the powders into the milling jar containing the correct type, size, and quantity of media. Be sure that all of the powders successfully enter the milling jar.** **Place the contaminated weigh dish in the marked region and the non-contaminated on the absorbent paper away from the contaminated pieces.**		**X**		**X**	X
11	**Place the lid and the lid clamp on the milling jar. Tighten the clamp to ensure the lid is sealed.**		**X**		**X**	X
12	**Transfer the milling jar out of the glove box. Check the jar for contamination with the Geiger counter.** **a. If there are no appreciable signals then proceed to**	**X**	**X**	**X**	**X**	X

	the next step. **b. If there is an appreciable signal;** **• Clean the outside of the jar/mill thoroughly with the Fantastic solution and a towel/wipe. Repeat until no appreciable signals are received.**					
13	**Fasten the milling jar to the PM100 planetary milling machine as described by the operating procedures for the machine. Adjust the rotational speed and milling duration accordingly**	**X**	**X**	**X**	**X**	X
14	**Before removing the milling jar after the milling procedure is complete, check the jar and mill for contamination.** **c. If there are no appreciable signals then proceed to the next step.** **d. If there is an appreciable signal;** **• Clean the jar/mill thoroughly with the Fantastic Solution and a towel/wipe. Repeat until no appreciable signals are received.**	**X**	**X**	**X**	**X**	X
15	**Transfer the milling jar and its contents back into the glove box.** **Be sure that all four glove box gloves still have the disposable gloves on them and that they are not perforated.**					
16	**Loosen the nuts on the lid clamp and remove the lid to the milling container. Work on the absorbent paper to reduce further contamination. Place the lid in the contaminated material marked section on the absorbent paper.**		**X**		**X**	X
17	**Remove the milling media with the same contaminated scoopula used to transport the UO_2 for weighing. Place the media into the contaminated weigh dish. Pour the powder mixture into the other weigh dish. Place both weigh dishes in, or around, the contaminated material marked region.**		**X**		**X**	X
18	**Place the contaminated milling media into a small zip-loc bag and seal for future use.**		**X**		**X**	X
19	**Using the same scoopula, fill the pellet die with the powder mixture.**		**X**		**X**	X
20	**Cover a majority of the lower platen with the absorbent paper prior to placing the die in the uni-axial press. Once the die is loaded, place a piece of absorbent paper between the upper platen and the plunger of the die. Press to the predetermined pressure for the predetermined time. Remove die.**		**X**		**X**	X
21	**Remove the pellet from the die. The pellet should fall from the die onto the paper covering the lower platen**		**X**		**X**	X
22	**Using forceps, place the pellet into the desired boat/crucible.**		**X**		**X**	X
23	**Make sure the furnace and furnace area is ready to accept the sample by doing the following:**		**X**	**X**	**X**	X

	a. Remove the end cap and gasket on the loading side of the furnace and place them close to the entrance of the furnace, b. A stainless steel guide rod is made readily available (for placement of the crucible in the hot zone of the furnace), c. A screwdriver to secure the end cap and gasket back on to the furnace, d. Tape a piece of absorbent paper under the loading side of the furnace tube to contain any possible spills that may occur during loading, and e. Mark an area on the absorbent paper to place all apparatuses used for handling the materials.					
24	**Transport the sample pellet(s) to the furnace for sintering.**	**X**	**X**	**X**	**X**	X
25	**Place the crucible directly into the tube of the furnace. Do not set the crucible down outside of the glove box and/or the furnace unless it is absolutely necessary. Use the guide-rod to place the crucible in the hot-zone of the furnace tube. Fasten the end-cap and gasket in place with the screw-driver.**	**X**	**X**	**X**	**X**	X
26	**Run the predetermined furnace/vacuum profile.**					
27	**Before leaving the work area, allow the second person monitor your hands (particularly the both sides of the outer gloves) using the geiger counter.** **a. If there is no appreciable signal, proceed to handle the Geiger counter.** **b. If there is an appreciable signal, safely remove the outer pair of gloves and dispose of in the special container labeled "Radioactive Waste" kept nearby the hood. Now have the second person check for any contamination on the inner pair of gloves.** **1. If there is no appreciable signal, put another pair of gloves on and proceed to the next step.** **2. If there is an appreciable signal, remove the gloves and have the second person check your bare hands for contamination.** **I. If your bare hands produce an appreciable signal, wash gently with soap and water. Repeat until there is no appreciable signal.** **II. If your bare hands do not produce an appreciable signal, put two more pairs of gloves on and proceed to the next step.**	**X**	**X**	**X**	**X**	X

NOTE: Have the second person dispense the soap onto your hands so as to not contaminate the soap dispenser.

28	**With the geiger counter, monitor the tightened end-cap, the screw-driver, the guide rod and the glove-box transfer chamber handle.** **a. If there are no appreciable signals then proceed to the next step.** **b. If there is an appreciable signal in any of the parts mentioned,** **1. Clean the part thoroughly with the Fantastic Solution and a towel/wipe.** **2. Again monitor for an appreciable signal. Repeat the process until there are no appreciable contamination signals.**	**X**	**X**	**X**	**X**	X
29	**With the geiger counter, monitor your laboratory coat and your close-toed shoes for an appreciable signal.** **a. If there are no appreciable signals then proceed.** **b. If there is an appreciable signal in any of the articles mentioned, carefully remove the article(s) and place it(them) in a sealed container. Label the container with a caution label bearing "Caution: Radioactive Material." Monitor both sides of your body (from head to toe) with the help of the stand-by personnel.** **1. If there are no appreciable signals then proceed to the next step.** **2. If an appreciable signal is obtained, DO NOT PROCEED until no appreciable signal is obtained.** **• Wash the contaminated area with soap and water and then dry the area with a clean dry tissue paper.** **• Again monitor the contaminated area for signal with the help of the stand-by. If there is any signal remaining, contact the RSO immediately.**	**X**	**X**	**X**	**X**	X
	NOTE: Be sure that the work area is marked with a caution tape bearing "Radioactive Material" for the duration of the experiment.					
30	**When the furnace profile is complete and it has cooled to room temperature, place the glove bag on the end of the furnace with the following placed inside;** **a. Screwdriver for furnace end caps,** **b. Sealable jar for the sample, and** **c. Stainless steel guide rod for the boat.**		**X**	**X**	**X**	X
31	**Seal the glove bag around the end of the furnace tube. Proceed to purge the bag with nitrogen multiple times.**		**X**	**X**	**X**	X
32	**Remove the end cap and set it down inside the glove bag.**		**X**		**X**	X

33	**With the stainless steel guide rod, slide the boat to the open end of the tube of the furnace. Remove the boat containing the sample. Place only the sample in the sealable jar in the glove bag**		**X**		**X**	X
34	**Remove the glove bag from the end of the furnace tube (be careful to keep the oxygen content within the bag as low as possible by sealing the bag from the furnace before it is removed from the furnace.) Transfer the glove bag and everything in it, into the glove box**		**X**		**X**	X
35	**Once the materials are in the glove box, remove the jar containing the sample and seal it in secondary containment for future analysis.**		**X**		**X**	X
36	**Remove the glove bag and all materials with in it from the glove box and check for contamination as in previous steps**	**X**	**X**	**X**	**X**	X
37	**Check the absorbent paper placed in all work areas with the geiger counter.** **a. If there are no appreciable signals then proceed to throw the absorbent paper in the common waste bin.** **b. If there is an appreciable signal in any of the sections of paper, place the paper in the radioactive waste container.**	**X**	**X**	**X**	**X**	X
38	**Place the end cap and gasket back on to the furnace. Check the system for contamination with the geiger counter.** **a. If an appreciable signal is received, clean the part thoroughly with the Fantastic solution and a towel/wipe.**	**X**	**X**	**X**	**X**	X
39	**Check all parts used throughout the process for contamination.** **a. If there are no appreciable signals then proceed to end the experiment.** **b. If there is an appreciable signal in any of the checked parts,** **1. Clean the part thoroughly with the Fantastic Solution and a towel/wipe.** **2. Again monitor for an appreciable signal. Repeat the process until there are no appreciable contamination signals. Dispose the towels/wipes in the Radioactive Waste Container.**	**X**	**X**	**X**	**X**	X

Radioactive Material Waste Removal:
Inform the RSO to pick the radioactive material waste once any of the containers become 80% full or in accordance with the Radioactive Materials Management Manual, section 11: Storage and Disposal of Radioactive Wastes.

Wipe Test:

Wipe tests must be performed every time a radioactive experiment is performed. The tests should follow the standard given in the Radioactive Materials Management Manual section 8: Labeling, Shielding, and Monitoring. The wipes should come from the following areas:

a. The floor area under the furnace,
b. The surface on the furnace table under the tube of the furnace,
c. The floor of the glove box
d. The transfer chamber and plate, and
e. At selected areas on the floor between glove box and the furnace.

All wipe tests should formally be recorded.